SPECIAL REPORT 91-3

2

In-Situ Heat Flux Measurements in Buildings

Applications and Interpretations of Results

Stephen N. Flanders, Editor

February 1991

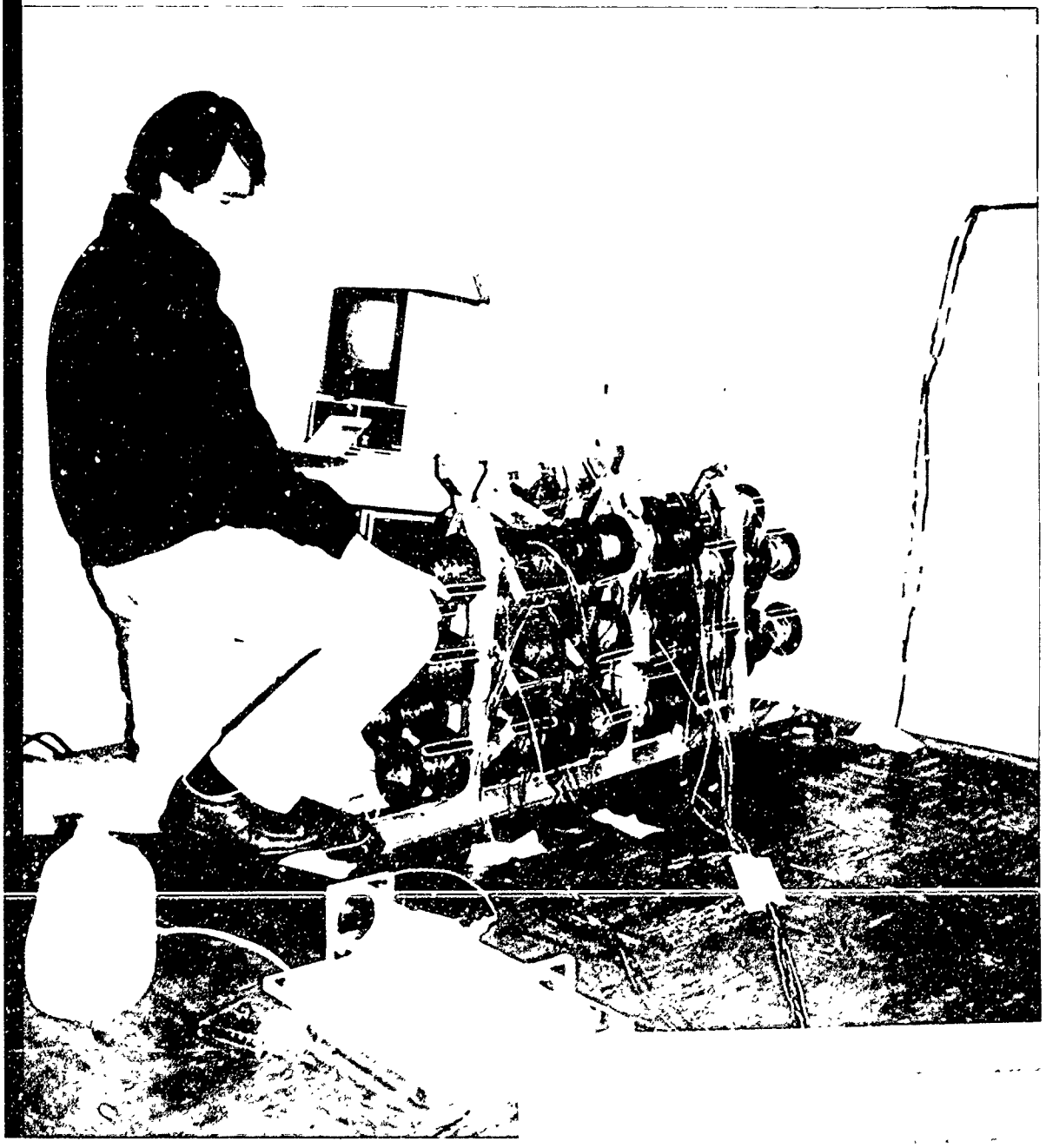

For conversion of SI metric units to U.S./British customary units of measurement consult ASTM Standard E380, Metric Practice Guide, *published by the American Society for Testing and Materials, 1916 Race St., Philadelphia, Pa. 19103.*

This report is printed on paper that contains a minimum of 50% recycled material.

Cover: Heat flux and temperature measurement of a building wall.

In-Situ Heat Flux Measurements in Buildings

Applications and Interpretations of Results

Stephen N. Flanders, Editor
U.S. Army Cold Regions Research and Engineering Laboratory
Hanover, New Hampshire

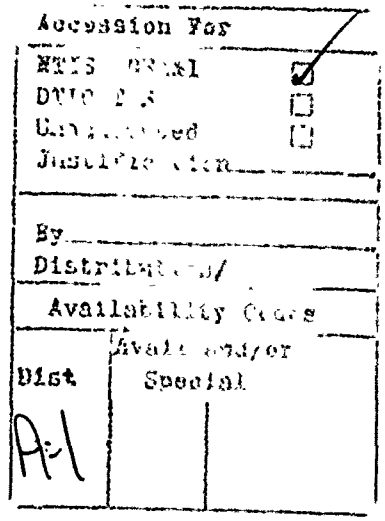

Proceedings of a workshop sponsored by

U.S. Army Cold Regions Research
and Engineering Laboratory

Building Thermal Envelope Coordinating Council

National Institute of
BUILDING SCIENCES

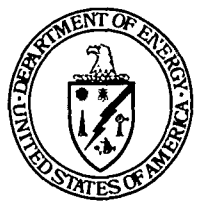

United States
Department of Energy

Special Report 91-3

FOREWORD

This publication contains papers that were the subjects of presentations at the Workshop on In-Situ Heat Flux Measurements in Buildings, held at the U.S. Army Cold Regions Research and Engineering Laboratory in Hanover, New Hampshire, on May 22–23, 1990. Stephen N. Flanders presided as workshop chairman and is the editor of this publication. The papers contained herein were each evaluated by two peer reviewers.

The workshop and this publication are sequels to a workshop held by the American Society for Testing and Materials (ASTM) in Philadelphia in 1982 and the proceedings of that workshop, *Building Applications of Heat Flux Transducers*, STP 855, published by ASTM in 1983. A paper that was submitted to be part of this publication by Yurii A. Kovalenko, Institute of Thermophysics, Siberian Branch of the USSR Academy of Sciences, arrived too late to be included in the workshop. This work is being published separately as a CRREL Special Report entitled, *Thermal Conductivity of Porous Media and Soils: A Review of Soviet Investigations.*

The workshop and this publication were sponsored by the U.S. Army Cold Regions Research and Engineering Laboratory, the Building Thermal Envelope Coordinating Council, the National Institute of Building Sciences, and the U.S. Department of Energy. In addition to Chairman Flanders, the workshop steering committee comprised William C. Brown, National Research Council, Canada; George Courville, Oak Ridge National Laboratory; Andre Desjarlais, Holometrix, Inc.; and Russel T. Mack, Dow Chemical U.S.A. Edmund A. Wright copyedited the papers in this publication.

LIST OF ATTENDEES

Ronald Atkins
USACRREL
72 Lyme Road
Hanover, NH 03755-1290

Troy Bearden
Dow Chemical
Texas Operations
B-2406
Freeport, TX 77541

William C. Brown
National Research Council Canada
Building M-24, Montreal Road
Ottawa, Ontario, Canada K1A 0R8

Douglas M. Burch
NIST
Room R320, Building 234
Gaithersburg, MD 20899

Jeffrey Christian
Oak Ridge National Laboratory
Building 3147
P.O. Box 2008
Oak Ridge, TN 37831-6070

Andre Desjarlais
Holometrix, Inc.
99 Erie Street
Cambridge, MA 02139

Ashley F. Emery
Dept. of Mechanical Engineering
University of Washington
Seattle, WA 98195

Prof. Robert Erickson
University of Minnesota
2004 Folwell Ave.
St. Paul, MN 55108

Hunter Fanney
NIST
Building 226, Room B322
Gaithersburg, MD 20882

Stephen Flanders
USACRREL
72 Lyme Road
Hanover, NH 03755-1290

Prof. William P. Goss
Gunness Laboratory 12
Mechanical Engineering Department
University of Massachusetts
Amherst, MA 01003

Frederik van der Graaf
TNO Institute of Applied Physics
P.O. Box 155
Delft, Netherlands 2600 AD

Dr. James Kirkwood
Ball State University
Department of Industry & Technology
Muncie, IN 47306

Timothy Larson
University of Minnesota
2004 Folwell Ave.
St. Paul, MN 55108

Dr. David J. McCaa
Certainteed Corporation
1400 Union Meeting Rd.
Blue Bell, PA 19442

Russel Mack
Dow Chemical
Texas Operations
Freeport, TX 77541

Charles Mitchell
AGEMA Infrared Systems
550 County Ave.
Secaucus, NJ 07094

Eugene L. Perrine
Consultant
10 Independence Square
Bloomington, IL 61704

Thomas W. Petrie
Oak Ridge National Laboratory
P.O. Box 2008
Oak Ridge, TN 37831-6070

Richard Piper
R.J. Kenney Associates Inc.
P.O. Box 1748
Plainville, MA 02762

Dr. Anne Silberstein
CRIR—Isover St. Gobain
B.P. 19
60290 Rantigny, France

Pierre Thery
Université des Sciences
de Lille Flandres Artois
Batiment P3 - 3e Etage—UFR I.E.E.A.
59655 Villeneuve d'Ascq
France

Jerry Wilson
US DOE
P.O. Box 5400
Albuquerque, NM 87115

CONTENTS

HISTORY OF HEAT FLUX TRANSDUCER USE

DESIGN, CONSTRUCTION, AND APPLICATION OF HEAT FLUX TRANSDUCERS TO THE STUDY OF INSULATIONS DURING THE 1950s

E.L. Perrine

Wiss, Janney, Elstner Associates
Bloomington, Illinois USA

ABSTRACT

A need for field performance data on insulations led to a search for suitable heat flux transducers. When commercially available transducers were not found, heat flux transducers were constructed using materials and designs similar to those which were being developed by the American Society of Heating and Ventilation Engineers at that time. Thin bimetallic ribbons, thin strips of electrical insulation and adhesive in sheet form were woven into matts which provided transducers with sensor areas of 100 square in. and larger. The units had low thermal resistance, stable calibration factors and good resistance to damage. Tests were performed under field conditions, on many insulated buildings, in various parts of the United States.

In-situ heat flux measurements have always been needed. They are needed because it is often impossible to predict the actual performance of insulation systems using the geometry of the construction and laboratory test data on the components. In 1951, when I began my career in thermal insulation, there were other, and larger, uncertainties than exist today. These included the accuracy of laboratory measured conductivities of building components, convection in insulations and air spaces, radiation, and moisture effects. The company which I joined in 1951 produced vermiculite. It was used as loose fill insulation and as aggregate in insulating concrete. The thermal performance of vermiculite truly was unknown for the following reasons:

1. Handbooks, and other books on insulation, which listed data from well-known laboratories, often reported, in the same tables, thermal conductivities for vermiculite of both 0.32 and 0.48 Btu-in./hr-sf-°F.[1] Other data in company files from outside test laboratories showed a range of more than two to one.
2. A study of fuel usage made in Chicago by the local gas company was also available. The attics in two groups of houses of similar construction had been insulated in the early 1930's with loose fill rock wool and vermiculite. The application thickness was 3 in. in all of the houses. Annual fuel bills over a few years' time showed no significant difference in the effectiveness of the two insulations. The same laboratory, U.S. National Bureau of Standards, that had found a "k" of 0.48 for vermiculite had reported a "k" of 0.27 for rock wool.[1] For both products, the insulation used in the houses was not the material tested by the laboratory.

3. Convection effects in attic insulations had been reported, but data were very limited.[2]
4. Radiation effects were recognized, but the effect on insulation performance in attics had not been quantified.
5. Mass effects were known to be significant. There was ample evidence that the mass of masonry walls and of concrete roof decks reduced peak heat loads. Substantially improved summer thermal performance of buildings often had been observed, but even rough quantitative evaluation methods had not been developed.
6. Moisture effects had been investigated, but data were sketchy. An article, by someone not connected with the company, concluded that each 1% increase in moisture increased the thermal conductance of organic materials by 4% and that of inorganic materials by 2%. We liked that because "k" tests are made in the oven dry condition, and most inorganic materials, including vermiculite, are less hygroscopic than organic materials.
7. There was another problem. It was nontechnical. The company was primarily a raw material producer. More than half of the ore produced was processed and sold by small licensee companies.

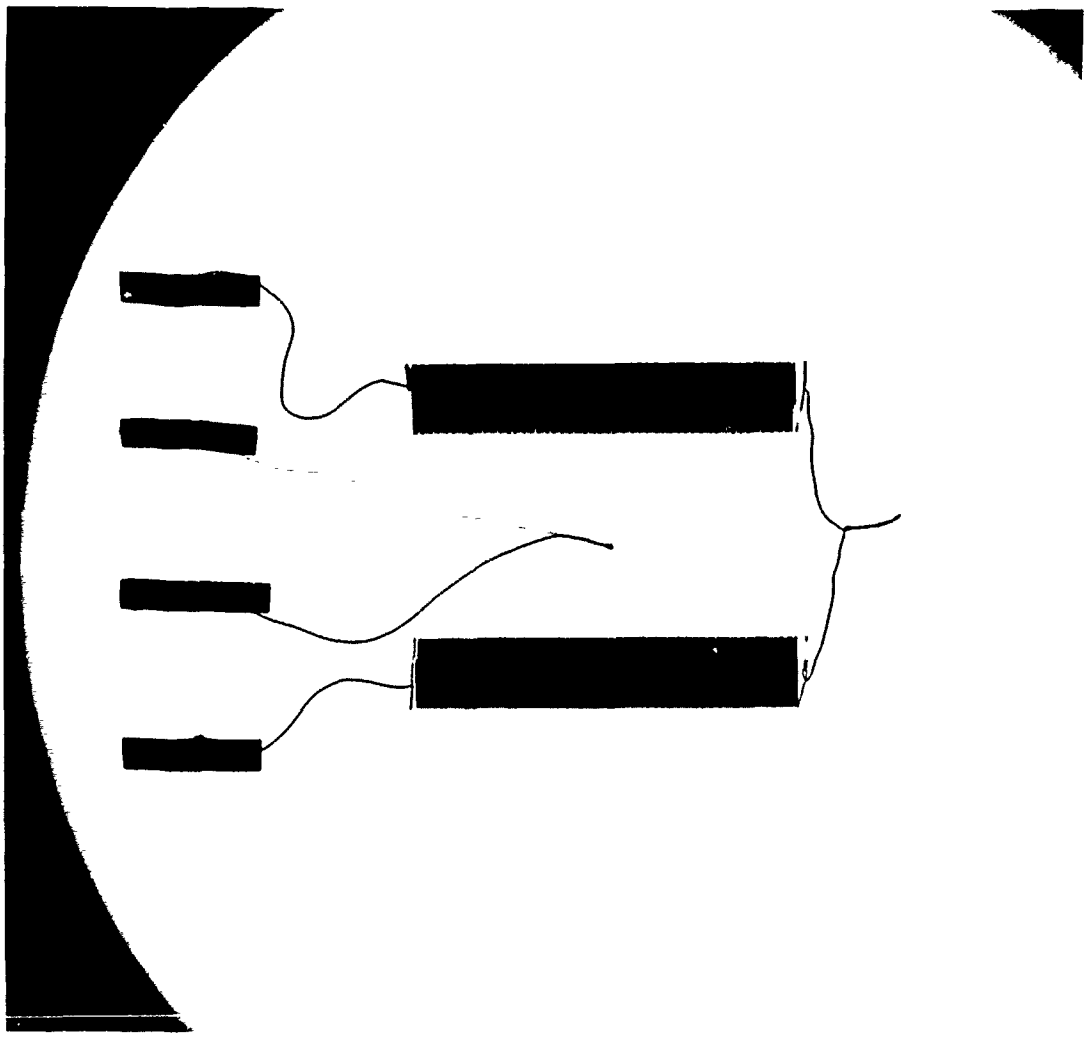

Figure 1 X-ray of a 1951 heat flux transducer showing small area sensor. Thermopile was formed by plating a material of low electrical resistivity on one-half of a winding of high electrical resistivity.

Several of these companies were very aggressive promoters. Like many of their competitors, they favored the use of the most advantageous test data, even if it came from little-known or unreliable laboratories.

The need for both laboratory and field data was obvious. Accurate, steady-state, laboratory data would determine if the significant variations in gradation and processing conditions, which could be employed in the vermiculite production, would result in the wide range of conductivities reported. But only field data would provide the needed in-use performance data for vermiculites and comparisons with other products. In-situ measurements would permit the observation of diurnal heat flux cycles. Thermal lags due to the mass of insulations and other building components could be evaluated. Effects of moisture in insulations under used conditions could be observed.

A search was made for commercially available heat-flux transducers. None of those that we located would provide us the instrumentation that we felt was desirable. The most commonly used transducer was about 5 in. square, but the sensing area in the unit was two strips, 2 in. long, spaced about 1 1/2 in. apart (Fig. 1). We were considering constructing our own transducers using fine thermocouple wire to build a large area thermopile on a thin layer of insulating material. Fortunately, before we embarked on such a construction program, we learned that the American Society of Heating and Ventilating Engineers (now the American Society of Heating, Refrigeration and Air Conditioning Engineers, ASHRAE) laboratory in Cleveland, Ohio, was building some large area, low thermal resistance heat flux transducers. We visited the laboratory and learned that the construction consisted of a thin bimetallic ribbon woven with strips of thin insulation. The bimetallic copper-constantan strip was formed so that the two metals were edge-to-edge in a 0.002-in.-thick ribbon. By notching the edges on alternate sides, to a point slightly more than one-half way across the strip, a series of alternating positive and negative thermocouples was formed (Fig. 2). When woven with the insulation material, the positive and negative thermocouples were on alternate sides of the insulation, forming a thermopile. The insulation used was a 0.020-in.-thick phenolic sheet (Fig. 3). Thin layers of electrical insulation were applied to both sides and thin anodized aluminum faces were applied to the outside of the assembly. All the components were laminated together with a heat activated adhesive. The ASHVE laboratory generously supplied us a list of all the materials used, the names of suppliers, and detailed construction techniques. This information was published later in the ASHVE Transactions[3]. Materials similar to those used by the ASHVE laboratory were obtained and units were soon produced.

Figure 2 A bimetallic ribbon notched to form a series of thermocouples for the thermopile in the heat flux transducers.

Most of the transducers constructed had a metering area approximately 10 in. square. The overall size was 11 in. square. There were 50 thermocouple pairs in the 100-in.^{2} metering area. By cutting the thermocouple and insulating strips narrower, a few transducers were constructed with 200 thermocouple pairs in the same metering area.

Initial output vs. heat flux calibrations were made using a guarded hot box apparatus as the heat flux source. Each of two transducers was sandwiched between two 1-in. pieces of insulation of known conductance. The guarded hot plate apparatus used was not of ideal dimensions because the test area was 8 in. square and the guard area was 4 in. wide. However, surface temperatures measured at the hot and cold plates were found to be uniform. These, with the known conductivities of the insulation layers, were used to quantify the heat flux. Additional calibration tests were performed with 1/8-in.-thick aluminum plates added adjacent to one side of the transducers. Also, tests were made with wider borders or guard areas on the transducers. Calibration differences, due to these varied test conditions, were all found to be under one percent. The differences were judged to be insignificant variations for the planned field studies. This was especially valid because the primary interest was to compare the installed performance of various insulations due to material properties and installation details present. Later, similar calibration tests were made with the transducers mounted on various specimens of known conduction undergoing tests on a calibrated hot box. Again, the calibration was not significantly different on low and high conductivity materials.

No calculations were made to evaluate the distortion of the heat flow path due to the additional insulation added in the metered area by the transducer. However, it was noted that the total thickness of the nonmetallic components (phenolic electrical insulation and adhesive) used in the

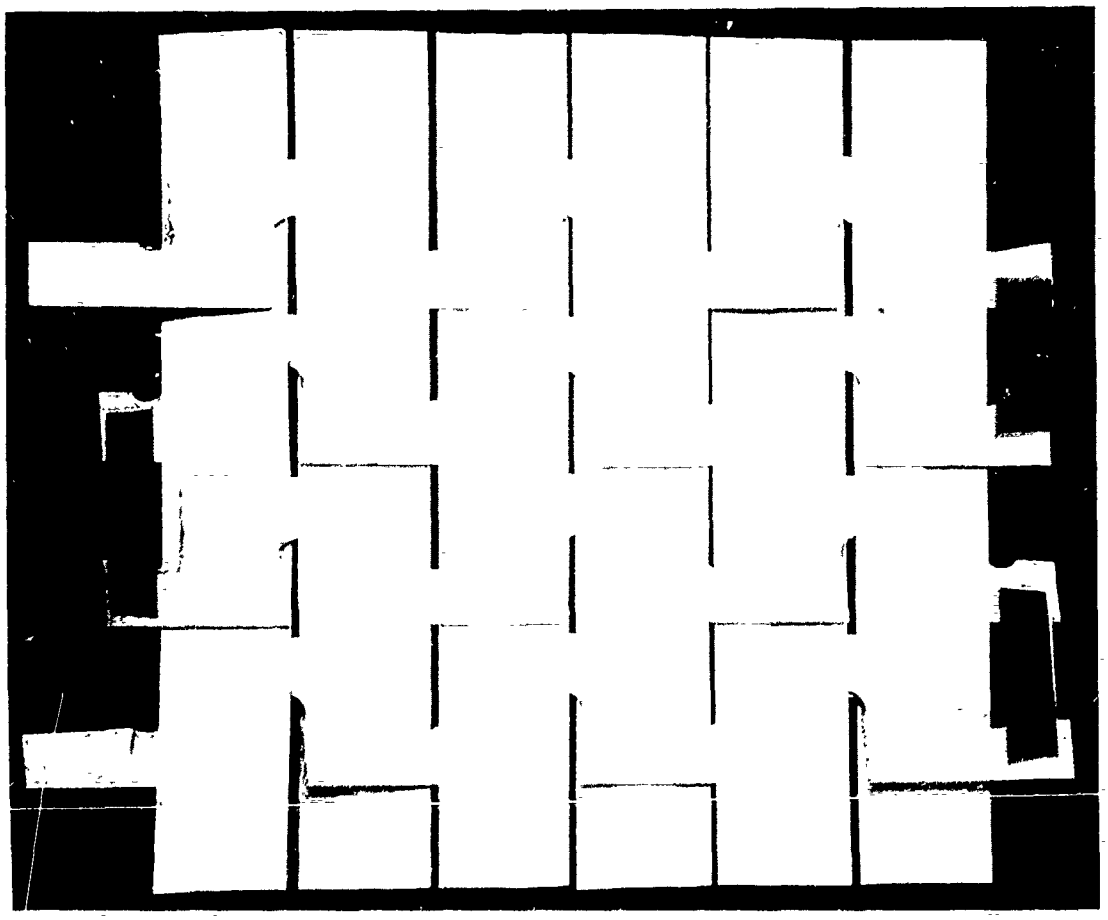

Figure 3 Weaving used in the construction of the heat flux transducers.

transducers was only approximately 0.035 in. This added less than two percent to the thermal resistance of even the lowest resistance building elements being evaluated.

For field use, the output of the transducers was sufficient to be read on portable, taut suspension, beam-of-light galvanometers. The only power required was a battery for the lamps in the galvanometers.

Support frames were constructed for the transducers which pressed them firmly to the building element being tested (Figs. 4 and 5). They also formed a tight seal between the edge of the transducer and the tested surface. Tests of this application method on smooth surfaces showed very small differences in measured heat flux when comparisons were made with fully adhered transducers.

HEAT FLOW METER DEMONSTRATED. Dr. George E. Ziegler (right), director of research for the Zonolite Company, and Eugene Perrine, senior physicist, demonstrate the heat flow meter they are using to obtain new facts about insulation. The instrument, which converts heat flow to electric current for measurement, is the newest scientific tool in the study of heat and insulation.

Figure 4 Frame used to hold heat flux transducer in contact with the building element being tested.

Initial tests in the laboratory showed a problem that still exists today. Wide swings in output resulted from even the smallest air currents. This caused us to try draft shields around the test areas and heavier aluminum faces on the exposed sides of the transducers. Only modest improvement resulted.

In most instances air temperatures and wind velocities were measured during field tests. These and the heat flux measurements were used to calculate the thermal performance of the building elements. In laboratory tests surface temperatures were also measured.

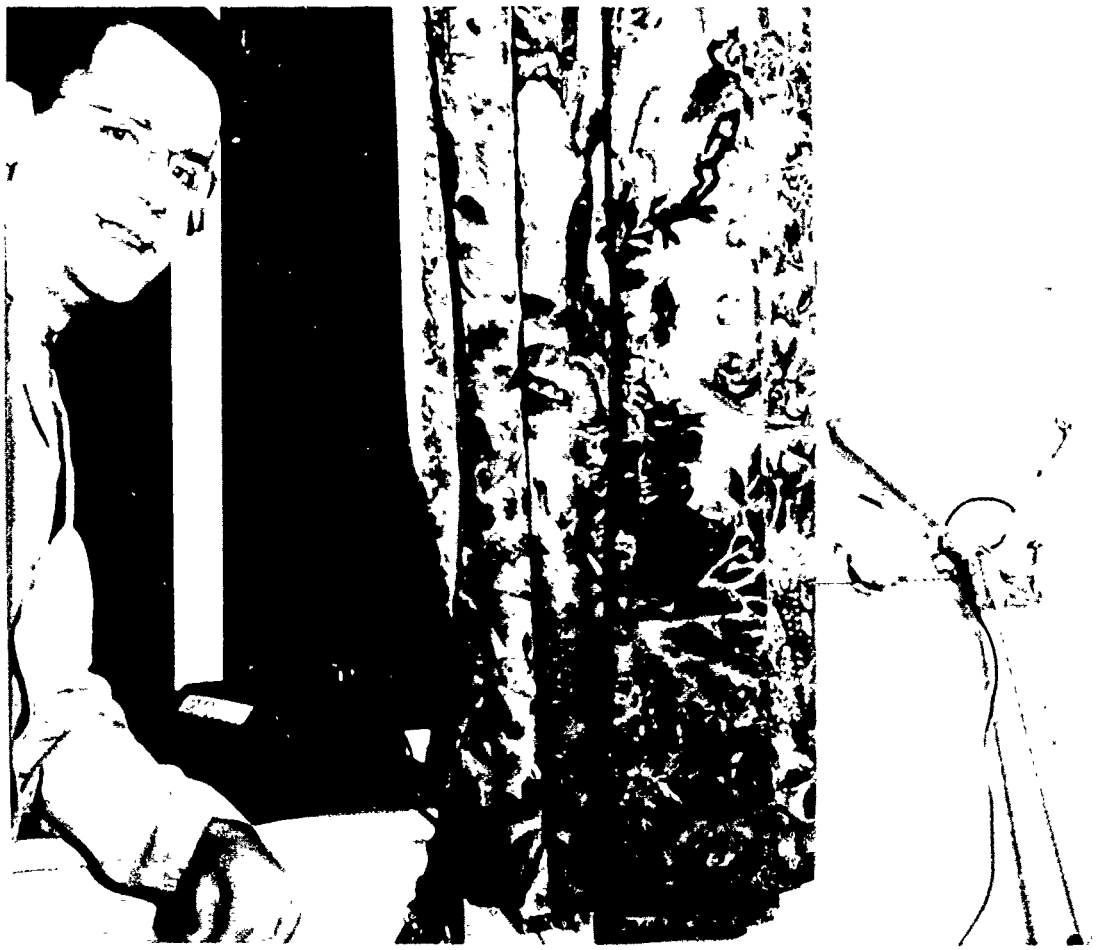

Figure 5 Heat flux meter in use.

A recorder, using a Polaroid camera back, was built onto one of the galvanometers (Fig. 6). This permitted limited visual averaging of the constantly changing deflection. With changes in recorder speed, data over periods from a couple of minutes to 24 hours could be recorded. A General Electric strip chart recording galvanometer was also used in some studies.

In most of the field studies the data taken was judged sufficient to evaluate the magnitude of specific differences in construction. It was seldom sufficient to provide precise resistance for the details present. And, because daily cycles vary from day to day, one always felt the need for much longer measurement periods or further tests on a hot box apparatus with programed diurnal cycles.

Initial heat flux tests were carried out in a few homes in the Chicago area. These included some wood frame houses where the attics had been insulated as part of a study by the local gas company in the early 1950's. In all cases tests were made both between ceiling joists and directly under joists.

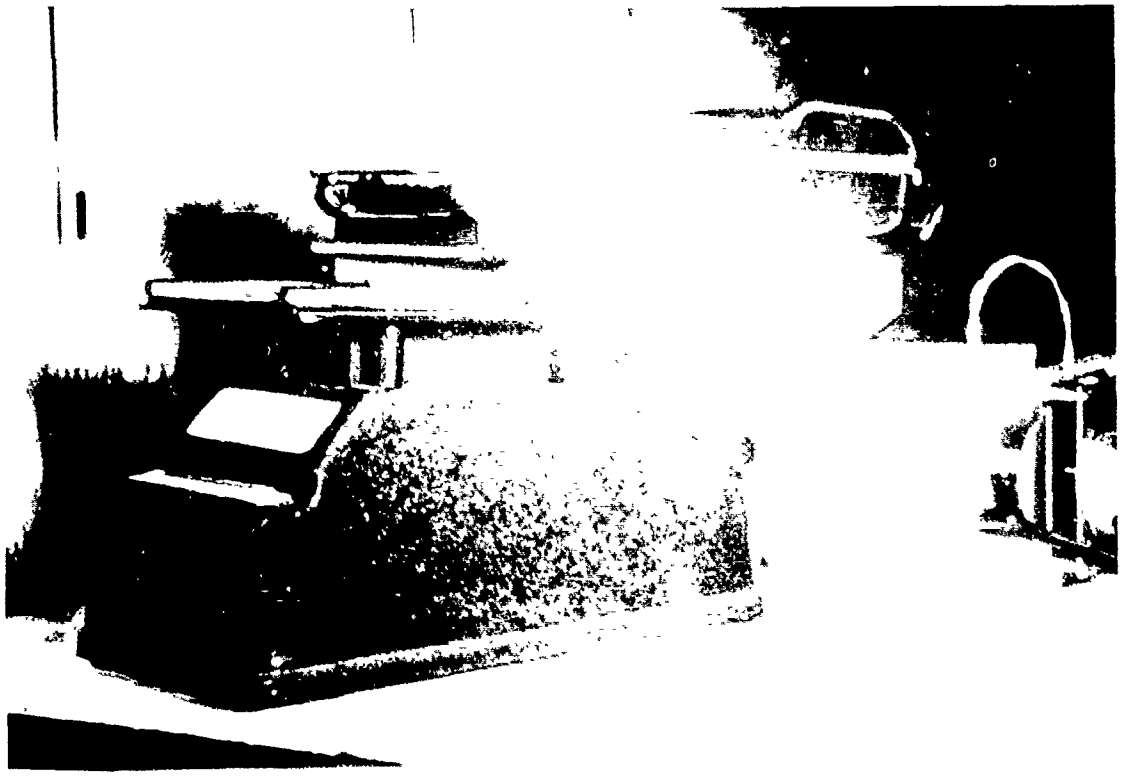

Figure 6 Recorder constructed for field used.

The difference in readings indicated the change in heat flux caused by 10 linear inches of joist. For the typical 16 in.-on-center joist spacing, this difference had to be reduced by ten percent to quantify the effect of the 9 in. of joist per square foot in the ceilings. The effects of other irregularities in the constructions, such as bridging and ill-fitting batts, were also evaluated. The heat flux data obtained in the houses used in the early 1930's gas company study were very limited and not especially useful. Floors had been added to some of the attics, some had been reinsulated, and materials were stored in others. We did observe a pronounced loss in thickness in some of the early mineral wool.

We then took the equipment to the Carolinas where a writer was doing some articles on the performance of insulation in walls and ceilings of houses. During our travel to the first house to be tested, we discussed the fact that if the owner had turned up the thermostat that morning, the heat flux would probably still be higher than normal for steady conditions. The first test location was a wall. The meter immediately read a heat flow inward on a day with a 35°F outside temperature. With a couple of questions, we learned that the owner made a practice of turning the thermostat high in the morning and then lowering it to the daytime temperature after the house had warmed. The temperature had been turned down one half hour before we arrived.

In Minnesota we measured heat flux in well-insulated buildings in cold weather. Results were mostly as expected. The high temperature differences made accurate comparisons of different constructions and insulations possible.

In Florida we checked both insulated ceilings and concrete block walls with and without insulation in the core holes. For the latter we constructed transducers of sizes such that the metering areas could be positioned to cover the same proportions of core, web and mortar joint as existed in the walls. This gave flux readings that did not have to be corrected for these differently performing areas. Some of the summertime attic insulation evaluations made in Florida showed

unexpectedly high results. Often the anomalies were easily explained when attics were inspected. In some attics insulation had lost thickness due to moisture exposure. Displacement by wind through vents was another cause. In others, high heat fluxes appeared to be due to radiation. Studies made later in a house in the Chicago area confirmed that some low density insulations did perform significantly better with an added radiation shield.

We also investigated the convection in concrete block walls by placing transducers at the top, center, and bottom on the interior side. Under winter conditions, large flux differences were measured. When the core holes in the blocks were filled with insulation, the convection was blocked. Heat flux was much more uniform over the surface of the wall. These tests were first performed under field conditions. Later they were repeated in a laboratory setup where the same wall could be tested before and after filling with insulation.

When performing tests on concrete block walls, care was taken, as much as possible, to include a proportional amount of web area in the actual test area. This was done by carefully positioning the 10-in.-square transducers or using special size transducers. For a block with a nominal size of 8 by 16 in. and three webs of 1 in. thickness there is about 22 $in.^2$ of web area in the 128-$in.^2$ gross area. The 100-$in.^2$ test area should include about 18 $in.^2$ of web area. This is accomplished by positioning the transducer so that it covers two adjacent webs and part of a web in the block above or below. The amount of joint area covered is not as critical, but it too can be approximated by the described transducer placement. With this technique it was not necessary to make additional calculations to determine the average heat flux through the wall being tested.

Other laboratory tests were made on insulated, porous block walls without an adequate vapor retarder coating. They could be opened at the top for inspection. When frost formed in the core holes, because of the lack of a vapor retarder, the frost was uniformly distributed. It was not deposited as blocks of ice at the bottom outside corners of the cavities, as is usually the case in empty cavity walls when moisture enters and the exterior surface of the cavity is below freezing.

Unexpected heat flux observations made in the field were often studied further in the laboratory. The transducers were frequently used in these laboratory tests. The nature of many specimens, or the types of tests, would have made the use of a guarded or calibrated hot box costly. Specimens were built into the tops or sides of temperature-controlled, insulated boxes placed in a constant temperature room. The transducers were attached, and tests were run using various moisture and temperature conditions.[4] This avoided the use of more expensive equipment for long periods of time. More thorough testing on other equipment was frequently done when the results indicated that such testing was warranted.

Many interesting studies were carried out both in the field and in the laboratory. The equipment cost was very low. Most tests were performed on existing constructions. Often the insulation used could be changed quickly after the completion of one test, and initial testing to determine time of equilibrium commenced on the next product or installation as soon as the following day. The number of tests that could be performed in a given period of time was very high because of the short downtime. The transducers were also a valuable addition to studies of dry and wet insulations in the roofs of test huts where the heat lags and daily reversal of heat flux was observed more accurately than with surface-temperature and energy-use measurements.

The durability of the transducers when given careful handling was excellent. No indications of delamination or significant changes in calibration were observed over a period of more than 15 years.

ACKNOWLEDGEMENTS

The author wishes to express appreciation to George E. Ziegler, who as Director of Research of the Zonolite Company, provided assistance and support in the carrying out of the heat flow transducer development and utilization, and to Wallace G. Smith, the instrument maker without whose skill transducers of the quality produced would not have been constructed.

REFERENCES

1. Close, Paul D., Building Insulation, American Technical Society, Chicago, 1951, p 150, Table 6A.

2. Wilkes, G. B., Heat Insulation, John Wiley & Sons, 1950, pp 81-88.

3. Huebscher, R. G., Schutrum, L.F., and Parmelee, G.V., A Low-Inertia Low-Resistance Heat Flow Meter, ASHVE Transactions, Vol. 58, 1952, Paper No. 1453, pp. 275-286.

4. Perrine, E. L., Moisture Accumulation and Movements in Roof Insulation, ASTM, STP 779, 1982, pp 41-53.

Eugene Perrine

Q: What measurement range did the described heat flux transducer work over?—Unsigned.

A: I do not recall determining the heat flux range over which the transducers could be used. They were used with fluxes from as low as 0.1 to as much as 100 $Btu/ft^2 \cdot h$.

Q: What was the composition of the insulating concrete which you mention in your presentation?—Unsigned.

A: Most of the heat flux studies on wet and dry insulating concretes were on vermiculite concrete, usually a mix of one 94-pound sack of portland cement with 6 cubic ft of vermiculite, plus an air-entraining agent. Additional tests were performed, using perlite and cellular concretes.

Q: You mention that you.were able to place the HFT on CMUs (concrete masonry units); such that you accounted proportionately for mortar joints, webs, and cavities. How did you convince yourself that your millivolt readings were representative of a whole wall, in light of three-dimensional heat flow effects in the CMU wall? The surface area proportional coverage (of the HFT) would not necessarily represent the heat flow proportional (distributions) at the surface.—Jeffrey Christian.

A: In 1955 the Vermiculite Institute had a series of hot box tests performed at the University of Pennsylvannia at University Park/State College, Pennsylvania. Concrete masonry units from the same lots of units used for those (hot box) tests were used to construct the test walls in our laboratory (for HFT tests). Tests on those walls and surface temperature profiles generated by the University of Pennsylvania convinced us that we were obtaining sufficiently accurate data. Some of the University of Pennsylvania test results still appear in the ASHRAE Handbook of Fundamentals.

ERROR COMPENSATION AND CALIBRATION OF HEAT FLUX TRANSDUCERS

SYSTEMATIC ERRORS WITH SURFACE MOUNTED HEAT FLUX TRANSDUCERS AND HOW TO LIVE WITH THEM

H.A. Trethowen

Building Research Association of New Zealand
Wellington, New Zealand

Abstract:

This paper is basically a tutorial on the use of a parametric model for the quantitative prediction of systematic errors with surface-mounted HFTs. Full details of this parametric model have been previously published. By use of progressive changes in a simple example, this paper shows how errors and fluctuations in the errors, can be determined approximately using the model. Effects such as contact resistance, HFT thermal resistance, wind, emittance matching, and sample properties are examined one by one. Some conclusions about the influen e of these errors are drawn.

A particular point made is that errors may be either stable, or highly sensitive to environmental changes. A particular value of this model is to enable the user to choose the measuring environment so that errors are stable and therefore correctable.

1. INTRODUCTION

Heat Flux Transducers (HFTs) are informative, cheap, and easy to use, but their behaviour is not simple. These valuable devices won't be reliable if used in a "catalogue engineering" manner - the selection must take account of a number of features of the item under test, and the environment it has to work in. Changes due to aging and environmental variations can be of great importance, and may not always be known exactly.

HFT's are so versatile that they can be discussed sensibly only within predefined limits, in this case to surface-mounted HFTs applied to building heat flux measurement in steady or slowly varying state.

Previous literature (1, 2, 3) has offered much generalized advice on how HFT's should be used. But because the purposes of HFT installations vary so widely, and so do the constraints, any

generalized advice may have to be tempered in some cases. This note gives such estimates of how significant a departure from this advice may be, and how to compensate for its effect.

Previous papers (1,3) have discussed HFT faults (such as sensitivity to lateral temperature gradients, large edge/face area ratio, improper calibration, etc.) This note deals exclusively with the behaviour of perfectly calibrated, ideal HFT's and is basically a tutorial on a parametric model first presented in reference (3).

2. OBJECTIVES AND DEFINITIONS

The usual objective when using HFTs is to find the value of heat flux which would have occurred in the undisturbed state - i.e. with no HFT present. But disturbance to heat flux is intrinsic to the use of passive HFTs. It is only possible to avoid disturbance in special, restricted - and usually transient - conditions. Therefore some systematic error is inescapable. Typically these errors will change with time or conditions, which are as important to the final accuracy and reliability as is the quality of the HFT itself, or its calibration.

A perfectly calibrated HFT is taken here to mean one in which the heat flux through the HFT itself is exactly represented by the output. The systematic error is taken to mean the difference between the heat flux in totally undisturbed conditions, and that indicated by a perfectly calibrated HFT. This error may be either positive or negative, corresponding respectively with the HFT indicating either too low (the usual case) or too high.

These systematic errors can be estimated using a parametric model, defined in Figure 1, which offers a quantitative estimate of the systematic error E for perfectly calibrated, unguarded, surface-mounted HFT's. It uses three dimensionless parameters H, Emin, and Emax. The model was introduced and justified in reference 1 on the basis of computer modelling and compatibility with published measured data. It describes the systematic error E as a power-law function of H, unless constrained by the limiting error values Emin or Emax. The three parameters have both common and independent factors.

Suppose that for some case the parameter H were to be varied from very small to very large (e.g., by varying the size L of the HFT). The error would initially remain nearly constant at Emin as H increased. But when H becomes large enough, error E would increase with H according to a power law, until it approached Emax, where E would again level off. The three stages in this description were named in ref. 3 as:

"Insulation-controlled regime" - This corresponds to an arbitrarily large HFT. The error is simply the resistance ratio of the HFT to that of the total wall, and is denoted as Emin.

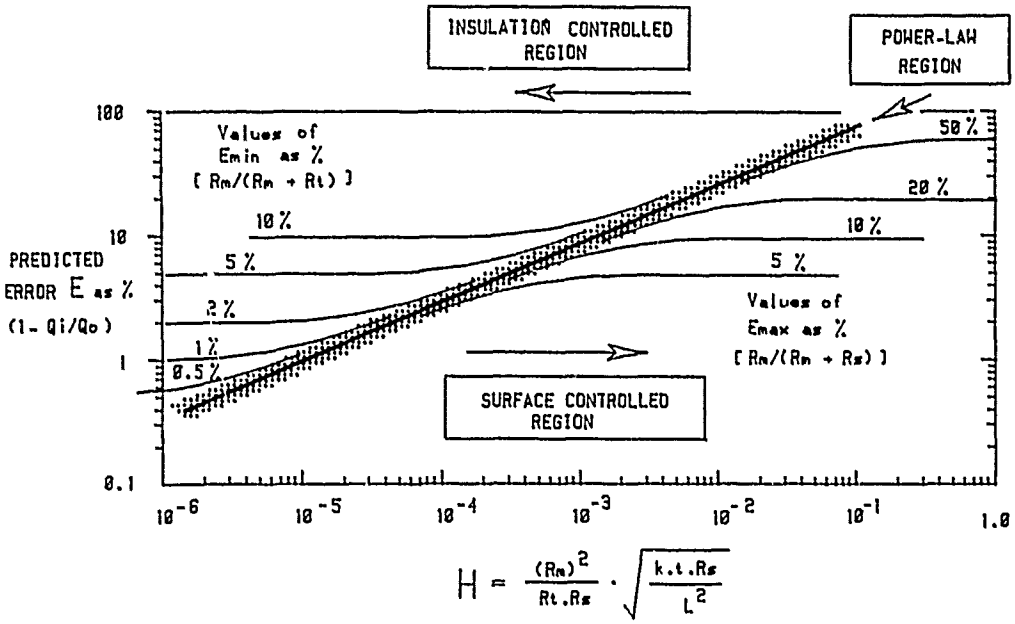

$$H = \frac{(R_m)^2}{R_t . R_s} \cdot \sqrt{\frac{k . t . R_s}{L^2}}$$

where

E = 1 - Qi/Qo
Qi = indicated heat flux
Qo = undisturbed flux
Rh = HFT series resistance
Rc = contact resistance
Rms = surface resistance over HFT
Rs = surface resistance over undisturbed structure
Rt = total thermal resistance of test structure
k = thermal conductivity of top substrate layer
t = thickness of top substrate layer
L = length or breadth of square HFT
= 2AB/(A + B) for rectangular HFT
s = sgn(m) (=±1, according to the sign of R_m)
c = fitted constant = 2.1136
n = fitted constant = 0.465

Rm = Rh + Rc + (Rms - Rs)
Ep = $S.C.H^n$
Emin = Rm/(Rm + Rt)
Emax = Rm/(Rm + Rs)

Figure 1. Parametric Model of heat flux transducer error (for surface mounted HFT without edge guards).

"Power-law regime" - This is dominated by edge leakage around the HFT perimeter. The error is a function of a dimensionless parameter "H," and is denoted as Ep.

"Surface-controlled regime" - This corresponds to an HFT placed on a substrate of infinite lateral conductance, or to a zero breadth HFT. The error is equal to the ratio of the effective HFT resistance to the surface resistance, and is denoted as Emax. The value of this model is that it is comprehensive, and thus offers the designer a way to compromise between conflicting needs. The actual errors predicted by the model are themselves only approximations.

3. THE BEHAVIOUR OF A SURFACE-MOUNTED HFT MEASURING SYSTEM

It can be seen from Figure 1 that the behaviour of an HFT measurement system depends strongly on a dimensionless parameter "H". An accurate system requires that H be made small enough. This would be approached by making the HFT effective series resistance Rm small or the size L large, whilst the higher thermal resistance, the better the accuracy of the HFT. There are several complications in manipulating the factors of "H". These will be discussed below.

The strongest single factor is the effective series resistance Rm, given by equation (1):

$$Rm = Rh + Rc + (Rms - Rs) \quad (1)$$

Where:

Rh - series thermal resistance of the HFT alone
Rc - thermal contact resistance between HFT and substrate
Rms - total thermal surface resistance over HFT
Rs - total thermal surface resistance over surrounding area

The quantity Rm is not only the strongest single factor in determining the measurement quality, it is also the most complicated. Most users of HFTs are aware of the value in choosing a low HFT resistance Rh. It is not so widely appreciated that it is not Rh alone, but the composite value Rm that controls accuracy.

The series thermal resistance of HFTs ranges widely. Commercial HFTs have been reported as having resistances from about 0.002 $m^2°C/W$ to 0.03 $m^2°C/W$. Special purpose HFT's vary more widely, and values up to 0.1 $m^2°C/W$ have been reported.

4. EXAMPLES

No step-by-step procedure for selecting HFT systems has yet been found, and so it is necessary to use iterative or trial-and error methods. In this paper we first take a typical example case to illustrate the use of Figure 1, and then in subsequent cases vary one

Table 1. Summary of Calculations for all Cases.

Physical quantity	EXAMPLE 1	2	3	4	5	6
	Case Number 1	2	3	4	5	6	7	8	9	10	11
k	0.16	0.16	0.16	0.16	0.16	0.16	0.16	0.16	0.16	150	0.16
t	0.01	0.01	0.01	0.01	0.01	0.01	0.01	0.01	0.01	0.001	0.01
L	0.05	0.05	0.05	0.05	0.05	0.05	0.05	0.05	0.05	0.05	0.5
Rt	2.0	2.0	2.0	2.0	2.0	2.0	2.0	2.0	2.0	0.3	2.0
Rs	0.09	0.09	0.09	0.18	0.18	0.04	0.04	0.05	0.05	0.09	0.09
Rh	0.01	0.01	0.01	0.01	0.01	0.01	0.01	0.01	0.01	0.01	0.1
Rc	0.001	0.011	0.001	0.001	0.001	0.001	0.001	0.001	0.001	0.001	0.001
Rms	0.09	0.09	0.18	0.09	0.18	0.04	0.05	0.04	0.05	0.09	0.09
Rm	0.011	0.021	0.101	-.079	0.011	0.011	0.021	0.001	0.011	0.011	0.101
$H*10^{-4}$	1.6	5.9	136.0	-59.0	1.1	2.4	8.8	0.018	2.0	104.0	13.6
Ep %	3.6	6.7	28.6	-19.4	3.1	4.4	8.0	0.45	4.2	25.3	9.8
Emin %	.55	1.0	4.8	-4.1	0.55	0.55	1.0	0.05	0.55	3.5	4.8
Emax %	10.9	18.9	53.0	-78.0	5.7	21.6	34.4	2.0	18.0	10.9	53.0
E%	3.6	6.7	25.0	-19.4	2.7	4.4	8.0	0.45	4.2	10.9	9.8

factor at a time, to show how apparently simple variations can produce major changes in the quality of measurement. The complete calculation data for all examples are summarized in Table 1, so that calculation may be traced through. The results of those calculations are presented in Figure 2 to illustrate their relation to "H" and the three operating regimes.

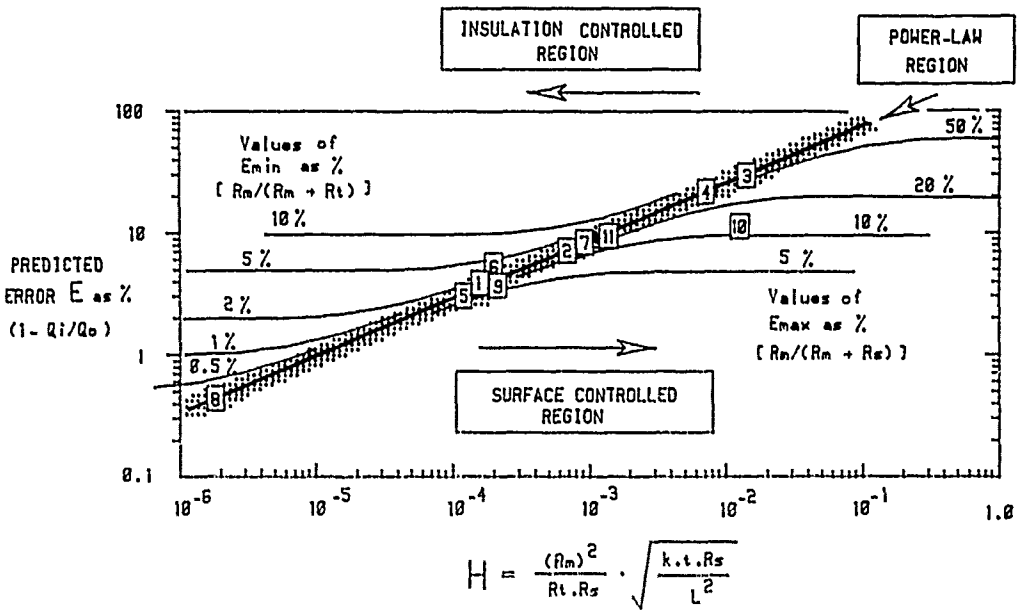

Figure 2. Locations of Example Cases from Table 1, on parametric correlation diagram.

EXAMPLE 1: A Base Case (Case 1 in Table 1)

A wall with 10 mm thick gypsum plaster-board lining (k = 0.16 W/m°C) has an overall thermal resistance expected to be about 2 m^2°C/W. The surfaces are nonreflective, air is nominally still, and an HFT of 50 x 50 mm and a series thermal resistance 0.01 m^2°C/W is to be used on the lining board. The surface is rough, so we allow a mean gap of 1 mm between HFT and plasterboard, and choose a filler paste of 1.0 m^2°C/W conductivity. We also intend to make the infrared emittance of the HFT the same as that of the surrounding plasterboard. Surface resistances and other thermal properties can be found from standard handbooks, e.g., ref (4).

Then:

(a) HFT resistance Rh = 0.01
Contact resistance Rc = 0.001
0.011

Wind speed = 0, Rms = Rs = 0.09
Rm = 0.01 + 0.001 + (0.09 - 0.09) = 0.011

(b) Then we find H, as:-

$$H = \frac{(0.011)^2}{2*0.09} \left[\frac{0.16*0.01*0.09}{0.05*0.05} \right]^{0.5}$$

$$= 1.6*10^{-4}$$

(c) We then have to check the limit values Emin and Emax:-

Emin = 0.013 / (0.011 + 2) = 0.0055 or 0.55%
Emax = 0.013 / (0.011 + 0.09) = 0.109 10.9%

(d) From Figure 1 we then see that for $H = 1.6*10^{-4}$; the error Ep from the power law effect is predicted to be 3.6%.

(e) Finally, because neither limit Emin or Emax approaches Ep, the final error E will be similar to the power-law error Ep.

We conclude that this selection would operate in the power-law regime, with a measurement error of about 4%. If the only in-service factor likely to change is the surface resistance, then the effect on H, and hence on systematic error, must remain very small. The predicted error of 4% should therefore be consistent, and may be used as a nearly constant correction to all heat flux data measured with this system.

EXAMPLE 2: Effect of Contact Resistance (Case 2 in Table 1)

For an HFT with no contact filler paste, we can expect the gap width between surface and HFT to be less than say 1 mm. It can be shown that for such small gaps the contact resistance will be dominated by air conduction, and will be about $0.04*b$ $m^2°C/W$ (where b is gap width in mm), regardless of surface emittance or orientation. Where filler pastes are used, the contact resistance might range from $0.001*b$ for conductive pastes ($k = 1.0$) to $0.003*b$ for less conductive pastes ($k = 0.3$). If a filler paste is used, it is therefore more important that the paste does not shrink, embrittle, or crack, than what the paste conductivity might be when new. It can be better to use no paste than one at risk of shrinking or cracking.

Suppose our HFT of resistance 0.01 has 1 mm of a conductive but brittle paste, which later cracks and forms a 1/4-mm-thick crack layer:

Then Rm would change from 0.011 to 0.021 (see Table 1).
H would change from $1.6*10^{-4}$ to $5.9*10^{-4}$.
Ep would change from 3.6% to about 6.7%.

As in example 1 the limiting errors (1% and 19%) do not impinge on the result, and this case also operates in the power-law regime. The consequence of cracking would thus be that an initial error within 4% might suddenly double, but there would be no physical indication of such a change.

EXAMPLE 3: Effect of mismatched Surface Resistance (cases 1,3,4,5 in Table 1)

Many authors, e.g., Flanders (1985), have drawn attention to the effect of differing emittance between the HFT and the surface it is mounted on. Using the parametric model we can describe in some detail the effect of a mismatch. The effect comes about by the influence on Rm of the term (Rms - Rs) in Eq. 1. This is dominated by any difference in emittance, although texture and edges can affect the convective heat transfer coefficients.

If both surfaces have the same emittance, the term (Rms - Rs) will always be zero or small. If an HFT surface is reflective and the surround is black, then (Rms - Rs) will be positive with a value of about 0.09 when there is no wind. The systematic error will increase since Rm will have risen from 0.011 to 0.101, but more importantly it will be strongly affected by any variation in wind strength. If the HFT were black and the surrounds reflective, then the (Rms - Rs) term will be negative, with a value of -0.09 at no wind. The value Rm, and hence measurement error may therefore become either positive or negative.

Table 2. Effect of mismatched emittance, no wind.

	wind = 0	
	Black HFT	Reflective HFT
	Error E%	
Black surface	3.6%	28%
Reflective surface	-19%	3.1%

The results for this condition can be seen in Table 2. If the HFT surface and the surrounding surface both have similar surface emittance, whether high or low, then the calculated error E remains low. However if the surface emittances differ, the error can not only increase tenfold, but can be either positive (reading too low) or negative (reading too high). All cases are in the power-law regime, although case 5 is nearing the Emax limit.

EXAMPLE 4: Effect of Wind (Cases 6 - 9 in Table 1)

For this example we consider the same conditions as in EXAMPLE 3, except that the wind strength is set to 3m/s. This lowers all surface resistances, and also decreases the differences due to emittance. Consequently the effects of surface emittance in EXAMPLE 3 remain but are less marked in this example.

Table 3. Effect of mismatched emittance, 3 m/s wind.

	wind = 3 m/s	
	black HFT	reflective HFT
	Error E%	
black surface	4.4%	8.0%
reflective surface	0.45%	4.2%

In the case of black HFT and reflective surround (case 8), wind has caused the calculated error E to reduce sharply, but has just failed to go negative - small changes to the surface resistances Rs or Rms may cause this to occur. Comparison of examples 3 and 4 shows that the effect of changing wind speed is severe if the surface emittances are mismatched, but quite minor otherwise.

EXAMPLE 5: Effect of High Conductivity Substrates (Case 10 in Table 1)

If there is a highly conductive substrate layer such as metal or concrete under an HFT, then it might be expected that this would have an effect on the heat flow measurement. The parametric model predicts such an effect, by the effect of the k*t term in "H". The effect is especially strong if the HFT is small (i.e., "L" is small), or sample resistance Rt is small.

Consider the case when the HFT from examples 1-3 is used to find heat flow from a machine hood, with a painted 1 mm aluminium skin, and insulation of 10 mm expanded polystyrene, i.e., R-value about 0.3 m^2 °C/W. The surface resistance remains at 0.09 m^2 °C/W.

From Table 1 we see that the power-law error Ep would be 25%. However the value Emax is lower than 25%. This case therefore must operate in the "surface-controlled" region. The calculated error E will be close to Emax, 10.9%.

If this is explored further by considering a drop in the surface resistance - if air speed increases for instance - then we find that the actual error will increase sharply. If the air speed increases to 3 m/s, and the surface resistance therefore falls to 0.04, then H does not change greatly but the value of Emax will rise to 22%, and the final error E will rise with it.

It is characteristic of the "surface-controlled" region that the measurement accuracy becomes dominated by the surface resistance Rs, with errors varying erratically with time in response to variations in wind speed.

EXAMPLE 6: Effect of large size, large R, HFT (Case 11 in Table 1)

If a large size HFT is required for some reason - say to span the framing pitch of a timber frame wall - then an HFT may not even need to have small thermal resistance. Consider Example 1, but with a large HFT of say 500 x 500 mm, and a large HFT resistance of 0,1 $m^2°C/W$. Then the value H will increase from $1.6*10^{-4}$ to $13.6*10^{-4}$, and the predicted error E will increase to 9-10%. However as in Example 1, this may also be seen to be a stable error that will not change significantly with air movement, and may equally be a usable option. In fact, such an option may be particularly resistant to change of contact resistance, since that factor can no longer have much leverage on the value Rm. The change that caused Example 2 to jump from 4% error to 9% error would here be able only to increase the error from 9% to some 10%.

SPECIAL CONDITIONS

Edge guards will clearly reduce edge leakage. In reference (3) the effect of edge guards was examined, and reported to vary as in equation 2. As edge guard width increased from zero, the calculated error dropped from its initial value E, to the value Emin:

$$\frac{E(w) - Emin}{E(0) - Emin} = e^{-(c.w)} \qquad (2)$$

where w = width of edge guard, m
c = fitted constant
e = 2.718 ...

The value of c varied from about 12 to 50 in different cases. Typically the value of E(w) approached within 10% of Emin when the value of edge guard width w exceeded 50 to 150mm width in the cases studied, in which the HFT width varied from 20 to 500mm. It is not known whether wider ranges occur. It should be noted that the error will not fall below the value Emin, even with perfect edge guarding.

A further special condition arises as in equation 3. It is evident that if R_m can be reduced to zero, then there will be no systematic error. This condition can in principle be achieved by setting:

$$Rm = 0 = Rh + Rc + (Rms - Rs)$$
$$\text{i.e., } Rms - Rs = Rh + Rc \qquad (3)$$

In our "base case" example, with (Rh + Rc) equal to 0.011, then we can achieve the no-error condition by choosing (Rms - Rs) to be also equal to 0.011, i.e., Rms as 0.09 + 0.011, or 0.0101. This can quite readily be done by choosing the emittance of the surrounding surface to be just a little lower than the HFT, about 0.6 to 0.7 in this case.

Such a move is really one of canceling the thermal imbalance created by the HFT, and could be regarded as being a method of edge guarding. However, such techniques are available only if one can have confidence that the surface coefficient (and hence wind speed) will remain at the design value, and thus would be feasible only in laboratory conditions.

CONCLUSIONS

1 Very high accuracy is not easily achieved. (To guarantee a 1% systematic error even in a "benign" case such as a well-insulated timber framed wall measured indoors, it may be necessary to use an HFT 500 mm square, resistance of less than 0.009, and contact resistance that is not only less than 0.002 but also never changes significantly in use.)

2 It can be better to use systems having stable (and therefore correctable) error rather than those with very small error, if that error varies with conditions.

3 Errors may vary widely from time to time in some cases, namely:

- where contact resistance between HFT and substrate changes
- where emittance of HFT and surrounding surface do not match
- where the HFT operates in the "surface controlled" regime.

4 Good reliability is greatly helped by using large HFT's. Size can be used to offset large HFT or contact resistance.

5 No HFT can be correctly described as having a particular universal accuracy. The accuracy will vary widely according to the usage of that HFT.

REFERENCES

1. ASTM — STP 885. Building Applications of Heat Flux Transducers. Special Technical Publication 855. American Society for Testing and Materials Philadelphia, 1983.

2. Flanders S.N. — Confidence in heat flux transducer measurements. ASHRAE Transactions, Volume 91, 515-531, Jan 1985.

3. Trethowen, H.A. Measurement errors with surface-mounted Heat Flux Sensors. Building and Environment, Vol. 21, No. 1. pp 41-56, 1986.

4. ASHRAE Handbook of Fundamentals. American Society of Heating, Refrigeration, and Air Conditioning Engineers, Atlanta, Georgia, 1989.

Harold A. Trethowen

Q: If we assume a wall construction comprising only a homogeneous layer of insulation, e.g., 200 mm thick, which value for t, the thickness of the surface layer, should I use in your formula expressing $H = f(Rms, Rs, h, t,$ etc.) to calculate the error E in the power law regime?—Rik van der Graaf.

A: The model doesn't strictly cater for this condition. The model was developed by traditional "dimensionless analysis," which is a pragmatic process aimed at getting practical answers to incompletely understood problems. The kt term in the model has been assigned wholly to the surface layer because that commonly dominates the lateral edge leakage. One can presume that for very thick or thin surface layers, some adjustment to the kt value might be desirable. For thin surfaces it might need increasing to allow for significant edge leakage in the next layer. For thick surfaces, including homogeneous walls, it might need limiting by restricting t to the depth of the major edge leakage—say, 10 mm.

Q: Are the curves presented based on first principles modeling, or empirical results?—Stephen N. Flanders.

A: The parametric model was derived from the results of finite difference modeling, then correlated by traditional dimensionless analysis. Finally, all available published measured data were compared with this model, and shown to fit it adequately. (See ref. 13 in the paper.) This information is partly given in para 1, page 2.

Q: How does a mismatch of the HFT guard with the HFT proper affect HFT bias?—Stephen N. Flanders.

A: Mismatch of the guard was not examined systematically in this study. However, in those cases where a mismatch arose, there seemed to be some sensitivity even to small mismatches (see the paper by this author in ref 1, STP 885).

Q: What is a representative error for an HFT installed at the inside surface of a conventional wood-frame cavity wall?—Douglas M. Burch.

A: There is no answer to this question. It depends on the way each project is designed. The purpose of this paper was to assist project designers to design their own error by understanding quantitatively the magnitude of different error sources, and particularly to design for stable error.

In our own projects we have used one design with a stable 6–7% error, and another with about 3–5%. I have avoided smaller errors because I regarded the price as too high—in terms of the error becoming erratic, rather than consistent.

AN HFT GUARD PLATE FOR EXTERIOR ENVELOPE SURFACE MEASUREMENTS

J. E. Christian

Oak Ridge National Laboratory
Oak Ridge, Tennessee USA

ABSTRACT

A calibrated slab-on-grade edge insulation test facility has been collecting hourly HFT (heat flux transducer) measurements at Oak Ridge National Laboratory (ORNL) since February 1989. This facility has been measuring in-service performance of foundation insulations applied to a monolithic poured slab-on-grade foundation. The site contains experimental prototypes of a calibrated HFT plate assembly. These were fastened to the exterior vertical face of the slab edge in two instrument planes cutting perpendicular to the slab edge and adjacent soil. The HFT guarding and masking technique applied could be beneficial to others interested in making heat flux measurements on the exterior face of building envelopes.

The guard was constructed of materials which produce a composite that has a measured thermal conductivity within 1.5% of the HFT and the same thickness as the HFT. The guard was designed to minimize the lateral heat transfer at the sensor. The guarded HFTs were sandwiched between two layers of a laminate acting as a mask that provides protection from the harsh conditions found in the adjacent soil. Provisions were made for this application to use the extended guards to help distribute uniformly the horizontal heat flow from the slab edge, yet minimize the potential artificial lateral heat path caused by the presence of the HFT guard. Three HFTs were installed at different vertical levels on both an insulated and uninsulated slab location. Prior to installing the HFT assemblies, they were calibrated in the ORNL Thermal Properties Laboratory using the Unguarded Thin Heater Apparatus. The in-situ field HFT measurements were validated with periodic laboratory measurements.

OBJECTIVE

The objective of this paper is to describe the development of a HFT plate assembly development and show some measured results that illustrate the benefit on exterior surface envelope heat flux measurements.

BACKGROUND

Recent modeling results suggest that adding slab-on-grade foundation insulation (at least R-0.88 $m^2 \cdot K/W$ [R-5 $ft^2 \cdot h \cdot °F/Btu$]) is as cost effective as meeting already acceptable insulation levels for above-grade walls (R-2.64 $m^2 \cdot K/W$ [R-15 $ft^2 \cdot h \cdot °F/Btu$]) and ceilings (R-5.28 $m^2 \cdot K/W$ [R-30 $ft^2 \cdot h \cdot °F/Btu$]) for most residential buildings in the U.S.[1]

Earth-contact heat transfer for slab-on-grade floors is a major component of the heat balance in many energy-efficient buildings, particularly residences, and can significantly affect heating and cooling energy consumption. This earth-contact heat transfer is particularly important in U.S. mild climate zones, because the most common foundation type in the southern states is slab-on-grade.

The motivation behind this HFT plate assembly development was to help:

- Collect validation data on well characterized foundation test sites,
- Develop a protocol for measuring the in-service thermal performance of foundation insulation, and
- Validate computer models which accurately account for both soil heat and mass transfer affecting foundation thermal performance.

TEST SETUP

The experiment utilizing the HFTs is being conducted at ORNL, utilizing the slab of an existing test facility, shown in Figure 1, the Roof Thermal Research Apparatus (RTRA). This facility is a long, narrow, unoccupied building, 3 x 8.5 m (10 x 28 ft) oriented with the long sides facing east and west. The test section for the slab-on-grade insulation experiment is on the east side of this building. One half of the east foundation wall is currently insulated, and the other half was left uninsulated. Figure 2 shows a floor plan of the facility and adjoining test section on the east side. Figure 3 is a cross section of the insulated test section of the RTRA where the instrument plane bisects the insulated test section. The circles indicate thermocouples and the squares indicate heat-flux transducer locations.

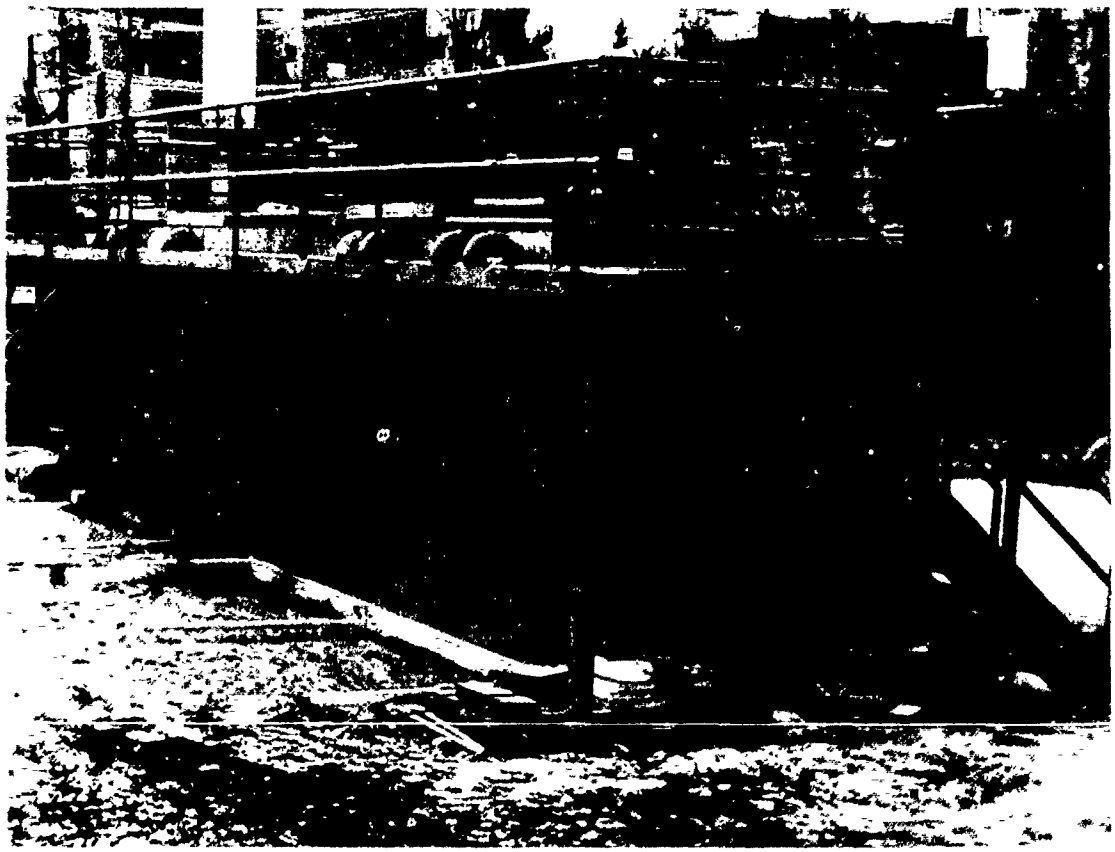

Figure 1. Building used for slab-on-grade insulation thermal-performance test.

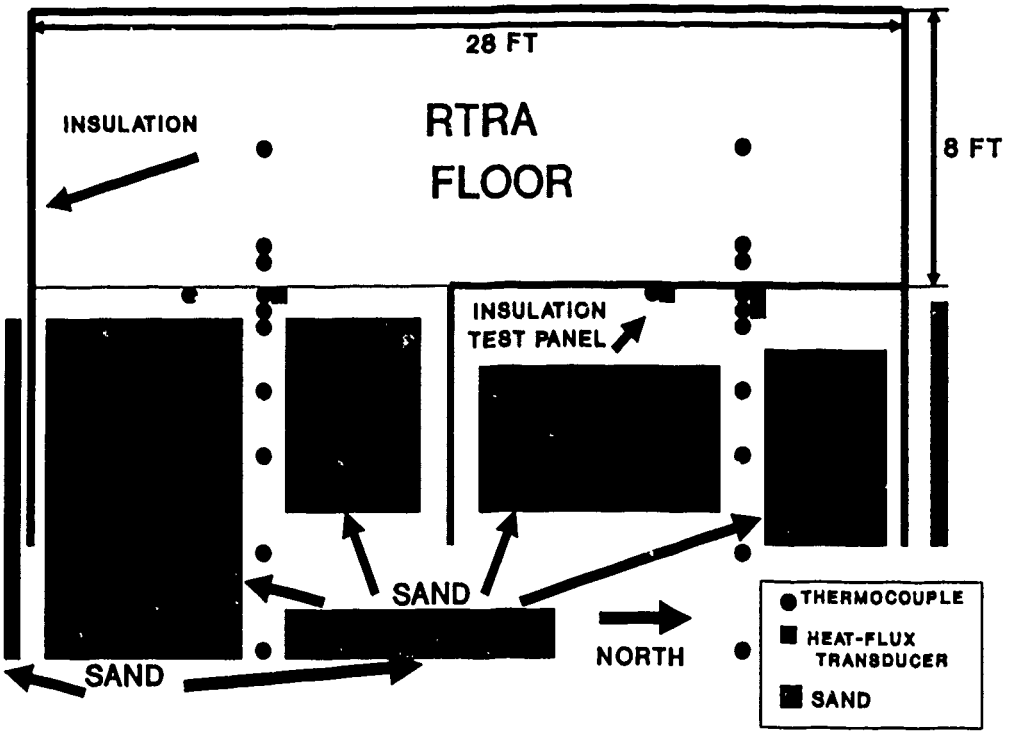

Figure 2. Sensor location on RTRA floor plan for slab-on-grade insulation test.

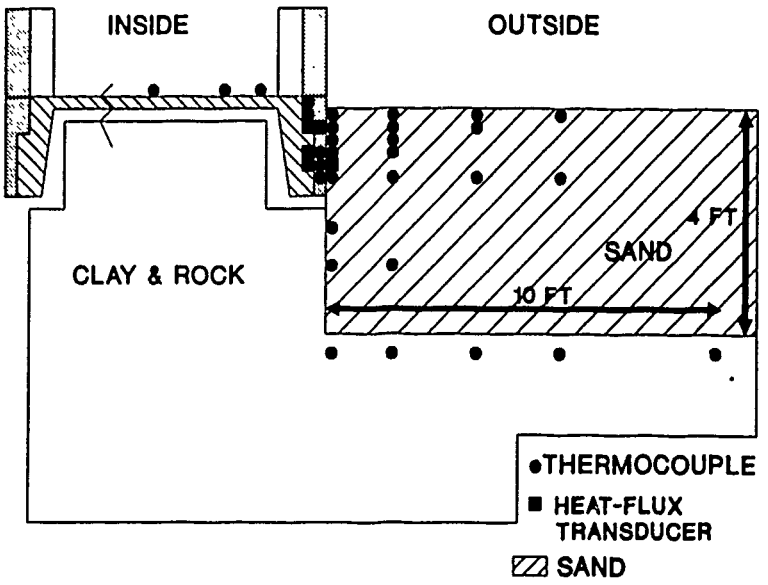

Figure 3. Instrument plane through insulated slab cross section.

The insulation is mechanically fastened with screws to the 0.6 m (2 ft) deep poured concrete foundation wall and could be easily removed and replaced with other samples. The other three walls have been insulated in a similar manner, but with more insulation, RSI=4.4 (R-25) at the top 0.254 m (10 in.) and RSI=2.2 (R-12.5) at the bottom 0.35 m (14 in.) in an attempt to reduce the heat loss in those directions and minimize the disruption of the two-dimensional heat flow from the test foundation section. Buried

insulation fins extend to the east from the test section at the northeast and southeast corners of the building. A third insulation fin extends east from the middle of the test wall, isolating the insulated and uninsulated sections.

The insulation test panel consists of two nominal 2-in.-thick layers of extruded polystyrene covering the top 0.254 m (10 in.) of the foundation wall, and a single nominal 2-in. layer covering the bottom 0.35 m (14 in.). The insulation used is an experimental extruded polystyrene blown with HCFC-22, which has about 5% of the ozone depletion potential of CFC-12.[2] At the time this developmental insulation was provided to ORNL by UC Industries, HCFC-22 was a candidate blowing agent replacement for CFC-12. Prior to field installation this material first underwent test characterization in the laboratory, and has been installed so that it can be easily removed for periodic thermal conductivity (k) measurements in the laboratory. Field thermal conductivity measurements have helped to determine if this insulation ages differently in the field than in the laboratory.

The in-situ soil on the east side was excavated and replaced with a homogeneous sand. The dimensions of the sand volume are about 1.2 m (4 ft) deep by 3.66 m (12 ft) wide by 9.75 m (32 ft) long, extending beyond the 8.53-m (28-ft) length of the RTRA by about 0.61 m (2 ft) on both sides. A 0.1-m (4-in.) polyvinyl chloride (PVC) drain is installed to lead excess moisture from the bottom of this sand volume to daylight.

An instrument plane cuts vertically through the middle of each test section and extends out through the soil to the east of the RTRA. Thermocouples have been installed on the slab floor and in calibrated experimental panels that form large guarded and masked heat flux sensor plate assemblies mounted on the exterior surface of the slab edge. Guarded heat flux sensors (HFTs) and thermocouples have also been mounted within the insulation test panel, giving a redundant set of measurements to evaluate the effectiveness of the experimental HFT guard plates. Six thermocouple rakes have been buried at various intervals along the instrument planes of each test section from the foundation wall out to about 3.2 m (10.5 ft) from the building.

HEAT FLUX TRANSDUCER PLATE ASSEMBLY

General Description

The HFTs mounted on the slab edge were surrounded by a 0.14-m (5.5-in.) x 0.14-m (5.5-in.) guard. This guard is constructed of materials that produce a composite that has a measured conductivity within 1.5% of the HFT. The measured k, perpendicular to the plane of the HFT, for a dissected thermopile-type HFT was 0.596 W/(m·K) (4.14 Btu-in./h·ft^2·°F). With the same measurement apparatus, the value for a small core of the composite guard was measured at 0.605 W/(m·K) (4.2 Btu-in./h·ft^2·°F). The material consists of a layer of phenolic laminate sandwiched between two layers of aluminum. Concentric squares were cut in the aluminum to minimize the lateral heat transfer to the HFT.

The guard was mounted in a larger plate, composed of the same composite as described above, sandwiched between two layers of PVC laminate to act as a mask for the HFT. The color of the PVC is very near that of the concrete. The PVC laminate is fastened to the aluminum with a contact cement. Before the 0.14-m (5.5 in.) x 0.14-m guard was mounted into the larger plates, the aluminum layers were machined, leaving thin cuts made in the aluminum to provide a break for the vertical heat transfer. These cuts were on 50-mm (2-in.) centers and ran the full length of the plates. Two different sizes of plates were made: 0.25 x 1.22 m (10 in. x 4 ft), which were mounted on the top portion of the foundation wall, and 0.35 x 1.22 m (14 in. x 4 ft), which were fastened to the bottom portion of the foundation wall.

There were a total of eight plates mounted on the test slab edge, four of which held HFTs. Two of the 0.25-m- (10-in.-) wide plates together held one HFT and were positioned so that the center of the HFT would measure the flux 51 mm (2 in.) above the grade line. Two of the 0.35-m- (14-in.-) wide plates each held two HFTs. One was positioned so as to measure the flux 0.2 m (8 in.) below grade, the other at 0.35 m (14 in.) below grade. This setup enabled three heat flux measurements at three different vertical levels on both halves of the test section.

The other four plates contain thermocouples to measure the vertical temperature profile within the plate. There are two thermocouples in the 0.25-m (10-in.) plate measuring temperatures at 51 mm (2 in.) above grade and 51 mm (2 in.) below grade. There are three thermocouples in the 0.35-m- (14-in.-) wide plate measuring at 0.15, 0.25, and 0.38 m (6, 10, and 15 in.) below grade. Temperature measurements are also made in the sand adjacent to the set on the uninsulated side, specifically to compare temperature profiles and ensure that excessive vertical heat flux has not been caused by the aluminum in these plates. The long horizontal breaks cut in the aluminum help to distribute uniformly the horizontal heat flow from the slab edge. These plates minimize the artificial vertical heat path that would cause heat to short-circuit the insulation and the sand, and give erroneous HFT readings. The plates do not extend all the way across the test sections mainly to keep the sections isolated from each other and the adjoining native composite of clay and rock. However, there are breaks in the aluminum layers in the vertical direction as well. They are located about 0.2 m (8 in.) from the ends of all the plates. There is about a 25-mm (1-in.) gap between the edges of the two plates mounted at the same elevation. The 51-mm (2-in.) offset on the foundation wall 0.25 m (10 in.) from the top also helps eliminate the possibility of vertical heat flux caused by the plates. There are redundant HFTs in the foam on the insulated side that will also be used to evaluate the effectiveness of these plates.

Before the plates were installed, the entire east foundation wall was given a smooth cement parget coat that filled in the small stone holes and leveled out the surface to minimize air gaps between the plates and the concrete. Once the HFT plates were fully assembled, they were transported to the thermal properties laboratory and laid out in the unguarded thin heater apparatus to obtain calibration.

HFT Location Considerations

One of the decisions during design of the experiments was the location of the HFTs. The choices included:

1. In the insulation on the surface in contact with the slab. One problem with this location is that the product being tested is slightly modified by having a small volume on the surface routed out to accommodate the HFT.
2. In the insulation under the protective covering on the outside. This has one major shortcoming. There will not necessarily always be a covering below grade. This leaves the HFT exposed to soil moisture and general mechanical and chemical abuse caused by the backfill.
3. In the concrete slab edge. This has the shortcoming of not allowing calibration of the HFT in situ. However, if the guarded sensor could be mounted in a portable plate, the HFT could be calibrated prior to installation. The plate could then be mounted in a parget coat of concrete on the slab edge. One major concern is that there is a lot of vertical heat transfer near the grade level, and precautions would need to be taken to avoid encouraging additional lateral heat transfer. Another concern is that it is desirable to keep the HFT away from the elements in order to avoid drastic fluctuations. This can be done in the insulated case, but cannot be done if an uninsulated case is to be measured.

4. In the concrete floor. Again, this would be difficult to calibrate in situ, and it would be difficult to tell where the measured heat at the slab floor was going; straight down, under the perimeter insulation, or through the perimeter insulation.

Before a final decision was made, a number of related considerations were incorporated. It was recognized that an exterior HFT location on a slab foundation wall raises several concerns: 1) a masonry wall may have vertical heat conduction near the ground level, 2) sensor placement should not contribute significant resistance to the construction, 3) highly conductive materials are unfavorable for HFT mounting sites, 4) wide temperature swings should be avoided, and 5) some heat flux transducers are damaged by moisture. The choice of the outside slab edge is a compromise between the least favorable site conditions with the location of maximum interest.

Having the HFT located in portable plates positioned to minimize the impact on the heat offers an intriguing bonus. There is the possibility of a calibrated slab edge with great flexibility for conducting multiple sample testing with minimum reconfiguration effort. Also, since slab insulation performance is of major interest, placing the HFT nearest the actual insulation enables minimum reliance on computer modeling to derive major conclusions. This is a desirable feature from a technology transfer perspective.

HFT Mounting Considerations

The next question then becomes, "How to mount the HFTs?" The importance of this decision is highlighted by ASTM STP 885,[3] which states, "accuracy is attainable to within 5% error in laboratory applications and within 5 to 20% for in-situ application for the careful user. Field-use errors on the order of 100% are not unusual if attention is not paid to proper technique."

Ideally, heat flux transducers should be located at sites with one-dimensional heat flux perpendicular to the sensor. It is standard to use surface-mounted sensors on the inside surface unless it is necessary to mount them on the outside surface. Consequently, not much research or development information has been published on external applications. Yet, these applications are used extensively and provide the researcher with great versatility. The ASTM workshop on HFTs recommended that work be done on the effects of external conditions on HFT operation, reliability, and accuracy.[3]

Installation of a heat-flux meter in a building wall typically distorts the heat flow through the wall so that careful interpretation of the meter output is necessary. The heat flow through the meter is usually not equal to that through the undisturbed material. If the meter has a higher conductivity than the surrounding material it displaces, it provides a low resistance path for the local heat flow. The heat flux through the meter is higher than the flux in the surrounding undisturbed material. Conversely, if the meter has a lower conductivity than its surroundings, it produces a locally high resistance path to heat flow and the flux through the meter is lower than the undisturbed flux. If a meter is placed on the outside of a wall, it can disturb the local convective heat transfer with the atmosphere, again giving a different flux through the meter compared to the surrounding undisturbed material. The meter must also have an emittance similar to the wall being tested when it is surface mounted.

It is desirable to minimize both the amount of one-dimensional heat-flux difference between the meter and surroundings, and the amount of three-dimensional distortion. The one-dimensional heat-flux ratio is an easy-to-calculate estimate of the true heat flux ratio. It is calculated by comparing the thermal resistance of a path through the meter to that of a path outside it. The three-dimensional distortion is that part of the distortion not included by the one-dimensional model. It is produced by the locally distorted three-dimensional heat flow around the meter, i.e., by the curvature of the isotherms in the vicinity of the meter. This distortion is mostly confined to the outer edges of the meter, typically decaying in the first 6.35 mm (0.25 in.) of a 51-mm (2-in.) square uniform meter.

A guard frame is a lateral extension to the meter, and is made of the same material as the meter (except that it contains no thermocouple junctions), so that a meter with a guard frame acts like a larger meter with its sensing area in its center, away from any three-dimensional distortion effects.

The type of heat-flux transducers selected for this experiment were the Hy-Cal 51- x 51-mm (2- x 2-in.) model BI-7. Because these sensors have metal cover plates, the surfaces provide easy paths for transmitting the disturbances produced around the edges of the meter into the meter's center sensing area. As a result, guard frames can be less effective on cover-plated meters. Bligh reports that a 12.7-mm (0.5-in.) wide guard only reduces the three-dimensional distortion by 30%.[3] Bligh states that if a cover-plated meter is fitted with a guard, and a thermal break is provided between the cover plate of the main meter and that of the guard frame, the mechanism for the easy transfer of lateral heat from the guard frame to the meter would be removed and the guard would be far more effective. The purpose of using a guard frame, therefore, is to reduce the three-dimensional distortion to a level where it can be ignored, and the simple one-dimensional model can be used. The guard should have similar construction and the same thickness and thermal resistance as the HFT.

Johannesson recommends using a guard six to ten times as wide as the thickness of the HFT and calibrating the sensor against a variety of substrates to determine the range of thermal conductivities for which it may be used.[3] The sensor should have the same absorptance as the surface to which it is applied to avoid spurious influences from short-wave radiation. Natural convection is reportedly a minor problem as long as the air gap between the sensor and the surface to which it is applied is less than 1 mm (0.04 in.). Good thermal contact between the surface and an HFT with a guard is more difficult to obtain with a larger area.

Flanders states that there is also a need to match convective effects on the HFT and the surface which is being characterized. The size of the guard would depend on the thickness of the construction to be measured, but 0.3 m^2 (3.2 ft^2) would suffice in most cases.[3]

Covering the HFT smooths the flow of air and offers the opportunity to match the absorptivity of the sensor to its surroundings. ASTM C1046-85 states, "For most nonmetallic materials, the absorptance is in the range of 0.85 to 0.9, and masking tape or a more durable alternative will suffice as a cover."[14] ASTM C1046 also states that a cover of about 0.093 m^2 (1 ft^2) is suggested for HFTs smaller than 0.1 m (4 in.) on one side. The method of installing the HFT in portable-guard plates can satisfy all of the above conditions and permits HFT calibration by a laboratory thermal-testing apparatus.

Construction

Based on the siting consideration listed above, it was decided the best location for the HFTs was on the slab edge, mounted in 0.14- x 0.14-m (5.5- x 5.5-in.) guards. The guards are constructed of materials which produce a composite that has a measured thermal resistance within 1.5% of the actual HFT. The measured k for a dissected HFT was 0.596 W/(m·K) (4.14 Btu-in./h·ft^2·°F). With the same cut-bar apparatus, the value for a small core of the composite guard was measured at 0.605 W/(m·K) (4.20 Btu-in./h·ft^2·°F). This apparatus uses a comparative longitudinal heat-flow measurement technique.[4] The error of these measurements is on the order of ±3%. Six-inch-square guard sheets of this material were epoxied together using an epoxy that handles freezing conditions well. The specific epoxy is APCO 5313, distributed by Chembar, Inc.[5] The guard-material composite consists of a layer of 1.59 mm (0.0625 in.) phenolic laminate sandwiched between two layers of 0.51 mm (0.02 in.) aluminum. Figures 4 through 6 show drawings of these guards. Note that the aluminum is removed around the opening for the HFT to avoid contact between the aluminum guard layers and the sensor. The concentric squares are cuts in the aluminum made after it is adhered to the phenolic that

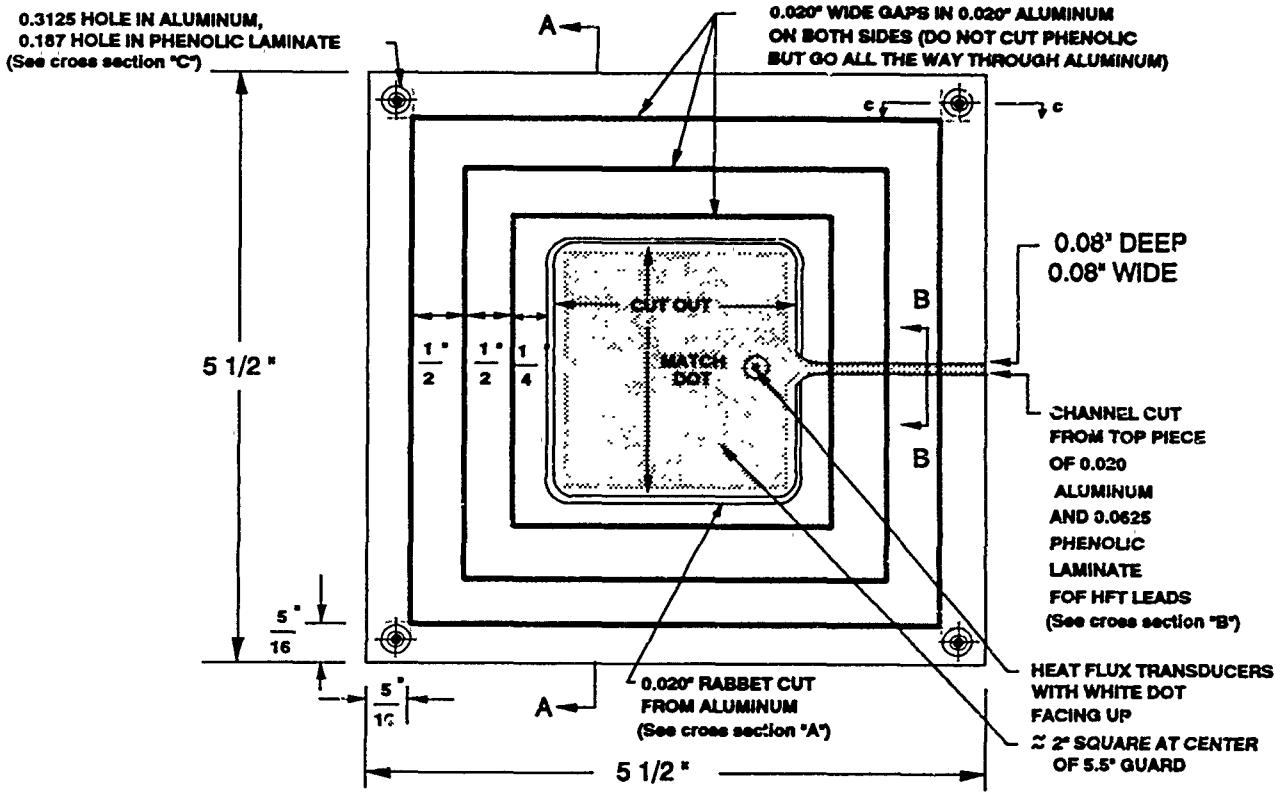

Figure 4. Top view of heat-flux transducer guard for 2- x 2-in. HFT.

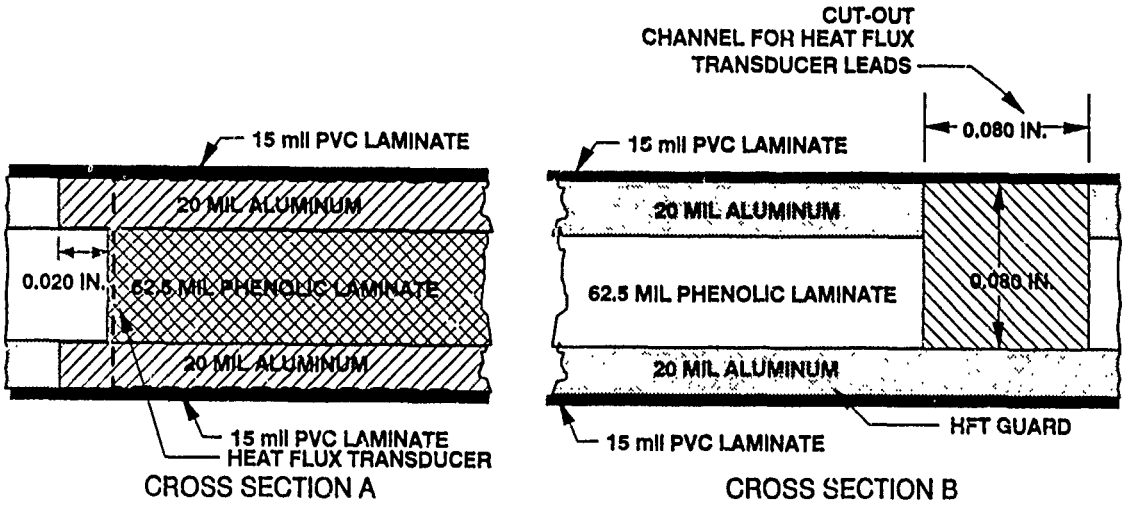

Figure 5. Cross section of heat-flux transducer guard showing lead wire channel and rabbet cut around the HFT opening to prevent aluminum from contacting the HFT.

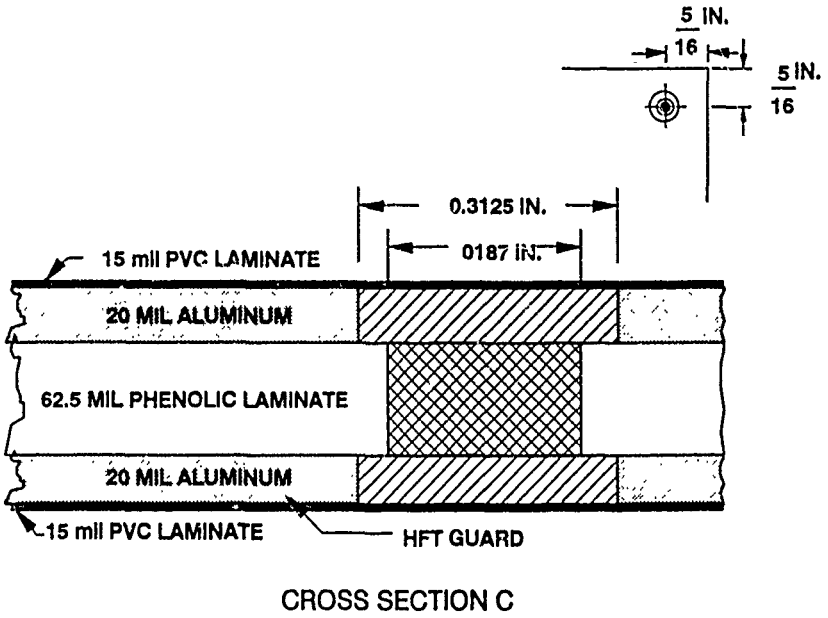

Figure 6. Cross section of heat-flux transducer guard showing holes for fasteners designed to prevent fastener contact with aluminum.

minimize the lateral heat transfer to the sensor. Four holes were drilled in the sensor guard to mount the HFT and 0.14- x 0.14-m (5.5- x 5.5-in.) guard separately or to provide better thermal contact between the HFT and envelope component when mounted in a larger plate.

For this application, the guard is mounted in a larger plate made of the same material as the guard, sandwiched between two layers of 0.38-mm (0.015-in.) PVC laminate that act as both a mask and a protective covering for the sensor. Using k reported for PVC of 0.16 W/(m·K) (1.12 Btu-in./h·ft^2·°F) the k-value of the entire

a.

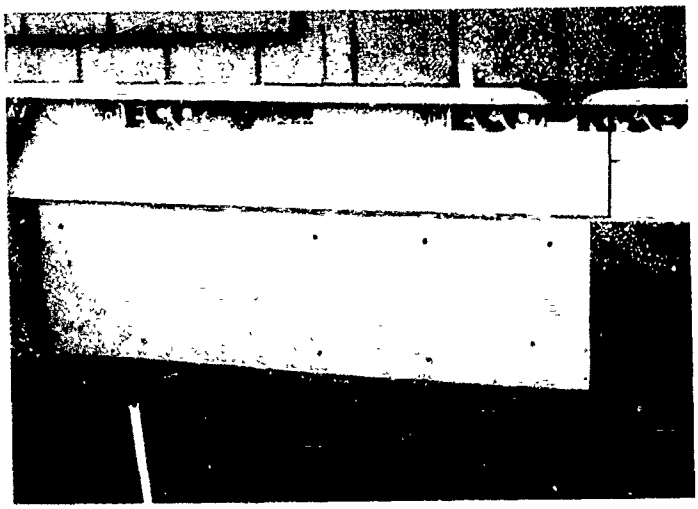

b.

c.

Figure 7. Photos of test insulation installation. (a) Foundation wall with heat-flux transducer plates prior to the insulation installation. (b) Top 0.25-m- (10-in.-wide pieces of XEPS installed. (c) Finished test panel before backfilling.

plate, which includes both cover sheets of PVC, is estimated to be 0.38 W/(m·K) (2.65 Btu-in./h·ft^2·°F). Considering the thickness of these plates, the *R*-value is only 0.09 m^2·K/W (0.05 h·ft^2·°F/Btu-in.). The limestone color of the PVC is very near that of the concrete, which implies an absorptance match. Figure 7 shows the HFT plate assemblies fastened to the foundation wall. The PVC laminate is fastened to the aluminum with a contact cement called "High Performance Contact Adhesive 1357."[6] It is recommended for both aluminum and plastics and maintains a reasonably good bond in a wide range of temperatures. It is a toluene-base adhesive, so it is possible to disassemble the plate cover by wetting the bond line with toluene and slowly pulling the laminate. This permits examination or replacement of the HFT, if necessary.

Figures 8 through 13 present a series of photos depicting the assembly of these plates. The first photo in Figure 8 shows the five layers used to assemble the HFT guard plates. First, the 0.14- x 0.14-m (5.5- x 5.5-in.) guard is assembled. Figure 9 shows the larger plate with the machined grooves in the aluminum layers and the 0.14- x 0.14-m (5.5- x 5.5-in.) guard. One piece of PVC is laminated to the backside before the HFT is mounted. Figure 10 shows HFT and thermocouple placement within the HFT guard plate. One of the vertical grooves in the aluminum is used to run the wire leads to the edge of the plate. Figure 11 shows the contact cement spread on both the aluminum and the PVC laminate. The area where the HFT contacts the PVC is not glued. Rather, a thin layer of heat-sink compound is spread over the HFT to provide good thermal contact between the plate and the PVC. Care was taken so that excess heat-sink compound would not be squeezed into the 0.51 mm (0.02 in.) channel separating the HFT from the aluminum in the guard. Figure 12 shows the back of the HFT guard plate with heat-sink compound over the location of the HFT. Guide holes were punched through the four

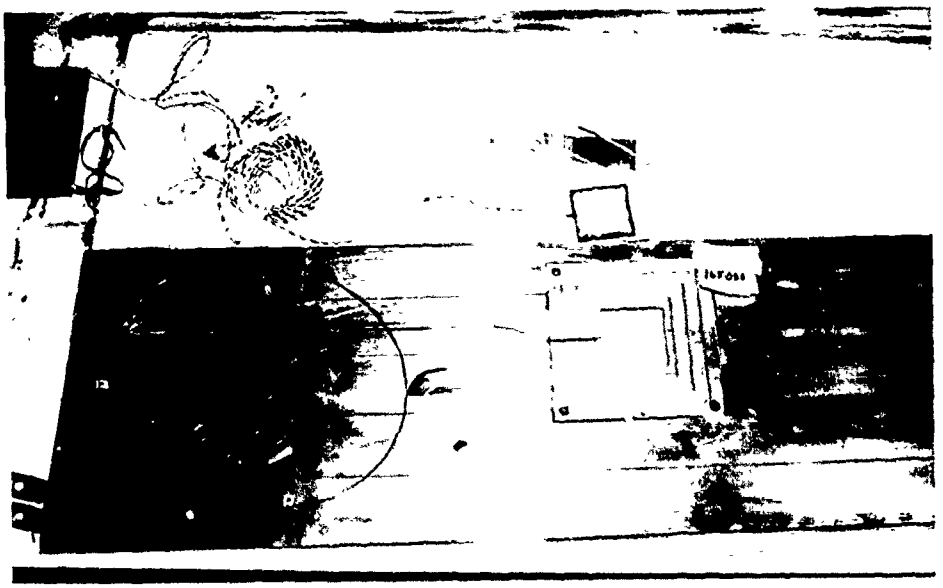

Figure 9. Larger plate with machined grooves and 0.14- x 0.14-m (5.5- x 5.5-in.) guard.

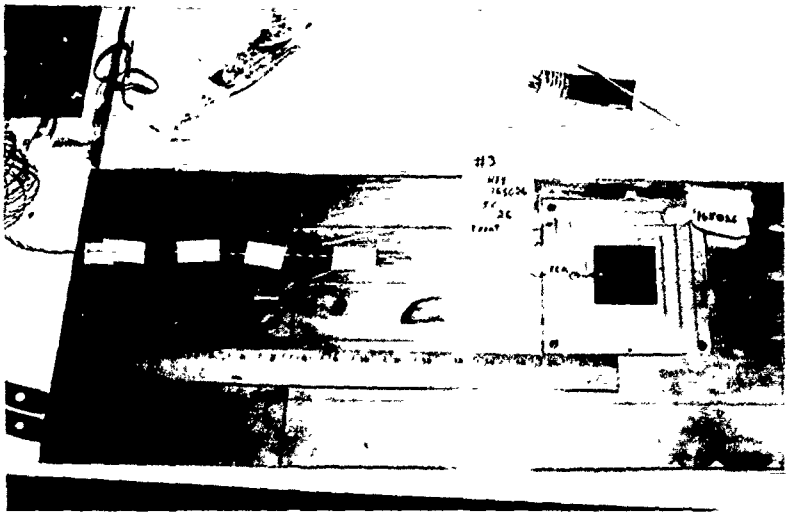

Figure 10. HFT and thermocouple placement within the HFT guard plate.

holes in the 0.14- x 0.14-m (5.5- x 5.5-in.) guards and sealed. It was judged that good thermal contact among all surfaces would be maintained without additional fasteners at these locations. If the data suggest poor contact, fasteners can be easily added later. Figure 13 shows fastened plates. About 10 screws were used to fasten each plate to the foundation wall.

The parget coat put on the slab test section, along with the flexibility of the panels, provides good contact between the plates and the foundation wall. Heat-sink compound was modestly spread on all surfaces between the HFT itself and the PVC, as well as between the PVC and the concrete, in an attempt to minimize contact resistances. A single thermocouple is mounted about a half inch away from the edge of each HFT in one of the grooves cut in the aluminum layer of the 0.14- x 0.14-m (5.5- x 5.5-in.) HFT guard.

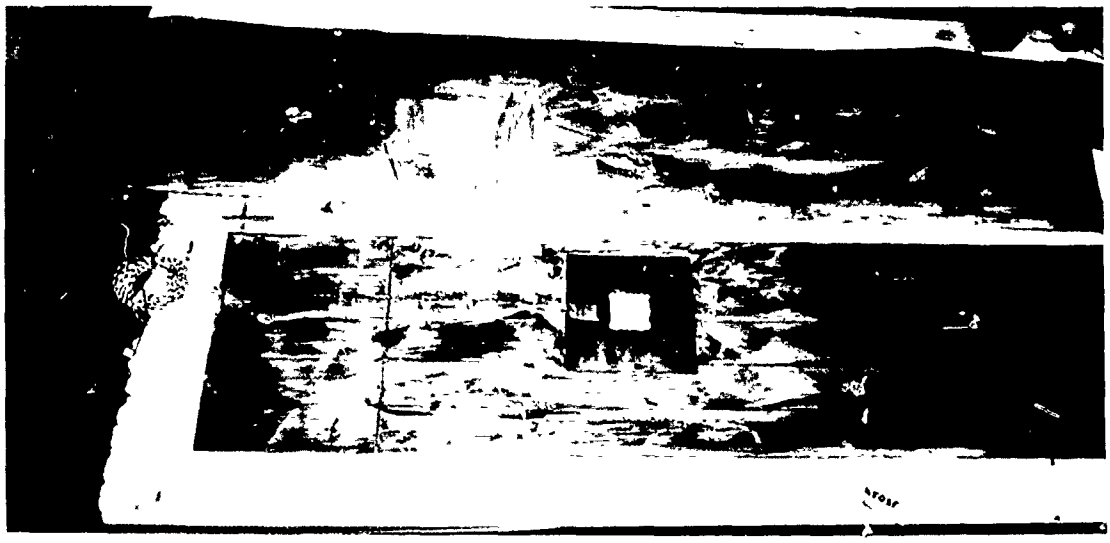

Figure 11. Contact cement on aluminum and PVC laminate.

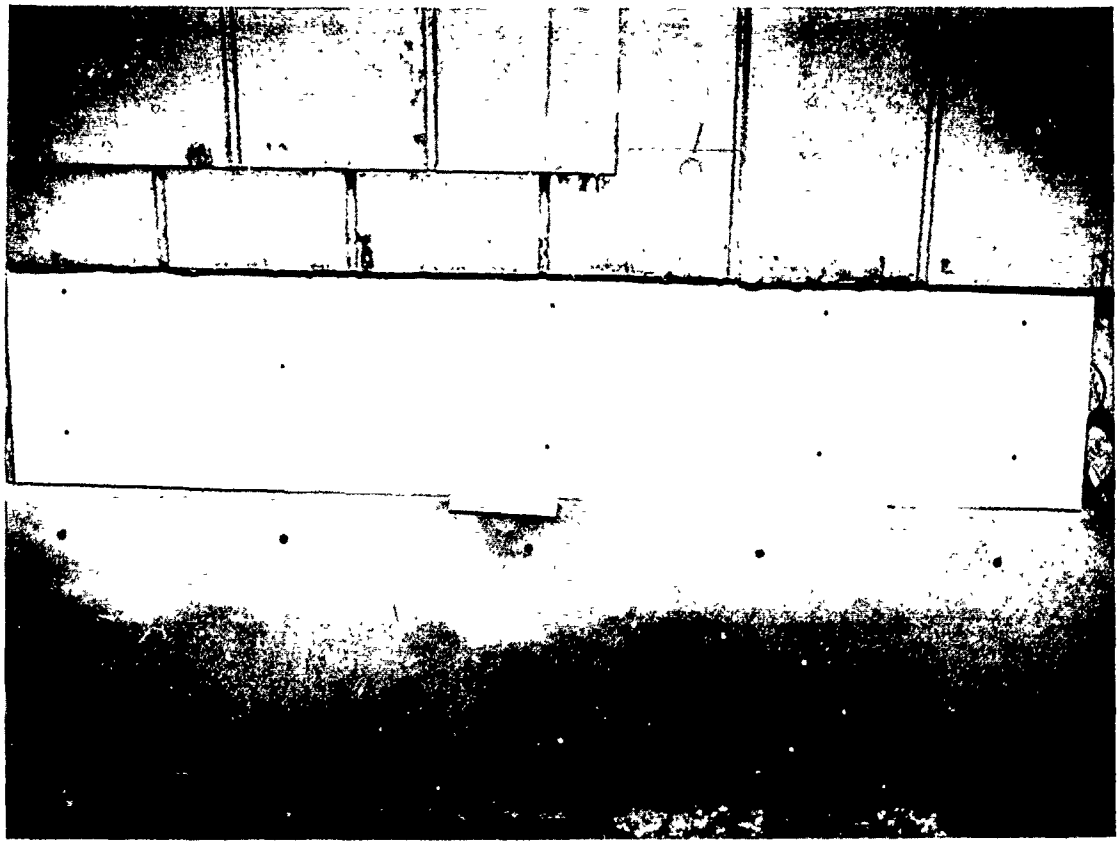

Figure 12. Back of HFT guard plate with heat-sink compound.

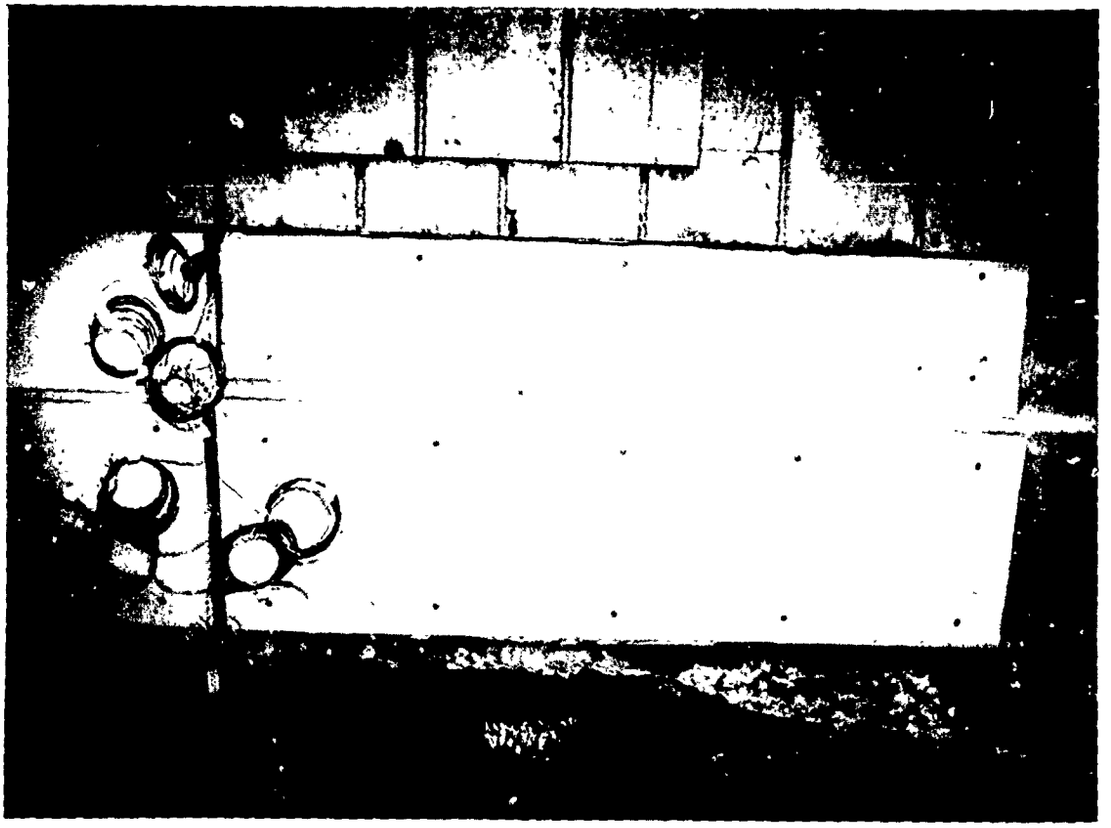

Figure 13. Plates fastened to foundation wall.

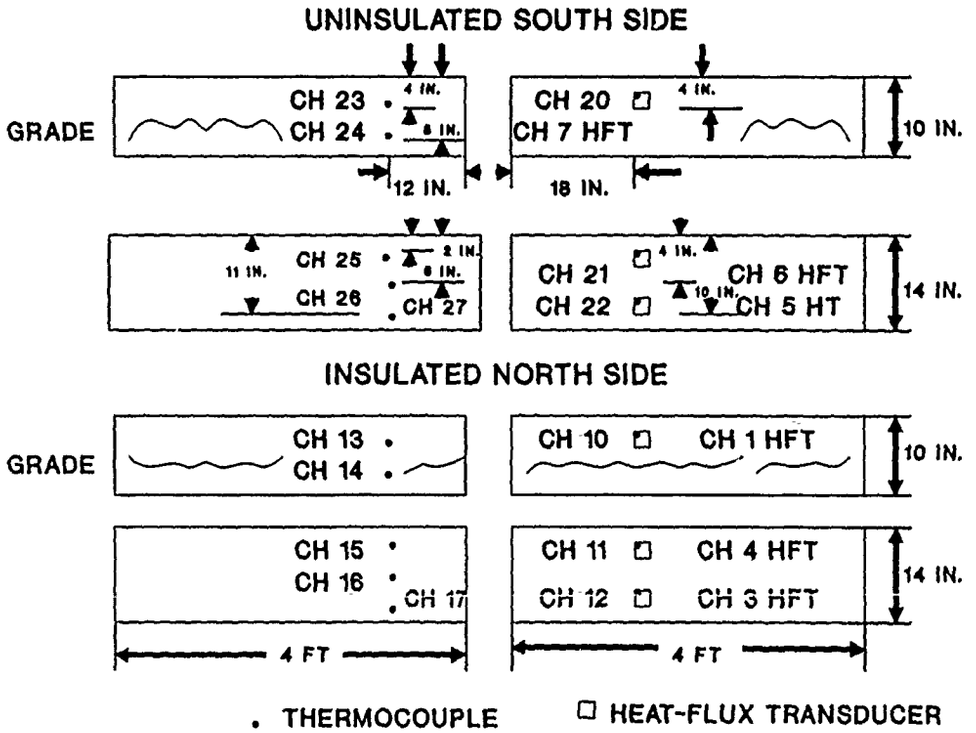

Figure 14. Heat-flux transducer guard plates showing the sensor locations and DAS channel number.

Figure 14 shows HFT and thermocouple locations in the eight HFT guard plates produced for this experiment. The top four plates are those positioned on the uninsulated south part of the east wall. The bottom four are those positioned on the insulated north part. The dots indicate the location of 30-gauge copper-constantan thermocouples. Labeled locations, shown on the top set of plates, are the same on the bottom set. The data acquisition channel numbers are also shown.

Before these plates were installed, the entire east foundation wall was given a smooth parget coat that filled in the small stone holes and leveled out the surface to minimize air gaps between the plates and the concrete. An acrylic resin bonding agent was used instead of water to better adhere the parget coat to the existing foundation wall. Plastic inserts were tapped into masonry holes drilled with a carbide-tip 6-mm (1/4-in.) bit. About 10 holes were drilled for each plate, for a total of 80 holes. Counter-sunk 25.4-mm (1-in.) screws were used to fasten the plates to the wall. Each hole in the plates was counter sunk to be almost flush with the exterior plate surface. This was necessary to minimize the potential air gap between the insulation and the plates. The screws provided sufficient strength to pull the plates tightly against the foundation wall.

Calibration

When heat flows through a heat-flux meter it generates an output voltage (electromotive force, emf) that is very nearly proportional to the heat flux. The aim of calibration is to find the coefficient of proportionality between the heat flux through the meter and its output voltage, i.e., its calibration factor, given by:

$$\text{Calibration Factor} = q_m/V, \qquad (1)$$

where q_m is the mean heat flux through the sensing area of the meter perpendicular to the meter surface and V is the meter output voltage.

The ORNL flat-screen insulation tester was used to calibrate the heat-flux transducers.[7] This apparatus provides an absolute method for determining the apparent thermal conductivity, *k*, of rectangular specimens and is an alternative to the guarded hot plate (ASTM C-518 1983).[8] The screen tester is used to obtain steady-state measurements of heat flux (q/A) and temperature difference (ΔT) across a horizontally mounted specimen of known thickness (t) from which *k* is calculated with Fourier's law for one-dimensional (steady-state) conduction heat flow:

$$\frac{q}{a} = -k\,\frac{dt}{dx} \approx k\,\frac{T_2 - T_1}{t} \qquad (2)$$

where T_1 is the temperature of the heat source of the electrically powered 0.9- x 1.5-m (3- x 5-ft) fine wire screen and T_2 is the average temperature of the water-cooled copper plates.

Eight heat flux transducers were calibrated simultaneously. Six of them were mounted in four heat-flux-transducer guard plates (two in each of two plates and one in each of two plates), and two were mounted in two different pieces of extruded polystyrene, which was to be installed in the slab-edge test section of the RTRA.

Since the flat-screen insulation tester can simultaneously measure heat flow across two rectangular specimens mounted above and below the screen, two stacks of foam boards and HFT guard plates were loaded. A layer of ~2-in. thick XEPS was placed nearest the screen, and two layers of plates were mounted near the heat sink plates, which were maintained near room temperature.

The measured calibration factors were compared to those provided by the manufacturer, and they were found to be on average about 12% below the manufacturer's

Table 1. Comparison of calibration factors from screen tester with those provided by the manufacturers.

SN	ORNL flux at 1 mV	HyCal flux at 1 mV	% ORNL/HyCal x 100
25	0.3751	0.4786	78.4
26	0.4489	0.4664	96.2
27	0.4074	0.4679	87.1
28	0.4114	0.4662	88.2
29	0.4129	0.4162	89.5
31	0.4011	0.4569	87.8
32	0.4027	0.4578	88.0
33	0.4220	0.4567	92.4
Average	0.4102	0.4640	88.5

factors, as shown in Table 1. This can be compared with unguarded HFTs mounted in insulation, which average 30 to 45% below manufacturer values.[9] This is not surprising if the manufacturer's calibration procedure is conducted in such a manner as to avoid the 3-D heat flow around the sensor, because the high conductivity of the HFT causes the heat to be channeled through the sensor when it is mounted within insulation, resulting in a higher flux than the average flux in the surrounding insulations. The resulting calculated calibration factor, then, is lower to account for this channeling.

The accuracy of the insulation screen tester to measure *k* for insulation samples is within 2%.[7] If the uncertainty of excessive lateral heat flow in HFT guard plates were minimal, the calibrating of the calibration factors for all eight of these HFTs could be considered to be ±2%. At this time the actual uncertainty has not been calculated; however, it is believed to be within 5%.

TEST SECTION: EAST SLAB EDGE

The experimental insulation used was processed on December 10, 1987. A few 0.61-x 0.61-m (2- x 2-ft) specimens were taken from this batch and a measured thermal conductivity value obtained using the ORNL screen tester and R-Matic. The R-Matic is a device that conforms to ASTM C-518 (Standard Test Method for Steady-State Heat Flux Measurements by means of the Heat Flow Meter Apparatus), which is a comparative test method rather than a primary measurement method.

Figure 15 is a plot that shows all the measured *k*-values along with the predicted decay of this material. The circle "O" is the UCI data point, the diamond "◇" is the TTU R-Matic, the open square "□" is the ORNL thin screen tester, and the solid square "■" is the ORNL R-Matic. The shape of the curve is similar to that of other insulation thermal aging curves. The curve is a projection based on the nature of thermal decay. The regression derived from all of the *k*-value measurements is shown by equation 3:

$$k = \frac{153.6467}{Age^2} - \frac{6.58793}{Age} + 0.262 \qquad (3)$$

where

Age = days since manufactured.
k = conductivity (Btu-in./h·ft²·°F), to convert to SI units multiply by 0.144.

The absolute differences between the measurements and predictions using this regression equation vary from 0.64 to 3.8%. The average density of this material was measured at 0.95 kg (2.1 lb/ft³). The thickness averaged around 48 mm (1.9 in.).

The thermal conductivity of HCFC-22 is greater than that of CFC-12. An XEPS blown with HCFC-22 will have a lower thermal resistance than the current product. The permeability of HCFC-22 in extruded polystyrene is also slightly higher than CFC-12. The aged resistivity of this material predicted by the aging equation is 0.67 m²·K/W (3.82 h·ft²·°F/Btu-in.).

The test material was placed in the ground in February 1989. The initial data collection began on February 13, 1989, that is 430 days after this insulation was manufactured. Using the curve shown in Figure 15, the estimated resistivity of the test material installed in February is 0.71 m²·K/W (4.05 ft²·h·°F/Btu). A 0.61- x 0.61-m (2- x 2-ft) section was removed from the test section 586 days after production, and its resistivity measured in the ORNL advanced R-Matic was 0.7 m²·K/W (3.99 ft²·h·°F/Btu) 24°C (75°F).

A 4.3-m (14-ft) section of the east slab edge is insulated. Three layers make up the insulation test section. Layer 1 consists of the 0.25-m- (10-in.) wide pieces that fit into

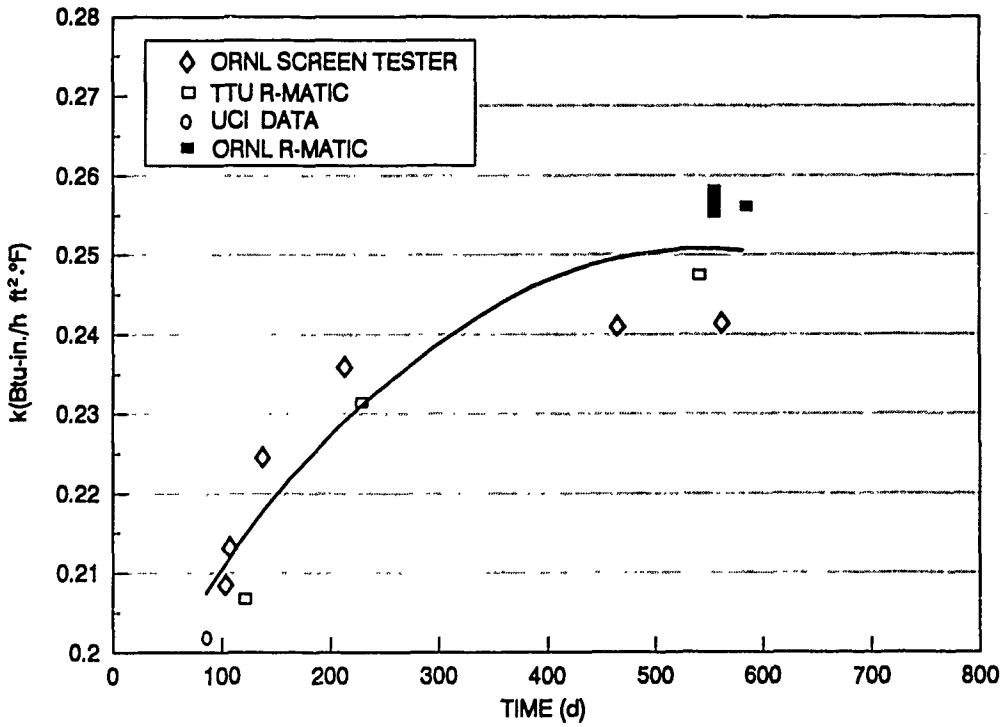

Figure 15. Laboratory thermal conductivity measurements of experimental XEPS and thermal aging predictions.

the slab-edge indentation. The middle 1.22-m (4-ft) section contains a guarded HFT that is routed into the panel to measure the heat flux of the slab insulation at about 51 mm (2 in.) above the grade level on the instrument plane, as shown in Figure 7b. This HFT is coated lightly on one side with heat-sink compound to ensure good thermal contact with the adjoining foam. The HFT and guard are then taped over using masking tape, although both the guard and the HFT holds with friction alone. No heat-sink compound is used on the exterior facing surface. The second layer of XEPS fits tightly over this HFT, and it was judged that good thermal contact between the HFT and the second layer of XEPS would be maintained.

Layer 2 consists of three pieces of 0.6-m (24-in.) wide XEPS. The second piece of XEPS in this layer contains a guarded HFT routed into the surface facing the heat flux transducer plates attached to the concrete foundation wall at the same height as the HFT in the instrument plane measuring fluxes 0.2 m (8 in.) below grade. However, the HFT is mounted about 0.91 m (3 ft) to the left of the actual instrument plane for this test section. The modeling suggests that approximately the same flux should be measured within this area. It was judged that placing HFTs on top of each other with only a single 38-mm (15-m) layer of PVC laminate between the two sensors may cause interference between sensors.

Layer 3 is the protective cover for the XEPS. Note that only the above-grade portion of the XEPS needs to be covered. However, if these panels are to be used as left-in-place forms for pouring the monolithic slab, the entire foam board needs to be covered to provide sufficient structural strength to hold the concrete until it sets.

Two sections were used to adhere a PVC laminate over the entire surface that was to be exposed to the soil. This covering provides sufficient strength to the XEPS/PVC composite board to be used as forms for monolithic, poured slab-on-grade construction. Builders would more readily insulate slab edges if there were an easier way to install the insulation. A left-in-place form that saves the cost of removing and cleaning up wood or metal foams is attractive to builders.

Before the insulation test panels were mounted, heat-flux–transducer guard plates were mechanically fastened to the foundation wall as shown in Figure 7. Recall that Figure 7 is a series of photographs illustrating the assembly of the insulation test section. The first photo, a, shows the four experimental heat-flux–transducer guard plates on the test section. The second photo, b, shows the 10-in. insulation pieces installed and the location of the HFT. The last shot, c, shows the assembled insulated section.

FIELD MEASUREMENTS USING THE HFT PLATE ASSEMBLY

The HFT plate assembly performance has been compared to careful steady-state laboratory measurements by comparing data taken on the same specimen of XEPS. The HFT and thermocouples placed in the instrumentation plane cutting perpendicular to the face of the slab insulation have been continuously monitored for almost two years. The sensors are automatically read every minute, averaged and stored hourly. The in-situ resistivity (R^*) can be calculated during the heating season by equation 4. The averaging technique was compared to more complex procedures, and found to provide similar R^* estimates during periods with no heat flow direction reversals:

$$R^* = \frac{\Delta T}{QXt} \qquad (4)$$

where

ΔT = average weekly temperature drop across the insulation
Q = average weekly heat flux measured at the surface of insulation
t = thickness of the insulation

Figure 16 is a plot of R^* for 32 weekly heating periods. The field measurement based R^* values normalized to 55 °F are plotted with "squares" in Figure 16. The HFT used to produce Q in equation 4 is shown in Figure 14, labeled "CH 4 HFT." This HFT is measuring heat flow from a foundation approximately 0.2 m (8 in.) below grade. The specimen age for these field measurements ranged from 430 to 860 days spanning two heating seasons.

The conductivity of this insulation varies with temperature in order to compare the field data with the laboratory measurements, all of the R^* are displayed as normalized values at 55°F. The values normalized using the linear regression equation 5.

$$R^*(55) = R(TM) - 0.013885 * (TM - 55) \quad (5)$$

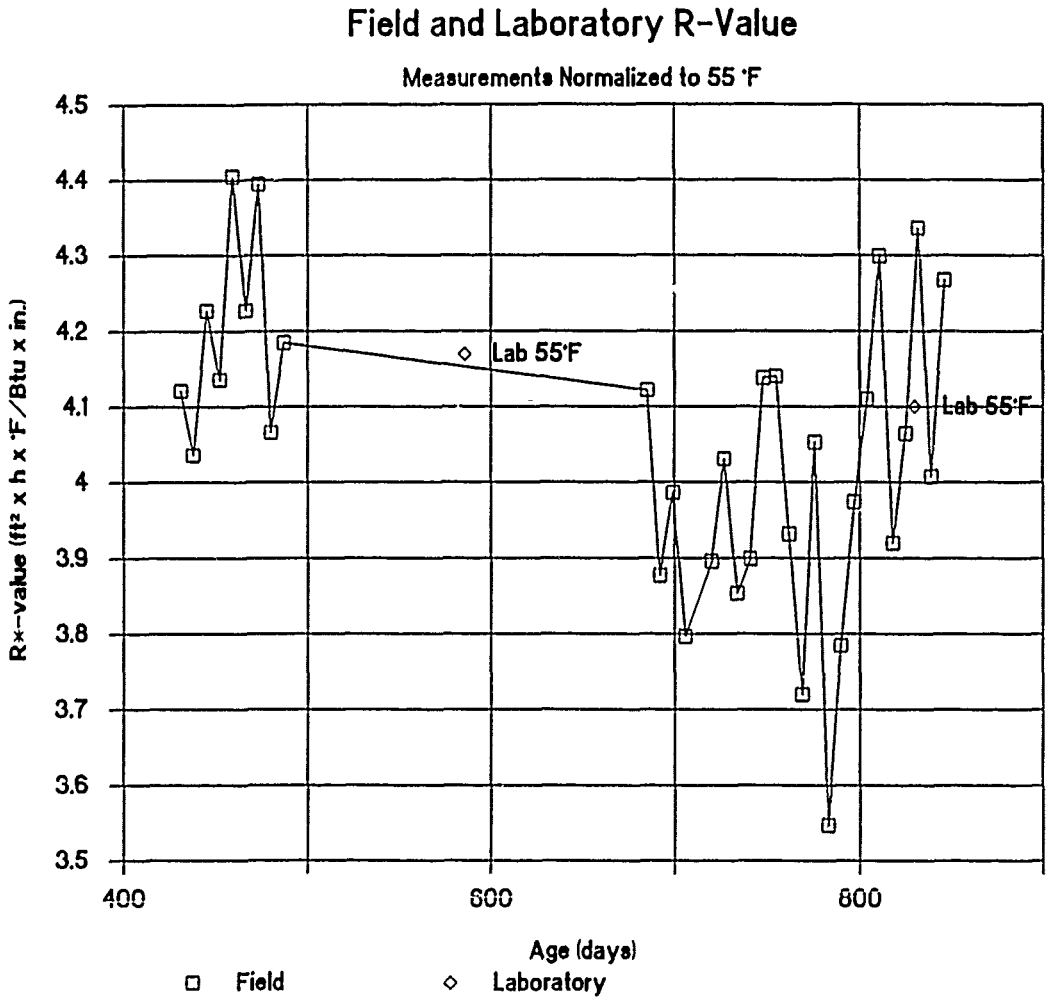

Figure 16. Average weekly field R-value measurements and normalized to 55°F vs sample age.

where

R(TM) = R-value derived from field measurements at in-situ temperature ($ft^2 \cdot h \cdot °F/Btu$)
TM = mean in-situ temperature of sample (°F).

The constant in equation 5 was obtained by linear regression of the thermal resistance measurements on the field specimen pulled in July 1989. The use of equation 5 provides an extrapolation very near the in-situ insulation temperature, which varied from 8 to 17°C (47 to 62°F) and minimizes the potential normalization error.

The averaged normalized R^* at 13°C (55°F) for the heating season from 430 to 500 days, representing the heating period from February 13 until April 12, 1989, was 0.74 $m^2 \cdot K/W$ (4.20 $ft^2 \cdot h \cdot °F/Btu\text{-in.}$). The average mean temperature of the insulation specimen over this period was 12.6°C (54.6°F). The average R^* for the same period one year later, 1989-90 heating season (day 760-860), was 0.718 $m^2 \cdot K/W$ (4.08 $ft^2 \cdot h \cdot °F/Btu$). The average mean temperature of the insulation specimen over this period was 13.3°C (55.9°F).

The field measurements suggest a slight aging effect (2.8% drop in R-value) of the insulation. The magnitude of the effect is vary small but roughly consistent with the laboratory measurements and model predictions.[10] Measuring in-situ R^* below grade is more difficult than steady-state laboratory measurements, and there is, consequently, more scatter in the data. In July 1989 (day 586), a sample from this field installation was removed and measured in the laboratory using the ORNL Advanced R-matic to measure steady-state resistivity. The reported resistivity at 12.8°C (55°F) was 0.734 $m^2 \cdot K/W$ (4.17 $ft^2 \cdot h \cdot °F/Btu$). This compares very well with the field measured resistivity, as shown in Figure 16. The same specimen was removed from the installation in March 1990. The R-Matic measurements and evaluation results in a dry sample resistivity at 12.8°C of 0.722 $m^2 \cdot K/W$ (55°F of 4.1 $h \cdot ft^2 \cdot °F/Btu$) at 830 days. This is about 1.3% below the previous 586 day laboratory measured value. However, the sample was found to have 0.3% moisture by volume. Using the effect of moisture relationship on the thermal performances of XEPS blown with CFC-12, the wet R-value can be expected to be about 1% less than a dry sample.[30] Both of the laboratory measurements are shown in Figure 16 as "◇". Taking into account that in the field the specimens are actually performing in a none-dry state, comparisons with steady-state laboratory measurements should be made cautiously. To reach steady state all of the moisture is typically allowed to escape from the specimen prior to recording the final laboratory measurement. Nevertheless, if the laboratory measurement in March of 1990 is reduced 1% to account for the moisture effect, the laboratory measurement would be 0.715 $m^2 \cdot K/W$ (4.06 $ft^2 \cdot h \cdot °F/Btu$). This compares well with the second half of the entire 1990 heating season average normalized resistivity at 12.8°C of 0.718 $m^2 \cdot K/W$ (55°F of 4.08 $ft^2 \cdot h \cdot °F/Btu$). The averaged resistivity at 12.8°C (55°F) for the entire 1989-1990 heating season from October to April 15, 1990 is 0.70 $m^2 \cdot K/W$ (4.0 $h \cdot ft^2 \cdot °F/Btu$). In general, the in-situ HFT measurements taken with this HFT plate assembly compare favorably to more carefully controlled laboratory steady-state measurements, and provide a most desirable insight into actual dynamic thermal performance of foundation systems.

DISCUSSION AND CONCLUSIONS

A well-characterized slab-on-grade foundation test site has been established. The design of this experiment has generated the development of an innovative HFT plate assembly for measuring heat flow on the exterior surface of building envelopes. The 1989 and 1990 winter heating-season performance data have been collected and preliminary

analysis initiated. The HFT plate assembly designed for this experiment appears to be performing very well compared to periodic steady-state laboratory thermal conductivity measurements taken in the laboratory, on the same field specimens.

The HFT plate assemblies have performed continuously for more than 15 months of continuous data acquisition. A more conventionally mounted HFT routed into the insulation fastened to the exterior foundation insulation in this experiment was found to be unreliable less than three months after installation and eventually failed completely. An earlier field monitoring project in 1980-82, on a bermed foundation wall at ORNL, also lost three critical HFTs that were routed into the inside surface of exterior foundation insulation in contact with the surrounding damp earth. The desire to make heat flux measurements on the exterior of the foundation wall, which is in contact with damp soil, is a challenging HFT application. The HFT plate assembly described in detail in this paper has proven to provide reliable data in one field experiment.

With many of the national building energy codes and standards ready for public comment and adoption, the issue of foundation insulation effectiveness will be debated. Having a reliable means of making thermal performance field measurements will be valuable in helping others measure for themselves the thermal performance value of foundation insulation in all building types and climatic conditions.

The information contained in this paper is intended to be the first step in proposing a reasonable protocol to help resolve regional conflicts relative to foundation insulation effectiveness. The potential versatility of the HFT plate assemblies described could make them part of an analysis procedure that helps researchers collect in-service thermal performance data on foundation insulation without depending extensively on complex numerical computer models.

ACKNOWLEDGMENTS

Research sponsored by the Office of Buildings and Community Systems, U.S. Department of Energy, under Contract DE-AC05-84OR21400 with Martin Marietta Energy Systems, Inc.

REFERENCES

1. Christian, J. E. and Strzepek, W.R., Procedure for Determining the Optimum Foundation Insulation Levels for New, Low-Rise Residential Buildings. ASHRAE Transactions, January 1987.

2. Montreal Protocol on Substances that Deplete the Ozone Layer. United Nations Environment Programme, Final Act, September 1987.

3. Bales/Bomberg/Courville, Eds., Building Applications of Heat Flux Transducers. ASTM STP 885, Philadelphia, PA, 1985.

4. Moore, J. P., Kollie, T. G., Graves, R. S., McElroy, D. L., Thermal Conductivity Measurements on Solids Between 20 and 150°C. Using a Comparative-Longitudinal Apparatus: Results on MgO, BeO, ThO_2, $Th_xU_{1-x}O_{2+y}$ and Al-UO_2 Cermets, ORNL-401, UC-25, 1978.

5. Hexcel Corporation - Chemical Products Division, Chatsworth, CA.

6. 3M/Adhesive, Coatings, and Sealers Division/3M, St. Paul, MN.

7. Graves, R. S., Yarbrough, D. W., and McElroy, D. L., Apparent Thermal Conductivity Measurements by an Unguarded Technique. Thermal Conductivity, 18, T. Ashworth and D. R. Smith, Eds., Plenum Publishing Corporation, 1985, pp. 339-355.

8. ASTM C177-76, Standard Test Method for Steady-State Thermal Transmission Properties by Means of the Guarded Hot Plate. Annual Book of Standards, Vol. 4.06, pp. 21-54, 1983.

9. Yarbrough, D. W., McElroy, D. L., and Graves, R. S., Thermal Resistance of Roof Panels and In-Situ Calibration of Heat-Flux Transducers. ASHRAE SP 49 Proceedings, ASHRAE/DOE/BTECC Thermal Performance of the Exterior Envelopes of Buildings III, Clearwater Beach, Florida, December 1985.

10. Graves, R.S., Yarbrough, D.W., Christian, J.C., and Destephen, M.R., Thermal Performance of a Closed-Cell Foam board Insulation Containing HCFC-22. Proceedings 1990 March California Insulation Conference.

11. ASHRAE 90.2P, Energy Efficient Design of New Low-Rise Residential Buildings. Public Review Draft, American Society of Heating, Refrigeration, and Air Conditioning Engineers, Inc., Atlanta, March 1989.

12. Council of American Building Officials, "CABO Model Energy Code: 1989 Edition," CABO, Falls Church, Virginia, March 1989.

13. ASTM C1046-85, 1986 Annual Book of Standards, Vol. 4.06, Thermal Insulation; Environmental Acoustics PCN:01-040686-10, American Society for Testing and Materials, 1916 Race Street, Philadelphia, PA 19103.

Jeffery E. Christian

Q: Can you provide information on how long HFTs maintain their calibrated sensitivities?—Douglas M. Burch.

A: The experience that I have had with HFTs indicates that the calibration sensitivities can remain very constant over time, given that they are protected from excessive moisture. We have checked the calibration of the HFTs used in a long-term roof insulation aging test after 9 months and found no significant drift in all six HFTs. The calibration procedure is the same as that described in the paper. It consists of removing a small section of the insulation test specimen containing the HFT, and using the thin screen tester in the laboratory to provide an absolute measurement of conductivity.

Q: Did you find differences between the calibration values measured by yourselves and the manufacturer?—Rik van der Graaf.

A: Yes. Table 1 in the paper shows the comparison of calibration factors from the laboratory screen tester at ORNL and those provided by the manufacturer. The ORNL-measured calibration factors were 4% to 22% lower than those by the manufacturer.

Q: In your finite difference calculations to assure two-dimensional (2-D) heat flow, how were you able to know the actual properties of the soil? In-situ soil exhibits spatial and temporal variations which affect the heat flow. A calculation based on constant properties may show a 2-D behavior, while the experiment may be highly 3-D. If a 3-D case exists, how would it affect your experimental conclusions?—Ashley Emery.

A: You make an excellent point. Indeed, the variability in soil thermophysical properties around a building site can frequently enhance 3-D effects. To avoid exposing this test to these uncertainties, only one side of this building is used to conduct the characterization of the heat flow. The inhomogeneous soil was removed and replaced with a well-drained homogeneous medium. Thermal insulation is used to isolate this well-characterized test area from the unknown soil spatial and temporal variations. The modeling of this experiment thus far has only assumed constant soil properties. We indeed have found that moisture behavior in this soil varies the heat and mass flow around the base of the building. One of the long-range objectives of this study is to determine the significance of soil moisture on the energy balance of a building. If it is found to be significant, then the model will be enhanced to account for variable soil properties, resulting from moisture flow.

DEVELOPMENT OF A METHOD TO ASSESS HFT SHUNTING ERROR

R. T. Mack — Dow Chemical
T.W. Beardon — Freeport, Texas USA

ABSTRACT

A critical parameter in the accuracy of surface-mounted heat flux transducers (HFTs) is the magnitude of "shunting" of the heat flow around the HFT, due to the thermal resistance of the transducer added to the existing system. Assuming the transducer is properly selected, calibrated, and installed so that instantaneous heat flux through the HFT itself can be accurately derived from the output voltage, the absolute magnitude of the heat flux through the same site, in the same thermal environment, and with the system in thermal equilibrium— but with the HFT removed— would be somewhat higher than the measured value. Usually, it is desirable to know the heat flux without the extra insulating effect of the transducer.

Several mathematical schemes have been proposed for determining the magnitude of the shunting error[1,2,3,4,5]. Our project concerns a technique wherein a quantitative heat flux mapping technique is used with a versatile heat flow source and various types of HFTs to test the accuracy of these (and possibly other) shunting error algorithms. The object is to empirically verify a practical and accurate method for factoring out shunting bias error, thereby improving the overall accuracy of HFT measurements.

This paper reports on progress toward developing such a procedure.

INTRODUCTION

What is "Shunting"?

Literature comprising the current body of knowledge in surface-mounted HFT measurements describes several potential sources of error. The focus of this paper is the potential error source which some authors have called "shunting". Shunting is the re-routing of some of the heat flow in the vicinity of the HFT thermopile, so that the true heat flux through the thermopile is not exactly identical in magnitude to the heat flux through the same portion of the test surface, but with no HFT mounted. If the thermal system is stable with time ("steady-state" heat flow)— or if heat flux sampling times and intervals are adjusted to compensate for non steady-state— and if the HFT is accurately calibrated, then shunting becomes the single most important source of surface-mount HFT error.

When an HFT is added to the convective and radiative resistances already existing at a surface, a local site is created which has a slightly higher overall resistance, even if the HFT is thin and has a high thermal conductivity. Like most flows, the heat will take the path of least resistance; a portion of the energy will divert from purely 1-dimensional flow, toward the edges of the HFT (see Figure 1).

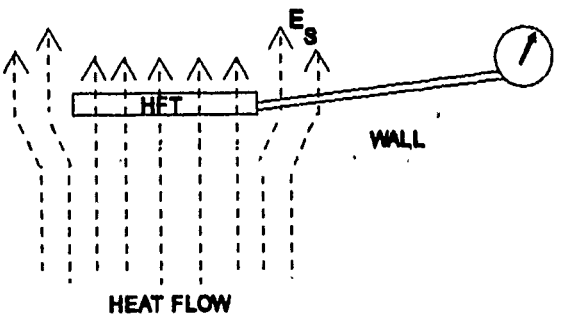

Heat Flow Shunting, Es
Figure 1

Electrical analogies have often been used to express thermal systems[6,7,8]. By way of an electrical analogy to describe shunting, we begin with Figure 2a— a bare wall described as a simple resistance circuit.

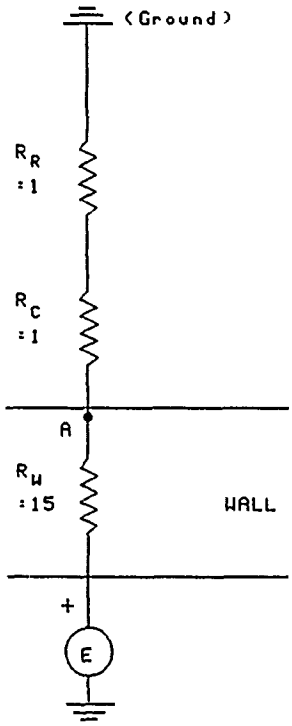

Resistances, Bare Wall
Figure 2a

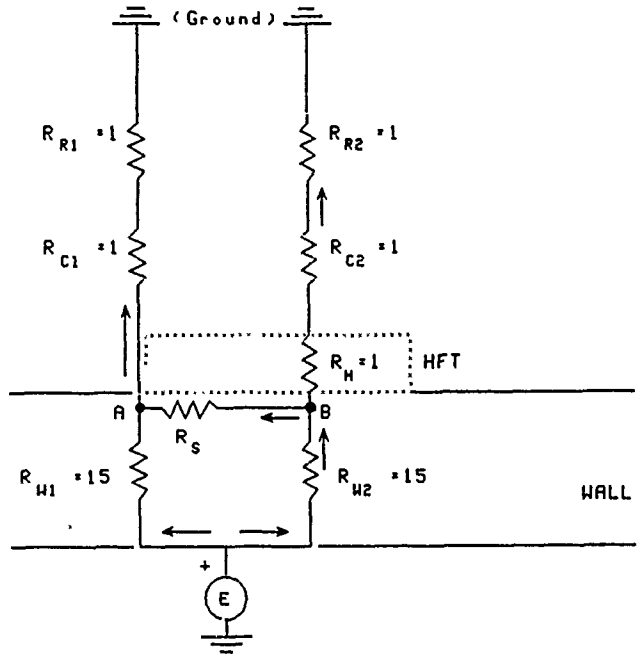

Resistances, Wall w/HFT
Figure 2b

For the bare wall of Figure 2a,

R_R = radiative surface resistance (arbitrary units)
R_C = convective surface resistance (arbitrary units)
R_W = overall resistance of the wall itself (arbitrary units)

The wall resistance, the convective resistance, and the radiative resistance are all homogeneous, so the flow is one-dimensional, and therefore "lumped" in the x-direction. The energy flow can be described by:

(Ohm's Law)[9] $I = E/R$ (Eqn.1)

where
I = current flow (energy), amperes.
E = electromotive force (potential), volts.
R = electrical resistance, ohms.

The heat transfer corollary is[10]:

$$Q = \Delta T/R \quad \text{(Eqn.2)}$$

where
Q = heat flow (energy), W.
ΔT = Temperature difference between two points (potential), K.
R = Thermal resistance, $K*m^2/W$.
Using Eqn.1 to solve for energy flow in Figure 2a.,

$$I = 75/17 = 4.4118 \quad \text{(Eqn.1a)}$$

Figure 2b demonstrates the effect of adding the extra resistance of a HFT to the system. The variable definitions, expressed in arbitrary units, are:

R_H = installed resistance of the HFT
R_S = resistance to shunting flows around the HFT
R_{R1} = radiative surface resistance, bare wall
R_{C1} = convective surface resistance, bare wall
R_{W1} = overall resistance of the wall itself, near HFT
R_{R2} = radiative surface resistance over HFT
R_{C2} = convective surface resistance over HFT
R_{W2} = overall resistance of the wall itself beneath HFT
W = width of the HFT in x

Here, the added resistance imposed by the HFT has disturbed the resistance field, so that resistance can no longer accurately be lumped in x, and there is some flow in the second dimension. That is, there is a component of flow which is parallel to the wall surface. This component R_S describes the shunting of the flow. It should be noted that this analogy is an extreme simplification: R_R and R_C are not constants, but change with surface temperature, and the shunting flows will cause changes in the surface temperature field. R_S is actually variable as a function of distance in x from the HFT center, so the shunting flow should actually be evaluated as an integral in x. Furthermore, shunting flows in and around real HFTs can be further complicated due to variations in conductivity within the HFT itself.

The simplification of Figures 2a and 2b should be sufficient, however, for HFT shunting concept familiarization. To proceed with the electrical model:

According to Kirchoff's First Law[11], the algebraic sum of all currents into a junction is 0. Therefore, at junction "A" in Figure 2b,

$$I_1 + I_5 - I_3 = 0 \qquad \text{or,} \quad I_3 = I_1 + I_5 \qquad \text{(Eqn.3)}$$

Likewise, at junction "B",

$$I_2 - I_5 - I_4 = 0 \qquad \text{or,} \quad I_4 = I_2 - I_5 \qquad \text{(Eqn.4)}$$

Kirchoff's Second Law[12] states that the algebraic sum of all potential differences around a current loop must equal zero. We can divide Figure 2b into three current loops (we must consider electrical "ground"-- or ambient "heat sink"-- the completion of the loop), and solve for the flows. The first loop models the normal flow beside the HFT. This loop proceeds from the source "E" through the left branch to "A", continuing on the left branch to "ground" (sink). In the process, it flows through R_{W1}, R_{C1}, and R_{R1}. From Eqn.3 and Ohm's Law,

$$R_{W1}(I_1) + (R_{C1} + R_{R1})(I_1 + I_5) = E \qquad \text{(Eqn.5)}$$

$$15I_1 + 2(I_1 + I_5) = 75 \qquad \text{(Eqn.5a)}$$

$$17I_1 + 2I_5 = 75 \qquad \text{(Eqn.5b)}$$

Most of the remainder of the flow is in the right branch, which proceeds from the source "E" through R_{W2} to "A", then on through the right branch through R_H, R_{C2}, and R_{R2}, and on to ground. From Eqn.4 and Ohm's Law:

$$R_{W2}(I_2) + (R_H + R_{C2} + R_{R2})(I_2 - I_5) = E \qquad \text{(Eqn.6)}$$

$$15I_2 + 3(I_2 - I_5) = 75 \qquad \text{(Eqn.6a)}$$

$$18I_1 - 3I_5 = 75 \qquad \text{(Eqn.6b)}$$

The last branch is the shunting flow. Proceeding from the source "E" into the right branch, the shunting current flows through R_{W2} to "B", as a part of the current in the right branch. At "B", however, the shunting flow detours through R_S to "A", and on up the left branch through R_{C1} and R_{R1}. Ohm's Law and Eqns. 3 & 4 suggest:

$$R_{W2}(I_2) + R_S(I_2 - I_4) + (R_{C1} + R_{R1})(I_1 + I_2 - I_4) = E \qquad \text{(Eqn.7)}$$

$$15I_2 + 1(I_2 - I_4) + 2(I_1 + I_2 - I_4) = 75 \qquad \text{(Eqn.7a)}$$

$$2I_1 + 18I_2 - 3I_4 = 75 \qquad \text{(Eqn.7b)}$$

Equations 5b, 6b, & 7b can be solved by substitution. In this case, the results are:

I_3 = 5.0279-- flow from the wall surface (left branch), arbitrary units.
I_4 = 3.5847-- flow from the HFT surface (right branch), arbitrary units.
I_5 = 0.6983-- shunting (transverse) flow, arbitrary units.

Notice that I_4-- the flow through the HFT surface-- is much less than the value solved by means of Equation 1a. In fact, it is only

$$100(3.58/4.41) = 81.25\% \text{ of the original flow.} \qquad \text{(Eqn.8)}$$

Most of this error is due to shunting of the flow, as can be seen from the value of I_5. The rest is due to the actual insulating effect of the HFT, in that the TOTAL flow from the wall is actually reduced slightly. The insulating effect of the HFT is taken to be a part of the shunting error by some authors. The major part of this project will deal with "true" shunting, but we hope to learn a little more about quantifying the insulating effect, as a side benefit.

Before we leave the shunting example, note that from the (arbitrary) values assigned to the resistances of Figures 2a & 2b, it can easily be seen that the higher the (installed) resistance R_H of the HFT, the greater the reduction in flow through the HFT, and the more flow through shunting resistance R_S. Thus we would expect that (all other variables being equal) a thicker and/or less conductive HFT would produce more shunting error than a thinner and/or more conductive HFT.

Also, the higher the conductivity of the outer wall material (referred to later in this paper as the "substrate"), the greater the shunting error, since R_S is an inverse function of the conductivity of the outer wall material (from Fourier's Law of thermal conduction).

And for any given values of R_s, the shunting fraction is reduced for wider HFTs, since R_s is a function of the length of the conduction path. This is one of the driving principles to the modern tendency toward larger HFT "guard" (non-thermopile) areas, and larger overall HFT surface areas.

Finally, if the values of R_R and/or R_C are reduced, shunting is greater because R_H becomes a larger fraction of the overall surface resistance. The model thereby supports H. Trethowen's "surface regime" arguments in his paper in these Proceedings.

Project Objectives

Usually, it is desirable to know the heat flux without the extra resistive effect of the transducer. The purpose of this project is to identify a method of known accuracy and reliability for predicting magnitudes of shunting bias error for HFTs with known thermal quantities, mounted on surfaces of known thermal conductivity, in environments with quantifiable convective and radiative potentials. The method will then be used for selection of the best HFT for any given surface-mount measurement circumstance, by means of comparative modeling. That is, the method will make it possible to select the HFT which offers the least bias error. Alternatively, the method might be used as an aid in decisions on whether more accuracy should be expected by measuring heat flux with an HFT, or by calculating flux from convection and radiation equations and surface temperatures. Finally, if the method proves to be sufficiently reliable, all or part of the shunting bias error can be factored out of the HFT measured values, to improve overall surface-mount HFT measurement accuracy. The key Tasks of the project are seen to be:

1. From the HFT literary body of knowledge, to choose HFT shunting error mathematical algorithms, and to identify independent variables for study.
2. To provide a suitable model wall.
   a. To provide interchangeable outer surfaces of several representative materials, comprising the range of interest of substrate conductivity.
   b. To provide outer wall surface finishes representing the range of interest for surface emittance values.
   c. To provide a reliable, repeatable, constant heat flow source through the wall. The heat flux shall be adjustable, but without a cyclic controller (in order to avoid transient effects). Because of the use of our patented heat flux mapping method, it is not necessary to provide highly isothermal heat flow from the surface. However, it is desirable to avoid gross heat flow anomalies, so that shunting effects can be more obviously manifested in the "raw" thermal image temperature and heat flux maps.
3. To produce heat flux maps of the surface of the bare model walls (no HFT mounted) at several average surface temperature increments comprising the surface temperature range of interest.
4. To provide several types of HFTs with accurate calibrations and measured thermal resistances, representing the range of interest in HFT types and sizes.
5. To mount the HFTs one-by-one on the model wall surfaces, and to produce heat flux maps of the surfaces with HFTs attached, at each of the temperature increments of Task 3.

6. To derive a method by which the heat flux maps of Task 3 can be compared to the heat flux maps of Task 5, to determine the overall magnitude of heat flux difference between the thermopile portion of the HFT and that same portion of the wall surface, with no HFT mounted. The results will be taken to be the incremental empirical values of shunting error, for the various systems and conditions modeled.
7. To compare the shunting values derived from the test data to predictions using the various mathematical modeling algorithms of Task 1, and to choose one or more of those algorithms to adapt to our standard heat flux mapping job procedures.

Though there are several potential uses for the results of this work, the project was conceived specifically to support improved low-flow accuracy in Dow's method for heat flux mapping. This method is founded in infrared thermal imaging and HFT technology. It has proven to be quite effective in high-to-moderate temperature difference industrial heat flux mapping applications. With improvements in surface-mount HFT accuracy and development of techniques to analyze and address non-steady heat flow situations (see Flanders/Mack paper in these Proceedings), the method could be extended to buildings and other low delta-T applications. (Our heat flux mapping method will be discussed in more detail in the DEVELOPMENT section of this paper, and in the APPENDIX.)

DEVELOPMENT

Task 1: Selection of Algorithms & Identification of Study Variables

For this investigation, several candidate algorithms were directly selected from the writings of other researchers, and other techniques may eventually be derived. The present candidates are described individually in this section:

Algorithm I Development: Perhaps the simplest model is provided by Gudni Johannesson[1]. His Eqn. 2.4.6. can be written

$$\frac{q_{meas}}{q_{act}} = \frac{R_s}{R_H + R_s} \qquad \text{(Eqn.9)}$$

Where

q_{meas} = heat flux, as measured by the HFT under evaluation, W/m^2.
q_{act} = actual heat flux density (without the added resistance of the HFT, W/m^2.
R_S = surface heat flux resistance (a combination of convective, R_C, and radiative, R_R, resistances), $K*m2/W$.
R_H = conductive heat flux resistance of the HFT (transducer), $K*m^2/W$.

Johannesson himself pointed out that the weakness of this model is that it neglects the effect of conductivity of the heat transfer surface that the HFT is mounted on (the substrate). This can be especially important in the case where the HFT is mounted on a metal surface.

Additionally, since the HFT surface will be at a temperature slightly different from the surface temperature of the unmetered portion of the substrate, the surface heat transfer coefficient will also be slightly different over the transducer. This slight difference is expected to have negligible effect, considering the low temperature drop across most commercially-available HFTs. Therefore, in this algorithm, all surface resistance calculations will be based on the temperature of the unmetered substrate surface.

The surface heat source will be oriented to simulate a warm horizontal surface, with heat flow upward. An appropriate equation for modeling convective flux is the Rice-Heilman equation[13] (also supported by ASTM C680).

$$qc = 3.152591 \left[C \left(\frac{39.37}{d} \right)^{0.2} * \left(\frac{0.55}{Tf} \right)^{0.181} * 1.8 \Delta T \right]^{1.266} \qquad \text{(Eqn.10)}$$

or, in terms of thermal resistance:

$$qc = \frac{\Delta T}{Rc} \quad , \quad Rc = \frac{\Delta T}{qc} \qquad \text{(Eqn.10a)}$$

so,

$$Rc = \frac{\Delta T}{3.152591 \left[C \left(\frac{39.37}{d} \right)^{0.2} * \left(\frac{0.55}{Tf} \right)^{0.181} * 1.8 \; T \right]^{1.266}} \qquad \text{(Eqn.11)}$$

where

qc = heat flux from the surface due to convection, W/m^2.
C = Shape constant. For horizontal, warm facing up is 1.79, nondimensional.
d = length of plane, m.
Tf = air film temperature (ambient temp + surface temp)/2, K.
T = temperature difference between surface and ambient air, K.
Rc = convective thermal resistance (resistance of the air film), $K*m^2/W$.

Likewise, the familiar Stefan-Boltzmann equation will be used to model radiative heat fluxes:

$$qR = o\, E(Ts^4 - Ta^4) \qquad \text{(Eqn.12)}$$

which can be re-written in terms of radiative resistance,

$$qR = \frac{Ts - Ta}{RR} \quad , \quad RR = \frac{Ts - Ta}{qR} \quad , \quad \text{or} \qquad \text{(Eqn.2a \& 12b)}$$

$$R_R = \frac{T_s - T_a}{o\,E(T_s^4 - T_a^4)} \qquad \text{(Eqn.13)}$$

q_R = heat flux from the surface due to radiation, W/m^2.
o = Stefan-Boltzmann constant; for S.I., = $5.699*10^{-8}$, W/m^2*K^4. [14]
E = surface emittance, non-dimensional.
T_s = surface temp, K.
T_a = ambient air temp, K.
R_R = radiative thermal resistance, $K*m^2/W$.

Next, Equation 9 is re-arranged

$$q_{meas} = \frac{q_{act} * R_s}{R_H + R_s}, \quad q_{meas}(R_H + R_s) = q_{act} * R_s \qquad \text{(Eqn.9a)}$$

$$q_{act} = \frac{q_{meas}(R_H + R_s)}{R_s} \qquad \text{(Eqn.9b)}$$

and Equations 9b, 11, & 13 are therefore combined to provide the first algorithm:

$$q_{act} = \frac{q_{meas}(R_H + R_C + R_R)}{R_C + R_R} \qquad \text{(Algo.I)}$$

Note: Here, R_C and R_R are as defined in Equations 11 & 13, and R_H is as defined in Equation 9, and identified through ASTM F433.

Algorithm II Development: Johannesson suggested a method to account for the conductivity of the substrate[15]— his equation 2.4.2 can be written:

$$\triangle Q_s = T_s * (R_H/R_W) * k_{sub} * (y/x) * C_H \qquad \text{(Eqn.14)}$$

where
$\triangle Q_s$ = transverse (shunting error) heat flow, W.
R_W = overall conductive thermal resistance of the wall cross-section (without the added resistance of the HFT), $K*m^2/W$.
k_{sub} = thermal conductivity of the substrate (outer surface layer of the wall), $W/m*K$.
y = thickness of the substrate, m.
x = distance from the edge of the HFT thermopile outward; can be set to be equal to the width of the HFT "guard" area (for determining quard effectiveness), m.
C_H = circumference of the metered area— or sensing region— of the HFT (the thermopile), m.

To convert to a ratio of measured to actual surface heat flux, as in Algorithm I,

$$\frac{Q_{meas}}{Q_{act}} = \frac{Q_{meas}}{Q_{meas} + \Delta Q_S} \qquad \text{(Eqn.15)}$$

or,

$$\frac{Q_{meas}}{Q_{act}} = \frac{Q_{meas}}{Q_{meas} + (R_H/R_W) * K_{sub} * (y/x) * C_H} \qquad \text{(Eqn.15a)}$$

and

$$Q_{act} = Q_{meas} + (R_H/R_W) * K_{sub} * (y/x) * C_H \qquad \text{(Algo.II)}$$

Notice that this algorithm neglects the influence of variation in surface resistances due to differences in windspeed and ambient temperature (effect R_C), and due to differences in radiant background temperature (effects R_R). These variables influence the overall magnitude of shunting, as pointed out in the electrical analogy (see **INTRODUCTION: What is "Shunting"**).

Algorithm III Development: Johannesson implies that a more ideal model should consider the effects of both substrate conductivity and variations in convective and radiative resistances. Harry Trethowen has been empirically refining just such a model for the last several years in New Zealand[4]. A good explanation of this technique is presented in Mr. Trethowen's contribution to the proceedings of this workshop[16], so we will illustrate here only the adaptation of his work for the purposes of this experiment.

$$Q_{act} = Q_{meas} + (E_S/100) * Q_{act} \qquad \text{(Algo.III)}$$

where

E_S = Trethowen's Ep, %, or
= Trethowen's E_{max}, %, or
= Trethowen's E_{min}, %.
----- whichever is appropriate in each case.

NOTE: E_S could be negative in some special cases. One example might be low R_H, high transducer emittance, and low substrate emittance.

The intent is to try several other algorithms, as well—especially from those sources cited[1,2,3,4,5].

Study Variables: From these algorithms, it can be seen that the variables of interest are:

1. The HFT Calibration Factor.
2. The thermal resistance of the HFT, R_H.
3. The width of the HFT guard area.
4. The emittance of the HFT and the substrate (wall surface layer).
5. The thermal conductivity of the substrate (wall surface layer).
6. The thickness of the substrate.

7. The thermal resistance of the wall, w/o HFT, Rw.
8. The HFT heat flux indication.
9. The temperature under the center of the HFT.
10. The ambient (convective) temperature, T_a.
11. The convective flow rate (wind speed).
12. The average radiant (heat-sink) temperature of the environment.
13. The heater heat flow output.
14. The temperature profile of the exposed surface of the HFT and surrounding substrate, and the area average.
15. The heat flux profile of the exposed surface of the HFT and surrounding substrate, and the area average.

Task 2: **Model Wall Development**

Substrate (outer wall surface): There has been considerable recent discussion in the HFT community regarding the effect of substrate conductivity— therefore, first priority in the study of the effect of wall variables was given to the comparison of shunting in two substrates which differ widely in thermal conductivity. These values are listed in Table 1, along with the substrate thicknesses.

Another parameter which will be varied in the course of these experiments is substrate thickness. Currently, only one thickness of each substrate has been tested. These thicknesses are also reported in Table 1.

Table 1: Substrate Characteristics

Material	Thickness* mm (in)	Conductivity W/m-K (BTU-in/ft²-hr-°F)
Copper	15.25 (0.60)	32.4513 (225)
Phenolic/ Fiber	1.626 (0.064)	0.3606 (2.5)

*average

Surface Finish: The "total normal" emittance of each of the substrates was measured using a differential thermopile emissometer, and a procedure which is being written into an ASTM standard test method. So far, experiments have used only one surface coating. The emittance value was found to be 0.95, for all temperatures of the test series.

Heat Source: Initially, the intent was to employ for this project the same guarded thin heater device which was the subject of the study in the report by Bearden & Mack in these Proceedings[17]. Because of delays in obtaining desired heating homogeneity on that device (no pre-existing temperature patterns which would mimic shunting patterns), another heat source was required. A device was built in our laboratory using a 0.6096m X 0.6096m (2ft X 2ft) silicon rubber heating blanket glued to a 3.175mm (1/8in) thick copper plate, painted on the measurement surface with high emittance primer. Test data using this heater began to show evidence of hysteresis, and repeatability soon became unacceptable. At first, the source of this error was not evident. Since time was short, the hot-plate type heater shown in Figure 3 was adapted to continue the experiments.

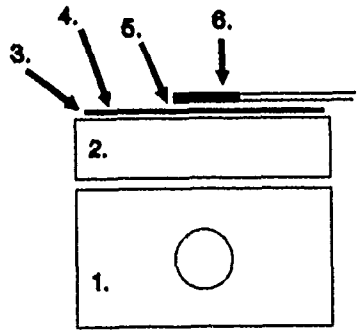

1. WAHL HS400 SURFACE TEMPERATURE STANDARD (HOT PLATE)
2. (STANDARD) WAHL HIGH CONDUCTIVITY TOP
3. HIGH TEMP CEMENT
4. 1/16 in. THICK CIRCUIT BOARD MATERIAL
5. DOW CORNING 340 HEAT SINK COMPOUND
6. HFT

Hot Plate-Type Heat Source W/Low-k Substrate Setup
Figure 3

Task 3: Heat Flux Maps of Bare Substrates

Equipment: The equipment utilized for the initial work on this project is described in Figures 4a & 4b. Figure 4a is a schematic representation, whereas 4b is a photograph of the actual laboratory setup.

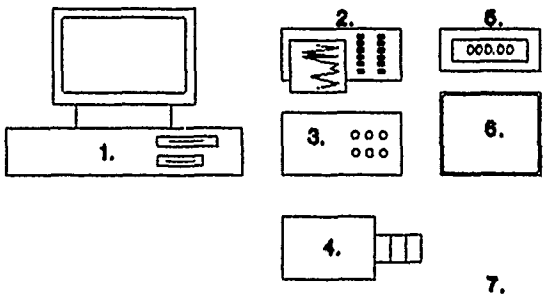

1. COMPAC 286e DESKPRO
2. A. E. TECHNOLOGY CO. MILLIVOLT STRIP CHART RECORDER
3. THERMOVISION 880 CONTROL UNIT
4. THERMOVISION 880 SCANNER
5. WAHL THERMOCOUPLE THERMOMETER
6. THERMOVISION 880 DISPLAY UNIT
7. WAHL HS400 SURFACE TEMP. STANDARD

Equipment Diagram
Figure 4a.

Equipment Photo
Figure 4b.

The experiments were originally begun with a long-wave (8-12 micron bandpass mercury-cadmium-telluride detector, LN_2-cooled) 25-frame/second infrared thermal imager loaned to us while our new short-wave imager (2-5.6 micron bandpass indium-antimony detector, LN_2-cooled) was being prepared. Unfortunately, all the experiments conducted during that period were flawed (mainly due to heater problems), so all the data used in this report relates to the short-wave unit. We used an off-the-shelf tempera-

ture mapping data processing system installed on a desktop computer. The imager manufacturer also provided a special software link to allow transfer of the thermogram data to files accessible to a market development version of our heat flux mapping programs (also installed on the desktop computer).

The ambient air temperature was measured using the same infrared pyrometer used for wall surface reference temperature readings. For ambient air, readings were taken from a low-mass target of known emittance. This data is included in Table 3.

The airspeed was measured using a hot-wire anemometer positioned slightly to the side of the hot plate, in order to measure the freestream velocity, rather than the natural convection currents induced by the hotplate itself. In all cases, the velocity was <0.015m/s (3ft/min).

Tests to date were conducted in a centrally-heated and cooled laboratory which has no significant hot or cold equipment (other than the test apparatus) and all "interior" walls (none exposed to the outside environment). The radiant environment temperature is therefore taken to be equal to the ambient air temperature.

The temperature map of the substrate was measured by means of the infrared thermal imager and computer/software (for converting the pixel voltage values into temperature values). Figure 5 is an example of a temperature map of a bare substrate (scale is in °F).

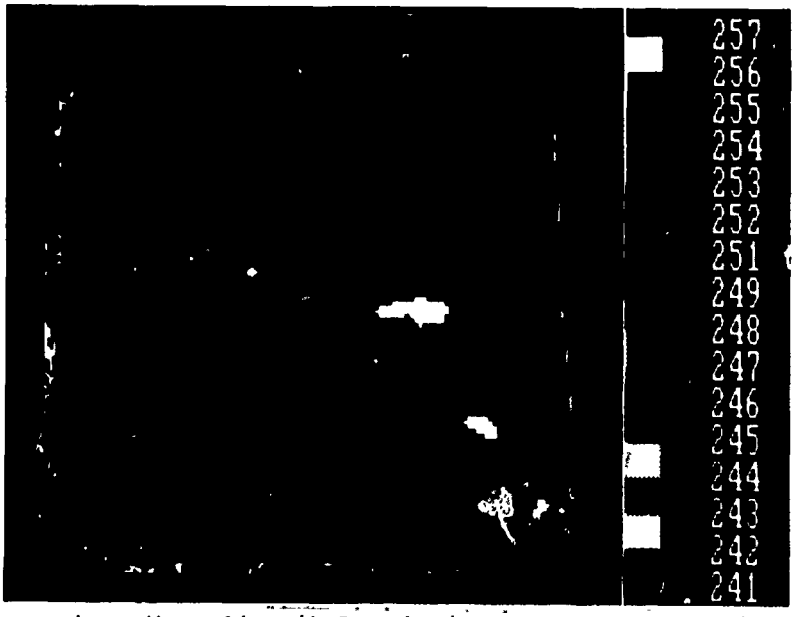

Temperature Map, Circuit Board W/O HFT, nom. 399.8K (260°F)
Figure 5

By means of a special routine for transferring temperature map pixel data, heat flux maps were produced, using computer programs for Dow's method for heat flux mapping. More details on the method itself can be found in the APPENDIX (Technology section). Special details that apply to specialized use of our method in this individual project are given under Task 6.

Figure 6 is a heat flux mapping table produced by means of Dow's method. This table is in essence a translation of most (Area 2) of the temperature map of Figure 5 into a heat flux map.

COLOR ZONE	ISO TEMPS, deg. C	ISO TEMPS, deg. F	COLOR AREA, sq-ft	LS RATE DENSITY Btu/h sq-ft	LOSS RATE Btu/h
	124.6	256.4			
WHITE			.00274	492.4	1.350
	124.5	256.0			
YELLOW			0.0319	489.7	15.63
	123.9	254.9			
ORANGE			0.0598	485.6	29.04
	123.3	253.8			
PINK			0.106	482.0	50.95
	122.6	252.8			
RED			0.0465	478.1	22.25
	122.1	251.7			
Dk.RED			0.0183	474.0	8.690
	121.5	250.6			
BROWN			0.0120	469.8	5.628
	120.9	249.5			
PURPLE			.00486	465.9	2.264
	120.3	248.4			
Lt.GRN			.00153	462.1	0.70498
	119.6	247.2			
GREEN			.00017	458.1	0.07766
	119.1	246.3			
Dk.GRN			.00031	454.1	0.14112
	118.4	245.0			
Lt.BLU			.00006	451.2	0.02550
	118.4	245.0			
AVRGS	122.9	253.3		481.6	
SUMS			0.284		136.7

Area 2 Heat Flux (Dow's Method), Bare Substrate, nom. 399.8K
Figure 6

Task 4: HFT Calibration, Resistance Measurements, & Emittance Matching

All the HFTs were calibrated by Holometrix, Inc. to ASTM F433 or ASTM C518 standards, and the transducer thermal resistances and conductivities were evaluated according to ASTM F433.

The width of the guard area is fixed for each type of HFT studied, as all are mass-produced units purchased "off the shelf". It is hoped that the data will reveal some evidence of the effectiveness of the guards on the various HFTs as work progresses, even though this variable is not controlled by the researchers. The width of the guards were measured by caliper or machinist rule, with the aid of x-ray, where necessary. These values are also to be found in Table 2.

Since emittance difference between the HFT and the substrate was not a high priority study variable, tests to date have all been with HFTs coated with the same paint as the substrate. Emittance was assumed to be identical.

Table 2: HFT Characteristics
*denotes averaged values.

Type	Material	Thick mm (in)	Gauge Size mm x mm (in x in)	Face Size mm x mm (in x in)	R-Value* m^2-K/watt (hr-ft^2-F/BTU)	Sensitivity* mv/(W/m^2) (mv/BTU/nft^2)
B (2 x 2)	Polyimide /Glass	2.87 (0.113)	36.83 x 41.66 (1.45 x 1.64)	5.08 x 50.8 (2.00 x 2.00)	0.00792 (0.045)	0.463 (0.147)
20457 -2	Polyester Film	0.13 (0.005)	12.7 x 16.26 (0.50 x 0.64)	19.05 x 25.4 (0.75 x 1.00)	0.00106 (0.006)	0.01161 (0.00368)

Task 5: Heat Flux Maps with HFTs Mounted on the Substrates

The temperature map of the HFTs and the surrounding substrate was measured by means of the infrared thermal imager and computer/software. Figure 7 is an example of a temperature map of a substrate with a rigid, 2X2 inch polyimide HFT installed, and the subsequent heat flux map of Area 1 (again, produced by our method for heat flux mapping). Other data was also collected as described for Task 3.

Note: The Example which begins with Figure 7 and continues throughout the DEVELOPMENT section is for the Rigid 2X2 HFT at nominal 399.8K (260 deg.F), using circuit board material as the substrate (between the HFT and the heater). The data of Task 3 and Figures 5 & 6 was used to adjust shunting calculations on both the Rigid 2X2 and the Film HFTs.

COLOR ZONE	ISO TEMPS, deg. C	ISO TEMPS, deg. F	COLOR AREA, sq-ft	LS RATE DENSITY Btu/h sq-ft	LOSS RATE Btu/h
	117.1	242.9			
RED			.00783	456.2	3.570
	116.4	241.4			
Dk.RED			0.0114	451.2	5.124
-- --	114.9	238.7			
BROWN			.00147	441.2	0.64815
	113.6	236.4			
PURPLE			.00093	431.4	0.40221
	112.1	233.7			
Lt.GRN			.00025	423.3	0.10764
	110.6	231.2			
GREEN			.00051	414.5	0.21076
	108.6	227.6			
Dk.GRN			.00014	402.9	0.05691
	107.9	226.1			
Lt.BLU			.00042	396.7	0.16813
	106.1	223.1			
Dk.BLU			.00048	385.6	0.18522
	105.0	220.9			
CYAN			.00025	378.8	0.09632
	103.9	218.9			
AVRGS	115.3	239.5		447.0	
SUMS			0.0236		10.57

Heat Flux Table, Circuit Board w/Rigid 2X2 HFT, nom. 399.8K (260°F)
Figure 7

Task 6: Method for Calculating Shunting Fractions from Empirical Data

Modeling Overall Shunting (uncorrected): Programs for our method for heat flux mapping were used in the alternate "theoretical" mode (Stefan-Boltzmann for radiant and Rice-Heilman for convective flux from the surface) to determine the heat flux profile of HFTs and the surrounding substrates. Specifically, the computer temperature maps were divided int areas of analysis which had been chosen to best resolve the shunting effect. The thermopile (metered) area of the transducer pixels was analyzed to represent the HFT-measured heat flux; Area 1 of Figure 7 is an example. The average overall heat flux was calculated (from an area large enough to circumscribe all shunting effects, or from the largest measur-

able area of the substrate or the heater face), and the percent difference between this average heat flux and the flux from the metered area was taken to be the "raw", or "uncorrected" shunting error for the particular operating condition (Figure 8).The flux table shown is for Area 2.

COLOR ZONE	ISO TEMPS, deg. C	ISO TEMPS, deg. F	COLOR AREA, sq-ft	LS RATE DENSITY Btu/h sq-ft	LOSS RATE Btu/h
	122.6	252.8			
WHITE			0.0388	493.6	19.13
	122.1	251.7			
YELLOW			0.140	487.4	68.12
	120.6	249.2			
ORANGE			0.0419	478.3	20.05
	119.1	246.5			
PINK			0.0161	468.8	7.550
	117.8	243.9			
RED			0.0127	457.0	5.810
	116.4	241.4			
Dk.RED			0.0203	450.2	9.145
	114.9	238.7			
BROWN			.00644	441.4	2.843
	113.6	236.4			
PURPLE			.00257	431.6	1.110
	112.1	233.7			
Lt.GRN			.00105	421.8	0.44089
	110.6	231.2			
GREEN			.00088	414.1	0.36270
	109.3	228.6			
Dk.GRN			.00048	403.2	0.19367
	107.9	226.1			
Lt.BLU			.00065	395.7	0.25711
	106.3	223.3			
Dk.BLU			.00073	386.0	0.28352
	105.0	220.9			
CYAN			.00057	378.2	0.21368
	103.3	217.8			
INDIGO			.00008	369.1	0.03129
	102.0	215.5			
BLACK			.00090	356.5	0.32227
	100.8	213.3			
AVRGS	120.0	248.1		478.5	
SUMS			0.284		135.9

Heat Flux Map, for HFT Overall Shunting Effect
1 = "metered area", 2 = total area evaluated for shunting
Figure 8

Note: although the "theoretical" mode is normally considered much less accurate than the primary (based on spot measurement of heat flux) Dow's method calculation, it is quite effective here, since the interest is in relative— rather than absolute— heat flux magnitudes. (Here, the theoretical mode is actually more appropriate to isolate the study variable, since the object of the study is an error variable associated with the HFT itself).

Modeling Shunting Details: Intermediate "windowframe" areas (hollow rectangles) were integrated for area-weighted average temperatures, between the metered area and the outer measurement perimeter. Heat fluxes were calculated from each windowframe increment, from both unmetered and metered images (Figure 9).

COLOR ZONE	ISO TEMPS, deg. C	ISO TEMPS, deg. F	COLOR AREA, sq-ft	LS RATE DENSITY Btu/h sq-ft	LOSS RATE Btu/h
	122.6	252.8			
WHITE			.00234	493.2	1.157
	122.1	251.7			
YELLOW			.00862	488.2	4.206
	120.6	249.2			
ORANGE			.00017	482.5	0.08178
	119.1	246.5			
PINK			.00000	0.00000	0.00000
	117.8	243.9			
RED			.00006	455.3	0.02572
	116.4	241.4			
Dk.RED			.00006	448.7	0.02535
	114.9	238.7			
AVRGS	121.3	250.4		487.2	
SUMS			0.0114		5.547

Heat Flux Map, for HFT Incremental Shunting Effect
Figure 9

Note: only 7 areas can be shown simultaneously, but the entire profile surface was analyzed, out to Area 2 in Figure 8. Area 7 is an example of small areas deleted from the analysis, due to shading effect of the HFT leads. The heat flux table included is for "Windowpane" Area 6.

For both metered and unmetered conditions, the calculated (incremental area, integral average) heat fluxes from each windowframe increment were plotted with respect to radial distance from the center of the transducer to the center of a side of the windowframe (Figure 10a & 10b— windowframe incremental heat fluxes are represented by the solid graph curve). To enhance visualization of the drop in heat flux beneath the HFT and the rise in flux just outside the HFT edges, the graph was plotted from the perspective of a cross-sectional view of the system— that is, looking at the HFT from the edge (side).

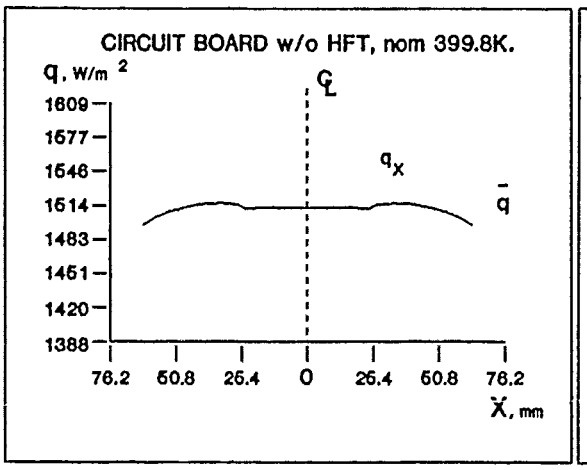

Figure 10a

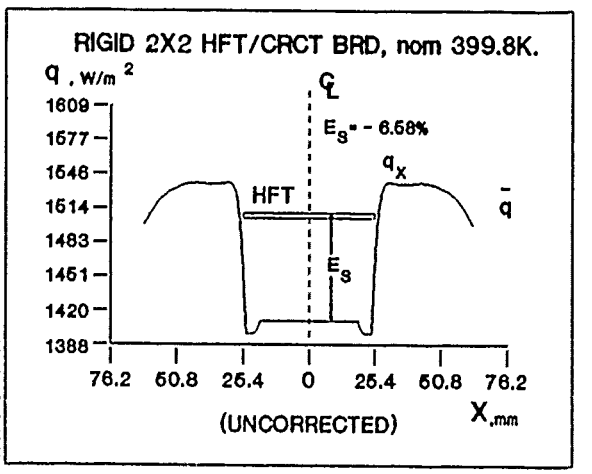

Figure 10b

Average Heat Flux Variation vs. Distance "X" from Center

With graphs 10a & 10b, we have the flux as a function of distance from the center of the thermopile, for the bare substrate (Figure 10a), and for the substrate with the rigid 2X2 HFT mounted (Figure 10b). From Figures 5 & 6 and Figures 7, 8, & 9, it can be seen that the heat flux actually varied somewhat from side to side— that is, heat flux on the right side of the HFT was not always exactly the same magnitude as flux on the left side. The technique of calculating area integral average flux for the windowframe increments did not differentiate between the sides, however— so the graphs were plotted as if the sides were in balance.

Notice that the heat flux in the unmetered condition has measurable variations across the width of the analysis area— that is, the substrate surface is not perfectly isothermal. Because the substrate is not perfectly isothermal, the flux plot of Figure 10b cannot be taken as a perfect representation of the effect of the HFT on the heat flux distribution at this condition. The effect of the initial maldistribution of flux should be factored out, in order to improve the representation.

Correcting the Flux Graphs: Average heat flux (dotted lines, Figures 10a & 10b) was drawn on each of the heat flux graphs, based on area integration of the largest rectangle analyzed (like Area 2 of Figure 8), with no areas subtracted except to account for shading by HFT leads. Then, for each windowframe increment, "delta values" were calculated relating the difference between heat flux from the windowframe increment and the average heat flux, as a function of the radial distance from the center of the transducer to the center of a side of the windowframe increment. For example, the average heat flux at (nominal) 126.7°C (260°F) with the rigid 2X2 HFT mounted is calculated based on pixel data from the overall area of analysis, and found to be 1509.5 W/m² (dotted line in Figure 10b). Next, the average heat flux from the area over the thermopile is calculated (from Area 1, Figure 7) to be 1410.1 W/m² (shown as the lowest part of the solid plot line in Figure 10b). For the metered condition, with the rigid 2X2 HFT, the percent difference (delta function) between the flux from the thermopile and the average flux from the overall area of analysis is

$$100 * (1410.1 - 1509.5)/1509.5 = -6.58 \qquad \text{(Eqn.16)}$$

— that is, 6.58% BELOW the overall average flux.

The same procedure was used to calculate delta functions for the unmetered condition. The dotted average flux line and the solid incremental flux line of Figure 10a indicate a slightly positive delta function in the area where the thermopile will be. Unmetered thermopile area delta function was calculated (as in Eqn.15) to be +0.43%— that is, 0.43% ABOVE the whole heater unmetered average (repeatability variation, approx. 0.23%).

Next, delta values from unmetered and metered conditions (of the same sample increments and radial locations) were combined by means of algebraic subtraction, and the remainders were used to correct the shunting graph for the effect of heater inhomogenicty. For the thermopile area at Nominal 126.7°C (260°F), the correction is

$$\Delta q_x = -6.58 - .43 = -7.01\% \qquad \text{(Eqn.17)}$$

— or in other words, heat flux through the thermopile is 7.01% less than it should be to provide an accurate local heat flux reading, given the existing state of the surface (with the HFT).

Besides the thermopile rectangle at the center, corrections are also calculated for all the windowframe increments. The resultant data points are used to draw corrected flux curves. An example of a corrected shunting graph is shown in Figure 11. Here, the upper dashed profile line represents the "raw" (uncorrected) heat flux, the dotted line represents the uncorrected average heat flux (both same as in Figure 10b.), and the lower dashed line is the heat flux variation at the same (nominal) temperature, but in the unmetered condition (same as in Figure 10a.). The solid line represents the heat flux variation, corrected for the original (unmetered) substrate heat flux inhomogeniety.

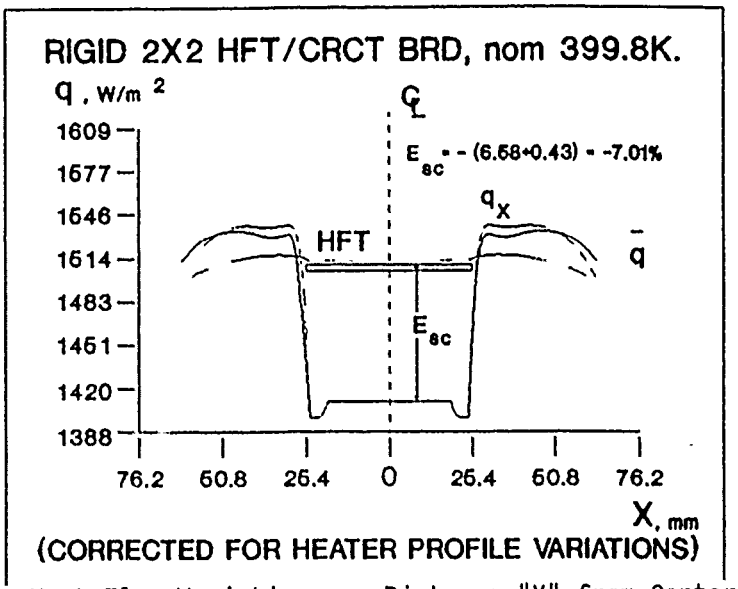

Average Heat Flux Variation vs. Distance "X" from Center
Figure 11

However, the existing state of the surface is not quite "natural", due to the slight insulating effect of the HFT. The small insulating contribution of the HFT is often considered separately from the thermopile shunting error, and we consider it outside the scope of the present project. However, since data was available, we decided to investigate the possibility of solving for this error component, as well.

The same delta value differences (as applied to Figure 11) were used to calculate the overall offset due to the insulating effect of adding the HFT over (a part of) the measurement surface. In this application, the individual delta differences were multiplied by the (windowframe or rectangle) areas for which they were calculated, and all these products were summed algebraically. This sum was divided by the total analyzed area, and then multiplied by the average heat loss for the metered condition to obtain the (projected) change from unmetered heat flux at the thermopile site, at these sample conditions. In the case of the example,

$$\frac{\sum\left(\Delta q_x * A_x\right)}{A} * \bar{q} = q_i = 0.04 \text{ W/m}^2 \qquad \text{(Eqn.18)}$$

where

Δq_x = algebraic difference between divergence of unmetered q_x from the unmetered condition average heat flux, and metered q_x from the average metered condition heat flux, W/m^2.

$\bar{q}$ = 1509.5 W/m^2.
= the average heat flux from the whole analyzed area, in the metered condition, W/m^2.

q_i = apparent magnitude of the effect on heat flow due to insulating effect of HFT (average), W/m^2.

A = overall area of analysis, m^2.

Ax = Area of increment X, m^2.

The result implies that installing the HFT caused an INCREASE in the average heat flux from the substrate, of 0.04 W/m^2. The validity of this result seems highly unlikely.

The example seems to illustrate that in the present practice, quantification of the pure insulating effect of the HFT (taken separately from shunting effect) is probably limited by the imprecision of the experiment. Accordingly, that error component will not be dealt with further in this report.

Results: All significant results are summarized in Table 3 and Figures 12a & 12b.

Test Results: HFT Shunting Error Trend Data for 2 HFTs

Table 3

HFT	Substrate	Ta, K	Tave, K	q, W/m	q meas, W/m	Δq, %
2x2 Rigid	Phenolic /Fiber	296.7	312.4	156.6	150.9	-3.88
		296.6	332.1	419.2	398.1	-5.12
		297.3	352.3	724.9	682.0	-6.07
		295.8	375.8	1147	1080	-5.83
		295.8	393.2	1509	1410	-7.01
Film	Phenolic /Fiber	296.5	309.7	141.8	135.7	-4.73
		296.6	331.4	473.2	451.4	-4.60
		296.8	357.5	746.1	712.0	-4.84
		297.0	375.5	1140	1096	-3.46
		297.6	396.1	1585	1533	-3.84

where,

T_a = ambient air temperature (also used as radiant background temperature), K.

T_{ave} = true average surface temperature of the whole area of analysis, K.

q = average (theoretical) surface heat flux from the whole area of analysis, W/m^2.

q_{meas} = average (theoretical) heat flux from the area over the thermopile, W/m^2.

Δq = shunting error, % (see Eqn.16)

Figures 12a and 12b present this data in graphical form.

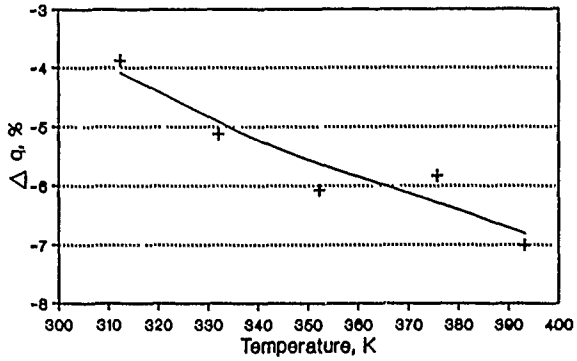

Figure 12a
Rigid 2X2 HFT Flux Error Trend
(versus Surface Temperature)

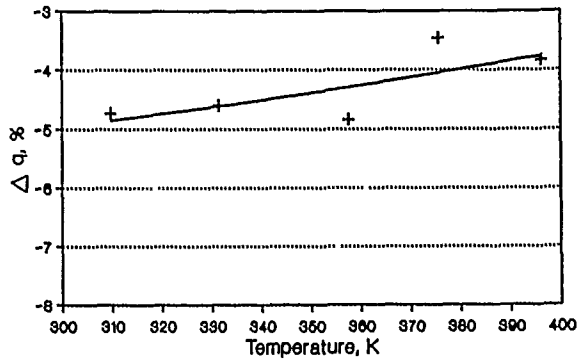

Figure 12b
Film HFT Flux Error Trend
(versus Surface Temperature)

The curve for the rigid 2X2 HFT was solved by means of a power curve fit; coefficient of determination was 0.88. The film HFT curve was solved by means of an eponential curve fit; coefficient of determination was 0.54. In both cases, linear equations fit almost as well.

Task 7: Testing & Selection of Mathematical Shunting Algorithms

Because the data is sparse and contains some questionable values, so far no attempt has been made to fit the data to any of the shunting algorithms.

SUMMARY

By way of a progress report summary, this section presents a review of the present status and future plans for each of the Tasks outlined in the DEVELOPMENT section:

Task 1 Update

HFT literature has been reviewed, and a set of candidate algorithms has been identified. There is as yet no reason to suspect that the set of candidate algorithms identified will not produce an adequate model.

Task 2 Update

It has become obvious that most of the problems and delays with the project are due to inadequate treatment of Task 2, the provision of a suitable model wall.

Several modifications are already underway. First, a new hot plate has been designed. The plate will be large enough to accommodate the new generation of large format HFTs; the plate will be 0.9144m square (3ft X 3ft). The plate will be heated from below by a flowing heat-transfer fluid which is heated by means of a constant-source, manually adjustable immersion heater isolated from all significant cyclic effects. Except for the test surface, the entire heat flow envelope will be well insulated. Fluid flows will be "tuned" to minimize temperature variations at the test surface.

Separate experiments will be conducted in order to identify a good range of thermally-stable surface coatings for adjusting the emittances of HFT and substrate. During the course of previous test work, considerable data had to be discarded due to the late discovery of a major difference in the surface emittance of the HFT and the substrate, after the substrate was re-coated. This was a non-graybody effect, due probably to a higher concentration of metallic pigment in the later coating (same can as originally used to coat both substrate and HFT).

Also, a set of good substrates (individually, thermally homogeneous— and collectively, providing a good range of thermal conductivity) is being assembled.

The thermal resistance of the bare wall (without HFT) will be varied in the course of the work by varying wall material and thickness. In experiments to date, no layers have been added beneath the substrates to simulate a real wall— so there is considerable room for more research here. When used, this wall material will be sandwiched between the heater and the substrate.

As the project progresses, the effect of air speed on shunting will be studied through the use of a variable speed fan, a plenum, and a diffuser duct.

Finally, it is hoped that a controllable environmental chamber can be located in order to conduct experiments with the heat sink colder or warmer than normal room temperature.

Task 3 Update

Based on the trial-and-error of this initial phase of the project, a new and more rigorous test discipline is being formulated, as well. Elements of the procedure will be modified based on the results of the mathematical error analysis planned for Task 6.

Task 4 Update

Originally, the plan was to run the test series for the four types of HFTs most often used by our group. In the course of calibrations at Holometrix, two of these HFT types were found to be basically flawed, and not suitable for our applications. This development has left us in need of replacements, and we have begun research in order to fill this deficiency. Several more types of HFTs have been acquired, and a few more will be obtained before they are all sent to Holometrix for calibration and thermal resistance measurements.

Task 5 Update

Whereas some of the Tasks have not yet produced the desired results, heat flux mapping of the HFTs has produced a welcome surprise: the high thermal and spacial resolution of the imaging equipment revealed thermal details relevant to the heat flux through the individual thermocouple elements of the HFT thermopiles. Figure 13a is an x-ray of an rigid 2X2 HFT—the light indications are details of the thermopile. Figure 13b is an infrared thermograph of the same HFT, at nominal 399.8K (260°F). Notice that the thermopile is quite recognizable, even though it is imbedded within a wafer of opaque polyimide.

Figure 13a
X-Ray of Rigid 2X2 HFT

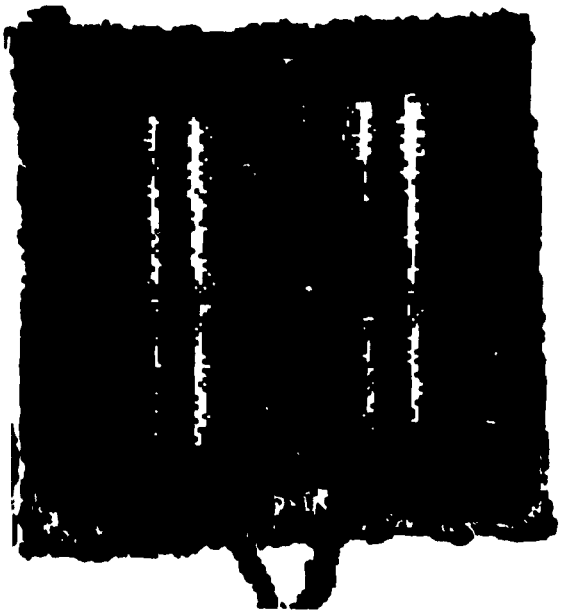

Figure 13b
Thermograph of Rigid 2X2 HFT

This capability will allow a slight modification to the data collection procedure, which should result in greatly improved accuracy in modeling the shunting flows. Before this part of the procedure is changed, the imaging equipment will be tested for accuracy of combined thermal and spatial resolution, according to a procedure known as Slit Response Function (SRF)[18]. If the SRF is insufficient using the standard calibration, a special calibration may be produced for use of the imager for quantifying the small thermal anomalies over the thermocouple junctions.

Task 6 Update

The procedure derived for extracting values of experimental shunting flux from the data of Tasks 3 & 5 appears to work reasonably well, in principle. However, there seem to be some opportunities for improvement:

First of all, note that the "corrected" curve in Figure 11 does not perfectly fit heat transfer logic; one would expect a rapid rise in heat flux just outside the guard, with a gradual and smooth decline toward the average unmetered heat flux line. The "dip" in the q_x line, and the decline below the average heat flux line may well be due to experimental error. Therefore, before proceeding with experiments, the error will be modeled using Taylor's Theorem (maximum error) and Pythagorian summation (probable error). If unacceptably large error sources are identified, equipment and/or procedures will be modified. In particular, we hope to improve the experiment to the point where HFT overall insulating effect can be quantified, as well as pure shunting error.

Table 3 and Figures 12a & 12b reveal two or three other areas of concern which should be addressed before experiments continue: First of all, the progression of shunting error with surface temperature increase (as indicated in the Δq column and Figure 12 graph points) is not smooth, and the immediate implication is that the shape of this function is being obscured within the experimental error band. Furthermore, the trends seem to indicate an increase in shunting effect with increasing temperature

for the rigid 2X2 HFT, while the opposite appears to be true for the Film HFT. We have no explanation for this at this time.

Since Task 7 has really not been attempted yet, there seems no need for a progress report. No changes are anticipated from the original plan.

A student engineer has been assigned to these Tasks virtually full time, and one or both of the authors will continue to participate on at least a part-time basis. Depending on other job priorities, it is anticipated that this project will identify a reliable HFT shunting bias correction by late 1990 or early 1991.

ACKNOWLEDGMENTS

The authors would like to thank Jenice Woodall for most of the data reduction of this project. Though she was working long hours and learning a completely new data processing technique— and though she was preparing for her marriage at the same time— Jenice did top quality work, and finished her part well ahead of deadlines.

We would like also to recognize the assistance of Phil Smith, Vicente Ribeiro, Chuck Mitchell, and their fellows at AGEMA Infrared. Without their kind favors this work would have been much more difficult.

Finally, our compliments to Norman Greene of International Thermal Instruments (ISI). His goods were under critical examination, but he never responded defensively to our requests. Instead, he was forthcoming and helpful in every way, as a fellow scientist with an interest in our research.

APPENDIX: Dow's Method for Heat Flux Mapping

Evolution:

Since our method for heat flux mapping is employed extensively as a tool in these experiments, and since this Method may be unfamiliar to many readers, a small section follows to describe the technology and its evolution.

Almost as soon is infrared temperature measurement devices began to become available, researchers began to anticipate infrared measurements in terms of heat flow, rather than temperature.[19] This was not hard to achieve, since radiometers must derive temperatures from radiant heat flux measurements. By 1981, spot pyrometers were offered with readouts in BTU/hr. (M.C. Products, Scottsdale, AZ). By about the same time, Viewscan Ltd. (Ottawa, Ontario, Canada) was marketing software which would produce two-dimensional temperature maps from infrared thermal images[20] (an improved version is now offered by AGEMA Infrared, Secaucus, NJ—under the name CM-Soft).

These early techniques sometimes worked well enough when the quantity desired was the radiant component of heat flux from a surface, because the instruments are true radiometers. Often, however, the total heat flux (radiative + convective) was of interest. Convective fluxes were solved from surface temperatures by means of equations based on Newton's Law of Cooling, and derived empirically in the laboratory (the Rice-Heilman equation previously mentioned is one example). When applied to real systems, these empirical equations either neglect important variables, or

employ them inaccurately. Large errors often result.

The need for a means of correcting these inaccuracies was well known to those using the methods.[21] HFTs had been (and are yet) often used in conjunction with thermal imagers, though mainly in that the imager is used only to locate the most appropriate site for the HFT installation[22,23]. Burch & Kusuda (NBS) even derived a method in which an HFT was used to measure heat input into a substitute target (a calibration device, used to quantify different parts of a thermal image by matching), and an infrared image was used as the format for reporting heat fluxes.[24]

Of all the preceding technology, however, a technique by Flanders and Marshall[25] for mapping building wall R-values probably represented the extent of the evolution. They calculated wall R-values at two (hottest & coldest) sites within a thermal image, based on inside and outside surface temperature difference and the heat flux measurements (by HFT) at the two sites. Then they solved R-value maps by linear interpolation between the two measured sites.

Technology

Our method was also derived in order to eliminate or compensate for the theoretical error.[26] In basic form, the method consists of a 2-dimensional heat flux map derived from a temperature map (typically, produced by an infrared thermal imager). In this way, our method is similar to McIntosh's, but different from Flanders & Marshall's. However, our method differs from McIntosh's in that with the Dow method, the map is corrected to heat flux values measured by means of a true, total heat flux measurement device (typically, a HFT). Heat fluxes at sites remote from the HFT— but within the defined area of the thermal image—are "scaled" from the HFT reference values by means of an equation derived from radiation and convection theory[27] (this is another way that Dow's method differs from the Flanders-Marshall method— theirs is a linear interpolation). An alternate route is provided in the software to allow uncorrected reports (based only on convection and radiation theory), when required. This project is an example of computations based on the alternate route.

For economic analysis, enhancements of Dow's heat flux mapping method map R-values and dollar-loss values. In cases where repairs or additional insulation are considered, the proposed system can be compared to the present system, and savings and Return-on-Investment (ROI) are mapped, as well.

Precision is very high, with over 40,000 elements of spatial resolution available (the pixels in the thermal image). Accuracy improvements are great, as well: the method is considered accurate and reliable in steady-state measurement when surface-to-air temperature difference is 15 deg. C (27 deg. F) or greater. Much smaller temperature differences have been handled successfully in the lab, and efforts are underway to extend the method to non-steady state measurements.

An interesting example of the improvement in accuracy which our method provides over pure convective and radiative temperature-based equations was illustrated during the shunting error experiments. Early in the work, we were basing the shunting analysis on the HFT output. We were working with a developmental heat flux mapping program, and it was discovered that this version contained erroneous constants in the Rice-Heilman equation. After de-bugging, we re-ran the data based on surface temperatures and radiation and convection equations (rather than HFT output), using both the original constants and the corrected constants: a typical data

point example indicated 47.8% difference for area-weighted average heat loss. (Differences of this magnitude can be found simply by selecting from among the many published convection equations.) When we ran the same data based on the HFT, however (the usual procedure with Dow's method), the difference in the result using the new constants was only 0.14% for area-weighted average heat loss! This illustrates that (because of the nature of the heat flux scaling equations), the accuracy of the radiation & convection equations has little bearing on the accuracy of the derived heat flux map. Accuracy of the heat flux map is almost completely defined by the accuracy of the imager temperature profile and by the accuracy of the HFT heat flux reference.

Currently, our method for heat flux mapping is being used for industrial heat flux surveys in these categories:

a. Acceptance Testing of new equipment and systems, to assure that new purchases meet requirements with respect to heat transfer.

b. Energy conservation studies for management decisions on repair or retrofit of insulation and/or heat recovery systems on existing equipment.

c. Support of Predictive/Preventive Maintenance (P/PM) programs.

d. Process Energy Balance Analysis, for system optimizing, and for process R&D.

REFERENCES

1. Johannesson, G.; Heat Flow Measurements, Thermoelectric Meters, Function Principles, and Sources of Error, Lund Institute of Technology, Lund, Sweden, 1982.

2. Wright, R.E.,Jr., Kantsios, A.G., & Henley, W. C., "Effect of Mounting on the Performance of Surface Heat Flow Meters Used to Evaluate Building Heat Losses", Thermal Insulation, Materials, and Systems for Energy Conservation in the '80s, ASTM STP 789, F.A. Govan, D.M. Greason, and J.D. McAllister, Eds.; ASTM, Philadelphia, 1983, pp.293-317.

3. Standaert, P.; Error Analysis of Heat Flow Meters, Katholieke Universteit Leuven, Belgium, 1984.

4. Trethowen, H.A.; "Engineering Application of Heat Flux Sensors in Buildings— the Sensor and its Behavior", Building Applications of Heat Flux Transducers, ASTM STP 885, E. Bales, M. Bomberg, & G. Courville, Eds.; ASTM, Philadelphia, 1985, pp.9-24.

5. Apthorp, D.M. & Bligh, T.P.; "Modeling of Heat Flux Distortion Around Heat Flux Sensors", STP 885, pp.45-64.

6. Holman, J.P.; Heat Transfer, McGraw-Hill, New York, NY, 1976, pp.24-31, p.86.

7. Kayan, C.F.; "An Electrical Geometrical Analogue for Complex Heat Flow", Transactions of the ASME, 1945, vol. 67, p. 713.

8. Wolfe, H.; Heat Transfer, Harper & Row, Cambridge, Mass., 1983, p. 7.

9. Halliday, D. & Resnick, R.; Fundamentals of Physics, John Wiley & Sons, New York, NY, 1974, pp.510-511.

10. Wolfe, p.7.

11. Halliday, p.529.

12. ibid., PP.523-524.

13. Turner, W.C. & Malloy, M.E.; Thermal Insulation Handbook, McGraw-Hill, New York, NY, 1981, p.50.

14. Holman, p.275.

15. Johanneson, pp.26 & 27.

16. Trethowen, H.A.; "Systematic Errors With Surface-Mounted Heat Flux Transducers— and how to live with them", Proceedings of the NIBS/BTECC/CRREL Symposium on In-Situ Heat Flux Measurements in Buildings, S.N. Flanders Ed., BTECC, 1991.

17. Bearden. T. & Mack, R.T.; "Verification of a Thin Heater Device as a Secondary HFT Calibration Source", Proceedings of the NIBS/BTECC/CRREL Symposium on In-Situ Heat Flux Measurements in Buildings , S.N. Flanders Ed., BTECC, 1991, pp. .

18. Ohman, Claes; "Measurement Versus Imaging in Thermography, What is Resolution", Proceedings of the Fifth Infrared Information Exchange—Book II, AGEMA Infrared, Secaucus, NJ, 1985, pp. 65-70.

19. Anderson, L.J.; "Energy Conservation With Thermography", Proceedings of the Infrared Information Exchange, AGA Corporation, Pine Brook, NJ, 1977, pp. 61-62.

20. McIntosh, G.B.; "Recent Advances in the Quantification of Heat Loss Using Thermography", Proceedings of Thermosense IV, SPIE— The International Society for Optical Engineering, Bellingham, Washington,1981, pp. 213-218.

21. ibid, p. 214.

22. Treado, S.J.; Thermal Resistance Measurements of a Built-Up Roof System, U.S. Department of Commerce/NBS/DOE//NTIS, Springfield, VA, 1980, p.5.

23. Flanders, S.N., & Marshall, S.J.; "In Situ Measurement of Masonry Wall Thermal Resistance", ASHRAE Transactions, Volume 88, Part 1, ASHRAE, New York, NY, 1982, pp. 677-688.

24. Burch, D.M., Kusuda, T. & Blum, D.G.; An Infrared Technique for Heat Loss Measurement— NBS Technical Note 933, U.S. Government Printing Office, Washington, D.C., 1977.

25. Flanders, S.N., & Marshall, S.J., "Interpolating R-Values from Thermograms", Proceedings of Thermosense IV, SPIE— The International Society for Optical Engineering, Bellingham, Washington, 1981, pp. 157-164.

26. Mack, R.T.; "Energy Loss Profiles: Foundation for Future Profit in Thermal Imager Sales and Service", Proceedings of the Fifth Infrared Information Exchange— Book I, AGEMA Infrared, Secaucus, NJ, 1985, pp. 15-24.

27. Mack, R.T.; Method for Heat Loss Survey— USP 4,896,281, US Patent Office, Washington, D.C., 1990.

VERIFICATION OF A THIN-HEATER DEVICE AS A SECONDARY HFT CALIBRATION SOURCE

T. W. Beardon
R. T. Mack

Dow Chemical
Freeport, Texas USA

ABSTRACT

This paper reports the "blind" output response check of two types of heat flux transducers (HFTs) by means of an open-sided Thin Heater Device. The device is designed to generate a one-dimensional heat flux that can be accurately monitored using a precision wattmeter. This known heat flux is then used to determine the calibration factor for each HFT placed on the device. The calibration results are compared to ASTM standard calibrations (ASTM F433-77, ASTM C518-85) performed on the same HFTs by Holometrix, Inc.

The calibration tests showed the HFTs to have much higher calibration factors than the values obtained by ASTM methods. The higher factors were due mostly to edge losses caused by a low face area/edge area aspect ratio. Modifications to provide even heat distribution across the device also increased the edge losses, contributing to the higher calibration factors.

INTRODUCTION

The increasing demand to measure heat flow through various bodies using nondestructive methods has created a greater need for the use of surface-mounted heat flux transducers (HFTs). However, in the past, HFTs have sometimes earned a bad reputation due to calibration inaccuracy [1]. Calibration techniques known to be accurate are described in ASTM C-1130-89. Unfortunately, these methods may be too expensive for some HFT users. Also, labs which offer these HFT calibration techniques are few, and the service is often expensive and time-consuming. A fast, low-cost secondary calibration technique is needed to support periodic verification of HFTs by end users, to assure continued accuracy.

This paper reports the "blind" output response check of two types of HFTs by means of an open-sided Thin Heater Device. The results are compared to ASTM calibrations performed on the same HFTs by Holometrix, Inc. Our calibrations were performed with and without edge guard masks surrounding the HFTs. The purpose of the masks was to study the shunting effects created when an HFT is added to a surface.

TECHNICAL APPROACH

A 10.16-cm x 10.16-cm Series 1000-S Primary Heat Flux Standard, manufactured by International Thermal Instrument Co., was used for this experiment. An open-sided Thin Heater Device is an assembly that can generate one-dimensional heat flow that can be accurately monitored. One-dimensional heat flow is achieved by using two heaters sandwiching an internal HFT as described in Figure 1.

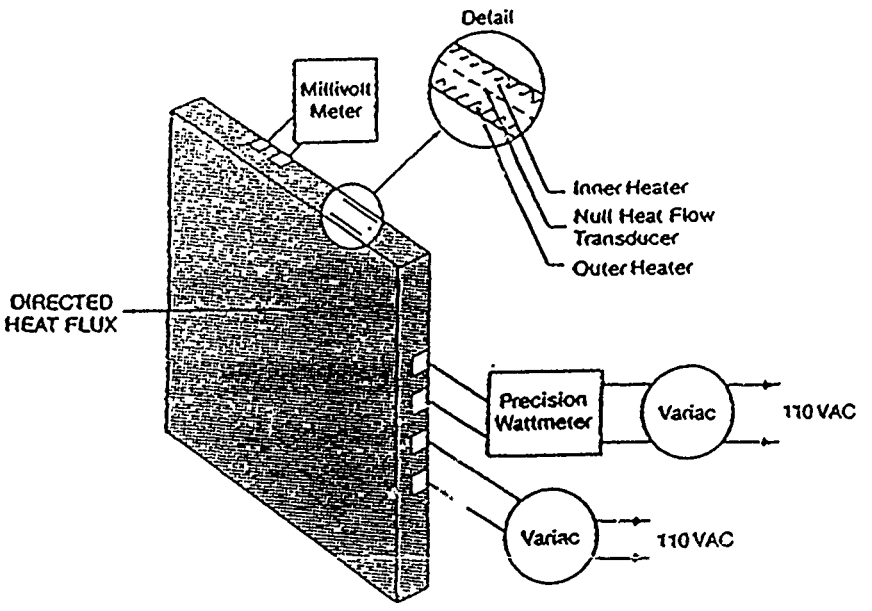

Figure 1. Series 1000-S Heat Flux Standard Assembly (Courtesy of ITI).

By connecting the internal HFT to a null voltage detector, the direction of the heat flow through the device can be determined by the polarity of the emf generated by the HFT. When no temperature differential exists across the internal HFT (there is no heat flow through the HFT), the null detector will indicate a zero millivolt output. After a test HFT has been placed on the metered side of the device and a "null" balance state has been achieved, the metered heater's outward heat flux can be used to calibrate the test HFT. To determine the calibration factor for a test HFT at a given temperature, the following equation is applied:

$$CF = q / A * V \qquad (1)$$

where

CF = calibration factor in $(W/m^2)/mV$,
q = the metered heater's heat transfer rate in watts,
A = the area of the Thin Heater Device in m^2,
V = the test transducer output voltage in mV.

Before running the calibration tests, thermal images of the Thin Heater were taken at the test temperature points to ensure that even heat distribution existed across the device. Even heat distribution is necessary since it is assumed that the heat flux across a test HFT is equal to the heat flux across the entire device. A fine chalk coating was first applied to the device to give it a uniform emittance. The emmitance of the chalk was measured to be 0.88 using a Devices and Services, model AE, emissometer.

Figure 2 shows the Thin Heater Device null balanced at 82°C. The thermal image of the device at this temperature revealed a temperature differential of approximately 40°C. The temperature differential across the heater varied from 10°C at 38°C to over 45°C at 104°C.

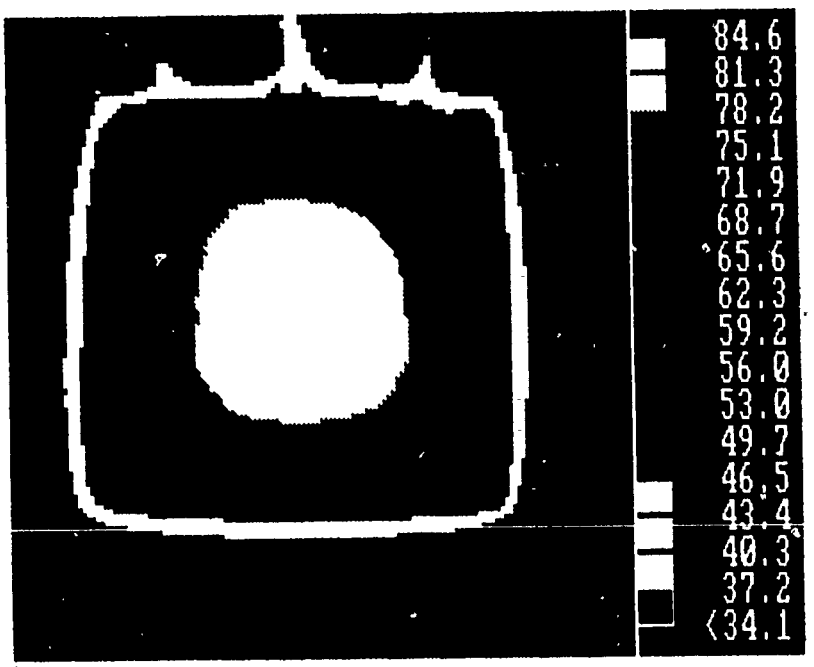

Figure 2. Thin Heater Device w/chalk at 82°C.

With the thermal anomalies present, an HFT of any size other than that of the Thin Heater Device itself could not be calibrated accurately. To better distribute the heat flow, various arrangements of high conductivity plates were coupled to the device using an assortment of semi-permanent bonding agents. The most successful arrangement was obtained using a copper plate/circuit board combination. A copper plate was coupled to the metered side of the device using a shellac gasket compound manufactured by Permatex. Then a thin circuit board plate was attached to the copper plate using the same shellac gasket compound. The addition of the two plates lowered the temperature differential from 40°C to less than 10°C at 82°C (see Figure 3). With a better bonding technique, an even lower temperature differential should have been reached. However, a limited time schedule necessitated the continuation of the calibration tests with the device in this state.

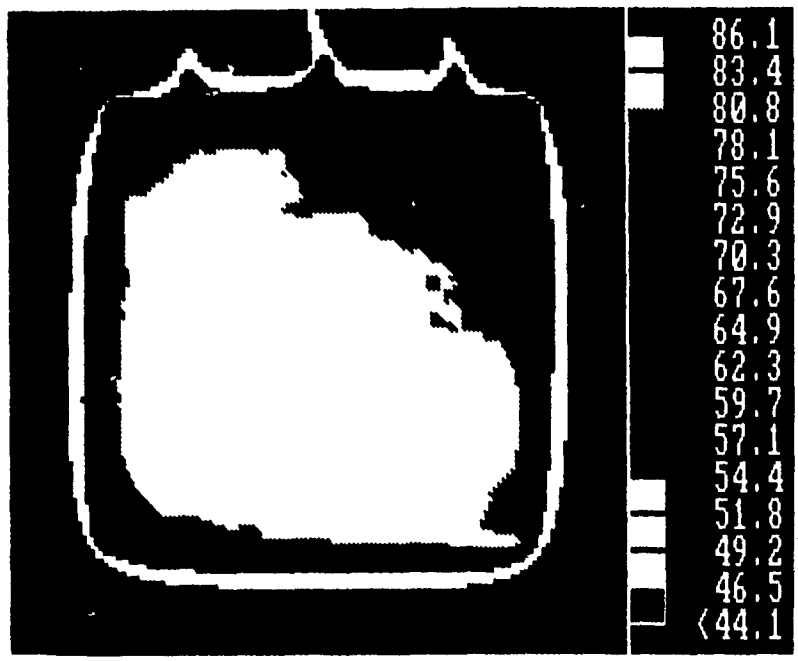

Figure 3. Thin Heater Device w/copper & circuit board at 82°C.

TEST SETUP

The two types of HFTs tested can be seen in Figure 4. Calibration tests were performed on two of each of these types of transducers. The first type of transducer tested was the International Thermal Instrument Co., Type B Thermal Flux Meter. The meter measures 5.08 x 5.08 x 0.159 cm. This type of transducer is a flat plate unit made of a polyimide-glass material. The second type of transducer tested was the RdF, Inc., Micro-Foil heat flow sensor. The Micro-Foil sensor has a very low thermal capacity and provides virtually an instantaneous measurement of heat flow rate. The Micro-Foil measures approximately 1.905 cm x 2.54 cm x 0.127 mm. An amplifier was used to boost the microvolt output of the RdFs to millivolts for the recording device being used.

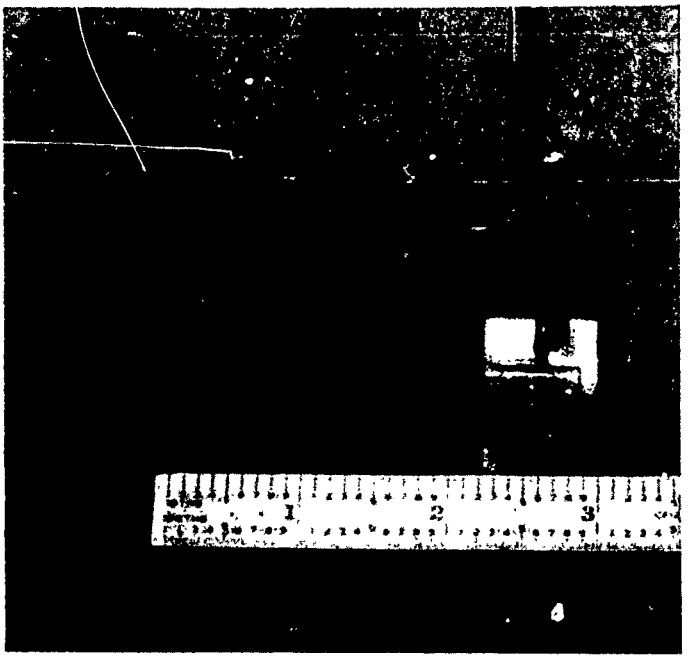

Figure 4. Two types of HFTs tested.

Figure 5 is a schematic of the Thin Heater Device as it appeared during the calibrations. The two plates are attached to the metered side

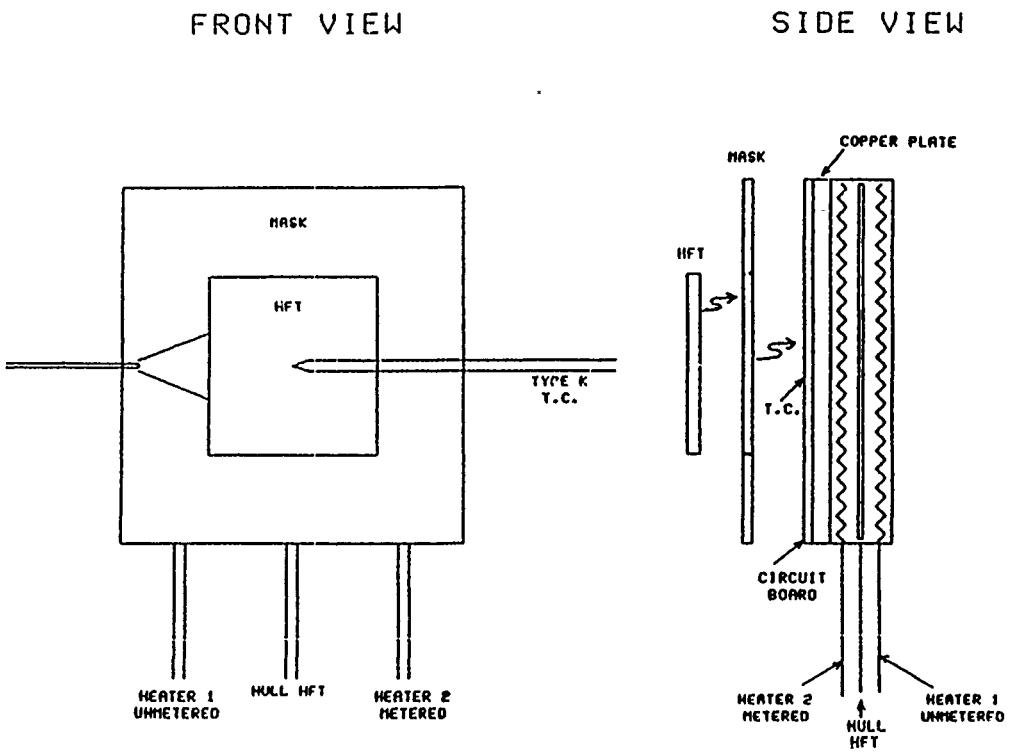

Figure 5. Thin Heating Device w/mask and HFT.

of the device as noted earlier. A type K thermocouple is bonded to the outer circuit board surface to provide an inner temperature reading for a test HFT.

A schematic of the overall test setup is illustrated in Figure 6a with the equipment names listed below it. Figure 6b is a photograph of the actual test setup used for the RdF calibrations.

The metered heater is connected to the watts transducer and digital meter to monitor the power supplied to it by the two variable transformers. Two transformers are connected in series for each heater to achieve finer adjustments when "null balancing" the device. The internal HFT is connected to a null microvolt detector. The type K

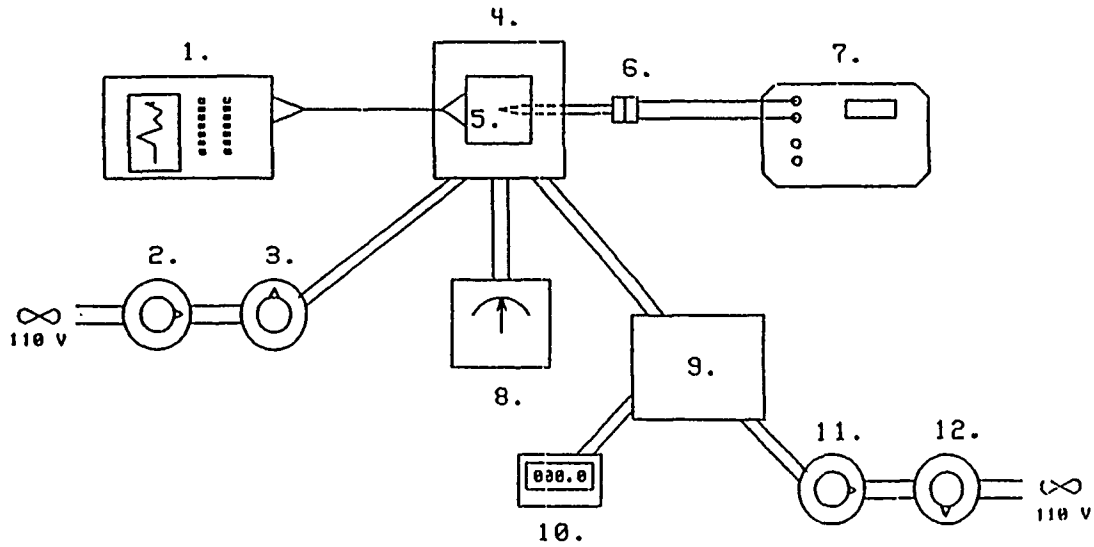

1. Acoustic Emission Technology Co., millivolt strip recorder
2.,3. Staco Inc., type 3PN1010, variable autotransformers for unmetered heater
4. ITI Series 1000-S w/mask
5. Test heat flux transducer
6. Type K "cement-on" thermocouple
7. Omega Omni-Cal thermocouple readout
8. Kiethly 155 null detector/microvoltmeter
9. OSI PC5-10DX5 watt transducer
10. NES Slimline Panel Meter, model 1DW-8220
11.,12. Staco Inc., type 3PN1010, variable autotransformers for metered heater

a. Schematic.

Figure 6. Test setup.

b. Photograph of instrumentation.

thermocouple is connected to a digital thermocouple display. The thermocouple, combined with a pyrometer, for outer surface temperature measurements, provide an average reference temperature for the calibrations. The output of the test HFT is measured using a millivolt strip chart recorder.

PROCEDURE

Masks and HFTs were attached to the device using Dow Corning 340 Silicone Heat Sink Compound. Data points were taken at nominal temperatures of 37.8, 60.0, 82.2, 104.4, and 126.7°C. To reach a data point, the power to both heaters was slowly increased, while keeping the internal HFT "null balanced," until the nominal temperature point was

reached. The device was allowed to operate at this temperature for approximately 10 minutes to ensure that an equilibrium state had been achieved. The ambient, surface, and inner surface temperatures were then collected. The test HFT output was integrated over a 1-minute time period. The heat rate of the metered heater was recorded as well as an average of the null microvolt detector. Data collected for the HFTs with and without masks can be found in Tables 1 through 4 in the appendix.

RESULTS AND DISCUSSION

As can be seen in Figures 7 through 10, the calibration tests showed the HFTs to have a much higher calibration factor than the values obtained by Holometrix, Inc. Several factors could contribute to this bias. For example, if the internal null HFT in the Thin Heater Device does not cover the entire heater interface adequately, then the unevenness of the heat generation already noted could cause undetected bi-directional heat flow. Most obvious, however, is the problem of edge losses. The 5.08- x 5.08-cm HFTs have been a standard within our group, and the small 10.16- x 10.16-cm Thin Heater Device was originally chosen as most appropriate for general work with the 5.08- x 5.08-cm HFTs. For accurate calibration, however, a much larger face area would be better.

The original Series 1000-S was already somewhat thick in relation to the face area. By the time we added the copper plate and circuit board

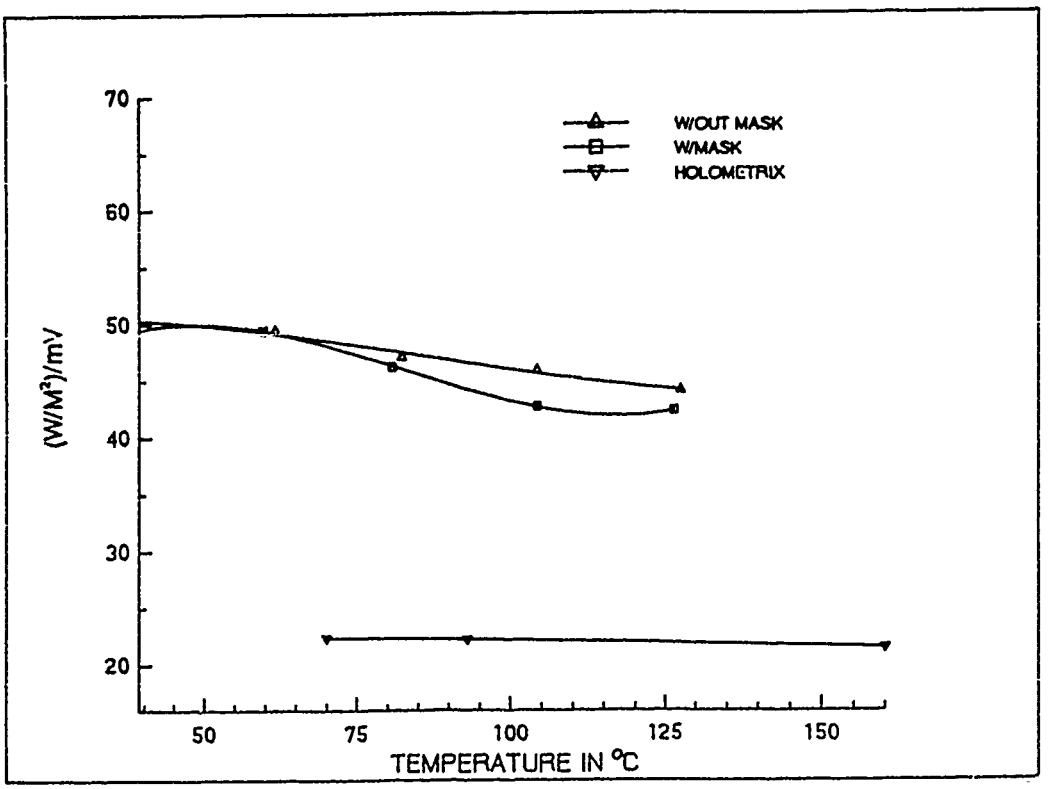

Figure 7. ITI #B-359 calibration curves.

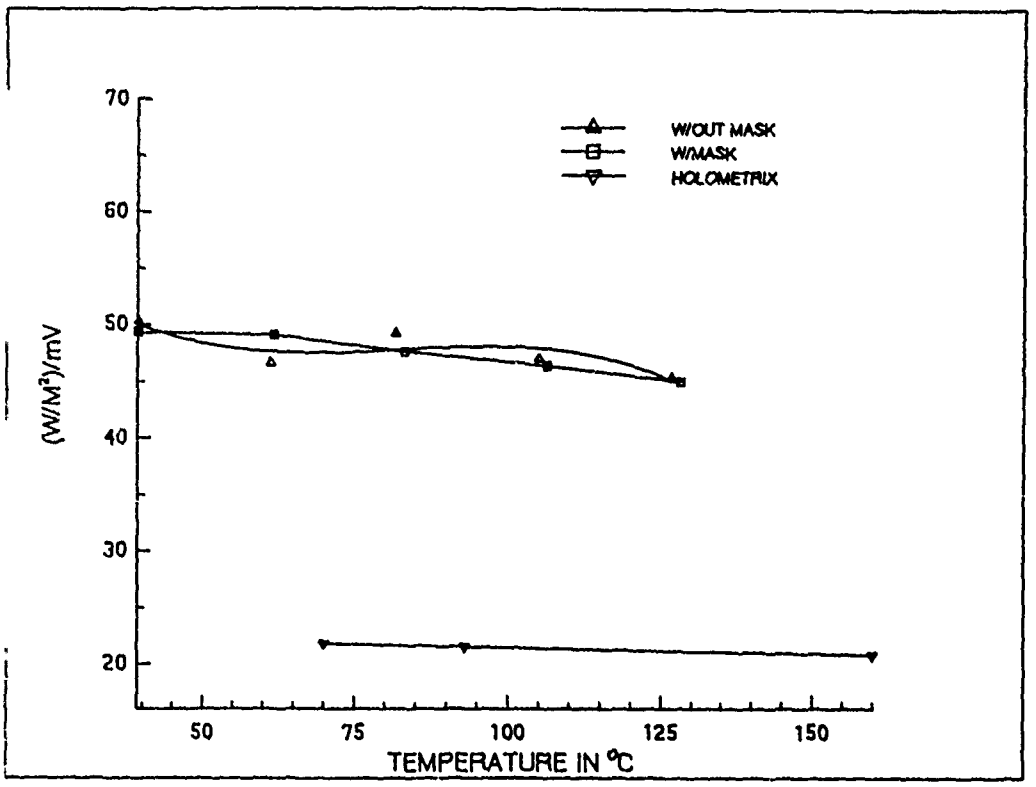

Figure 8. ITI #B-360 calibration curves.

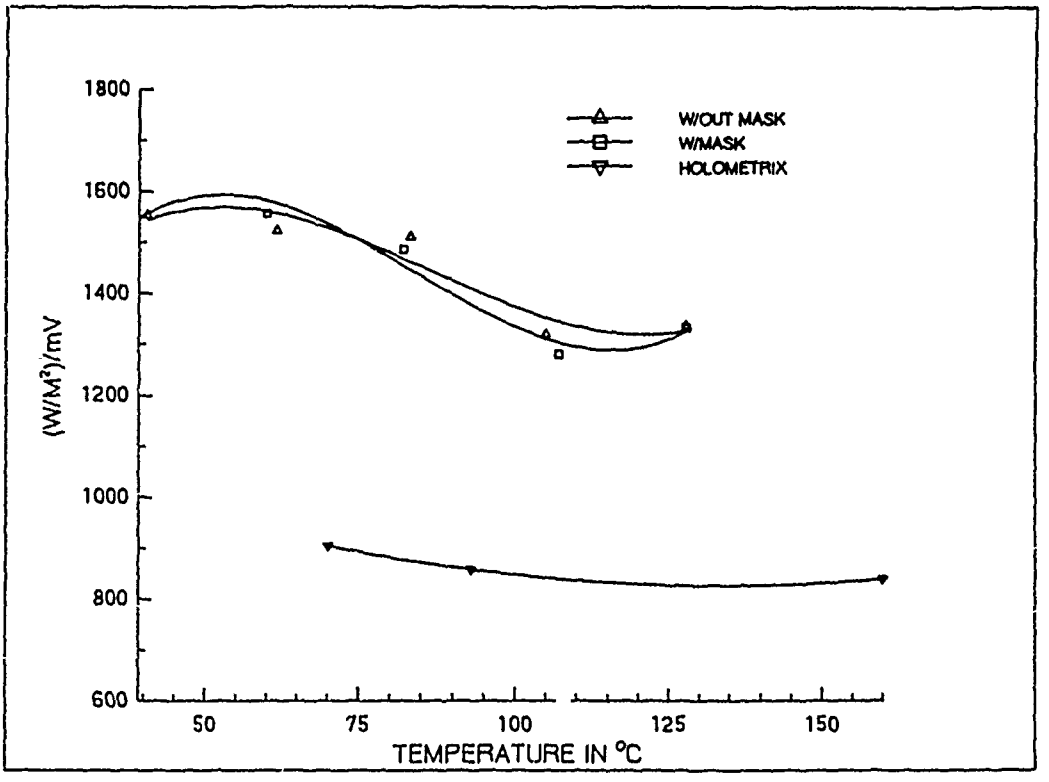

Figure 9. RdF #1285 calibration curves.

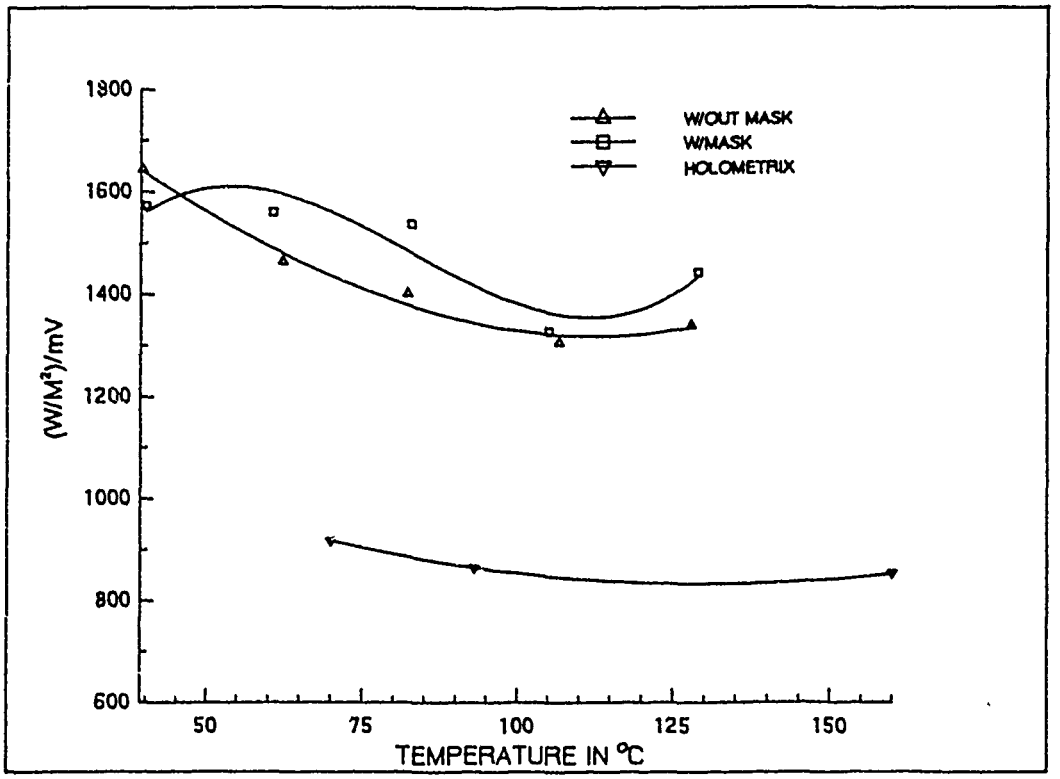

Figure 10. RdF #1286 calibration curves.

material (to better distribute the heat) and the mask and HFT to be calibrated, it became a stretch of the imagination to look at the device and still consider it a "thin heater." Furthermore, the thermal nature of the added layers is sure to have caused increased edge spill - that is, higher heat flow rate density from the edges of the copper than from the calibration face.

Another error source that affected the repeatability of the experiments became apparent during the RdF calibrations. When temperatures greater than 65°C were achieved, the output of the RdF transducers became very erratic. To study the cause of this error, we coupled an RdF transducer to a hot-plate and obtained thermal images at 65°C and 121°C. At the same time, the output of the transducer was being recorded on a millivolt strip chart recorder. It was determined that at 65°C the RdF's output varied 16%, and at 121°C, the output varied 33%. Upon examining the thermal image film, it was discovered that the free convection boundary layer on the horizontal hot-plate was actually turbulent at 121°C, with the transition from laminar flow taking place somewhere between 65°C and 121°C [2]. This turbulence accounted for not only the high variance but also the high unrepeatability of the RdF calibrations.

CONCLUSIONS

The general trend of the thin heater calibration curves for the ITI transducers agreed substantially with Holometrix data trends, giving us

at least some hope for the future of this technique. Improvements should be possible through the use of full-coverage null HFTs, careful attention to even heat distribution, perhaps some insulation of the edges, and - most of all - a much higher face area/edge area aspect ratio. It was determined that further refinement in the calibration technique is needed before the effects of using edge-guard masks can be thoroughly studied.

Future related experiments involve varying the external radiant and convective environment around the (exposed) calibration side of the Thin Heater/HFT assembly using setups described in these same proceedings by Mack and Bearden[3]. The object of this phase will be to investigate the theory that "field" calibrations of HFTs may be necessary, because "lab" calibrations may no longer be effective when field variables are present.

ACKNOWLEDGMENTS

The authors wish to thank Mr. Norman Greene of International Thermal Instrument Company (ITI) for his help in supplying us on short notice with thin heater modifications which greatly helped our work, and for his advice on thin heater technique.

REFERENCES

1. Apthorp, D.M. & Bligh, T.P.; Heat Flux Meters: Calibration, Heat Flux Distortion and Installation. Massachusetts Institute of Technology, 1983.
2. Incropera F. P. & De Witt D. P.; Fundamentals of Heat and Mass Transfer. John Wiley & Sons, New York, NY, 1985, p. 427
3. Mack, R.T. & Bearden, T.W.; Selection of a Method to Compensate for HFT Shunting Error. This volume.

APPENDIX

Table 1. ITI #B-359 calibration data.

ITI #B-359 w/out mask

T ambient (°C)	22.83	22.50	22.72	22.78	23.00
T surface (°C)	38.89	60.56	80.56	103.89	125.56
T thermocouple (°C)	39.72	61.67	82.67	106.11	127.89
Emittance	0.95	0.94	0.94	0.93	0.93
Null detector (uV)	15.0	30.0	30.0	60.0	60.0
HFT output (mV)	5.4	15.4	25.2	39.8	55.2
Wattmeter (W)	2.8	7.4	12.8	19.3	25.8

ITI #B-359 with mask

T ambient (°C)	22.61	22.67	22.78	22.78	22.72
T surface (°C)	38.89	61.11	82.22	105.00	127.22
T thermocouple (°C)	39.50	62.11	84.17	107.22	129.17
Emittance	0.95	0.94	0.94	0.93	0.93
Null detector (uV)	15.0	30.0	30.0	60.0	60.0
HFT output (mV)	5.5	15.8	27.5	43.3	61.2
Wattmeter (W)	2.8	8.0	13.5	20.7	28.4

Table 2. #B-360 calibration data.

ITI #B-360 w/out mask

T ambient (°C)	23.33	23.28	23.44	23.50	23.44
T surface (°C)	38.89	61.11	81.11	103.33	126.11
T thermocouple (°C)	39.39	62.06	83.44	105.06	128.89
Emittance	0.95	0.94	0.94	0.93	0.93
Null detector (uV)	15.0	30.0	30.0	60.0	60.0
HFT output (mV)	5.4	14.7	27.4	40.8	55.2
Wattmeter (W)	2.8	7.5	13.3	19.3	25.1

ITI #B-359 with mask

T ambient (°C)	22.61	22.67	22.78	22.78	22.72
T surface (°C)	38.89	61.11	82.22	105.00	127.22
T thermocouple (°C)	39.50	62.11	84.17	107.22	129.17
Emittance	0.95	0.94	0.94	0.93	0.93
Null detector (uV)	15.0	30.0	30.0	60.0	60.0
HFT output (mV)	5.5	15.8	27.5	43.3	61.2
Wattmeter (W)	2.8	8.0	13.5	20.7	28.4

Table 2. #B-360 calibration data.

ITI #B-360 w/out mask

T ambient (°C)	23.33	23.28	23.44	23.50	23.44
T surface (°C)	38.89	61.11	81.11	103.33	126.11
T thermocouple (°C)	39.39	62.06	83.44	105.06	128.89
Emittance	0.95	0.94	0.94	0.93	0.93
Null detector (uV)	15.0	30.0	30.0	60.0	60.0
HFT output (mV)	5.4	14.7	27.4	40.8	55.2
Wattmeter (W)	2.8	7.5	13.3	19.3	25.1

Rdf #1285 with mask

T ambient (°C)	23.06	22.89	23.00	22.94	22.78
T surface (°C)	38.33	60.00	82.22	107.22	127.78
Emittance	0.95	0.94	0.94	0.93	0.93
Null detector (uV)	15.0	30.0	30.0	60.0	60.0
HFT output (mV)	0.169	0.448	0.769	1.430	1.875
Wattmeter (W)	2.7	7.2	11.8	18.9	25.8

Table 4. RdF #1286 calibration data.

Rdf #1286 w/out mask

T ambient (°C)	22.44	22.44	22.67	22.61	22.50
T surface (°C)	39.44	62.22	82.22	106.67	127.78
Emittance	0.95	0.94	0.94	0.93	0.93
Null detector (uV)	15.0	30.0	30.0	60.0	60.0
HFT output (mV)	0.165	0.477	0.823	1.403	1.875
Wattmeter (W)	2.8	7.2	11.9	18.9	25.9

Rdf #1286 with mask

T ambient (°C)	22.94	23.00	22.94	23.22	22.89
T surface (°C)	40.00	60.56	82.78	105.00	128.89
Emittance	0.95	0.94	0.94	0.93	0.93
Null detector (uV)	15.0	30.0	30.0	60.0	60.0
HFT output (mV)	0.154	0.441	0.788	1.424	1.720
Wattmeter (W)	2.5	7.1	12.5	19.5	25.6

MEASUREMENTS WITH HEAT FLUX TRANSDUCERS

THE USE OF COMBINED REFLECTIVE AND NORMAL HEAT FLUX TRANSDUCERS IN DETERMINING CONVECTIVE HEAT TRANSFER COEFFICIENTS AND ROOM THERMAL RADIATIVE BALANCE

A. F. Emery
C.J. Kippenhan
K.H. Nocolaisen
J.L. Garbini
J.H. Heerwagen
D.R. Heerwagen
G.B. Varey

Department of Mechanical Engineering
and College of Architecture
and Urban Planning
University of Washington
Seattle, Washington USA

ABSTRACT

This paper describes the use of pairs of normal and reflective heat flux sensors to determine the convective and radiative components of heat flux to a wall, ceiling, or floor. In a long term experiment, readings were monitored on all walls in a room of a typical residence and temperatures were measured on the wall surfaces at the location of the transducer pairs and on other surfaces. The flux measurements from the pairs were used to compute convective coefficients and the radiative exchange. Radiative balances were made, using either measured wall temperatures to compute the fluxes or measured fluxes to estimate wall temperatures. The use of measured wall temparatures yielded computed fluxes which were significantly different from the measured fluxes. However, the use of measured fluxes predicted temperatures which were within a few degrees of the measured values at all times. The paper describes these computations and presents results which indicate that heat fluxes computed using measured surface temperatures cannot be used in conjunction with normal heat flux sensors to estimate either radiative fluxes or the convective heat transfer coefficients.

INTRODUCTION

Most residential building energy codes specify the construction in terms of specific component performance. Typical specifications are R19 for walls, a minimum U value of 0.4 for windows, etc. In general, the codes also permit exceptions to these component specifications if the user can demonstrate through steady state calculations or simula-

tion that the total energy use is less than that of a comparable building constructed to the specifications. Both sections of the code, the specifications and the exception, assume that the different components do not interact thermally with each other and that the total energy use can be determined by steady state calculations or experiments.

Recent changes in the electric generation capability and demand in the Pacific Northwest have led to an increased awareness of the need for conservation in residences. To increase the quality of the housing stock, significant changes were proposed in the State of Washington Uniform Building Energy Code. These changes are listed in Table 1.

Table 1
Component Specifications

Component	Pre-1980	Proposed Code
Wall	R-11	R-19
Floor	R-11	R-19
Ceiling	R-19	R-38
Door	R-2	R-14.5
Window	Single Glazing	Triple Glazing
Heat Recovery	none	Required
Infiltration	none	0.1 ACH natural 0.5 ACH supplementary

The aim of these changes was to reduce heating energy requirements in electrically heated houses to 2 kW/year-sq ft of floor area. The end effect was to be the elimination of the need for new power plants -- whose cost was estimated to be equivalent to 3.6 - 4.4 cents/kW-hr. To pacify prospective owners, the state legislature required that the additional building costs would be recovered within 7 years from the savings in heating costs.

Local builders noted that many of the houses and apartments built to the current code were meeting the energy use limits and questioned the cost figures used in the analyses of projected savings. To answer these questions, the legislature mandated that 4 test houses and a test cell be constructed and monitored. Full details of the houses and the experimental protocol are given in references (1) and (2). The measurements were not only to answer the questions raised by the builders, but also to provide data to fine tune the building energy simulation programs used to estimate savings.

Simulation programs range in complexity from single node, steady state models to fully transient, multi-node, multi-zone models. The complex models usually incorporate variable surface heat transfer coefficients whose values are usually taken from standard sources such as the ASHRAE Handbook of Fundamentals. Under some conditions, these standard values must be modified for accurate simulations (3). The most refined models also include the intersurface long wave radiation heat exchange, which has been shown to be important in estimating thermal comfort (4).

In this paper we describe a series of experiments and calculations to evaluate the temporal history of the surface convective heat trans-

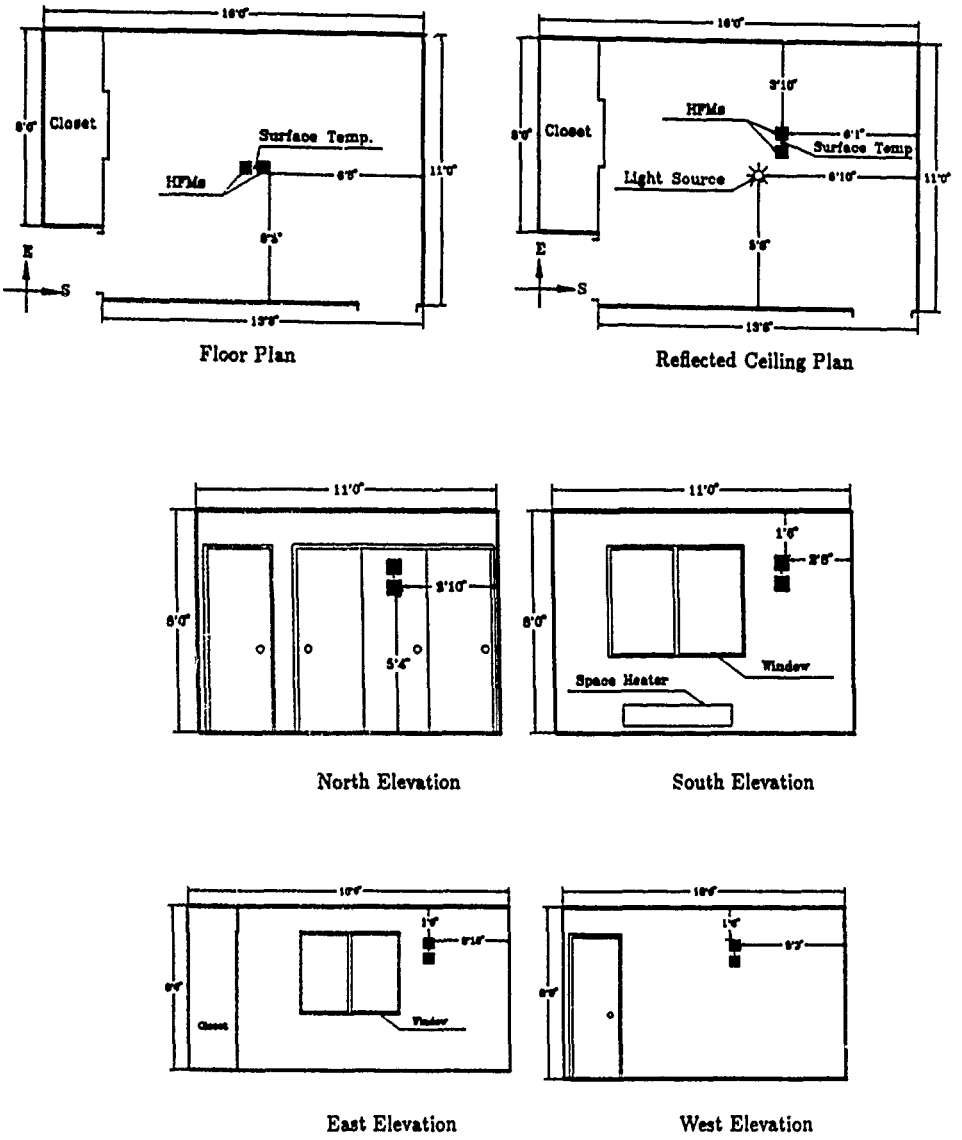

Figure 1. Schematic Showing Sensor Placement

fer coefficients and to determine the radiative heat exchange between surfaces in a typical residential room with an eye to understanding the degree of accuracy attainable in simulations.

INSTRUMENTATION

Figure 1 shows the location of the surface heat flux sensors used to measure the total and convective fluxes. The east and south walls are exterior walls, the remainder of the surfaces are internal. The sensors were mounted in pairs at locations on the walls where thermography had shown the thermal conditions to be representative of the entire wall. One transducer was a standard meter with a slightly patterned, light brown finish. The long wave emissivity approximates that of the room surfaces. The other meter had a copper foil surface with a polished gold finish. The surface emissivity was approximately 0.02. This meter reflected nearly all of the incident radiation and thus measured only the convective heat flux. The difference in the reading of the two sensors is the radiative flux. Two temperature sensors were mounted as closely as possible to the sensors. One sensor recorded the surface temperature of the wall and the other recorded the air temperature outside of the boundary layer. The instantaneous convective heat transfer coefficient could be determined by using the difference in temperatures and the convective flux. Details of the heat flux meter installations and calibration are given in reference (5).

Initially, temperature sensors were located only at the heat flux transducer sites. Later, in response to the preliminary analyses of the radiative fluxes, additional temperatures were measured on the door surfaces and on the window curtains. These curtains were drawn at all times to eliminate the effects of transmitted sunlight and the room lights were always off. The heat fluxes and the temperatures were measured every 30 seconds and 15 minute averages were recorded for subsequent analysis.

SIMULATION MODEL

Figure 2 illustrates the different heat fluxes associated with a surface. For analysis we assume

1. The surface emissivity equals the surface absorbtivity
2. The surfaces are opaque and grey
3. The incident radiation and the temperature are constant over the entire surface
4. Each pair of sensors experience the same convective boundary conditions.

For the "normal" transducer, the measured flux is *

$$q_n = q_{cond} = q^n_{conv} + q_i - q_o \qquad (1)$$

*Symbols are defined in the Nomenclature

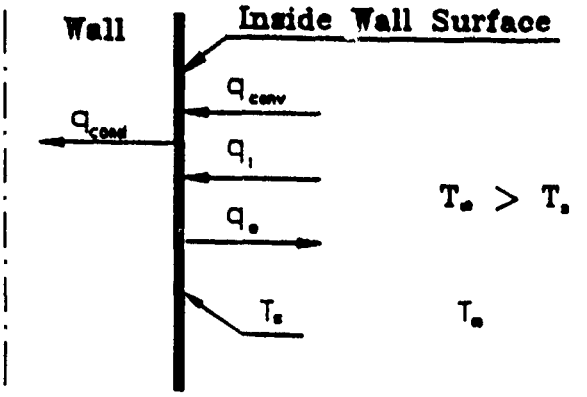

Figure 2. Heat Flux at the Inside Surface

while for the "reflective" transducer, it is

$$q_r = q_{cond} = q^r_{conv} \tag{2}$$

As equations 1 and 2 stand, they are of little value. If the convective heat transfer were the same, i.e.,

$$q^n_{conv} = q^r_{conv}$$

then by subtracting the sensor readings, we would obtain

$$q_r - q_n = q_o - q_i = \frac{Q}{A} \tag{3}$$

where Q/A is the net outward radiative flux from the surface. That is, the difference in the transducer readings would be a measure of the net radiative transfer to the surfaces. Unfortunately, in general the convective flux is not equal because the surface heat transfer coefficients and surface temperatures of the two sensors will be different. If the convective coefficients are equal (as they appear to be based upon a number of measurements of temperature and flow field) then equal fluxes require equal surface temperatures.

We have made a number of thermographic measurements of the sensor pairs at different times. When the curtains were closed and the room temperature changed slowly, as was the case in the experiments described in the paper, the two sensor temperatures were within 0.1°F. This experimental evidence supports our assumption of equal fluxes. Based upon this assumption, the largest error in the measured flux will be of the order of 0.1 Btu/hr-sq ft.

A simple one dimensional thermal solution, using equal convective coefficients, suggests that the temperatures will be different by several degrees because of the nearly perfect reflection of radiation. We have recently performed a number of numerical simulations of the transient heat transfer in the walls on which the HFTs were mounted using measured inside and outside temperature histories. During the early morning hours, whose data are described in the paper, the mean air tem-

perature is slightly higher than the mean radiant temperature and varies because the heaters are continually turning on and off. Under these conditions, the wall capacitance effects are important and the simulations indicate that the temperature differences will be of the order of 0.1°F. On the other hand, if the mean radiant temperature is higher, then the differences range between 0.5°F and 0.9°F, depending upon the time constant of the room temperature. In the experiments, the wall temperatures were always slightly lower than the air temperature, and thus the mean radiant temperature was lower, and the differences are computed to be small. In addition, the variation of temperature on the different surfaces also induces a small lateral conduction in the substrate under the sensor which tends to further reduce the differences.

For a surface, the outward radiative flux, q_o, can be represented as

$$q_o = \epsilon\sigma T^4 + \rho q_i \tag{4a}$$

$$= \epsilon\sigma T^4 + (1-\epsilon)q_i \tag{4b}$$

where $\rho = 1 - \epsilon$ for opaque grey surfaces. The incident flux on surface k can be related to the outward radiative flux from the other surfaces through

$$q_{ik} = \sum_{j=1}^{N} F_{j-k} q_{o,j} \tag{5}$$

where F_{j-k} is the viewfactor from surface j to surface k. These were computed using the View program of reference 6. The net radiative flux can be expressed as

$$\frac{Q_k}{A_k} = \frac{\epsilon_k}{1-\epsilon_k}(\sigma T_k^4 - q_{o,k}) \tag{6a}$$

$$= q_{o,k} - \sum_{j=1}^{N} F_{k-j} q_{o,j} \tag{6b}$$

If an enclosure has surfaces *1,2,... m* with known surface temperatures and surfaces *m+1, m+2, ... N* with known heat fluxes, the system of equations representing the radiative heat balance is

$$\sum_{j=1}^{N} [\delta_{kj} - (1-\epsilon_k)F_{k-j}] q_{o,j} = \epsilon_k \sigma T_k^4 \qquad 1 < k < m \tag{7a}$$

$$\sum_{j=1}^{N} [\delta_{kj} - F_{k-j}] q_{o,j} = \frac{Q_k}{A_k} \qquad m+1 < k < N \tag{7b}$$

After the values of $q_{o,k}$ have been determined, equation 6a can be used to find the unknown values of T or Q. The experiments have measured values of T_k and Q_k for each surface. If we used the measured temperatures, then solution of equations 7 leads to the radiative fluxes which can be compared to the measured fluxes to gain a measure of the accuracy of the simulation. Conversely we can use the measured fluxes to predict the surface temperatues.

It should be noted that a unique solution for the fluxes can be found by using the surface temperatures. However, if the measured fluxes are used, then at least one surface temperature must be specified to obtain a solution to the heat balance equations.

SIMULATIONS

The first simulations were done by dividing the room into 6 surfaces, the four walls, floor and ceiling. All surfaces were presumed to be uniform in temperature and radiative flux. This was clearly not the case for the east and south walls because of the windows, but it was thought that the closed drapes would eliminate much of the variation. The 24-hour period of simulation was chosen as one for which the measured fluxes were found to be significantly greater than the experimental error of the heat flux sensors throughout the entire period.

Table 2
Surface Heat Fluxes for 6 Surfaces Calculated
by Using The Measured Surface Temperatures

Time	East Wall		South Wall		Floor	
hours	Meas.	Calc.	Meas.	Calc.	Meas.	Calc.
.4	.324	1.285	.191	-.254	-.488	-1.929
.6	.288	1.317	.153	-.335	-.516	-1.851
.9	.338	1.272	.170	-.301	-.426	-1.867
1.1	.128	1.213	.192	-.135	-.264	-1.413
1.4	.009	.984	.062	-.184	.008	-.763
1.6	.053	.636	.047	-.157	.090	-.388
1.9	.079	.395	.021	-.217	.130	-.153
2.1	.091	.237	.020	-.172	.166	-.002
2.4	.053	.087	-.005	-.220	.190	.090
2.6	.066	.026	-.003	-.289	.203	.217
2.9	.024	-.180	.002	-.325	.154	.153
3.1	.075	-.204	-.053	-.440	.057	.120
3.4	.131	-.166	-.187	-.772	-.361	-.643
3.6	.294	.172	-.079	-.743	-.491	-.983
3.9	.358	.372	-.015	-.779	-.587	-1.338
4.1	.338	.632	.096	-.726	-.603	-1.437
4.4	.298	.722	.120	-.605	-.648	-1.675
4.6	.308	.894	.130	-.545	-.629	-1.756
4.9	.315	1.068	.161	-.629	-.609	-1.771
Average value	0.188	0.566	0.054	-0.412	-0.243	-0.915
Average error		-0.379		0.466		0.671

Table 2 lists the measured and predicted heat fluxes for a portion of the day. The computations were made using the measured surface temperatures. We see that not only are the measured and predicted fluxes substantially different in magnitude, but frequently in sign. A second calculation was made using the measured temperature on the north wall and the measured heat fluxes on the other walls. These results are presented in Table 3 where it is seen that the temperatures are in very good agreement. On the north wall, the measured and predicted heat fluxes were in error by an amount similar to that shown in Table 2.

In order to improve the predictions, temperature sensors were installed on the doors and the drapes. In addition, the room was modeled as having 20 surfaces (Figure 3). These surfaces were created by subdividing the original surfaces into areas that were felt to be more uniform in temperature and flux. Unfortunately, heat flux sensors could not be mounted on the drapes. In the calculations, fluxes were used where measured, while other surfaces were assigned their measured temperatures. Surfaces whose temperatures were not measured, were assigned a weighted average of nearby surfaces and local air temperatures. Table 4 lists some of the results obtained. As before, predicted temperatures on those surfaces with measured fluxes are in good agreement with the measured values. Likewise, predicted fluxes on those surfaces that were assigned the measured temperatures are in poor agreement with the measured fluxes. However, although the measured and predicted fluxes differ in magnitude, they generally did agree in sign. Thus it appears that a better representation of the surface temperature variations did eliminate some of the error in the predicted heat fluxes.

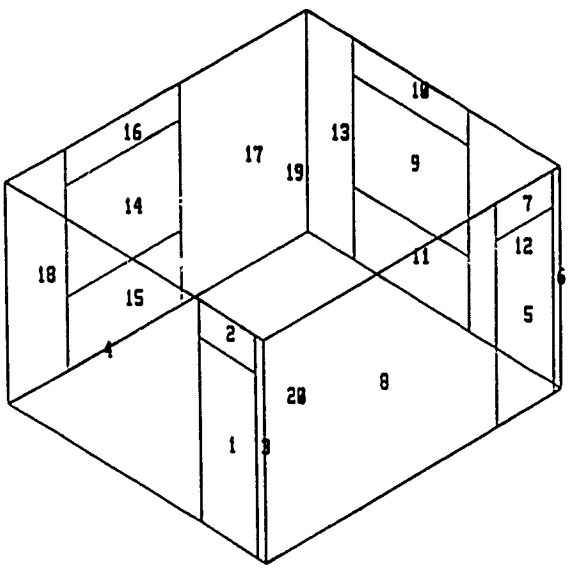

Figure 3. Room 7, House 1, Modeled by 20 Surfaces

These results are not unexpected because the temperature appears in the equations to the 4th power, and thus the predictions are expected to be sensitive to small variations in temperature. To study this effect, the temperature of the ceiling was increased by 7°F. The result was an increase in the predicted fluxes in the order of 150% for most of the other surfaces. A similar calculation was made using an increase in the flux of surface 3 of 10%. The resulting absolute surface tempera-

tures increased by less than 0.12°F, which is far less than the 2.5% expected from a sensitivity analysis of the flux-temperature relationship of equation 4.

Table 3
Surface Temperatures for 6 Surfaces Calculated
by Using The Measured Surface Heat Fluxes

Time	East Wall		South Wall		Floor	
hours	Meas.	Calc.	Meas.	Calc.	Meas.	Calc.
.4	69.130	66.241	67.797	66.179	66.319	65.536
.6	69.216	66.170	67.773	66.100	66.445	65.473
.9	69.130	66.162	67.767	66.066	66.391	65.499
1.1	68.763	66.219	67.599	66.354	66.469	65.913
1.4	67.900	65.770	66.885	65.886	66.379	65.824
1.6	67.037	65.606	66.364	65.662	66.163	65.684
1.9	66.413	65.536	65.896	65.536	65.964	65.616
2.1	65.837	65.301	65.506	65.285	65.664	65.397
2.4	65.347	64.982	65.104	64.970	65.394	65.129
2.6	64.980	64.894	64.721	64.874	65.196	65.040
2.9	64.601	64.663	64.499	64.679	64.949	64.799
3.1	64.441	64.319	64.253	64.225	64.787	64.316
3.4	65.096	64.148	64.559	63.846	64.733	63.708
3.6	65.800	64.664	64.985	64.330	64.829	63.959
3.9	66.431	65.195	65.398	64.873	64.961	64.353
4.1	66.970	65.347	65.752	65.162	65.178	64.515
4.4	67.361	65.370	66.184	65.244	65.274	64.532
4.6	67.722	65.529	66.448	65.409	65.406	64.705
4.9	68.108	65.687	66.591	65.594	65.622	64.875
Average value	66.851	65.358	66.004	65.278	65.585	64.993
Average error		1.499		0.727		0.592

CONVECTIVE COEFFICIENTS

Since the reflective heat flux sensors measure the convective flux only, it is possible to use this information and the local air-surface temperature difference to compute the surface convection coefficient. Figure 4 illustrates the temporal behavior of the convective coefficient on the east wall and the floor. In the early morning, about 2 AM, the electric baseboard heater comes on and sets up an upward flowing warm air current over the east wall. As shown on the figure, this results in an increasing coefficient. Later, about 6 AM, the heater turns off and the air gradually cools down, resulting in a reduction in upward velocity, then stagnation, and finally a downward flow. As a consequence the coefficient decreases. When the flow is slow, the temper-

ature difference becomes very small, smaller than the level of accuracy of the readings.

Table 4
Calculations Based Upon Measured Heat Fluxes
and Additional Measured Temperatures
20 Surface Model

Time	East Wall		South Wall		Floor	
hours	Meas.	Calc.	Meas.	Calc.	Meas.	Calc.
.3	-.205	-2.826	-.011	1.241	70.086	71.065
.6	-.216	-2.809	-.018	1.147	69.827	70.879
.8	-.217	-2.713	-.013	1.159	69.671	70.460
1.1	-.223	-2.789	-.017	1.229	69.395	70.278
1.3	-.215	-2.762	-.023	1.155	69.160	70.016
1.6	-.219	-2.728	-.029	1.262	68.980	69.710
1.8	-.217	-2.936	-.028	1.130	68.686	69.709
2.1	-.219	-2.735	-.026	1.093	68.560	69.441
2.3	-.217	-2.613	-.030	1.003	68.277	69.261
2.6	-.215	-2.695	-.027	1.007	68.055	69.029
2.8	-.222	-2.574	-.030	1.068	67.917	68.679
3.1	-.208	-2.657	-.027	1.010	67.604	68.421
3.3	-.218	-2.654	-.028	1.008	67.550	68.217
3.6	-.170	-2.590	.017	1.100	67.538	67.867
3.8	-.150	-2.667	.217	1.766	67.490	67.728
4.1	-.298	-3.119	.184	1.598	67.484	68.455
4.3	-.409	-3.205	.190	1.574	67.520	68.768
4.6	-.427	-3.738	.231	1.162	67.526	69.312
4.8	-.426	-3.399	.197	1.423	67.550	69.050

Consequently, coefficients were not evaluated for temperature differences less than 1°F (approximately 3 sigma of the temperature sensors), thus the gaps in the time history. This process of heating and cooling is repeated several times throughout the day, with the corresponding cycling of the coefficient. During the early afternoon,about 4 PM, after the sun had moved off the east wall and onto the south wall, the temperature difference remained below the limit of accurate resolution for most of the surfaces in the room, except the floor. Although the floor coefficient displays some of the same trends in the early morning when the room air is cool, during the rest of the day it remains relatively constant. As expected, the coefficients for the other walls behaved similarly to those for the east wall although the coefficients were always smaller since the heater was located only on the east wall. The ceiling, bathed by the rising air, displayed the same temporal history. In the early morining hours when the air rose over the east wall but did not bath the entire ceiling, the ceiling coefficients were lower than those of the east wall. Later in the day, when all the walls experienced similar air flows, all surfaces had approximately equal convective coefficients.

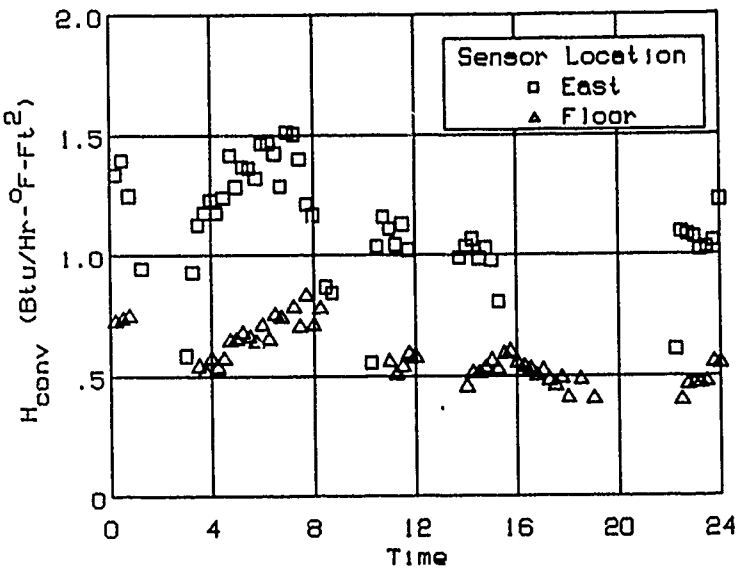

Figure 4. Variation of Convective Heat Transfer Coefficients over a 24 Hour Period

CONCLUSIONS

These results emphasize the complexity needed for an accurate simulation of heat transfer in a typical residential room. Convective coefficients vary by a ratio of 2 to 1 (rising to 3 to 1 when flow reversal is present) for surfaces strongly affected by rising warm air. The floor, which is less affected showed variations in the range of 1.5 to 1. When the air currents are minimal, local air-surface temperature differences are of the order of 1°F. Simulations made to estimate overall room energy losses are generally accurate, reference 1, because they are dominated by infiltration and window effects and because the time increments of simulation are usually long in relation to the cycling time of the coefficients. However, simulations made to estimate local effects must take into account both the time changing coefficients and the existence of very small temperature differences.

The results also indicate the sensitivity of the internal radiation to the measured temperatures. Clearly, radiative fluxes cannot be accurately predicted using measured temperatures for rooms in which the surface temperature differences are small (less than 5F). Small errors in the temperature measurements and variations of the temperature over the surfaces, coupled with the relatively small temperature differences between the several surfaces of the room lead to unacceptable sensitivity of the computed fluxes. On the other hand, measured fluxes can be used to provide reasonably accurate estimates of the surface temperatures, at least to within 1°F.

Unfortunately, it is far easier and cheaper to measure temperatures than it is to measure fluxes. Thus, although internal radiation exchange may have a strong effect on local conditions and human comfort, accurate assessments of these effects are unlikely to be achieved in practice. From an energy point of view, two factors make the sensitivity of radiative fluxes less likely to be as important: 1) because radiation is a zero sum game (i.e., the net transfer by radiation from all surfaces is zero); and 2) because in real situations where radiation is likely to be important, one can expect significant temperature differences between surfaces (e.g., between internal walls and glazing), which will both increase the radiative fluxes and decrease the sensitivity to errors in the surface temperatures.

NOMENCLATURE

A	area, sq ft.
F	radiation view factor
q	heat flux, Btu/hr-sq ft-F
Q	net radiative heat lost from a surface
T	temperature, F or K
α	absorptivity
ϵ	emissivity
ρ	reflectivity
σ	Stefan-Boltzmann constant
δ_{ij}	Kronecker delta

Subscripts

cond	conductive
conv	convective
i	incident radiative flux
k	surface number
o	outward radiative flux
n	normal transducer
r	reflective transducer

REFERENCES

1. Emery, A. F., Kippenhan, C. J., Vary, G. B., Garbini, J. L., Heerwagen, J. H., and Heerwagen, D. R., The Thermal Interaction of Envelope Components in Standard and Improved Houses in the Pacific Northwest, *ASME HTD-Vol 123*, 1989
2. Evaluation of 86-87 Heating Season Data, Report 1, Washington State Energy Office/University of Washington Contract 86-34-02, October 1, 1987

3a. Emery, A. F., Kippenhan, C. J., Heerwagen, D. R., and Varey, G. B., The Simulation of Building Heat Transfer for Passive Solar Systems, *Energy and Buildings*, Vol. 3 , pp. 287-294, 1981

3b. Emery, A. F., Heerwagen, D. R., Kippenhan, C. J., Stoltz, S. V. and Varey, G. B., The Optimal Energy Design of Structures by Using the Numerical Simulation of the Thermal Response - with Emphasis on the Passive Collection of Solar Energy, *Energy and Buildings*, Vol. 1, pp. 367-382, December 1978

4. Emery, A. F., Heerwagen, D. R., Kippenhan, C. J. and Varey, G. B., The Numerical Simulation of the Thermal Response of Architectural Structures with Emphasis on Radiant Exchange and Human Comfort, *Proceedings of the 1978 Heat Transfer and Fluid Mechanics Institute*, pp. 21-34, Stanford Univ. Press, June 1978

5. Kippenhan, C. J., Emery, A. F., Heerwagen, D. R., Garbini, Nicolaisen, K. H., and Vary, G. B., On the Extensive Use of Heat Flux Sensors for Evaluating Residential Building Component Performance - Calibration and Deployment, *Proc. In-situ Heat Flux Measurements in Buildings*

6. Emery, A. F., Johansson, O. ; Lobo, M. and Abrous, A., A Comparative Study of Methods for Computing the Diffuse Radiation Viewfactors for Complex Structures, to be published *ASME Journal of Heat Transfer*, 1990

Ashley F. Emery

Q: How did you average in the framing members in the heat flux values?— Timothy Larson.

A: The HFTs measuring the flux, on which the quasistatic U-values were computed, were mounted over the wall cavities at sites selected by IR imaging. Thus the results apply only to portions of wall that contain insulation cavities.

AN EVALUATION OF THE HEAT FLUX TRANSDUCER TECHNIQUE FOR MEASURING THE THERMAL PERFORMANCE OF WALLS

D.M. Burch
R.R. Zarr

National Institute of Standards
and Technology
Gaithersburg, Maryland USA

ABSTRACT

Four wall specimens were instrumented with heat flux transducers and tested in a calibrated hot box to determine the accuracy of the heat flux transducers. The heat flux transducers were installed at the interior surface of the wall specimens and exposed to different steady and dynamic (i.e., time-dependent) temperature differences using a calibrated hot box. Two of the wall specimens were composed of homogeneous, and monolithic material layers, which yielded virtually one-dimensional heat flux. The other two wall specimens were composed of conventional wall construction with wood structural members, which yielded a two-dimensional heat flux pattern. The heat flux transducers were previously calibrated by exposing them to a uniform heat flux in a guarded hot plate.

The steady-state and transient heat flux transducer measurements agreed within 5% of the calibrated hot box measurements. These results indicate that, when heat flux transducers are carefully calibrated and installed, they provide accurate measurements of heat flux in walls.

INTRODUCTION

In two recent field studies (Flanders 1985 and Fang and Grot 1985), heat flux transducers (HFTs) were used to measure the thermal resistance of building components. When measured thermal resistances were compared to predicted thermal resistances using steady-state theory, large observed differences (e.g., 25-75%) between measured and predicted results were common. These large discrepancies could either mean that the HFTs gave inaccurate results or that the predicted wall performances departed from actual performance.

When HFTs are used in field experiments, several factors give rise to a large difference between measured and predicted thermal

performance. The HFT may be incorrectly calibrated or improperly installed. The HFT may be inadvertently placed in line with thermal anomalies (i.e., missing or compressed cavity insulation) or in line with a thermal bridge (i.e., a firestop). In addition, the predicted performance may depart significantly from actual performance due to the use of erroneous handbook property data in predictive models.

In this paper, the accuracy of the HFT is experimentally investigated under laboratory conditions. The HFTs were carefully calibrated by exposing them to a uniform heat flux using the National Institute of Standards and Technology (NIST) 1-m Guarded Hot Plate. They were carefully installed using a surface adhesive to ensure intimate contact between the HFT and the surface. A guarded ring was used with each HFT to minimize deflection of the undisturbed wall heat flux. Moreover, the wall specimens were carefully constructed to be free of thermal anomalies and thermal bridges.

DESCRIPTION OF HEAT FLUX TRANSDUCERS

The HFTs consisted of 48-mm-diameter (3-mm-thick) circular disks made of tan polyvinyl-chloride filler material, each having an embedded spiral of helically wound wire comprising a large number of thermocouple junctions in series. Two wires attached to each transducer served as leads for the thermopile. When heat passes through the HFT, a temperature difference, proportional to the heat flux, develops across the circular disk. The embedded thermopile generates a direct current millivolt signal that is directly proportional to the sensed temperature difference or heat flux.

METHOD OF HEAT-FLUX-TRANSDUCER CALIBRATION

The HFTs were embedded in a composite sandwich assembly and exposed to a steady and uniform heat flux in the NIST 1-m Guarded Hot Plate (see Fig. 1). The temperature of the back-flow plate was

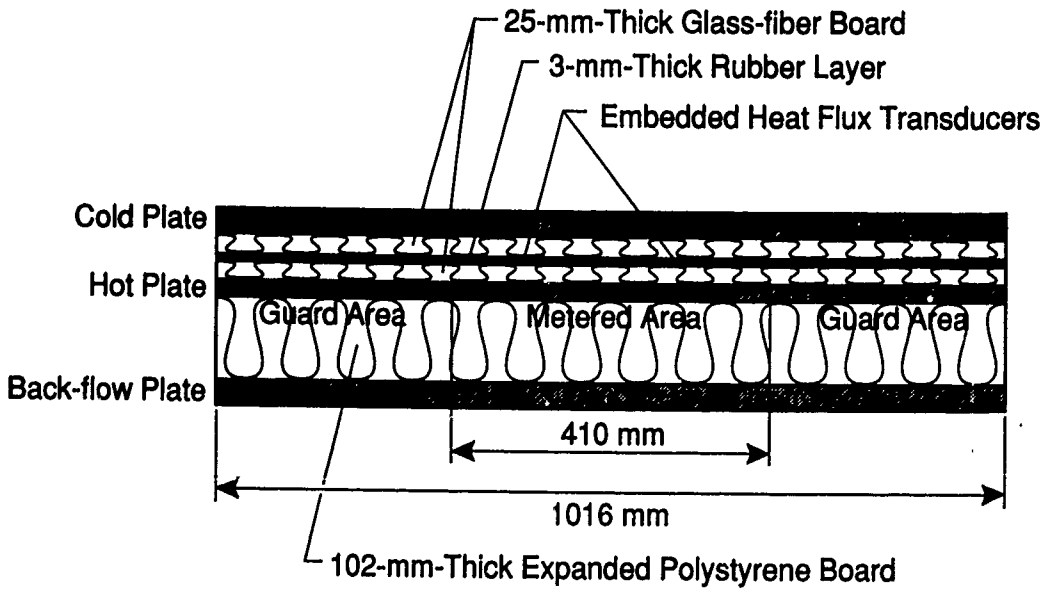

Figure 1. Illustration of the calibration of HFTs in the NIST 1-m Guarded Hot Plate.

adjusted to be the same as that of the hot plate. Under this condition, all electrical energy released by the hot plate was dissipated as a heat flux from the hot to the cold plate. After reaching a steady state, measurements for the heat flux and millivolt output for each HFT were recorded at 1-minute intervals for an 8-hour period. The sensitivity (expressed in millivolts per W/m^2) for each of the HFTs was determined by dividing the measured millivolt signal for each HFT by the heat flux.

The composite sandwich assembly was composed of an upper 25-mm-thick glass fiber insulation board, 3-mm-thick rubber layer, and a lower 25-mm-thick glass-fiber insulation board. Circular openings in the rubber layer were cut out, and the HFTs were mounted in the circular openings. Calibrations were conducted at a temperature difference of 17°C between the hot and cold plates at the following mean temperatures: 32.5°, 15.5°, and 4.8°C. The resulting HFT sensitivities were fit to a linear function with respect to mean temperature.

DESCRIPTION OF WALL SPECIMENS

The four wall specimens consisted of a polystyrene wall, a composite masonry wall, a well-insulated wall and a superinsulated wall (see Table 1). The polystyrene and composite masonry walls were constructed of homogeneous layers of materials, yielding virtually a one-dimensional wall heat flux during the calibrated-hot-box (CHB) tests. On the other hand, the well-insulated and superinsulated walls were constructed of conventional building materials and contained wood structural members that produced a two-dimensional wall heat flux pattern during the CHB tests.

Table 1. Description of Wall Specimens.

Polystyrene Wall
- 100-mm expanded polystyrene insulation

Composite Masonry Wall
- 100-mm expanded polystyrene insulation
- 140-mm solid concrete block

Well-Insulated Wall[1] (see Fig. 2)
- 13-mm gypsum board
- 0.10-mm polyethylene vapor retarder
- 51- X 67-mm wood-framing section with compressed R-1.9 $m^2 \cdot K/W$ glass-fiber blanket insulation
- Staggered 51- X 67-mm wood-framing section with compressed R-1.9 $m^2 \cdot K/W$ glass-fiber blanket insulation
- 19-mm polyisocyanurate insulation
- Air infiltration retarder
- 13-mm wood siding

Superinsulated Wall[1]
- Same as well-insulated wall, except 89-mm glass-fiber blanket insulation sandwiched between wood-framing sections

[1] Further information on the well-insulated and superinsulated wall specimens is available in Zarr et al. (1986).

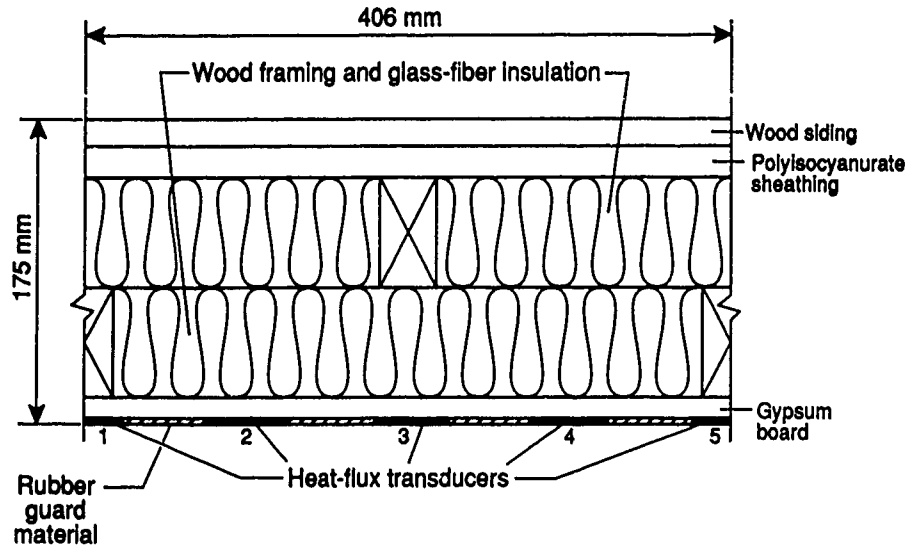

Figure 2. Cross section of the well-insulated wall specimen.

Installation of Heat Flux Transducers

At the geometric center of the polystyrene and composite masonry wall specimens, a single HFT was attached to the interior wall surface using epoxy as shown in Fig. 3. A guard ring, made of the same material as the HFT, was installed with the HFT, in order to minimize deflection of the undisturbed wall heat flux.

For the well-insulated and superinsulated wall specimens, the heat flux pattern repeats itself between framing members. Near the geometric center of each of these walls, the interior surface between two framing members was instrumented with a row of HFTs as shown in Fig. 2. The HFTs were attached using room-temperature-vulcanizing (RTV) rubber. A rubber guard material was used to minimize deflection of the undisturbed wall heat flux.

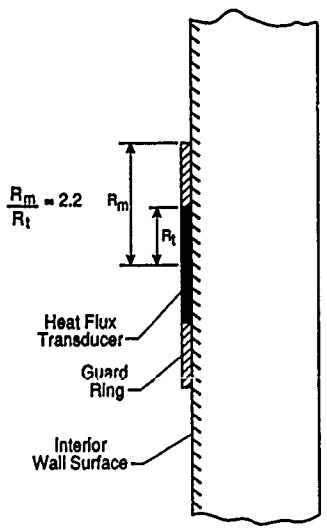

Figure 3. Method of installing a HFT at an interior wall surface.

CALIBRATED-HOT-BOX TEST PROCEDURE

Each of the four wall specimens described above was installed in a 3.0 X 4.6-m support frame and sandwiched between the metering and climatic chambers of a CHB as shown in Fig. 4. Uniform streams of conditioned air may be delivered to either the top or bottom of vertical plenums formed between a baffle and opposite sides of the wall specimen. Either a steady-state or time-dependent excitation function was generated in the climatic chamber. The metering chamber was operated at a typical indoor steady temperature condition and served as a calorimeter. For the CHB measurements, the air speed was adjusted and maintained at about 0.3 m/s in the metering chamber and at about 1.1 m/s in the climatic chamber.

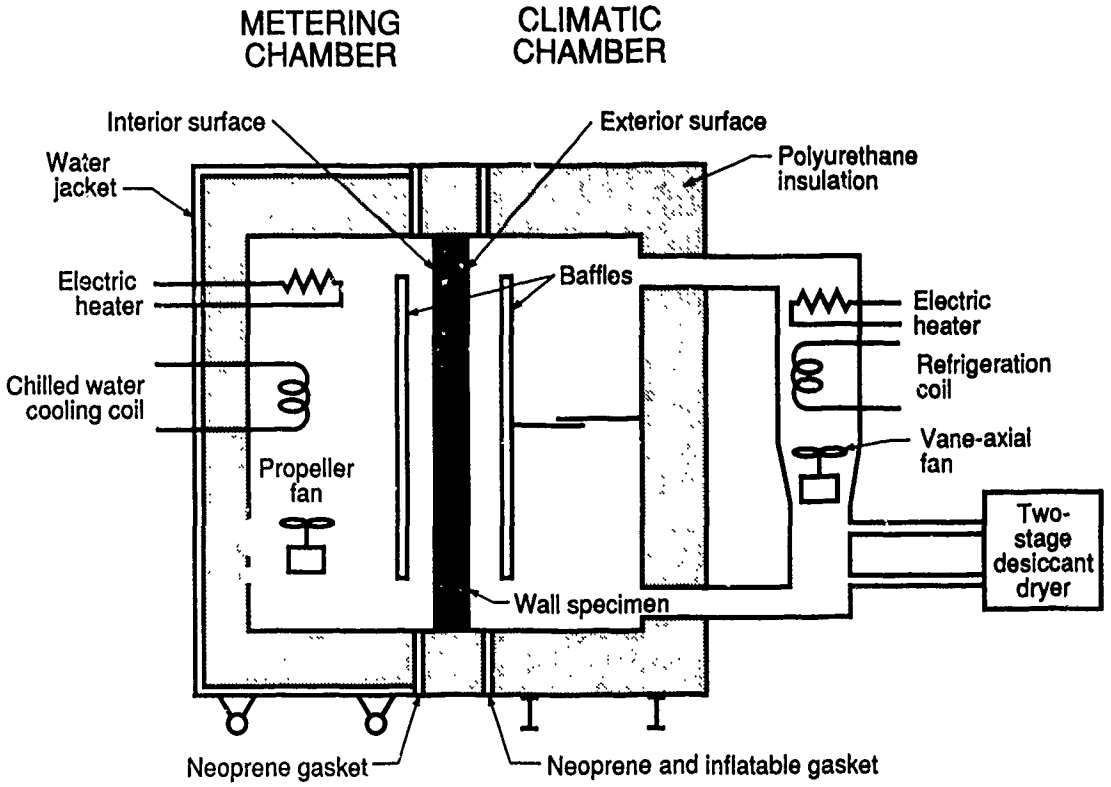

Figure 4. Calibrated-Hot-Box test procedure.

The heat transfer rate at the interior surface of the specimen (Q_{sp}) was determined at hourly time steps from the following energy balance equation:

$$Q_{sp} = Q_h + Q_{bl} - Q_{inf} - Q_{box} - Q_{fl} - Q_{stor} \quad (1)$$

All electrical powers, heat transfer rates, and energy storage rates in the above equation are averaged over a one-hour period to smooth out fluctuations. The terms Q_h, Q_{bl}, Q_{inf}, Q_{box} were measured directly. For steady-state tests, the rate of energy storage (Q_{stor}) in the metering chamber was equal to zero. The heat flux (q_m) at the inside surface of the specimen was determined by dividing the specimen heat transfer rate (Q_{sp}) by the specimen surface area.

The heat transfer rate (Q_{fl}) that flanks the wall specimen and passes through the specimen support frame was predicted using a finite-difference model described by Zarr et al. (1987). The flanking heat transfer rate generally was less than 7% of the net power delivered to the metering chamber. For dynamic tests, the requirements of ASTM standard steady-state test method C 976 (ASTM, 1989) pertinent to dynamic testing were followed. The total energy storage rate (Q_{stor}) within the metering chamber was predicted using transfer function equations derived from a series of calibration tests described by Burch et al. (1987).

The foregoing procedure has been shown to yield closure of the energy balance for the metering chamber within 2% under steady-state conditions (Zarr et al. 1987) and within 4% under dynamic conditions (Burch et al. 1987).

RESULTS

Steady-State Heat Flux Comparisons

One-Dimensional Heat Flux Comparison: The polystyrene and composite masonry wall specimens were installed in the CHB and exposed to several temperature differences. After the specimen heat transfer rate reached a steady-state condition, the heat flux measured by the HFT attached at the center of the wall specimen (q_{hft}) and that measured by the CHB (q_m) were averaged during periods ranging from 12-31 hours.

A plot of q_{hft} versus q_m for the polystyrene and composite masonry walls is given in Fig. 5. The diagonal solid line represents perfect agreement between q_{hft} and q_m. Note that the heat flux transducer measurements are within 5% of the CHB measurements.

Two-Dimensional Heat Flux Comparison: The well-insulated and superinsulated wall specimens were also installed in the CHB and exposed to several steady-state temperature differences. After the specimen heat transfer rate reached a steady state, the heat fluxes sensed by the row of HFTs (see Fig. 2) were measured during periods ranging from 12-13 hours.

The average heat flux through the instrumented section was determined by the equation:

$$q_{hft} = [(A_1 \cdot (q_1/2) + A_2 \cdot q_2 + A_3 \cdot q_3 + A_4 \cdot q_4 + A_5 \cdot (q_5/2)]/A_t \quad (2)$$

Here A_1, A_2, etc., and q_1, q_2, etc., are surface areas and heat fluxes for each HFT, and A_t is the total surface area of the instrumented section. In the analysis, two sets of surface areas were used: equal areas and parallel-path areas. For equal areas, $A_1 = A_2 = A_3 = A_4 = A_5$. For parallel-path areas, the areas correspond to portions of the instrumented wall section containing framing and insulation (see Fig. 2). Note that in both cases the first and last areas are half size.

A comparison of the average heat flux measured by the row of HFTs (q_{hft}) and that measured by the CHB (q_m) for the well-insulated and

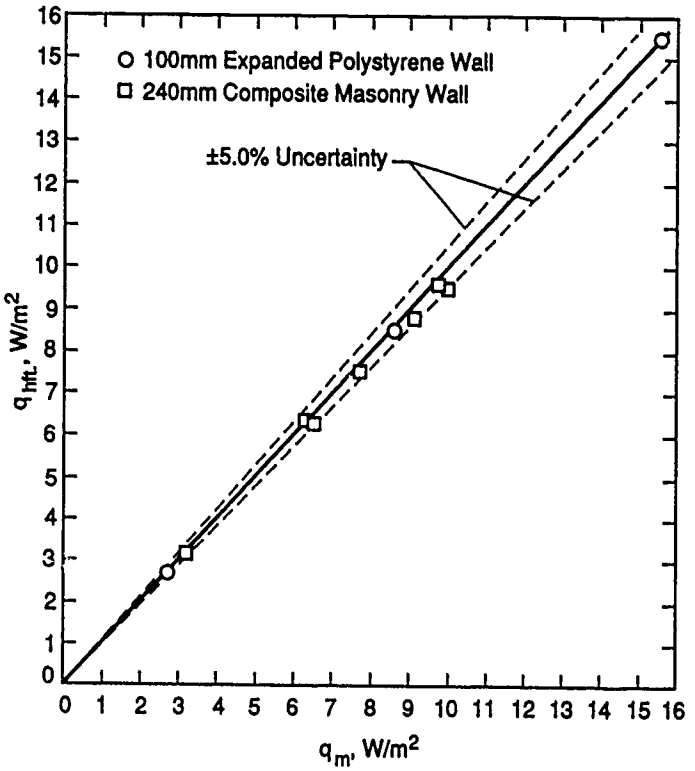

Figure 5. Comparison between the steady-state HFT and CHB measurements for the polystyrene and composite masonry walls.

superinsulated wall specimens is given in Fig. 6. Note that, when equal areas are used to determine q_{hft}, HFT measurements are within 4.5% of the CHB measurements, except for the mild summer test. The HFT measurements determined by parallel-path areas provided less agreement with the CHB measurements. Both sets of HFT measurements tended to be less than the CHB measurements, because the HFT measurements did not include heat conduction through the sill plate at the top and bottom of the wall specimen.

For one of the CHB tests of the well-insulated wall specimen, the heat fluxes measured by the row of HFTs were compared to the heat flux profile predicted by a finite-difference model (Zarr et al. 1987). In the finite-difference analysis, the thermal conductivity of the materials comprising the wall section were based on NIST 1-meter Guarded-Hot-Plate measurements.

The results of this comparison are given in Fig. 7. The HFT measurements agree very well with the heat flux profile predicted by the finite-difference model. The maximum difference between the predicted and measured results is about 9%. Note that when the HFTs were placed on the surface where the heat flux profile departs from one-dimensional behavior, the HFT measurements are smaller than the predicted profile. This is because a HFT placed in a two-dimensional heat flux pattern responds only to the normal component of the sensed heat flux.

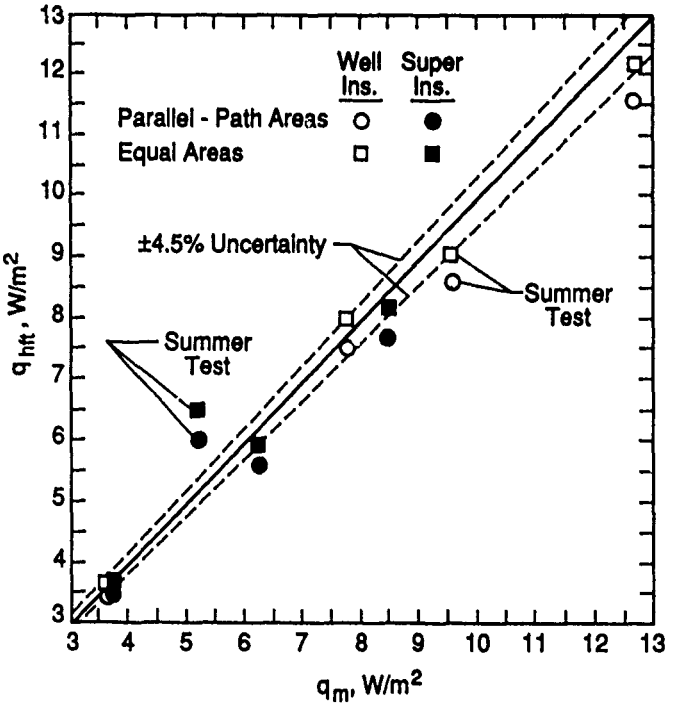

Figure 6. Comparison between the steady-state HFT and CHB measurements for the well-insulated and superinsulated wall specimens.

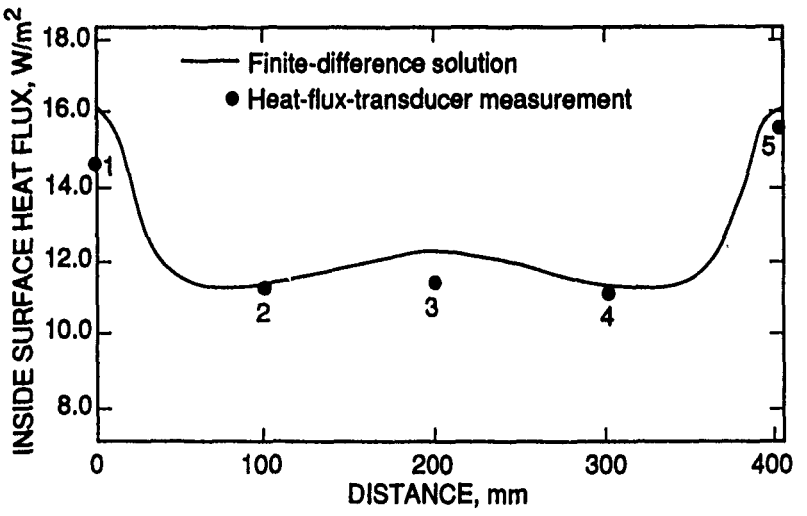

Figure 7. Comparison between steady-state HFT measurements and predictions using a finite-difference model.

Dynamic Heat Flux Comparison

While the composite masonry wall was installed in the CHB, the diurnal temperature cycle shown in Fig. 8a was repeated in the climatic chamber until a periodic specimen heat transfer rate occurred in the specimen. The specimen heat flux measured by the CHB is

plotted as a function of elapsed time in Fig. 8b. The heat flux measured by the HFT installed at the center of the wall specimen and that predicted using a one-dimensional analytical model (Walton 1983) are also given on the plot. All heat fluxes are hourly average values. Note that the HFT measurements track the CHB measurements more closely than the predictions by the one-dimensional model.

Hourly HFT measurements are plotted versus the CHB measurements in Fig. 8c and are within 3.5% of the CHB measurements. This agreement is excellent in view of the fact that the CHB measurements themselves are uncertain by 4%.

SUMMARY AND CONCLUSIONS

HFTs installed at the interior surface of wall specimens provided heat flux measurements within 5% of calibrated-hot-box measurements when they were used under controlled steady-state and dynamic laboratory conditions. That is, the wall specimens were carefully constructed to be free of thermal bridges and thermal anomalies; the HFTs were carefully calibrated by embedding them in a composite sandwich assembly and exposing them to a uniform heat flux in a guarded hot plate; the HFTs were installed using an adhesive compound that provided intimate contact between the surface and the HFT, and the HFTs were installed with a guard ring to minimize deflection of the undisturbed wall heat flux.

Moreover, good agreement between HFT measurements and heat flux predictions was obtained when measured thermal conductivity values were used in the theoretical predictions.

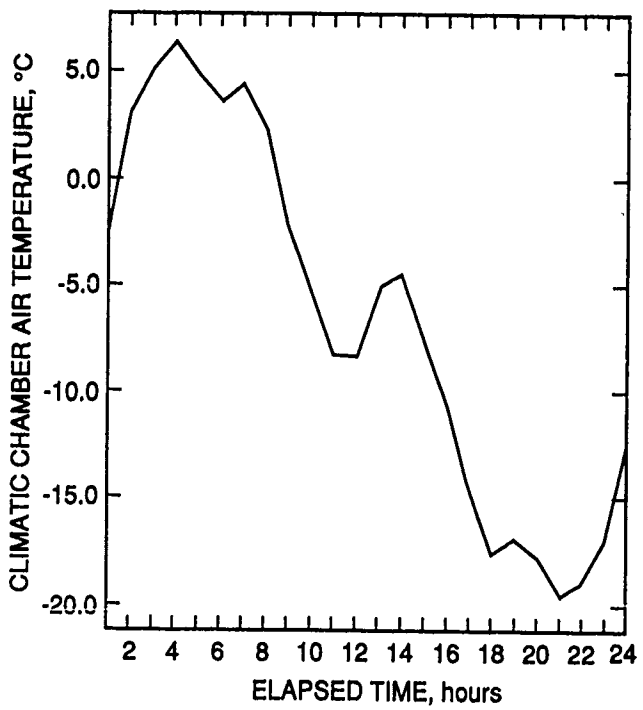

a. Diurnal temperature cycle.

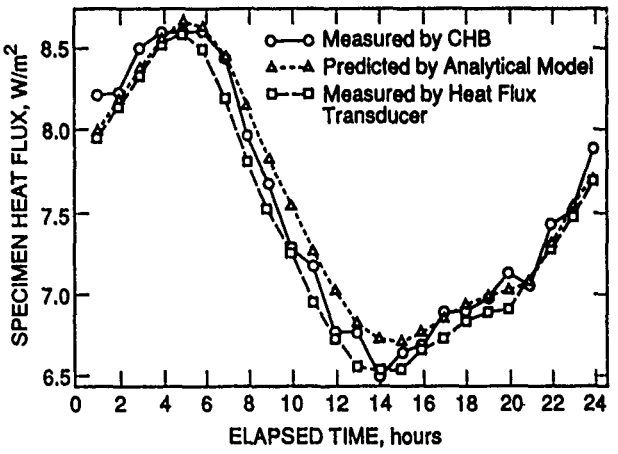

b. Plot of heat fluxes versus time.

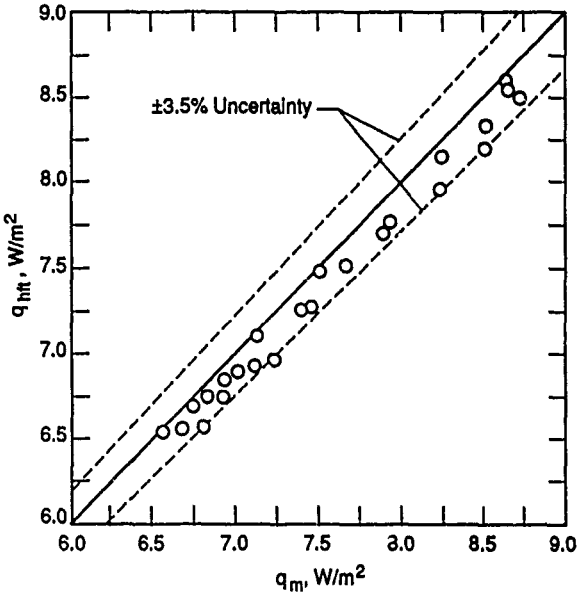

c. Heat flux comparison.

Figure 8. Comparison between time-dependent HFT and CHB measurements for the composite masonry wall.

REFERENCES

ASTM. 1989. Thermal Performance of Building Assemblies by Means of a Calibrated Hot Box. ASTM Standard Method of Test C 976-82, 1985 Annual Book of ASTM Standards, Vol. 4.06, pp. 468-487.

Burch, D.M.; Zarr, R.R.; Faison, T.K.; Licitra, B.A.; and Arnold,C.E. 1987. A Procedure for Measuring the Dynamic Thermal Performance of Wall Specimens Using a Calibrated Hot Box, ASHRAE Transactions, V. 93, Pt. 2.

Fang, J.B. and Grot, R.A. 1985. In Situ Measurement of the Thermal Resistance of Building Envelopes of Office Buildings, ASHRAE Transactions, V. 91, Pt 1.

Flanders, S.N. 1985. Heat Flow Sensors on Walls - What Can We Learn, Building Applications of Heat Flux Transducers, ASTM STP 885, p.140-159.

Walton, G.N. 1983. Thermal Analysis Research Program - Reference Manual, NBSIR 83-2655, National Bureau of Standards.

Zarr, R.R.; Burch, D.M.; Faison, T.K.; Arnold, C.E.; and O'Connell, M.E. 1987. Calibration of the NBS Calibrated Hot Box, Journal of Testing and Evaluation, V. 15, No. 3, pp.167-177.

Zarr, R.R.; Burch, D.M.; Faison, T.K.; and Arnold, C.E. 1986. Thermal Resistance Measurements of Well-Insulated and Superinsulated Residential Walls Using a Calibrated Hot Box, ASHRAE Transactions, V. 92, Pt. 2.

Douglas Burch

Q: For your steady-state measurements, what was the range of ΔTs across your test specimen?—Jeffrey Christian.

A: For the steady-state measurements, the temperature difference across the wall specimens ranged from 8°C to 54°C.

Q: Why were data from summer tests, using the cooling coil, considered to be outliers?—Thomas Petrie.

A: The data for the summer tests were considered to be outliers because the measurement of the rate of heat removed by the cooling coil (Q_C) is considerably less accurate than the measurement of the heater power (Q_h) and the blower power (Q_{bl}). The measurement Q_c involves taking the product of the mass rate of liquid flow and temperature difference across the cooling coil. Moreover, in calculating the net rate of heat removed from the metering chamber, one must take the differences between Q_C and the net heat input to the metering chamber (Q_h and Q_{bl}), which causes the difference to be more uncertain than Q_c.

Q: All dynamics measurements fell to one side of ideal agreement between HFT-measured heat fluxes and calibrated hot box (CHB) values. Why?- -Thomas Petrie.

A: The authors are unable to explain the systematic bias between the HFT measurements and the CHB measurements in Figure 8c.

Q: What were the size and thickness of the HFTs?—Rik van der Graaf.

A: The HFTs were 48-mm-diameter and 3-mm-thick disks.

Q: Are the thermal conductivities of the HFT material and the rubber guard region equal?—Rik van der Graaf.

A: The material used for the circular guard rings used with the single HFTs for the polystyrene and composite masonry walls was identical to that for the HFTs. For the well insulated and superinsulated walls, the guard material was similar, but not identical to that for the HFTs.

DETERMINING THE THERMAL ADMITTANCE OF A WALL FROM IN SITU MEASUREMENTS OF HEAT FLUX AND SURFACE TEMPERATURE AT THE SAME LOCATION

S. Bellattar
B. Duthoit
P. Thery

Laboratoire de Mesures Automatiques
U.S.T.L.F.A.-Villeneuve d'Ascq, France

ABSTRACT

Thermal admittance of building envelopes is an appropriate parameter for characterizing heat transfer through walls under unsteady state conditions. Because the typical calcullated values are usually determined from handbook values of material properties, they have several drawbacks: they do not take into account degradation effects or construction irregularities and they do not take into account multidimensional heat flow. This paper examines the use of in-situ measurements, of heat flow and surface temperature to determine the thermal admittance of walls. A first objective is to explore the problems associated with interpreting in-situ heat flux and temperature measurements, rather than the problems associated with the measurement themselves. The recent developments in thermal system analysis lead to processing heat flux and temperature as signals that can be used to determine thermal admittance.

INTRODUCTION

There has been considerable interest recently in the heat flux transducer as a sensor for direct measurement of heat flow rate through materials and systems in building and industrial applications. This type of sensor is being used more and more for experiments under transient conditions, however, "in situ measurements" are frequently reported with unresolved difficulties and problems. Because all walls contain some thermal mass and since surface temperatures and heat fluxes are always fluctuating, there are a number of basic problems in interpretation of the output voltage of a heat flux sensor positioned on a wall surface. Even in the case where the sensor thickness is very low and where the

thermal resistance of the sensor is small in relation with the wall resistance, the sensor can change the surface resistance, causing lateral heat transfer at the surface. Changes in surface resistance are caused by mismatches of either convective heat transfer coefficients or infrared or solar emissivities.

The problem associated with making heat flux measurements has been discussed extensively in the literature(1). The purpose of this paper is to explore the problems associated with interpreting heat flux and temperature measurements rather than the problems associated with the measurements themselves. The focus is on the interaction of the envelope thermal mass with the fluctuations in heat fluxes and temperatures that occur during in-situ measurements. The recent developments in thermal system analysis lead to regarding heat flux and temperature measurements as signals, from power spectral considerations in the frequency domain, from which can be determined various thermal characteristics such as thermal admittance.

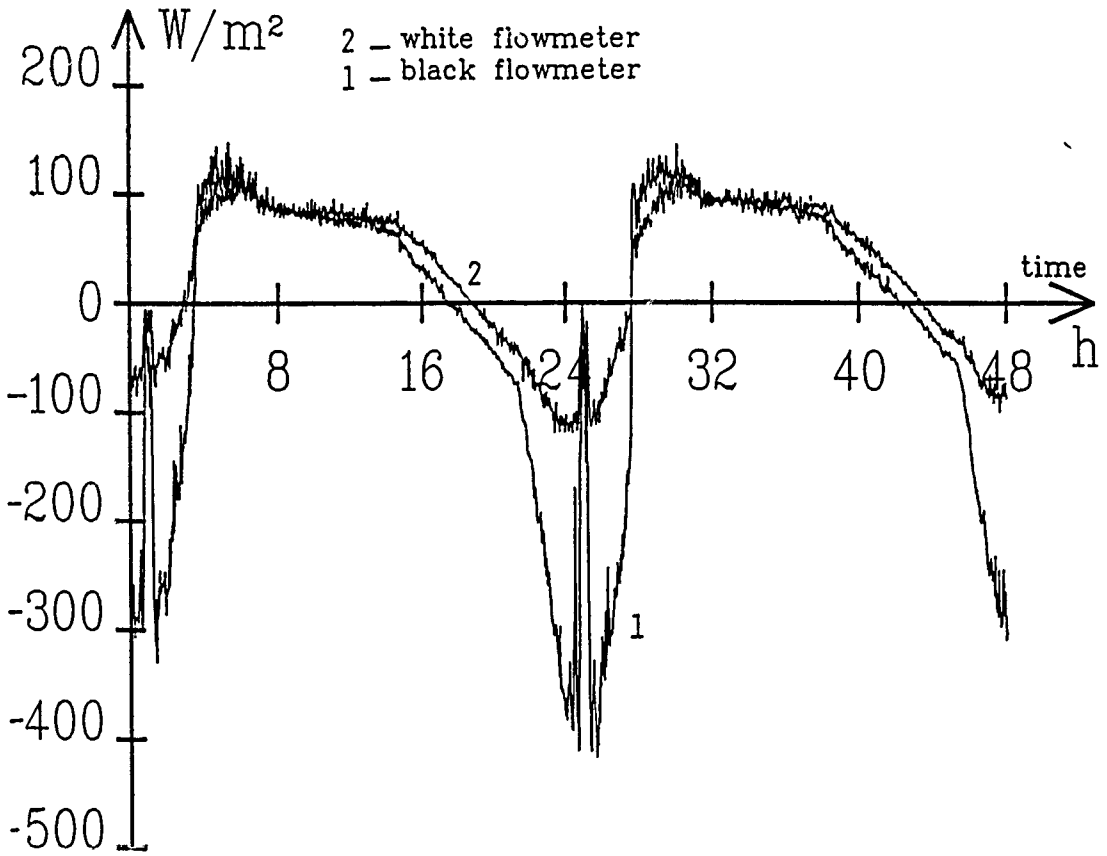

Figure 1a. Plot of the heat fluxes measured.

THEORY

Because a given sensor cannot conform to the radiative properties of all surfaces especially in the solar spectrum where color is important, the heat flowing through a H.F.T. as well as its average temperature will be influenced by the sensor emissivity. For example, if the measuring surfaces of two H.F.Ts positioned on a wall surface are covered with black and white adhesives there will be a difference between the actual temperatures $\theta_b(t)$ and $\theta_w(t)$ of the surfaces covered by the black and white coatings :

$$\theta_d(t) - \theta_b(t) - \theta_w(t) \qquad (1)$$

In the same way, since energy balances are strongly influenced by the sensors emissivities, there will be a difference between the actual heat flows :

$$\Phi_d(t) - \Phi_b(t) - \Phi_w(t) \qquad (2)$$

where Φ_b and Φ_w are actual heat fluxes through the cross-sectional surface areas covered by the black and white coatings.

For example, let us consider (in Fig. 1) a plot of fluxes measured with "black" and "white" sensors, the corresponding surface temperatures,

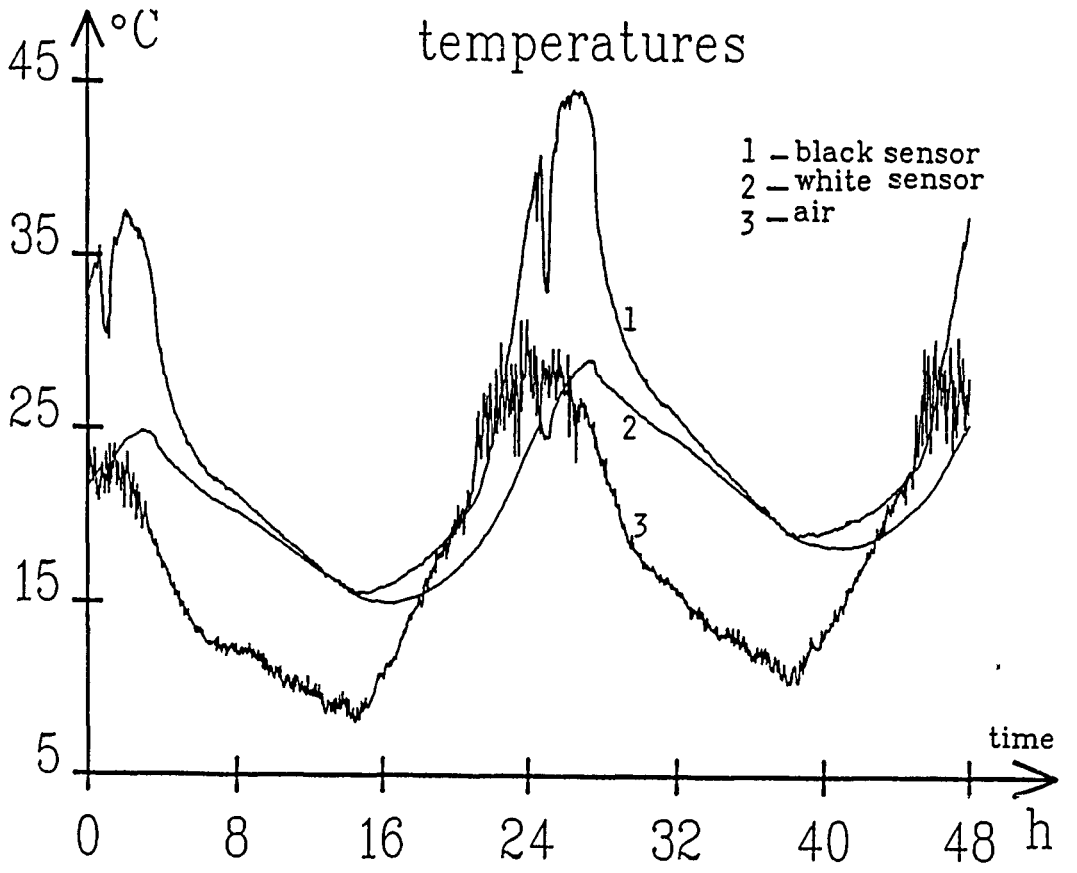

Figure 1b. Plot of the corresponding surface temperatures of the air temperature.

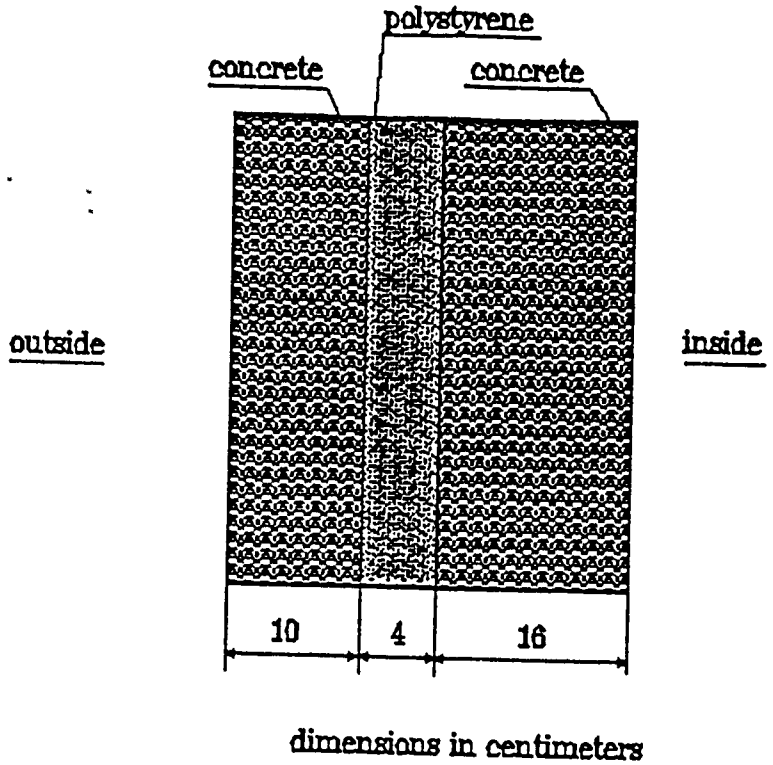

Figure 2 : Experimental wall.

the outside air temperature measured in September 88 on a wall section exposed to natural weather conditions on one side and subject to the periodic night-day heating on the other side. The experimental wall section was a structure of three layers : 16 cm of concrete, 4 cm of polystyrene and 10 cm of concrete represented schematically in Fig. 2. The "black" and "white" sensors were attached on the external face of the wall with an appropriate adhesive such as silicon grease. From the plot shown in Fig. 1, it clearly appears that the outside air temperature drives the variations in flux and temperature of the "white" sensor. A similar pattern is apparent on the sensor covered with a black coating although the daily influence of solar insolation magnified the surface temperature by more than 50 %.

As a result, the differences $\Theta_d(t)$ and $\Phi_d(t)$ clearly appears to depend only on solar insolation. In fact, these differences are very important under dynamic conditions and the main effect of the solar insolation is to give strong fluctuations in the data. Even in stationary processes with locally constant air temperature, quantities $\Theta_d(t)$ and $\Phi_d(t)$ may be regarded as correlated noise components. This well-known phenomenon is caused by random heating of the surface by solar radiation and by turbulent mixing of the temperature profile in the air.

The physical state of any surface element of a wall surface is then determined by measuring at every time the actual values of the surface temperature, and the hat flow into it, which are related by the thermal admittance of the wall. The thermal admittance is the functional relationship between the heat flow and the surface temperature which may be

expressed either in the time or in the frequency domain. Its expression may be very complex but in the special case of unsteady-state conditions any wall may be regarded as being infinite in thickness. The simplest way to establish the "surface temperature-heat flow" relationship is to start with a frequency domain analysis of the heat transfer through the wall. There are three steps for determining the relation between the correlated quantities $\Theta(t)$ (temperature variations) and $\Phi(t)$ (heat flux) from a systems point of view in the frequency domain.

1. Resolve the temperature change $\Theta(t)$ into series of simple sinusoidal components of angular velocity ω.

2. Calculate the heat flux amplitudes of each sinusoidal component. Letting $\mathfrak{F}(\omega)$ be the Fourier transform of the input $\Theta(t)$ and $\mathfrak{F}(\omega)$ the Fourier transform of the output heat flux $\Phi(t)$, it follows from the solution of the heat equation 4 that when the surface temperature is a harmonic function of time we have for the heat flux :

$$\mathfrak{F}(\omega) = b\sqrt{j\omega}\ \mathfrak{F}(\omega) \qquad (3)$$

where j is the symbol associated with imaginary numbers, $\sqrt{-1} = j$.

From that general equation, we obtain for the Fourier transforms of $\Phi_b(t)$, $\Phi_w(t)$, $\Phi_d(t)$:

$$\mathfrak{F}_b(\omega) = b\sqrt{j\omega}\ \mathfrak{F}_b(\omega) \qquad (4\text{-}1)$$

$$\mathfrak{F}_w(\omega) = b\sqrt{j\omega}\ \mathfrak{F}_w(\omega) \qquad (4\text{-}2)$$

$$\mathfrak{F}_d(\omega) = b\sqrt{j\omega}\ \mathfrak{F}_d(\omega) \qquad (4\text{-}3)$$

The amplitude of the heat flux involves the thermal constants in the combination $b = \sqrt{\lambda\rho c}$ (where λ thermal conductivity and ρc volumetric heat capacity) and so provides a means of measuring this quantity.

3. Finally, we have to add the heat flow inverse Fourier transforms for the separate components.

That frequency domain analysis introduces the thermal effusivity $b = \sqrt{\lambda\rho c}$ which can be determined at every frequency from the ratio of the complex amplitudes of the heat flux and surface temperature measured at every angular velocity ω.

In the case of random data there is an interest to introduce the following power spectral densities :

- First $\mathfrak{F}(\omega)\ \mathfrak{F}^x(\omega)$ (where $\mathfrak{F}^x$ denotes the complex conjugate of $\mathfrak{F}(\omega)$) which describes in the frequency domain the dependance of the temperature data at one time on the values at another time.

- And then $\mathfrak{F}(\omega)\ \mathfrak{F}^x(\omega)$, which describes in the frequency domain the dependance of the heat flux data at one time on the temperature data at another time.

For random data, heat flux and surface temperature variations are statistically dependent quantities whose spectral densities are related by the following equations :

$$\mathcal{F}_b(\omega)\ \ \mathcal{F}^x_b(\omega) = b\sqrt{j\,\omega}\,\mathcal{F}_b(\omega)\ \mathcal{F}^x_b(\omega) \qquad (5\text{-}1)$$

$$\mathcal{F}_w(\omega)\ \ \mathcal{F}^x_w(\omega) = b\sqrt{j\,\omega}\,\mathcal{F}_w(\omega)\ \mathcal{F}^x_w(\omega) \qquad (5\text{-}2)$$

$$\mathcal{F}_d(\omega)\ \ \mathcal{F}^x_d(\omega) = b\sqrt{j\,\omega}\,\mathcal{F}_d(\omega)\ \mathcal{F}^x_d(\omega) \qquad (5\text{-}3)$$

From that equation, the thermal effusivity $b = \sqrt{\lambda\rho c}$ can be determined in the frequency domain by plotting the modulus of the cross spectral density $\mathcal{F}(\omega)\ \mathcal{F}^x(\omega)$ against the modulus of the following quantity $\sqrt{\omega}\ \Theta(\omega)\ \Theta^x(\omega)$.

Taking the inverse Fourier transforms of the power spectral densities gives the autocorrelation of the surface temperature data :

$$R_{\Theta\Theta}(\tau) = \lim_{T\to\infty} \frac{1}{T} \int_0^T \Theta(t)\ \ \Theta(t+\tau)\ d\tau = F^{-1}\,|\mathcal{F}(\omega)\ \mathcal{F}(\omega)| \qquad (6\text{-}1)$$

which is a real even function of the time delay τ.

$$R_{\Theta\Phi}(\tau) = \lim_{T\to\infty} \frac{1}{T} \int_0^T \Theta(t)\ \ \Phi(t+\tau)\ d\tau = F^{-1}|\mathcal{F}(\omega)\ \mathcal{F}^x(\ )| \qquad (6\text{-}2)$$

$R_{\Theta\Phi}$ is a real-valued function but does not necessarily have a maximum at $\tau = 0$; it is not an even function. From the classical properties of the convolution product denoted $\circledast$, we obtain by introducing the weighting function :

$$u(\tau) = \frac{b}{\sqrt{\Pi\,\tau}} = F^{-1}\,(b\sqrt{j\,\omega}) \qquad \Pi = 3{,}1416 \qquad (7)$$

$$R_{\Theta\Phi}(\tau) = \int_0^\infty u(\tau-t)\ \frac{d}{dt}\ R_{\Theta\Theta}(t)\ dt = u(\tau) \circledast \frac{d}{dt}\ R_{\Theta\Phi}(\tau) \qquad (8)$$

Since the cross-correlation function and the convolution product are proportional, the following equation shows how to determine the thermal effusivity :

$$b = \frac{R_{\Phi\Theta}(\tau)}{\frac{1}{\sqrt{\Pi.\tau}} \circledast R_{\Theta\Theta}(\tau)} \qquad (9)$$

in the time domain from the correlation functions of the data.

The principle of measuring in-situ thermal effusivity is then based on the fact that the temperature variations measured in the plane of a sensor positioned on a wall surface are correlated with the heat flow variations measured at the same location to give a cross-spectral density directly proportional, in the frequency domain, to the power spectral density of the surface temperature variations.

It may be noted that since measurements are available for the air temperature, it is possible to estimate the value of the thermal parameters used to model the heat transfer between the wall surface and the air from the relation between cross correlation and autocorrelation functions.

MEASUREMENT TECHNIQUE

The previous formulation regards heat flux and surface temperature measurements as signals that may be handled from power spectral considerations, independent of their waveforms, at high immunity to disturbances, in the frequency domain. In fact, surface temperature and heat flow simultaneously measured on a wall surface are affected by the frequency response of the sensor positioned on it. The main problem that is posed in practice is then to clarify the circumstances in which the operational errors are minimized to give a functional "heat flow - surface temperature" relationship unchanged by the measuring operation.

As in steady-state conditions the operational error in heat flux measurements is attributed to the difference between the original heat flux to be measured and the local heat flux penetrating through the transducer. For a sensor operating in quasi-steady-state conditions, the rate at which heat is stored is negligible as compared to the rate at which heat flows through the sensor, and we can use the steady calibration with very little error. The temperature difference between the end faces of the sensor is then proportional to the heat flowing through them. The heat flow sensor follows very closely the steady-state Fourier law, even if the well is undergoing a dynamic temperature rise. As a consequence, when using a sensor of negligible thermal resistance with that of an air film at a solid/gas interface, its presence does not upset the thermal field at the wall surface and the "heat flow-surface temperature" functional relationship may be expected to be unchanged. It is then essential to ensure quasi-steady-state operation of the sensor to avoid operational error. Estimating the extent to which this requirement is met is simplified by comparing in the frequency domain the input thermal impedance of the wall surface with and without a sensor on it.

The effect of a thin heat flow sensor (whose thermal properties are known) on the estimation of the input thermal impedance of a concrete wall (16 cm in thickness) having its back face maintained at a constant temperature has been simulated and represented in Fig. 3.

In the low frequency range that impedance is equal to the sum of the thermal resistances. The main type of error encountered in the use of heat flow sensor is then the error caused by its thermal resistance. For a wall of sufficiently high input thermal impedance, this loading effect can be neglected in the frequency range where the sensor operates in quasi-steady-state conditions. That result holds in the wide range of frequencies where the in-situ measurements are taking place, in which the input impedance of the wall undergoes wide variations in modulus and phase.

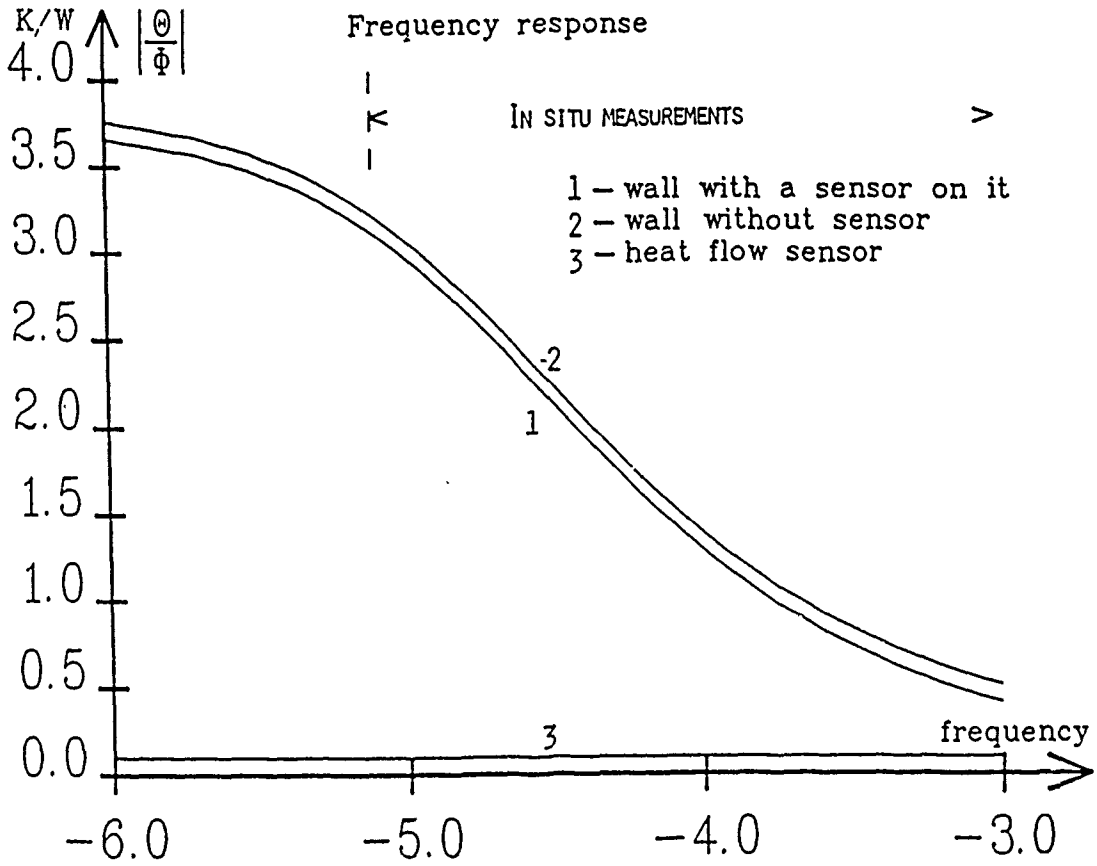

Figure 3 : Thermal input impedances of the wall, the wall with a sensor on it

It is only in the high frequency range that the sensor works as a thermal capacitor positioned on the wall surface. The quasi-steate-operation is then not fulfilled ; the rate at which heat is stored in the sensor is of the same order of magnitude of that transmitted through the sensor and the steady calibration is not valid.

In practice, the implementation of such measurements needs a device capable of simultaneous measurements of heat flux and mean temperature of the measuring surface. These needs are met by using a new heat flux meter designed in our laboratory and described in the literature(2). This is basically a thin electroplated thermopile in the form of a printed circuit (thickness 0.1 mm, transverse dimension 25 cm x 25 cm) which can be used to measure at the same time, the heat flowing through the measuring section and the average temperature variation of that surface. The transverse dimensions, which may be increased up to 50 x 50 cm by using a guard ring of the same material, are sufficient to ensure one-dimensional heat transfer inside the wall under unsteady-state conditions. It was shown that such a bimetallic printed circuit can be used for simultaneous measurements of heat flow and surface temperature. On the electrical output side of the sensor, we have a Thevenin, equivalent consisting of an open circuit voltage proportional to the heat flow to be measured :

$$V = K\Phi \qquad \text{where} \qquad K = 70\ \mu V/W.m^2 \tag{10}$$

for a transducer of transverse dimensions 25 x 25 cm, in series with a metallic resistance whose value is controlled by the average temperature of the bimetallic printed circuit :

$$R = R_0(1 + \alpha\bar{\Theta}) \tag{11}$$

with $\alpha = 4.10^{-3}/°C$ and $R_0 = 200\ \Omega$

For the simultaneous measurement of the average temperature and heat flow, a Wheatstone bridge driven by an a.c. carrier was included[2] to the sensor output in order to convert the variation of electrical resistance (proportional to the temperature change to be measured) into a proportional electric voltage.

Another way to perform simultaneous measurements of heat flows and temperature changes is to include a thermocouple in the measuring cross section.

The experimental configuration comprised a low level multiplexer and a programmable digital voltmeter driven by a microcomputer. The desk calculator is used for data collection and time averaged computation.

EXPERIMENTAL DATA

As an application let us determine the thermal effusivity from the heat flux and surface temperature measurements. The theory given above gives the heat flow fluctuations at the surface in terms of those of temperature at the surface. In the mathematical problem, the semi-infinite solid is initially assumed to be at zero temperature and the end $x = 0$ is kept at a definite temperature change. That assumption holds only for quick unsteady-state fluctuations of the surface temperature having a sufficiently high frequency content to validate the semi-infinite model with zero initial conditions. That hypothesis is independent of the transducer colors, and the measurement with the "black" and "white" transducers will give the same relations between the correlation functions, as will the difference between the measurement with the "black" and "white" sensors. As an example, let us first show how to handle the dependent quantities Θ_d Φ_d in order to determine the thermal effusivity from the high frequency behavior.

High frequency domain analysis

Given thermal signals over the sampling time (A-B) shown in Fig. 3a (representing $\Theta(t)$ or $\Theta(t)$) from a stationnary random signal, a smooth signal may be estimated as follows :

$$\overline{\Theta_d(t)} = \frac{1}{T}\int_{t-\frac{T}{2}}^{t+\frac{T}{2}} \Theta_d(t)\, dt$$

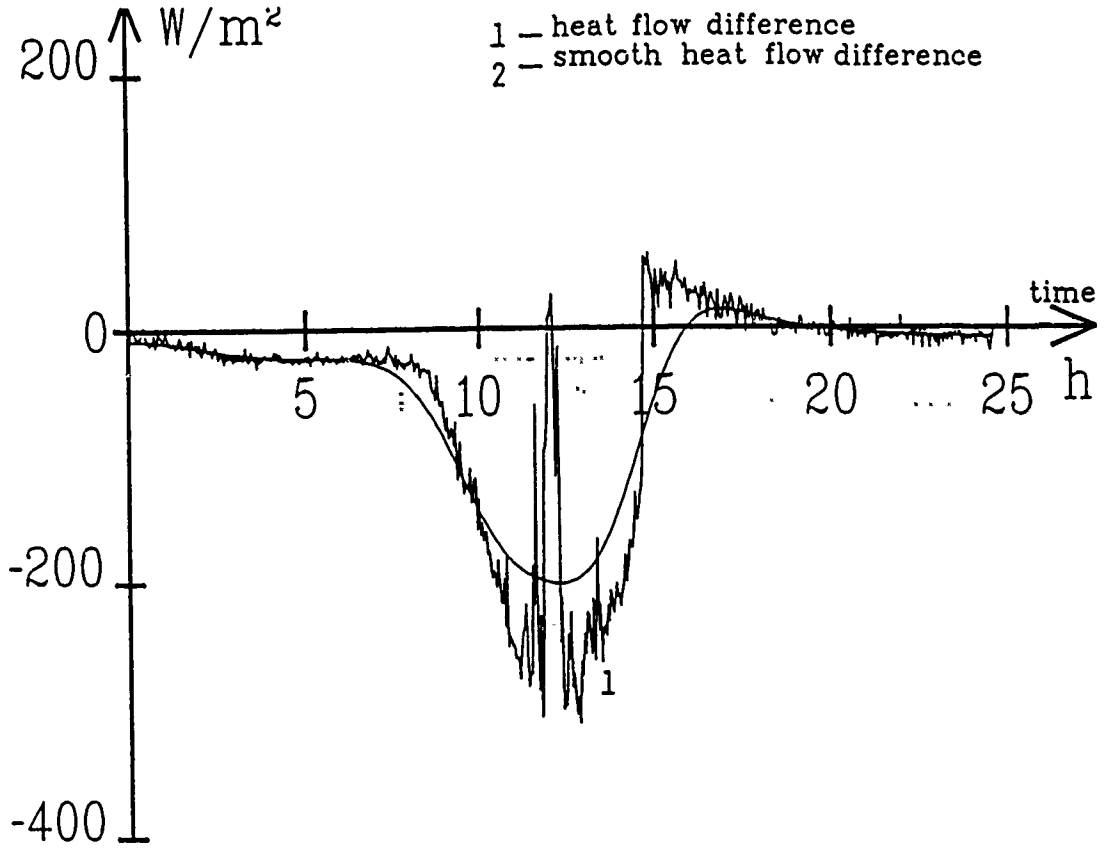

Figure 4b : Experimental heat flow difference and smooth heat flow difference.

On the other hand, the high frequency contents of the thermal signals (Fig. 5a and 5b) are obtained from the differences between ϕ" the actual heat flow and surface temperature variations θ" and their smoothed versions.

The autocorrelation function $R_{\theta"\theta"}(\tau)$ of the high frequency variations of the difference between the surface temperatures is shown in Fig. 6. The analytic curve obtained by convolving $R_{\theta"\theta"}(\tau)$ with the weighting function $b/\sqrt{\pi t}$ is shown in Fig. 6b together with the curve obtained by cross-correlating the heat flux difference $\Phi_d(t)$ and the surface temperature difference $\Theta_d(t)$. A good agreement was obtained over the sampling time for the value b = 2000.

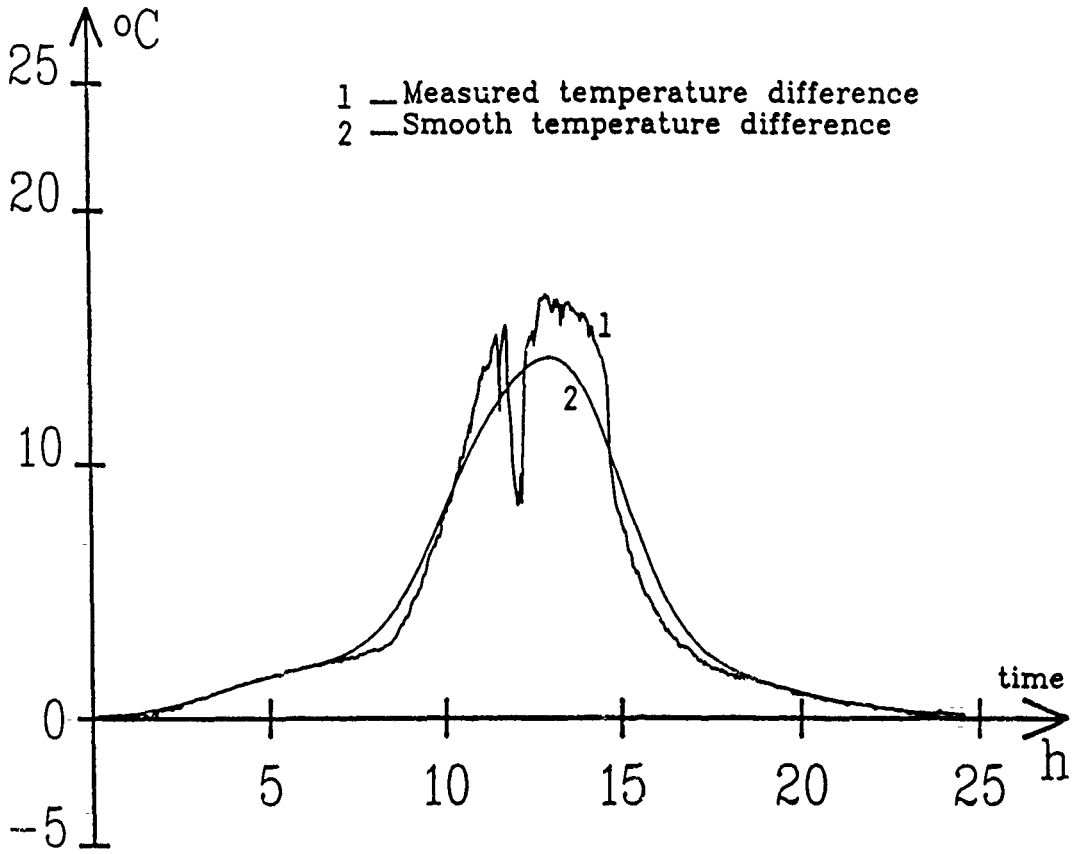

Figure 4a : Experimental temperature difference and heat smooth temperature difference.

The smoth values of $\overline{\Theta_d(t)}$ and $\overline{\Theta_d(t)}$ are estimated by simply averaging the instantaneous value of the signal over an appropriate value for the integration time T and are shown in Figure 4a and 4b.

Figures 4a and 4b are plots showing the effect of a Blackman window (Fig. 4c) low pass filter with a specified cutoff frequency defined in the following part.

The low pass filtering yields a smooth version of the underlying low frequency wave.

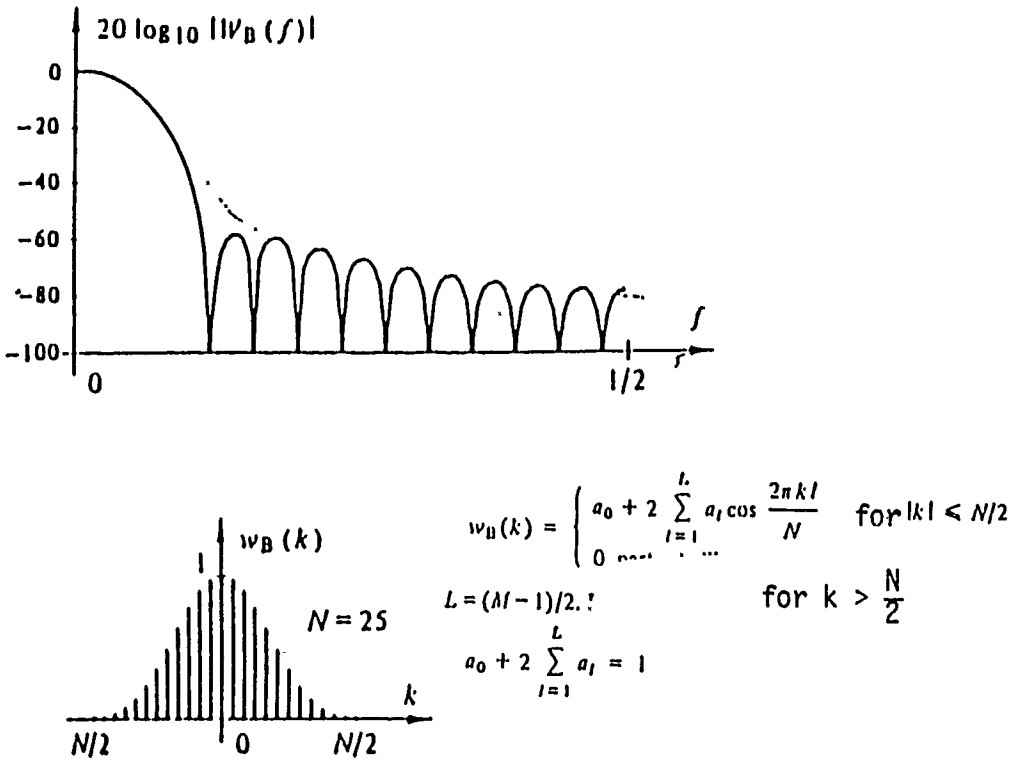

Figure 4c : Blackman window.

Moreover, by taking the numerical Fourier transform of the data, it was observed that the modulus of the cross-spectral power density $|\hat{\Phi}(\omega)_{\hat{\Theta}X}|$ was equal to the quantity $b\sqrt{\omega_{\hat{\Theta}\hat{\Theta}}\omega_{XX}}$ for the special value b = 2000 (Fig. 7).

A good agreement was then obtained over the sampling time for the value b = 2000 in either the time or the frequency domain.

As a result, on account of the good fitting between the experimental and simulated data (Fig. 8), the basic hypothesis of a semi-infinite medium with zero initial temperature may be considered as being satisfied in the high frequency domain.

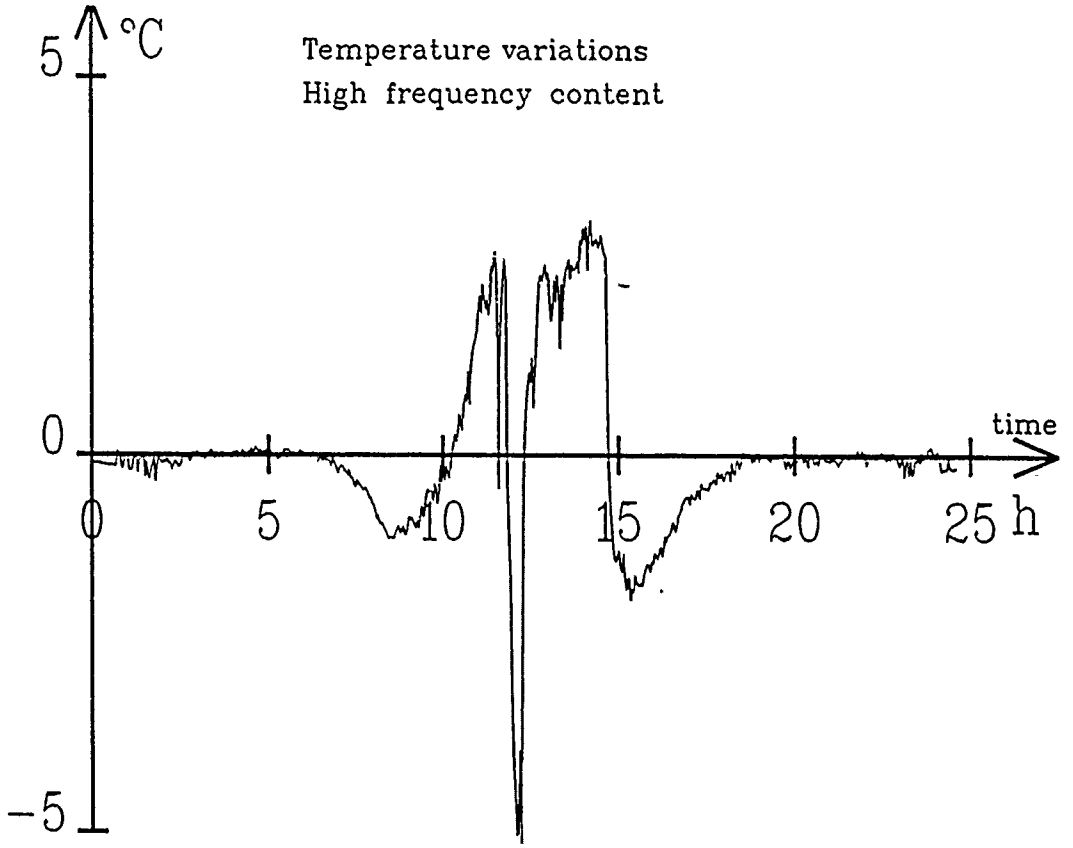

Figure 5a : High frequency content of the temperature difference.

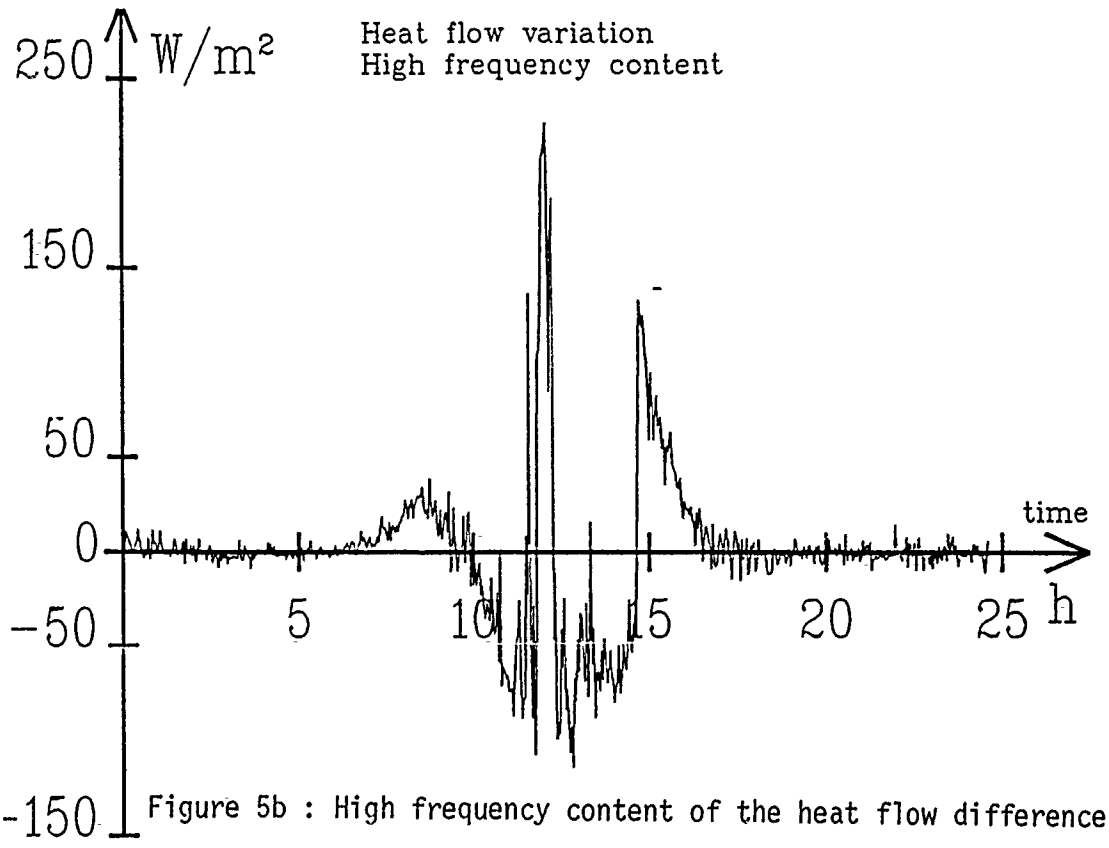

Figure 5b : High frequency content of the heat flow difference.

Under such circumstances, there is interest in taking the solution of the heat equation in the form of a wave train travelling in the direction of x positive. That is, if we define the temperature condition at the origin x = 0 (i.e., at a wall surface) from the frequency content $\Theta(0, \omega)$

$$\Theta(0,t) = \frac{1}{2\pi} \int_{-\infty}^{+\infty} \Theta(0,\omega) \cos \omega t \, d\omega$$

The corresponding solution representing the temperature and heat flow throughout the positive half of the medium at any time is given by :

$$\Theta(x,t) = \frac{1}{2\pi} \int_{-\infty}^{+\infty} \Theta(0, \omega) \, e^{-x \sqrt{\frac{\omega}{2a}}} \cos\left|\omega t - x \sqrt{\frac{\omega}{2a}}\right| d\omega$$

where a represents the diffusivity.

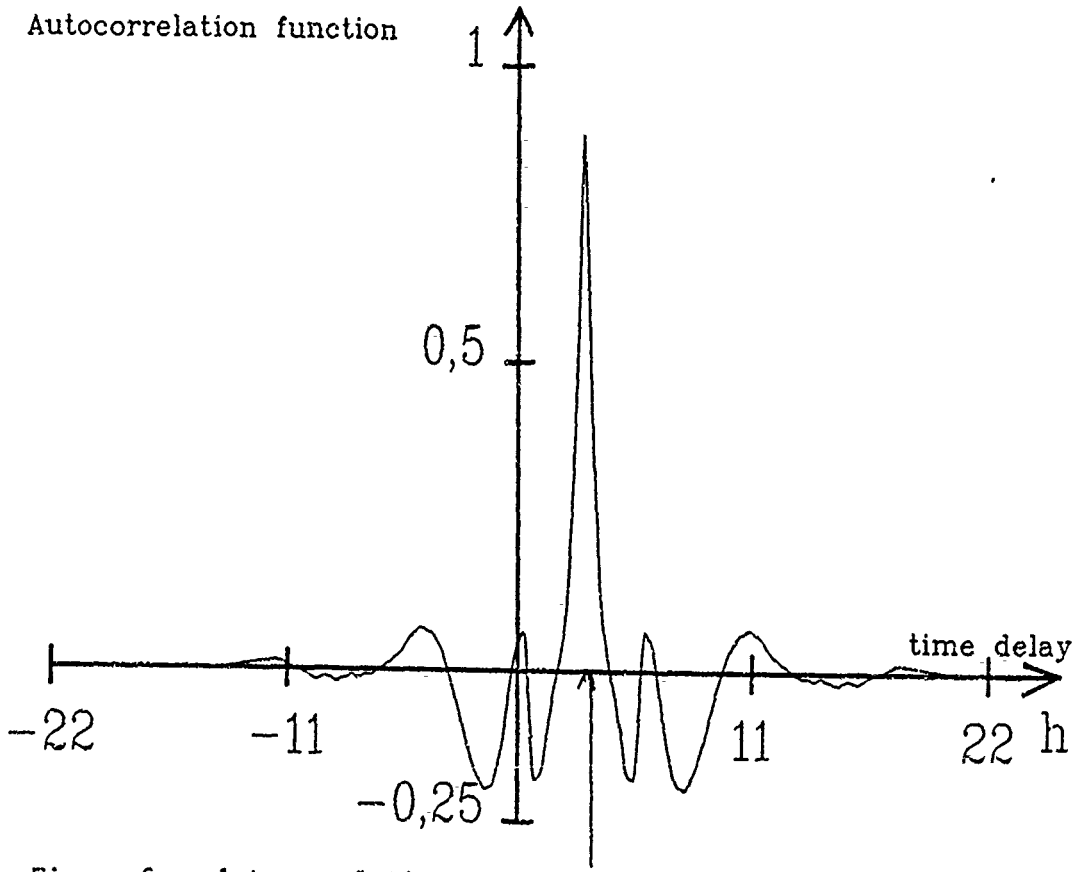

Figure 6a : Autocorrelation function of the high frequency content of the temperature difference.

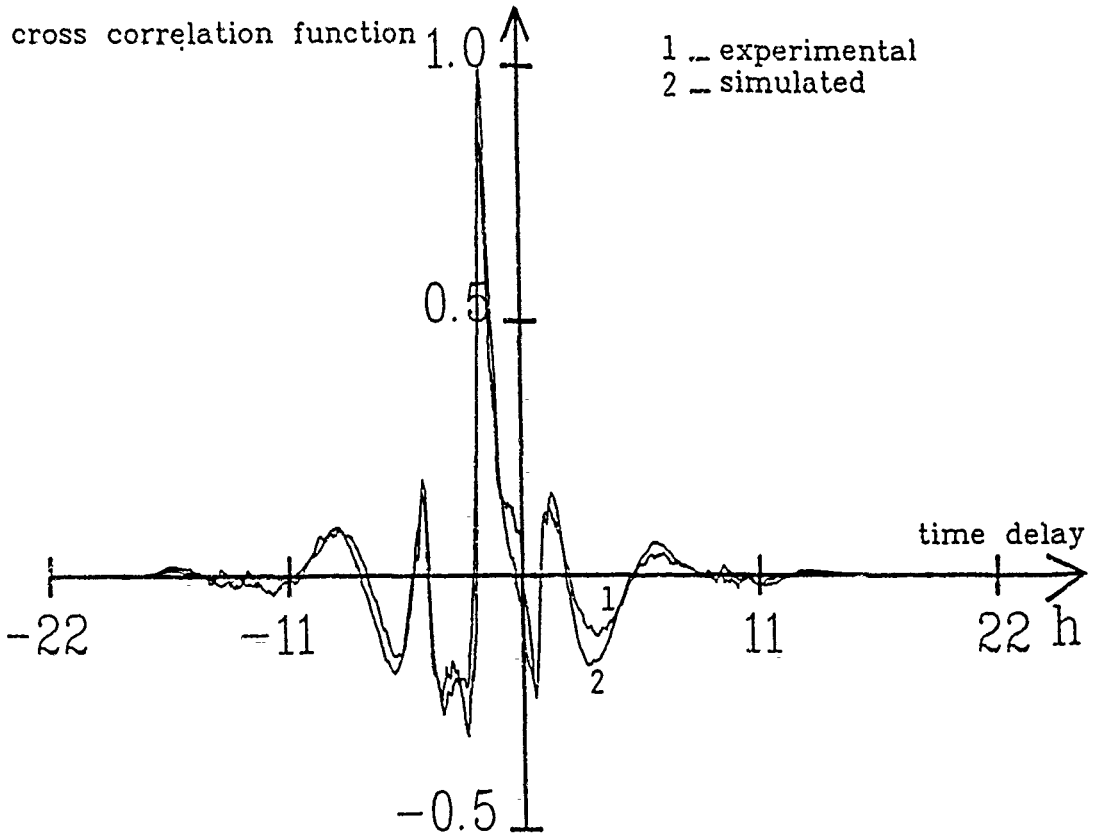

Figure 6b : Cross-correlation function (experimental) and convolution product simulated.

From this we obtain :

$$\phi(x\ t) = -\lambda \frac{\partial \Theta}{\partial x} = \frac{\sqrt{\lambda \rho c}}{2\Pi} \int_{-\infty}^{+\infty} \Theta(0,\omega)\ e^{-x \sqrt{\frac{\omega}{2a}}} \cos\left|\omega t - x \sqrt{\frac{\omega}{2a}} + \frac{\pi}{4}\right| d\omega$$

From that solution of the temperature and heat flow produced in the medium by the generation of a temperature variation $\Theta(0,t)$ at the origin, it clearly appears that the heat waves produced by the high frequency content of the temperature change at the surface will die away before they reach the back face of the wall and the heat transferred to the wall oscillates near the surface.

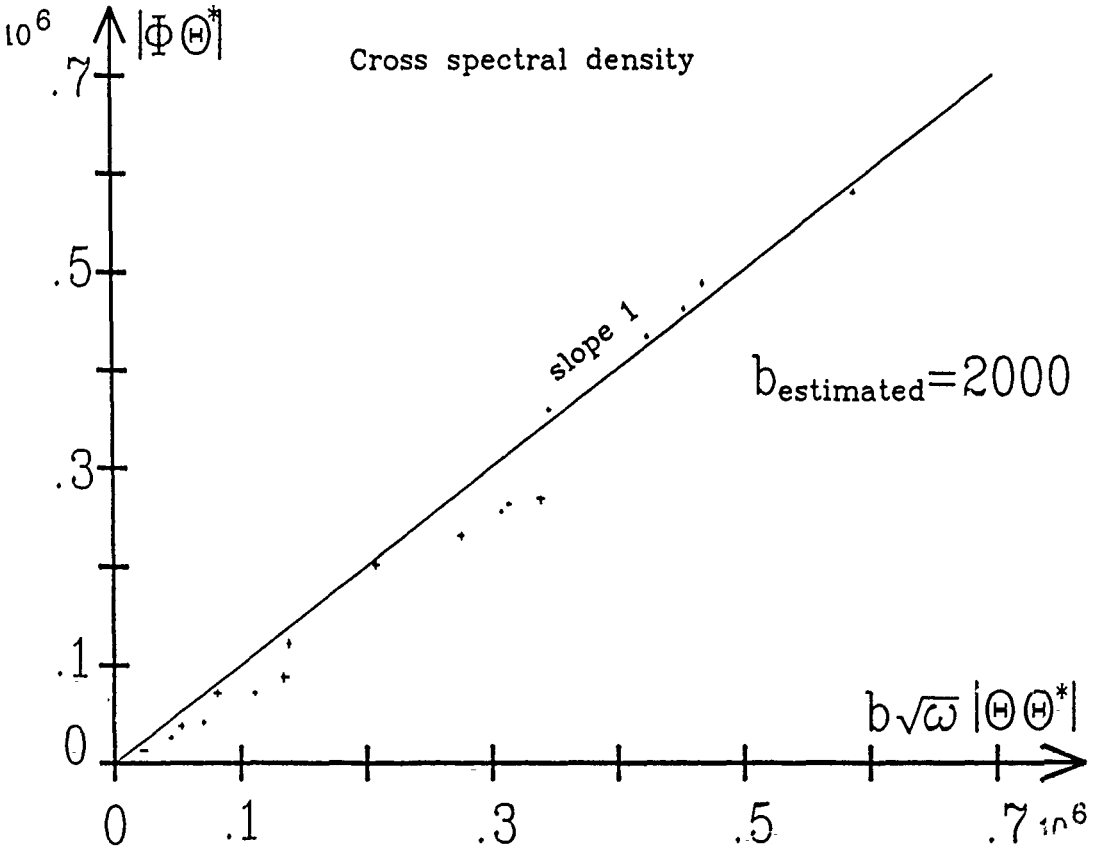

Figure 7 : Determination of the thermal effusivity from the power spectral densities.

The amplitude of the temperature and heat flow oscillations diminish as exp -x Φ $\sqrt{\omega/2a}$ and thus fall off more rapidly for large ω. The higher harmonics disappear most rapidly as we move into the wall. At the back face of the wall the amplitudes of the waves are reduced by the factor exp -L $\sqrt{\omega/2a}$ so that the high frequency waves are very strongly attenuated. This implies that the train wave solution for the semi-infinite solid can in fact be used for a wall whose thickness is one or two wavelengths given by :

$$\lambda = \frac{2\Pi}{\sqrt{\omega/2a}} < L$$

From that result, when using a digital filtering of the data, there is an interest in specifying the cutoff frequency of the Blackman window to be :

$$f_c > \frac{2a}{L^2}$$

Analysis of smooth data

As mentioned the previous theory shows that each partial wave is propagated with an unaltered period inwards and that the amplitudes of the shorter periods diminish more rapidly a those of greater so that the space variation takes a simpler form, consisting of low frequency waves which persist to the back face of the wall. It is then of fundamental importance to determine what arrives at a boundary at which radiation takes place or at which there is a change in the wall properties. At the boundary separating two different media in contact, the positive wave train on arrival at the boundary gives rise to a transmitted wave train and a reflected wave train in a manner exactly analogous to the transmission and reflection of a plane wave in the corresponding optical problem. Reflected wave trains are necessary to fulfill the conditions at the boundary of separation on the back face and may violate in turn the conditions to be fulfilled at the origin (that is at the wall surface). In that case additional wave trains must be introduced in order to fulfill the required conditions at the wall surface. In the most general case, the thermal admittance measured on a wall will depend on the reflected wave trains at both faces of the wall. Moreover, the basic hypothesis of a semi-infinite solid initially at zero temperature is not always fulfilled. Another practical problem is that of the initial conditions which are supposed zero.

The only interest in using the differential quantities $\Theta_d(t)$ and $\Phi_d(t)$ (instead of Θ_b, Φ_b) is to start with dependent quantities having clearly defined beginnings and ends, that is, well-specified initial conditions, since Θ_d and Φ_d are both zero during the night.

The analytic heat flow difference obtained by convolving the smooth temperature difference $\overline{\Theta}_d(t)$ with the weighting function $1/\sqrt{\Pi t}$ is shown in Fig. 9 for b = 2000. A good agreement is obtained between those simulated, and the experimental cross-correlation function is found in the first part of the sampling time when the hypothesis of a semi-infinite medium is satisfied.

For small values of time the heat equation solution with zero initial condition may be regarded as a wave train traveling onward without interruption. That hypothesis was valided by experiments on heat pulse transmission through a wall(5).

An explanation of the part where the two curves differ may be the presence of reflected wave trains.

Another problem with the interpretation of the data in the low frequency range is in relation with the lateral heat transfer at the

surface caused by different mismatches or either convective heat transfer coefficients or infrared solar emissivities at the surface of the black and white sensors.

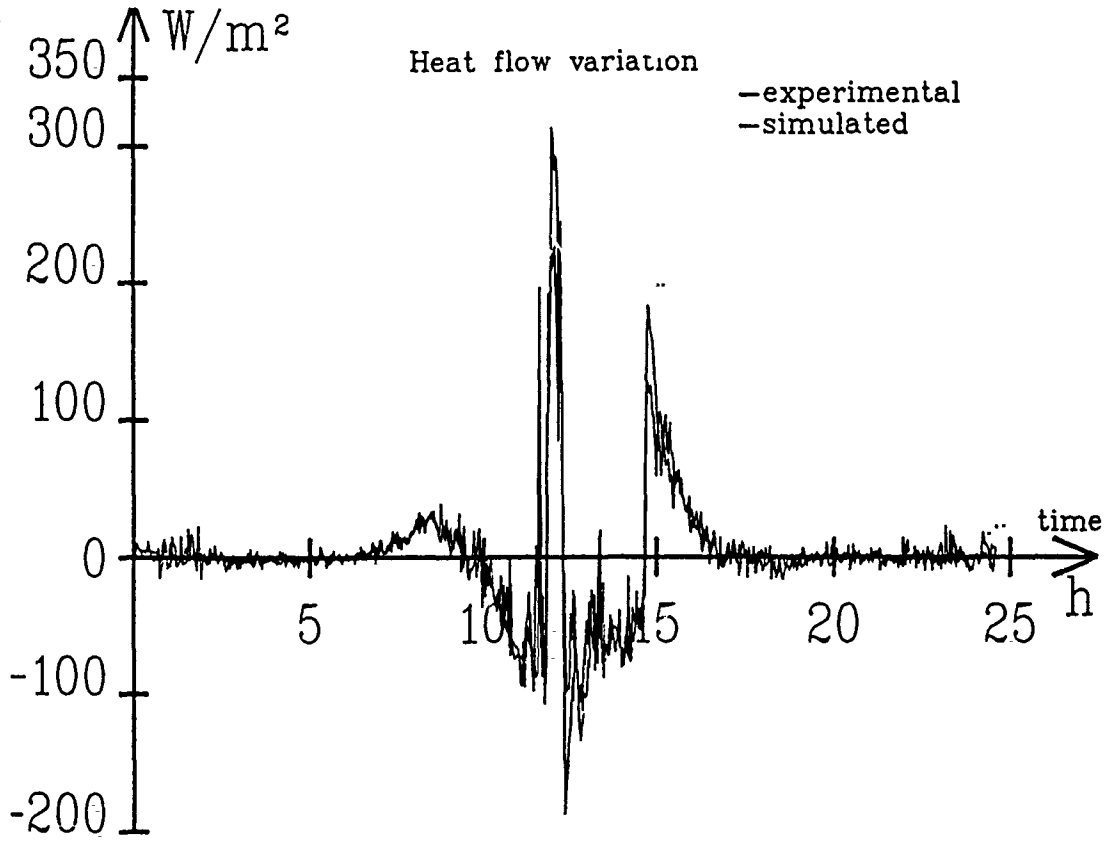

Figure 8 : Convolution of the high frequency content with the weighting function $b/\sqrt{\pi t}$.

CONCLUSION

The original objective of the paper was to show the applicability of regarding heat flux and surface temperature measurement as signals in order to determine the thermal admittance from a frequency domain analysis of the data obtained during exposure of the wall to its natural environment. The solar insolation appears as a transient random process acting as an input on the wall surface to give strong fluctuations of the temperature and heat flow data. From the previous analysis only the high frequency results can be explained from the hypothesis of purely one-dimensional heat transfer in a semi-infinite medium, and are sufficient for determining the thermal effusivity of the first layer of the

wall. The applicability of the low frequency results could be to estimate the thickness of that first layer of the wall from the in-situ measurement of the thermal admittance.

In fact, transverse heat transfer is also expected to occur when using sensors covered with adhesives of low emissivity. Another way to obtain information about transient lateral heat transfer would be to analyze in the low frequency range the variation in thermal admittance obtained from (Θ_d, Φ_d) ; (Θ_b, Φ_b) ; (Θ_w, Φ_w) measurements.

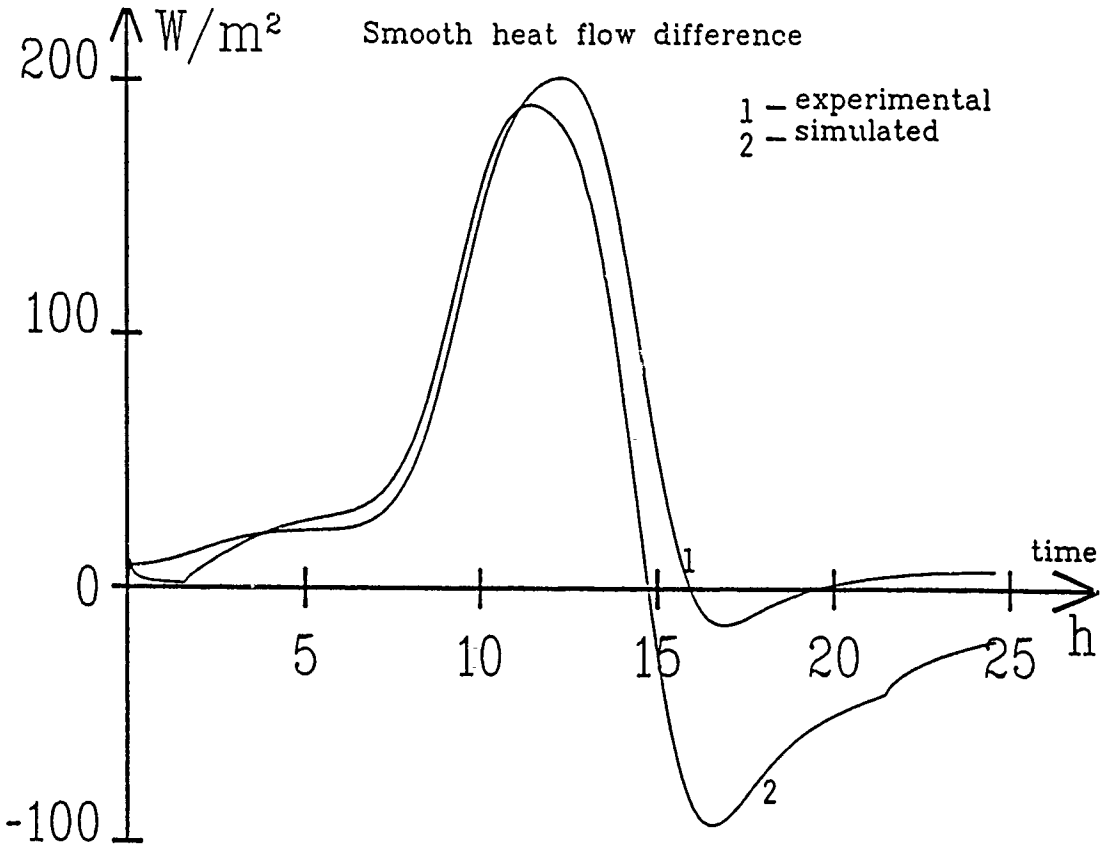

Figure 9 : Convolution of the smooth temperature difference with the same weighting function.

REFERENCES

1. E.B., M.B., G.E. (1983)
Building applications of heat flux transducers. ASTM STP 885

2. D.L. and P.T. (1983)
Apparatus for simultaneous temperature and heat flow measurement undertransient conditions.
Rev. Scient. Instrum. 54, 374-380

3. B.D., L.O. and P.T. (1986)
"Application des méthodes de la théorie du signal à l'analyse des échanges thermiques in situ"
Entropie, 125-130-135

4. H.S. C. and J.C. J. (1959)
Conduction of heat in solids. 2nd ed. Oxford : Clarendon press.

5. R.A. K. and P.T. (1982)
Thermal diffusivity determination by cross correlating injected and transmitted heat pulses through a wall.
J. Appl. Phys. 53, 2875-2886.

ON THE EXTENSIVE USE OF HEAT FLUX TRANSDUCERS FOR EVALUATING RESIDENTIAL BUILDING COMPONENT PERFORMANCE—CALIBRATION AND DEPLOYMENT

C. J. Kippenhan
A.F. Emery
K.H. Nicholaisen
G.B. Varey
J.L. Garbini
D.R. Heerwagen

Department of Mechanical Engineering
and the College of Architecture
and Urban Planning
University of Washington
Seattle, Washington USA

ABSTRACT

Four homes, two built to existing housing standards and two to proposed energy conserving standards, were specially built and extensively instrumented to characterize energy use. Energy flow through the envelope—ceilings, floors and walls were measured. Before installation of the 134 Heat Flux Transducers (HFTs) employed, laboratory tests were conducted, to develop mounting procedures suitable for testing periods of several years' duration, and to verify the manufacturer's calibrations of these devices. Quasistatic U-values were computed from *in situ* measurements of heat flux and temperatures in the four houses, two of which were occupied and two which were unoccupied. In addition, measurements were made on a wide range of ceiling, floor and wall sections, comprising the envelope of a full size test cell located centrally at the same site. Quasistatic U-values computed from these measurements were then compared to steady-state U-values found in Handbook listings.

INTRODUCTION

The study of heat flux transducer (HFT) use described here found its origins in research mandated by the Washington State Legislature. The Northwest Regional Power Planning Council proposed a set of standards for building construction, called Model Code Standards (MCS), with the intent to conserve electrical energy in residential buildings. These studies at the University of Washington, Departments of Architecture and Mechanical Engineering, were aimed at collecting and interpreting detailed data on the performance of building envelope components. In addition to measurements of heat transfer through the envelope, the energy use by appliances, heaters, lights and water was measured, as were the quantities of infiltration and ventilation air. The latter was important, not only because it represented a sizeable fraction of loss but also because special infiltration control measures had been incorporated into MCS.

Four full-sized dwellings were constructed, one pair according to the MCS, the other pair to standards in effect prior to 1980. The quality of construction is detailed in Table 1. One MCS and one pre-1980 has been occupied during the academic years 1986-1987 and 1987-1988. An identical pair was left unoccupied, but with all appliances in place. Since September 1988 all four houses have been occupied. The occupants have been an ongoing series of families of graduate students matched in terms of ages of children.

The instrumentation of interest consisted of heat flux transducers applied to the inside surface of each ceiling and external wall surface in each of the nine rooms. In the unoccupied houses HFT were also applied to the floor. Details of attachment will be discussed later. Each HFT was complemented with four temperature sensors, mounted in close proximity to each HFT, to measure the temperature of the inside air, inside surface, outside surface and outside air. The outputs from these devices were taken every 30

Table 1. Summary of Test House Construction Details

	House Characteristics	
	Pre 1980 Houses (II and IV)	MCS Houses (I and III)
Ceiling insulation	R-19	R-38
Wall insulation	R-11	R-19
Floor insulation	R-11	R-19
Windows	Single glazed	Triple glazed
Doors	Solid core wood	Insulated steel
Infiltration control	Kraft-backed wall vapor barrier	Continuous vapor barrier/insulation
Mechanical ventilation	(Heat recovery ventilator present but for experimental purposes only*)	HRV operational

*An HRV system is included in all houses to provide mixing of air required for the infiltration measurements but does not introduce outdoor air.

seconds, averaged over a 15-minute period, and stored in the memory of one of two data acquisition systems (DAS).

A test cell, located in the center of the housing group, served the dual purpose of housing the DAS, the Constant Concentration Tracer Gas system for measuring air rates; and providing a variety of envelope sections each with different insulation levels. Each of these ceiling, floor, and wall sections was instrumented similarly to those of the house envelopes. The multitude of other data recorded, such as weather, power to all devices, thermostat setting, etc., is not of particular interest here and hence will not be detailed.

In summary, we note that data from 134 HFTs and approximately 500 temperature sensors have been recorded over a two-and-one-half year period. Some results of this very large amount of data will be discussed later. We will first describe experiments aimed at developing mounting techniques for the HFT. Figure 1 shows the thermal circuit for an envelope component. In addition to the resistances of the several layers and the inside and outside convection/radiation, the capacitances for thermal storage are shown. Mounting an HFT introduces two additional resistances (the resistance of the bonding agent and that of the transducer — R_c and R_m) and modifies the convective film coefficient. For heavily insulated walls (i.e., R22) these

effects are small. Thus the flux of heat transferred through the wall can be determined from the measured output and the manufacturer's calibration constant (MCC). If the wall is thermally lightweight such that the additional resistances or changing the convection coefficient alters the overall wall resistance, then the flux passing through the transducer will not be an accurate measure of the flux passing through the unmetered sections of the wall. In transducers mounted where local air temperatures or velocities vary continuously, our preliminary experiments showed relatively high frequency variations in heat flux (on the order of 20 seconds). For typical building walls, the presence of large thermal capacitances at the wall surface results in most of the heat flowing to only a limited depth in the wall; that is, the circuit is effectively grounded at point G. Thus the wall appears to have a much smaller resistance than the steady-state value, and attachment of the transducer significantly affects heat transfer. To estimate heat

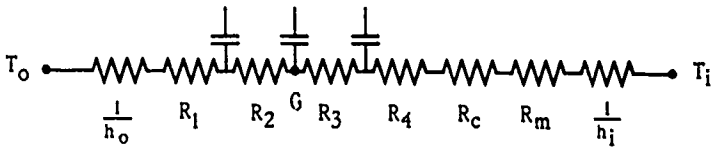

Figure 1. Envelope Thermal Circuit

transfer through a standard wall, a correction must be applied to the measured heat flux. The effect is the same as using a modified calibration coefficient. We term this modified coefficient the effective calibration constant (ECC), and the first part of the paper describes a series of experiments to estimate its value in comparison to the MCC.

MOUNTING AND CALIBRATION TESTS IN THE LABORATORY:

For these calibration experiments the HFTs were mounted on a vertical 4-ft-square panel as shown in Figure 2. A 1-m-square area, centered on the

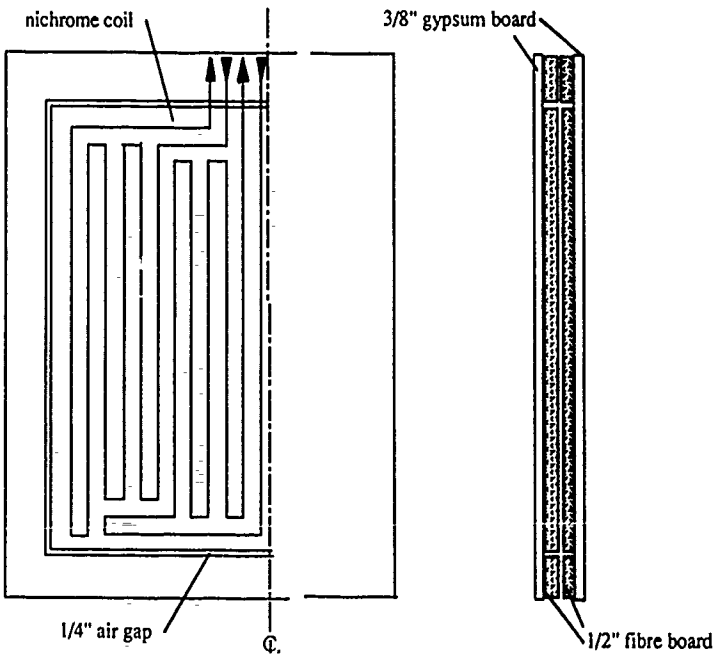

Figure 2. Heated Test Panel

panel, was heated by electrical current dissipated in a nichrome wire array, laid out to generate uniform flux. The wire array was mounted on a 1/2-inch-thick fiberboard and was covered with a like fiberboard. This assembly was sandwiched between a pair of 3/8-inch gypsum boards. To minimize edge losses an insulating 1/4-inch air gap separated the heated square from the surrounding 4-inch-wide unheated fiberboard. Thus two 1-m-square surfaces transferring a uniform heat flux to the room air and surroundings were available for HFT mounting, one on each side of the panel. These surfaces replicated those in the houses where flux measurements were to be made.

The laboratory in which these tests were conducted is a large subterranean room where the radiant environment is essentially independent of time and date. The panel assembly was positioned so that symmetry of the heated boundary layer flowing over the panel could be determined by shadowgraph viewing of the convection patterns.

A uniform flux of approximately 6-7 W/sqm (1.9-2 Btu/sqft-hr) was dissipated. The AC supply voltage was transduced to a small DC signal for power measurement. This and the channels for output voltages of the HFTs was sampled every 20 seconds by a DAS and recorded on tape. The final reduction of the data was then accomplished with a PC where the files read from the tape were averaged and merged with the appropriate conversion factors to yield a time series of ECCs. These were expressed in units of Btu/sqft-hr-mV — thus they are reciprocal sensitivities. After several trials were made to determine the appropriate averaging interval, the period of 30 minutes was selected. This choice faithfully retained the trend of the scattered individual points.

Mounting procedures using several contact or matching agents between the HFT and the surface as well as agents to clamp or maintain contact were studied. The final selection of 4-inch-square meters had an unpainted matte light brown surface that was judged to match the radiative properties of the envelope surfaces under test. In order to evaluate the random errors a 3 x 3 Latin square experimental design orthogonalizing three levels (high medium and low) of MCC with position on the panel (row and column) was used. However, for greatest efficiency of experimental design, groups of three DAS channels were also orthogonalized to isolate the order of reading (the sum of squares attributed to this, if found nonsignificant, could then be pooled into that for random error in the analysis of variance (ANOVA) of the resulting Graeco-Latin square used to interpret the results).

A series of experiments using matching agents between the HFTs and the surface, such as gel toothpaste, commercial heat sink paste and clamping with masking tape, exhibited excessive random error. In anticipation of a very long duration of testing in the houses, invariance of the calibration constant with time was also of importance. This will be discussed in a later section.

This led to development of mountings using carpet tape, a double-sided tape developed to hold indoor/outdoor carpet in place. Strips of approximately 1-3/4-inch-wide tape were cut to length, carefully butted and burnished on the surface to form a patch of same size as a HFT. The tape protective layer was removed, the HFT applied and burnished to form a tight bond. The results of a typical Graeco-Latin square design are shown in Table 2. The MCC now is clearly the dominant effect. The position and channel effects can be lumped as a measure of random error, and an f test

Table 2. Graeco-Latin Square and Analysis of Variance HFT Mounted with Carpet Tape on Test Panel

Manufacturer's Calibration Constant			HFT Layout		
8.19	6.56	5.36	11	12	13
6.67	5.38	8.32	21	22	23
5.44	8.36	6.86	31	32	33
Effective Calibration Constant			Orthogonalization		
9.12	7.44	5.64	a1	b3	c2
8.36	6.14	8.97	b2	c1	a3
6.12	9.19	7.61	c3	a2	b1

Analysis of Variance	Sum of Squares	Degrees of Freedom	Mean Square
Mean	7.655		
Rows	0.275	2.000	0.137
Columns	0.320	2.000	0.160
Channel	0.073	2.000	0.037
Calibration	14.796	2.000	7.398
Total	15.464	8.000	
Error	0.668	6.000	0.111
Variation/Mean*Mean	0.002		
Deviation/Mean	0.044		

confirms that the ECC strongly correlates with the MCC. The series of these experiments has also resulted in a measure of the increase in calibration constant (decrease in sensitivity) of approximately 13 % due to mounting. The high degree of correlation of the ECCs with the MCCs gives us confidence in the validity of the manufacturer's calibration procedure. Moreover, the pooling provides a good estimate of the random error (5% of mean).

Installations on ceiling surfaces, where the adhesive bond is in tension, cannot satisfactorily be made using a pressure sensitive medium such as carpet tape. Here a casein base carpenter's glue, applied to a paper towel sandwiched between the HFT and surface, and clamped in place during setting proved adequate. (The towel when soaked with water allows later removal without destroying the HFT.) The increases in calibration constant and error statistics are essentially the same as those for carpet tape.

MODIFICATION OF HEAT FLOW DUE TO TRANSDUCER PRESENCE:

As stated earlier, mounting an HFT on a surface alters the length and direction of the heat conduction path, and may change the convection and radiation transfer to the surroundings. For brevity, studies of these influences were named edge effects. Figure 3 shows the increase of the calibration constant in percent of the MCC for each of the nine HFTs mounted in a 3 x 3 array. The results are shown for four tests in which the horizontal and vertical spacing was altered. For two successive periods the spacing was between 2-2.5 inches, then was reduced to zero, and then increased to 1.5 inches. The zero spacing case is essentially a composite 12-inch-square HFT. Except for two sensors (HFTs 12 and 21) the differences between the four cases fall within the bounds for random error. Note that even for the very center HFT (22) there is no appreciable difference in the measured

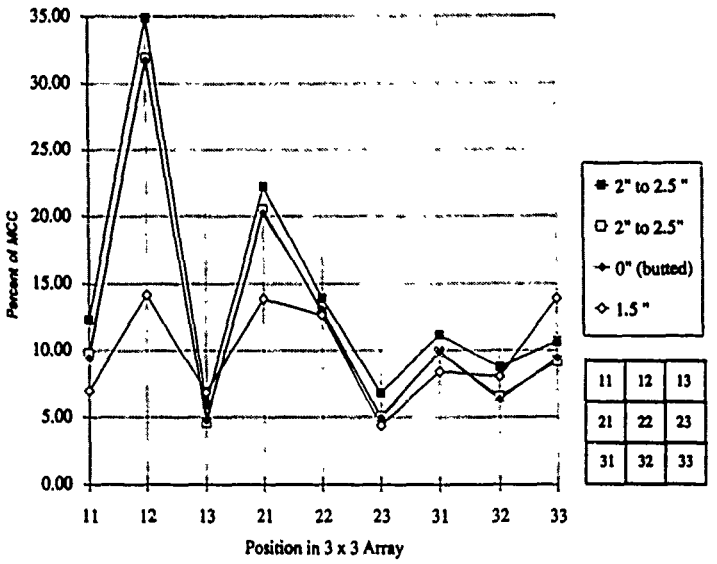

Figure 3. Effect of Spacing (Edge Effect) between HFT in 3 x 3 Array ECC Increae in Percent of MCC

calibration constant. The slightly lower values for the 1.5-inch spacing (excluding HFTs 12 and 21) is quite likely due to greater skill in mounting expected with progress along the learning curve. The effect that must be attributed to removal and reinstallation of the sensors necessarily confounds the effects due to spacing. This does not, however, negate the conclusion that modification of heat flow due to edge effects is small.

CONVECTION EFFECTS:

From examination of the raw data showing the HFT outputs every thirty seconds, it was clear that the heat transfer of the test surface to the environment, through the combined convective and radiative mechanisms undergoes large temporal swings. While averaging over sufficiently long time periods dampens out these fluctuations, still preserving the general trend, the need for a more detailed study seemed obvious. A number of investigators have written on this subject. [1,2] Two studies were instituted to examine the effect, one employing forced convection produced by a large fan, the other a perturbation of natural convection by moving occupants. The low resistance of the test panel layers makes effect of convective changes and mounting on ECC significant, as is the case in the house envelope where the high layer resistance is shorted by the storage capacitances.

In the first of these studies a large laboratory fan was positioned so as to direct a stream of air obliquely downwards and parallel to the test panel surface. The data for three Latin squares, representing the same HFTs before, during and after blowing were studied. Air velocities on the order of 1000 fpm were obtained. Figure 4 shows the change of ECC in percent of MCC for each of the nine HFT in the Latin square. An increase between two to ten percent is seen for the forced convection case.

This prompted the second study of convection effects, which was aimed at assessing the influence occupants have on changing the natural

convection patterns in a room or space. This was done by choosing data for groups of three consecutive days in the middle of week for four different weeks. The data taken on the test panel in the laboratory were then partitioned into two time periods.. The periods chosen were midnight to 6:00 AM, representing the unoccupied portion, the period 09:00 AM to 5:00 PM, representing occupied as well as data for the entire 24 hours. The ECCs, again expressed as the increase in percent of MCC, were computed for each period. The results in Figure 5 are representative of the data so obtained. The

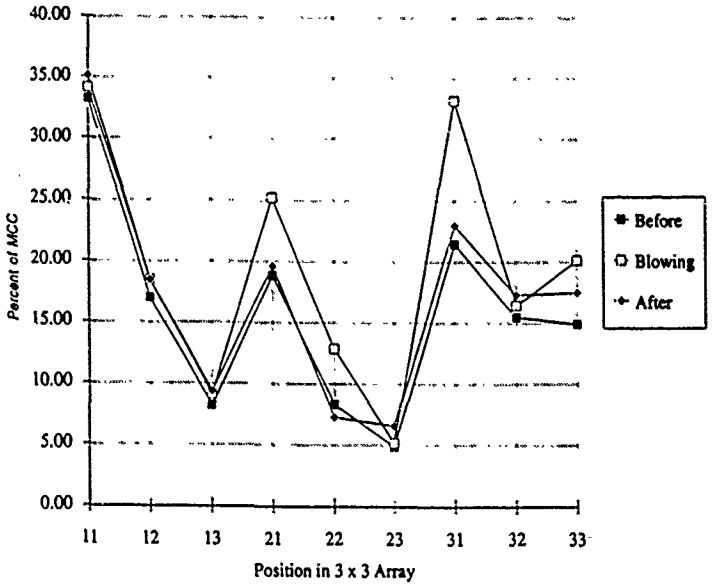

Figure 4. Effect of Forced Convection over HFT in Array
Air Flow is in 13 to 31 Direction
ECC Increase in Percent of MCC

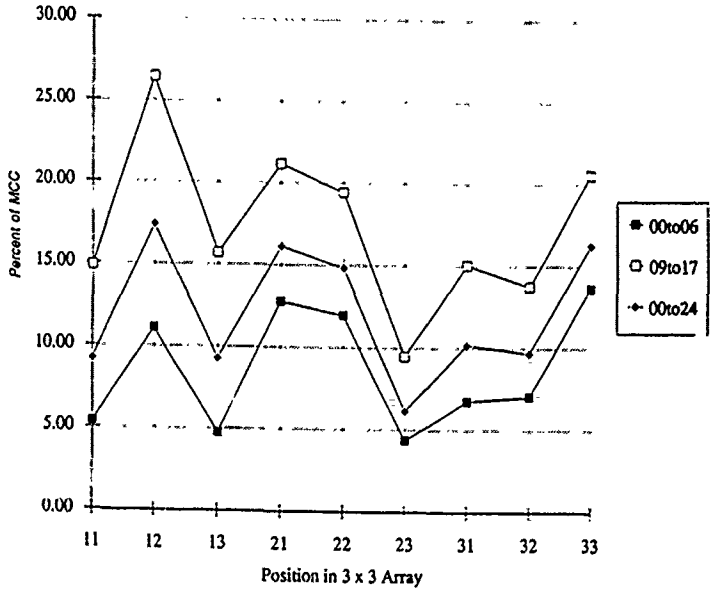

Figure 5. Effect of Occupant Induced Convection on HFT in Array
ECC Increase in Percent of MCC

quantities plotted and the arrangement are the same as in Figure 4 except that all convection changes are occupant induced. This second test was deemed reasonably representative of the environment in which HFTs were to be deployed in the occupied houses.

INVESTIGATION OF THE INFLUENCE OF AGING:

The fact that the HFTs were to be kept in service on the surfaces of the house envelopes raised the question of temporal changes. As data on the sundry mounting techniques were being gathered, reexamination of the data as a time series of daily averages of calibration coefficients was possible. The results for carpet tape are of primary interest and are shown in Figure 6. The daily average ECC for three representative HFTs is plotted every other day for the entire period, starting when they were mounted on day zero. The trend is towards a slightly smaller ECC (hence slightly increased sensitivity). This would suggest that the bond is growing slightly stronger, probably because of chemical or physical improvements.

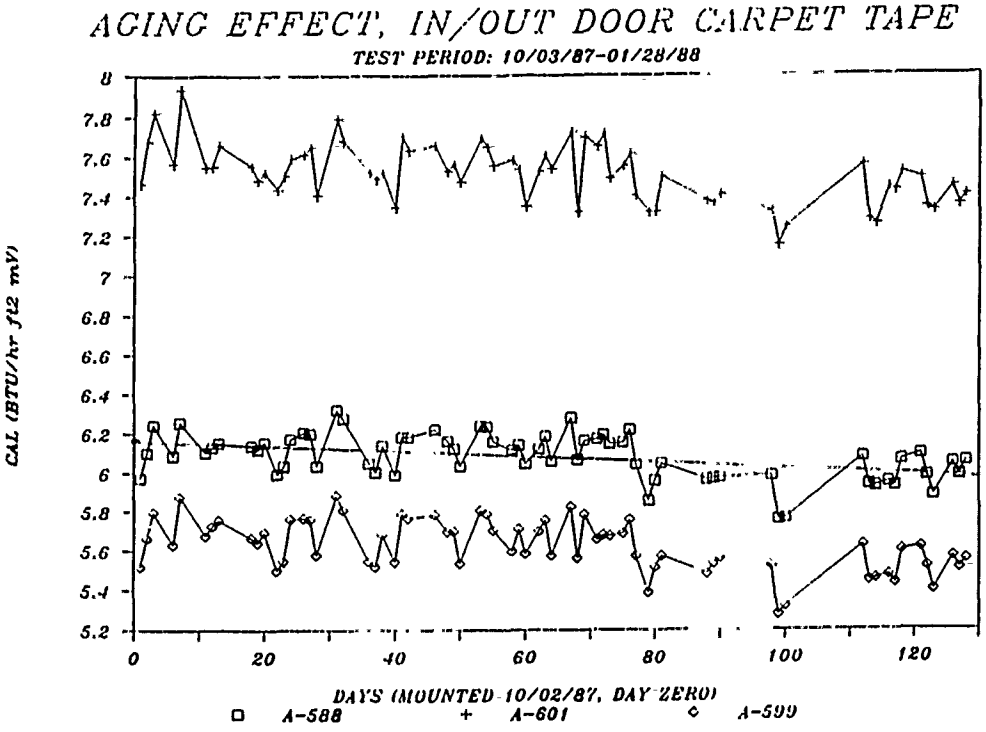

Figure 6. Measured HFT Calibration Constant vs Days since Morning

SUMMARY

This concludes the discussion of the laboratory tests on the heated panel where approximately 50 individual HFTs were grouped into 23 experimental designs. The result of the 10 designs using 20 HFTs mounted with carpet tape or carpenters glue on the laboratory test panel and subjected to normal 24 hour schedule can be summarized as follow. The ECCs, expressed in terms of heat flux divided by output voltage, are increased by somewhere between 10 and 15% over the corresponding MCCs. Because of the

excellent correlations between the ECCs and MCCs, it was concluded that determination of individual ECCs for each of the 134 HFTs was not justified. The manufacturer's calibrations would account for inherent differences. Thus, in the reduction of data from the test cell and houses for the second part of this paper, the manufacturer's calibrations have been used. An increase of the fluxes and U-values computed from the data by a factor of 1.13 may be justified. From the results of the Graeco-Latin designs (Table 2 is typical) employing the mounting procedures finally used in the test houses and cell, the random error associated with mounting effects is estimated to be 5% or less.

QUASISTATIC U-VALUES FOR HOUSE AND TEST CELL SECTIONS:

Quasistatic values for the ceiling, floor and wall sections found in the test cell construction have been computed using heat fluxes measured by these HFTs and temperature differences computed from measurements of inside and outside temperatures. The results characterize the U-values for the cavities between framing members where the HFTs were installed. All in all, there were 134 HFTs deployed for use in field measurements. Of these, 105 were installed in the (30-x45-ft) test houses and 29 in the test cell. The four houses were arranged in line, west to east as follows:

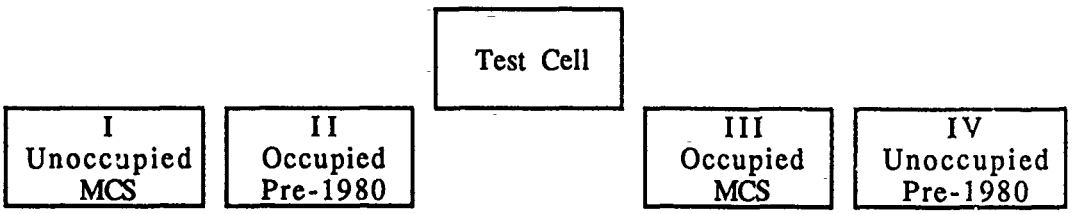

The two occupied houses (II and III) each had 20 transducers, the two unoccupied houses (I and IV) had 35 and 29, respectively. (Six highly reflective HFTs were mounted in the southeast bedroom of House I for a study of radiative transfer described in a another paper [6].) The 9 additional transducers were used for measuring floor fluxes in the unoccupied houses. Locations for the HFTs representative of the surface were selected by prior thermographic inspection. At each of the wall sensors sites 4 temperatures were measured using two-terminal integrated circuit temperature sensors (hereafter denoted as AD590s). This included inside air approximately 1-ft away from the wall, inside surface temperature attached to the wall, outside surface temperature under the bevel siding attached to the sheathing, and outside air approximately 1-ft under the eaves. The outside locations required a compromise in order to protect the AD590s from the weather. At the ceiling and floor transducer locations two temperatures were measured, inside air and inside surface. The attic air and crawl space air were measured at three locations. Air temperatures were also measured at the thermostat locations, and at four elevations on stratification strings for two rooms in each of the four houses.

Each of the AD590s was calibrated in the laboratory in a thermostatically controlled bath, in air inside a protective glass tube sealed at the immersed end. The bath temperature, as measured by a certified platinum resistance thermometer, was also continuously recorded. The individual corrections from the bath temperature were curve fitted by polynominals up to order five.

The temperature and HFT signals were read every 30 seconds, averaged over a 15-minute period and stored by a large commercial data acquisition system. The data stream was then read into a mainframe computer for processing with calibration data. The fluxes measured by the HFT and the temperature differences from the inside to the outside made possible the determination of U-values. Of principal interest here are the quasistatic values obtained by integrating both flux and temperature difference over periods of time sufficiently long to approach asymptotic values that can then be compared with steady-state U-values, tabulated in handbooks such as the ASHRAE Handbook of Fundamentals. The principles and underlying theory of such integrations have been discussed by several workers [3,4]. The quotients of successive sums of heat flux, measured by the HFT, are divided by the corresponding sums of temperature difference across the envelope section:

$$U = \Sigma\, Qi \,/\, \Sigma\, \Delta Ti \;,\; i \text{ from } 1 \text{ to end of integration period}$$

When these successive quotients are plotted against time, a curve of fluctuating U-values results, resembling a damped oscillation, which after a sufficiently long period achieves an asymptotic value—the quasistatic U-value (Figure 7). The factors that influence results so obtained include the

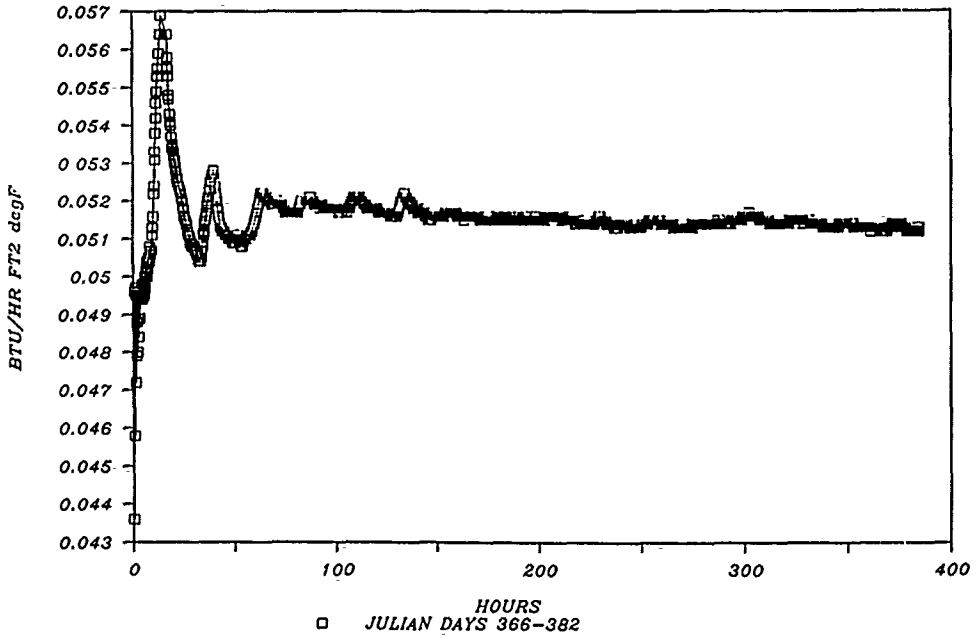

Figure 7. Quotients of Successive Heat Flux Sums over Successive Inside Air-Outside Air Temperature Differences

magnitude of the temperature difference, solar radiation if present, convection, and air leakage within the envelopes [1]. Determinations of quasistatic values were made over ten-day periods in September, January and February. For the walls, the local air-to-air temperature difference measured at the HFT site was used. Most of the walls were in north facing rooms, but a small number faced south. The rooms in the houses were grouped in two zones for infiltration measurements. For the ceiling and floors, successive quotients of area averaged fluxes for each zone were

divided by the inside air-attic air, or inside air-crawlspace air temperature difference measured nearest the zone. For the test cell the temperature differences in the denominator were formed between the inside air at the HFT to the attic air for the ceiling, to the crawlspace air for the floor, and to the average north outside air for the walls.

The temperature differences for the September period were on the order of 10°F, smaller than desired so these U-values are not reported here.

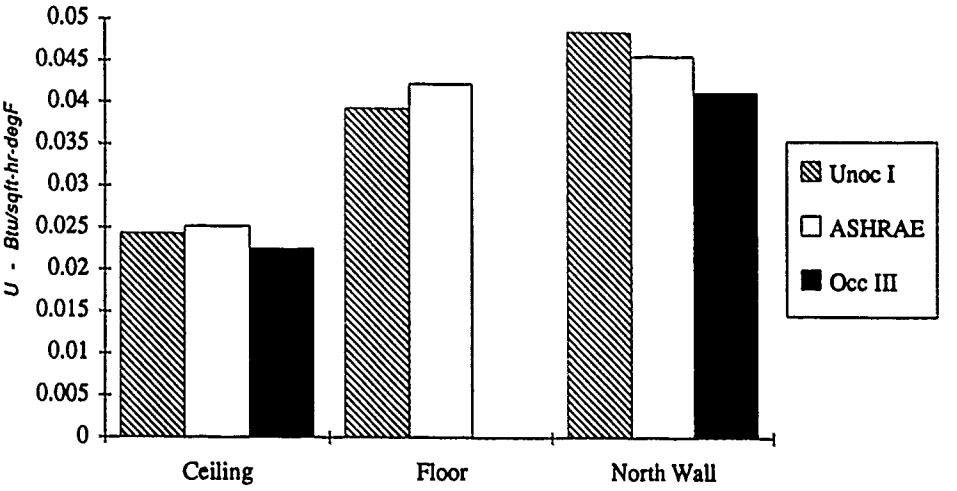

Figure 8. Measured and Handbook U-Values in MCS Test Houses Occupied and Unoccupied.

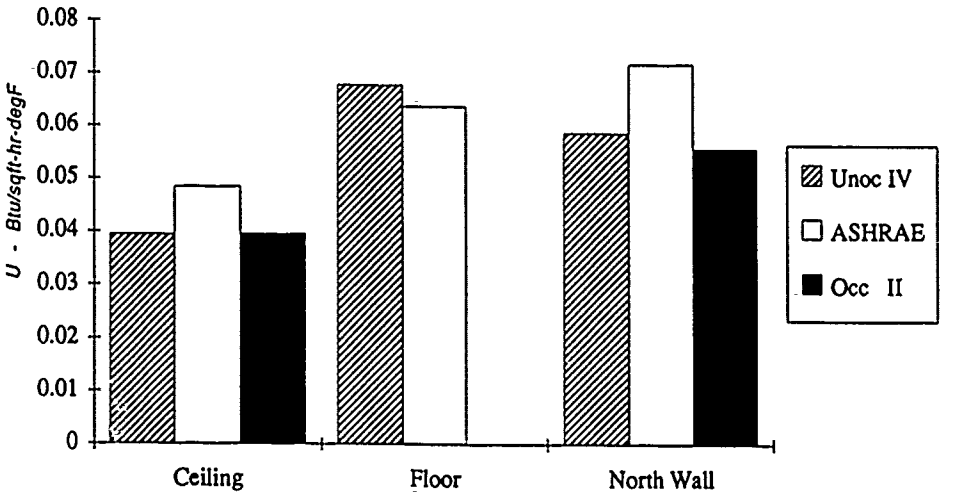

Figure 9. Measured and Handbook U-Values in Pre 1980 Test Houses Occupied and Unoccupied

Similarly measurements made on south facing walls are excluded because of the effect of insolation. The results for January-February and on the north side for houses are given in Figures. 8 and 9 for MCS and pre 1980 houses, respectively. The ordinate is in units of Btu/sqft-hr-°F and the bars compare the unoccupied, ASHRAE and occupied ceiling, floor and north walls. The agreement is quite good for the MCS houses, and not too bad for the ceiling and floor of the pre 1980. Some of the differences between the measured and

handbook values for the north facing walls, however, are greater than the combined errors of accuracy and precision for HFT attachment stated in the summary of the previous section. The results obtained on the several constructions in the test cell are shown in Figure 10 for ceilings, Figure 11 for floors, and Figure 12 for north walls. Here the values obtained by integration of the measurements are shown as bars on the left, and the ASHRAE values are the bars on the right. Some results are slightly higher,

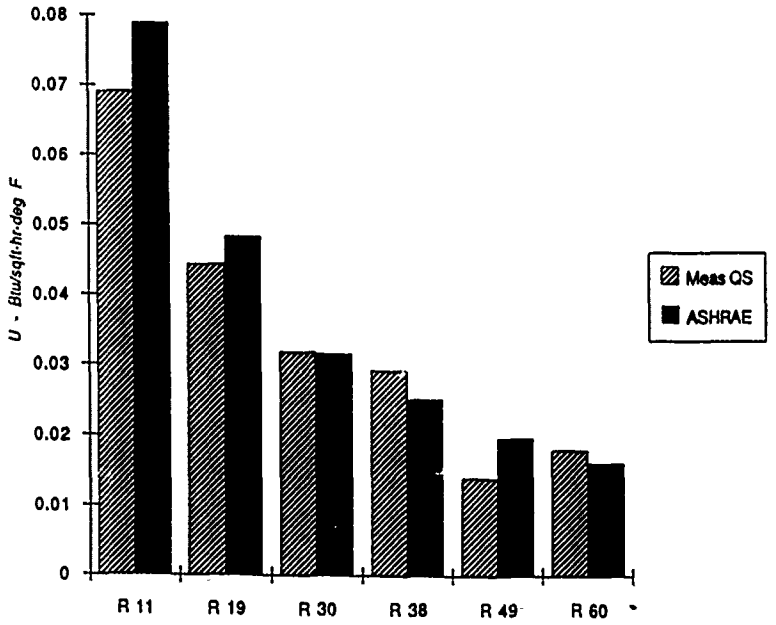

Figure 10. Measured and Handbook U-Values in Test Cell Ceilings

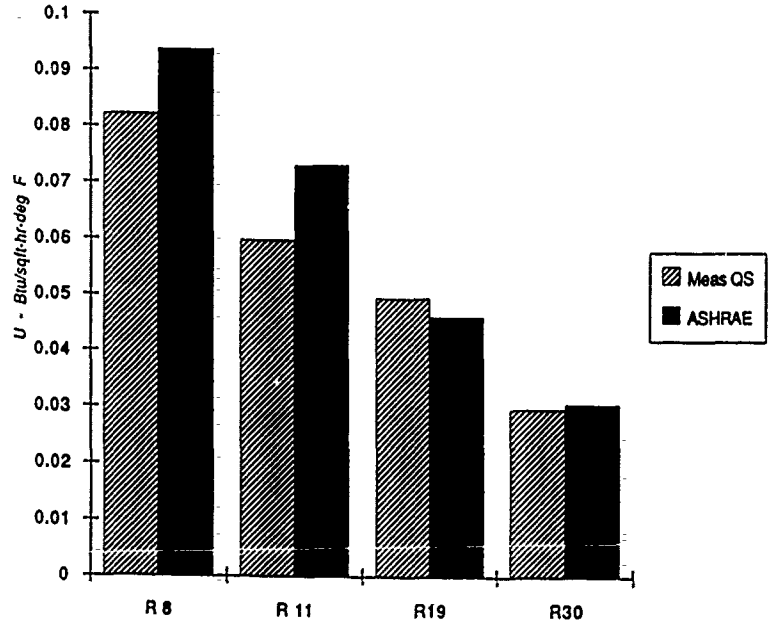

Figure 11. Measured and Handbook U-Values in Test Cell Floors.

some slightly lower than the handbook values, but fall within the band of accuracy and precision errors. However, for the very highly insulated ceiling sections, there is a reversal — the U-values are higher for the higher R-rating. These two ceiling sections are a composite of several layers of batt insulation. The possibility of convective currents augmenting conduction is substantial. Discrimination between very high insulation levels is difficult, as well as being sensitive to installation practices.

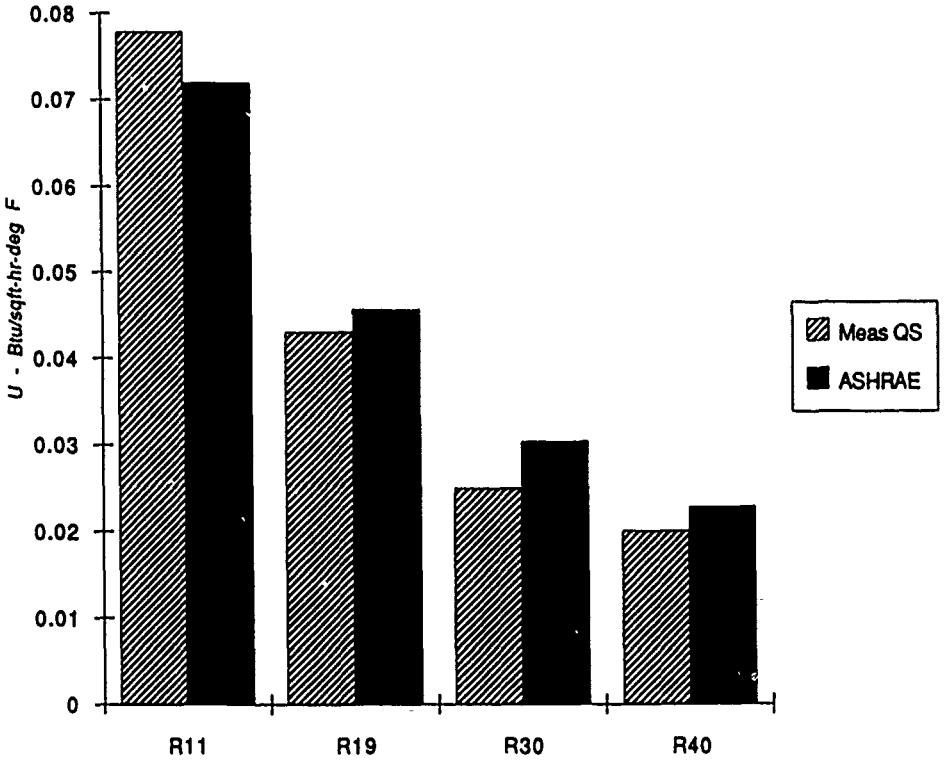

Figure 12. Measured and Hanbook U-Values in Test Cell North Facing Wall

It has been suggested [5] that acceptably accurate results can be obtained in less time if the heat flux series is shifted with respect to the temperature difference series. Lagging the heat fluxes in the numerator of the successive flux/delta T quotients by starting one phase shift time period later did reduce the initial amplitude of the dampened response curve, but did not diminish the time to asymptote. This can be seen in Figure 13 where the flux has been lagged behind the temperature by 4 hours, the phase shift determined from the graph of q and delta T vs time (both lagged and unlagged are the same at approximately 50 hours). The reason for their subsequent divergence up to 200 hours is not clear.

The presentation of results to an audience of lay persons such as lawyers, accountants, developers, and home builders presents a real challenge. This is particularly the case when building codes and similar instruments are under consideration. The use of steady-state or quasistatic U-values as standards of comparison is misleading because of the implication that savings are in direct proportion to the U-value ratings. Clearly steady-state values serve well in energy simulation models, but these are not comfortable concepts to this audience. Figure 14, which shows not only the development of the familiar quasistatic U, but which has superimposed the

wildly fluctuating instantaneous quotients (dynamic U-value) may perhaps be useful to convey the notion that other factors such as insolation and thermal storage decrement the book U-values and hence the energy savings.

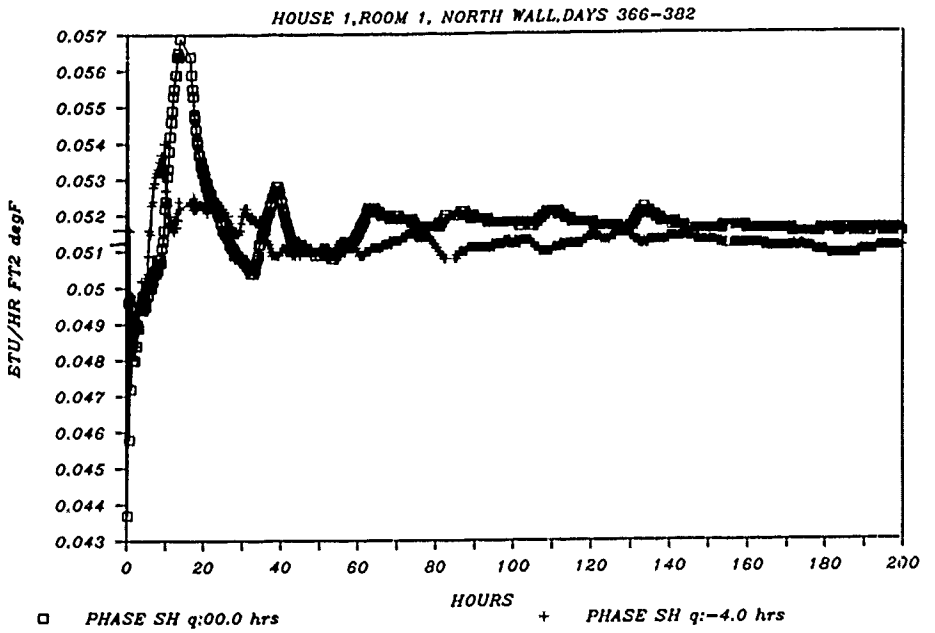

Figure 13. Quasistatic U-Value Determinations with Lagged Heat Flux and Without

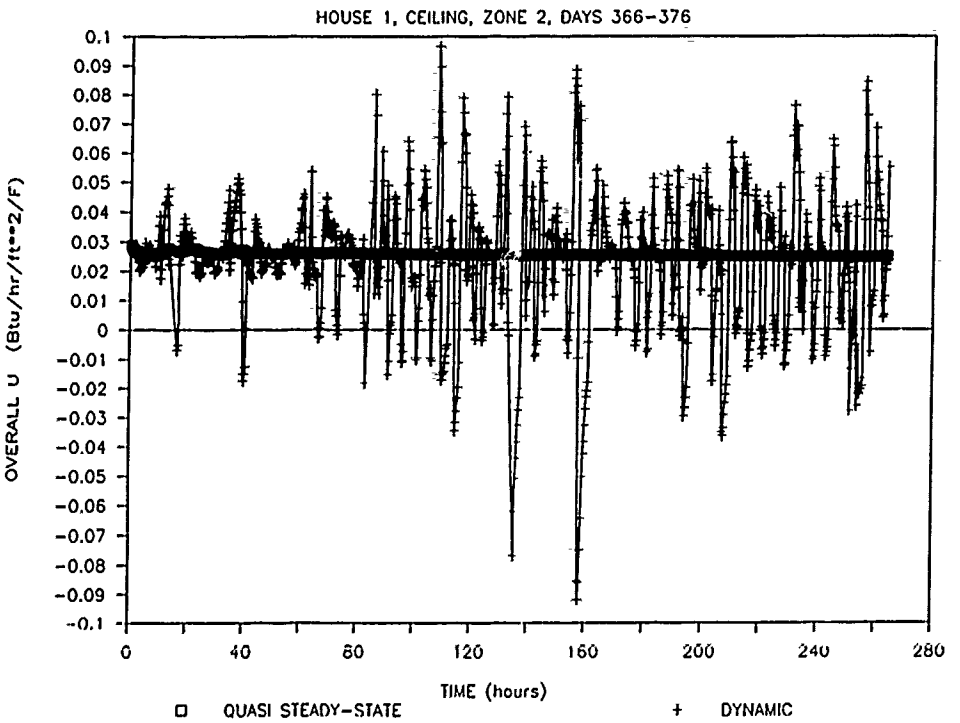

Figure 14. Developing Quasistatic U with Instantaneous Values Superimposed

CONCLUSIONS:

The effect of application techniques for surface mounting of HFTs expressed as effective calibration constants (ECCs) relating heat flux to the output voltage has been described. Techniques for attachment of HFTs to envelope surfaces, which are suitable for long-term use (years), have been developed. Statistical estimates of the random error in the ECC, due to surface mounting, have been given. The use of HFTs, mounted using the techniques developed, has been presented for a range of ceiling, floor and wall resistances in unoccupied test spaces. Finally, measurements made in family occupied houses are compared to those in identical unoccupied spaces. Comparison of the U-values computed from the HFT and temperature difference data are found in reasonable accord with handbook values.

ACKNOWLEDGEMENT:

The research on which this paper is based was funded by The Washington State Energy Office, Contract # 86-34-02.

REFERENCES:

1. Flanders, S. N. Confidence in Heat Flux Transducer Measurements of Buildings. ASHRAE Transactions, Volume 91, Part 1 (1985)

2. Grot, R. A. Measurement Methods for Evaluation of Thermal Integrity of Building Envelopes. NBSIR 8-2605, Nov 1892

3. Flanders, S. N. and Marshall, S. J. In Situ Measurements of Masonry Wall Thermal Resistance. ASHRAE Transactions, Volume 88, Part 1 (1982)

4. Anderson, B. R. The Measurement of U-Values on Site. Proceedings of the ASHRAE/DOE/BTECC Conference, Clearwater Beach, Florida, Dec 1985

5. Brown, W. C. and Schuyler G. D. In Situ Measurements of Frame Wall Thermal Resistance. ASHRAE Transactions, Volume 88, Part 1 (1982)

ldk

Charles Kippenhan

Q: Did you obtain any evidence of a temperature dependence of thermal properties?—Stephen N. Flanders.

A: Data were taken over the period of an entire year. These spanned average outdoors temperatures between 44°F and 79°F and indoor-outdoor temperature differences between 0°F and 51°F. Budgetary considerations prevented an analysis of the data set to establish a dependence of U-values on temperature.

CALCULATIONAL TECHNIQUES

USING PARAMETER ESTIMATION TO ANALYZE BUILDING ENVELOPE THERMAL PERFORMANCE

J.V. Beck	Michigan State University East Lansing, Michigan USA
T.W. Petrie	Marquette University Milwaukee, Wisconsin USA
G.E. Courville	Oak Ridge National Laboratory Oak Ridge, Tennessee USA

ABSTRACT

Field measurements on building envelope components are useful when installed thermal performance can differ from design performance. This difference can result from effects such as material degradation, water intrusion or improper installation. For evaluation of tests on real roofs under actual conditions, there is a need for an accurate and reliable analysis technique to extract information from field data. The purpose of this paper is to describe the computer program PROPOR, based on parameter estimation techniques, which can be used on field data. PROPOR is applied to two simple situations to validate its reliability, flexibility and versatility: one is an idealized thermal problem that has an analytic solution; and, the other is a test of a fully instrumented test section under carefully controlled conditions in the Large Scale Climate Simulator at the Oak Ridge National Laboratory. PROPOR assumes that heat flow is one-dimensional and involves heat conduction only. Layered systems can be accommodated. The outputs are the apparent thermal conductivity and the product of density x specific heat, both as functions of temperature if desired. Subroutines are also used that indicate the expected convergence of results (sensitivity coefficients), that examine the correctness of the initial model (residual analysis) and that provide an estimate of the precision of results (confidence intervals).

INTRODUCTION

An important activity at the U.S. DOE Roof Research Center at the Oak Ridge National Laboratory (ORNL) in the area of thermal evaluation of building envelopes is the use of field measurements for determining the thermal performance of roofs. An outdoor facility, the Roof Thermal Research Apparatus, and an indoor facility, the Large Scale Climate Simulator (LSCS), are available to do tests on sections of actual roofs. Both thermocouples and heat flux transducers are used to acquire steady- state and dynamic thermal performance data.

The measurements are carefully made. Thermocouples are made from the same spool of wire to achieve an important factor for accurate measurement of temperature differences. The heat flux transducers are calibrated with the sensors surrounded by the same materials as in the actual test configuration.

A number of techniques have been proposed to analyze the data from dynamic experiments; for example, the commonly used averaging method (Flanders, 1980; Courville and Beck, 1989; Courville and Childs, 1989). The temperatures at a point in a roof vary in an approximately sinusoidal manner, sometimes with the heat flow being both positive and negative during the same test period. In some seasons, such as the spring and fall, there can be days or even weeks when the average heat flux is nearly zero. This causes difficulty in the use of the averaging method, since the predicted thermal resistance (R-value) for such conditions has large errors.

Obtaining an accurate R-value is of paramount importance. Moreover, the R-value of test specimens depends upon the specimen mean temperature. Being able to quantify this dependency is often important. Yet, the averaging technique does not provide an implicit method of relating R-value to temperature. Finally, another need in analysis techniques is to specify the confidence intervals of the parameter estimates.

Computer program PROPOR (denoting PROPerties, Oak Ridge) satisfies all these needs. It can use arbitrary time variations of the surface temperatures as boundary conditions. PROPOR can be used when the average heat flow is near zero, unlike the averaging method. It can calculate the R-value (via the apparent thermal conductivity) as a function of temperature, thereby solving the problem of what is the temperature at which to assign R-values. It has a statistical basis that includes a calculation of the confidence regions.

Several data sets can be combined and analyzed by PROPOR. For example, data from early in a test could be analyzed for an interim estimate of thermal conductivity. Meanwhile, the experiment would be continued until another set of data was obtained. If the added data improved confidence to acceptable limits, the test could be terminated and complete post-processing done.

The purpose of this paper is to describe the characteristics of PROPOR and to use two thermal problems to validate the strength of this technique. One has an exact solution and the other is a carefully chosen simulation of roof behavior in the Large Scale Climate Simulator. Both problems are ones where only the limits of PROPOR will affect the accuracy of its estimates. There is no uncertainty in the

exact solution and very little in the data from the LSCS that provide input to PROPOR in these demonstrations.

PROGRAM PROPOR

Program PROPOR estimates the thermal properties of heat conducting solids. It is based on parameter estimation techniques (Beck and Arnold, 1977). For an insulation in which one-dimensional, transient conduction is the sole heat transfer mechanism, the governing equation, allowing for variable properties, is

$$\frac{\partial}{\partial x}\left[k\frac{\partial T}{\partial x}\right] = \rho c\frac{\partial T}{\partial t}; \quad q = -k\frac{\partial T}{\partial x} \tag{1}$$

where T is temperature, q is heat flux, x is position, t is time, k is thermal conductivity, ρ is density and c is specific heat. PROPOR solves equation 1 numerically using the Crank-Nicolson method to obtain a finite difference approximation. The boundary conditions are the measured temperature or heat flux histories at each side of the roofing materials, which are singled out for estimation of their parameters.

The thermal properties usually calculated are the thermal conductivity as a function of temperature and a constant value for the product of density x specific heat. The R-value at a given T is obtained from the k-value at the same temperature. The estimates of thermal conductivity (for example, k_1 at some T_1 and k_2 at some other T_2) and a ρc value are obtained by minimizing a sum of squares function **S** with respect to the estimates. The Gauss linearization method (Beck and Arnold, 1977) is used to minimize **S**. The sum of squares function is defined as

$$S = \sum_{i=1}^{I}\sum_{j=1}^{J}(Y_{ji} - T_{ji})^2\sigma_{T_j}^{-2} + \sum_{i=1}^{I}(F_i - q_i)^2\sigma_{q_i}^{-2} + \sum_{m=1}^{M-1}(k_{m+1} - k_m)^2\sigma \tag{2}$$

where

Y and F are measured temperatures and heat fluxes, respectively.
T and q are corresponding calculated temperatures and heat fluxes.
k denotes estimates of thermal conductivities.
σ_T^{-2}, σ_q^{-2} are weighting factors and σ is a regularization parameter.

Three terms are given by the three summations. The first is for the difference between the measured temperatures, Y_{ji}, at location x_j inside the roofing materials for time t_i and the corresponding temperature, T_{ji}, calculated by equation 1. The square of each temperature difference is weighted by the reciprocal of the approximate variance of Y_{ji}, which is denoted $\sigma_{T_j}^2$. The second summation is for a single internal heat flux if measured by a heat flux transducer. F_i is then the measured heat flux and q_i is the heat flux calculated by equation 1 for time t_i. Measured temperatures or heat fluxes, distinct from the ones

used to minimize S, are used as boundary conditions for equation 1. The weighting factor in the second summation is the reciprocal of the approximate variance of F_i, which is denoted by σ_{qI}^{-2}. The weighting factors, σ_{Tj}^{-2} and σ_{qI}^{-2}, account for the different magnitudes of measured temperatures and measured heat fluxes in their respective units. Typically, temperature numbers are 10 to 100 times larger than heat flux numbers in USCS units. The results herein were obtained in USCS units and converted to SI.

The last summation in equation 2 is a regularizing term whose purpose is to restrict any large variations in the estimated k_m components when several data sets ($M \geq 2$ in number) are combined to improve the accuracy of estimations. The summation is weighted by the regularization parameter σ, which can be chosen anywhere in a large range of values. If σ is set equal to zero, there is no regularization or smoothing of the k versus T relation. If σ is made relatively large, k will approach a constant value over the range of T values. The data base for equation 2 is usually a set of temperatures and heat fluxes measured at equal time intervals. The index i refers to the number of time steps (with total I) and the index j denotes the number of thermocouples placed within the sample (with total J). If a heat flux were measured at more than one internal site, another index would be required in the second summation.

The form of the input and output for PROPOR is very flexible. Measured temperatures or heat flows can be used as boundary conditions. One or many interior temperature and heat flux sensors can be utilized. The thermal properties can be constant or functions of temperature. If k only is a function of temperature, one to four values for k at different temperatures as well as ρc can be estimated (Courville and Beck, 1988). The test specimen does not have to be a single material; thermal properties for more than one material can be found from the same experiment. Greater or smaller amounts of output can be selected, but a very important part of the output is prediction of confidence intervals for the parameter estimates. They are computed taking into account the correlation in the measurement errors.

APPLICATION OF PROPOR

Figure 1 is a typical test configuration for an insulated flat roof. Four layers of board insulation are bounded by the deck on the bottom and a waterproofing membrane on top. Five thermocouples and one heat flux transducer provide inputs to PROPOR. A week's worth of hourly values for Y_1 and Y_5, which vary with outside and inside environmental conditions, are the boundary conditions for solving equation 1. Hourly values of Y_2, Y_3, Y_4 and F are the measured values introduced into equation 2. Thus, J = 3, since three internal temperatures are being measured, and I = 168, the number of hours for one week.

PROPOR also requires an input parameter file arranged as a series of data blocks that describe control parameters, geometry, time steps, property values and the desired output information. The program, as currently configured, runs on an IBM Personal Computer AT or compatible

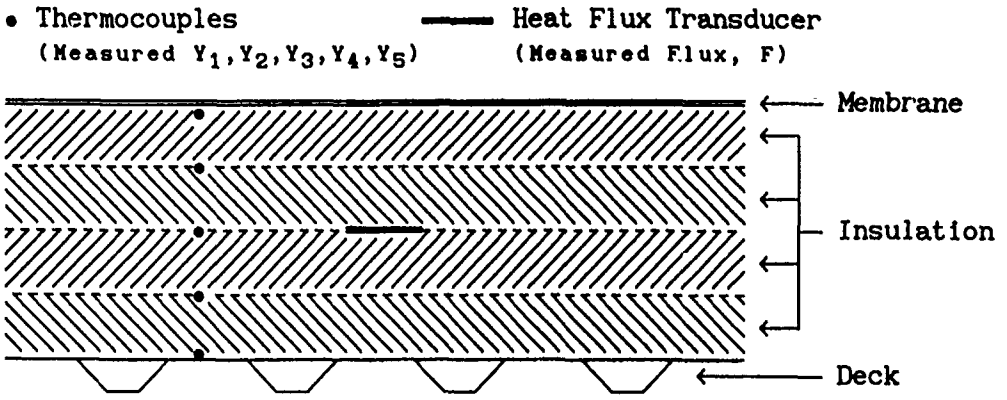

Figure 1. Typical test configuration for an insulated flat roof.

equipped with a math co-processor. The run time depends upon the quantity and quality of the input temperature and heat flow data. For a typical problem [168 time steps, uncertainties in $\Delta T < 0.1°C$ (0.2°F), and uncertainties in heat flux < 0.3 W/m^2 (0.1 $BTU/h \cdot ft^2$)], the run time is between 0.5 and 2 minutes.

IDEAL CASE STUDY

Important features of PROPOR can be illustrated when the program is applied to a problem that has an exact solution. In this case, the solution for specific values of properties can be used to generate a set of exact temperatures and heat flows. These, in turn, can be put into PROPOR to test its ability to reproduce the thermal properties.

A transient heat conduction problem is considered that simulates outdoor heating and cooling conditions. The problem is one-dimensional heat transfer through a homogeneous slab with values of the thermal properties k and ρc, the thermal conductivity and the product of density x specific heat, respectively, assumed to be constant. The temperature at x = 0 (inside) is fixed at T_0 and the temperature at x = L (outside) has the average value T_L with a superimposed sinusoid of amplitude ΔT_L and frequency ω or,

$$T(0, t) = T_0; \quad T(L, t) = T_L + \Delta T_L \sin(\omega t) \tag{3a}$$

The initial temperature distribution is assumed to be linear in x,

$$T(x, 0) = T_0 - \Delta T_{ss} \cdot \frac{x}{L}, \qquad \Delta T_{ss} = T_0 - T_L \tag{3b,c}$$

The transient heat conduction equation with constant properties is

$$k \frac{\partial^2 T}{\partial x^2} = \rho c \frac{\partial T}{\partial t} \tag{3}$$

The solution of the above problem can be given in the form (Carslaw and Jaeger, 1959)

$$T = T_0 - \Delta T_{ss}\cdot\frac{x}{L} + \Delta T_L\left[\frac{x}{L}\sin(\omega t) + \frac{2}{\pi}\sum_{m=1}^{\infty} m^{-1}(-1)^m B(m,t)\sin(m\pi\frac{x}{L})\right] \quad (4)$$

where

$$B(m,t) = \frac{N(m,t)}{D(m)} \quad (5a)$$

$$N(m,t) = Hm^2\pi^2[\cos(\omega t) - \exp(-m^2\pi^2 Fo)] + \sin(\omega t) \quad (5b)$$

$$D(m) = H^2m^4\pi^4 + 1, \quad H = \frac{k}{\rho cL^2\omega}, \quad Fo = \frac{kt}{\rho cL^2} \quad (5c,d,e)$$

The heat flux for equation 4 can be found from $q = -k\frac{\partial T}{\partial x}$, *viz.*,

$$q = \frac{k\Delta T_{ss}}{L} - k\Delta T_L\left[\frac{1}{L}\sin(\omega t) + \frac{2}{L}\sum_{m=1}^{\infty}(-1)^m B(m,t)\cos(m\pi\frac{x}{L})\right] \quad (6)$$

For dimensionless times Fo > 0.5, the exponential term in equation 5b is negligible and the temperature distribution is periodic in time.

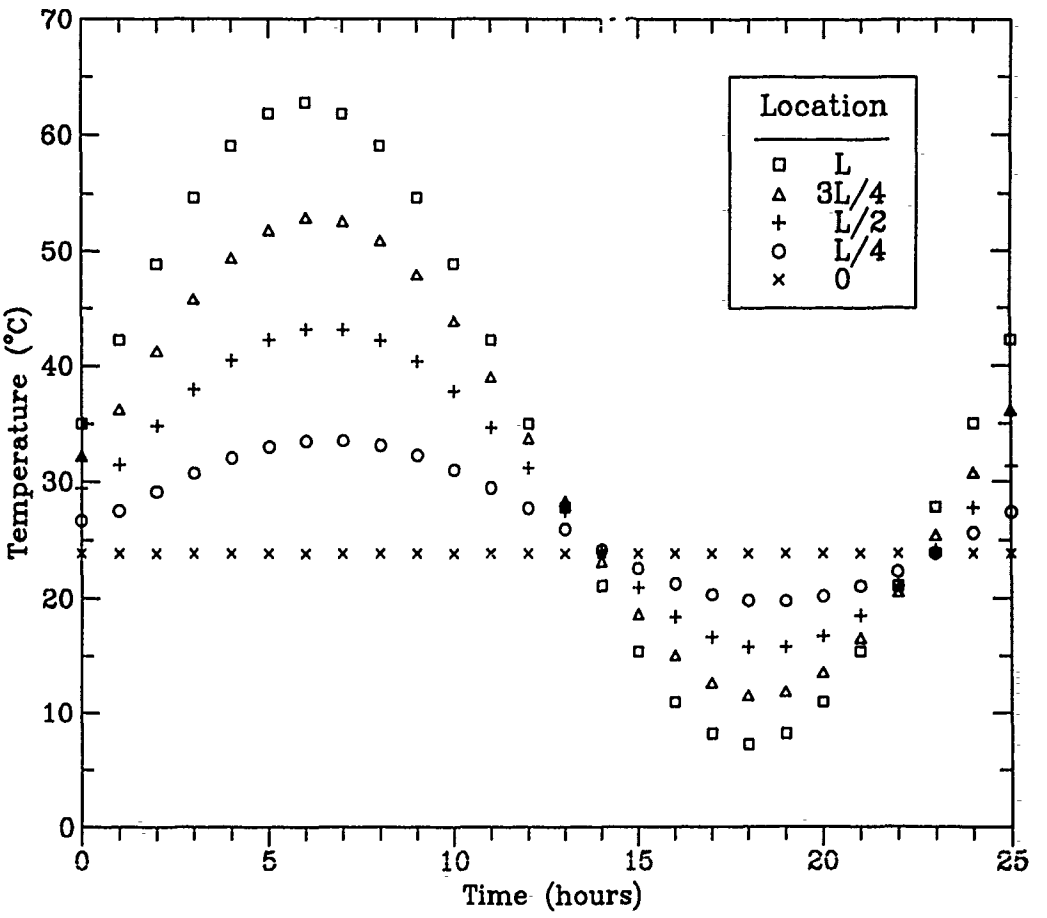

Figure 2. Test case for PROPOR. Calculated temperature profiles for H = 1.

RESULTS OF ANALYSIS

The equations above for sinusoidal heat transfer approximate the diurnal variations in temperatures and heat fluxes when heating and cooling a roof. A realistic set of values are the inside temperature at 24°C (75°F) and the outside surface temperature varying from 7° to 63°C (45° to 145°F) in a period of 24 hours, so that the frequency ω is equal to $2\pi/24$ with time given in hours. These values result in ΔT_{ss} = -11°C (-20°F) and ΔT_L = 28°C (50°F). For illustration, let the value of dimensionless thermal diffusivity H be 1, corresponding to k = 0.035 W/m•K (0.02 BTU/h•ft•F), ρc = 26.8 kJ/m^3•K (0.4 BTU/ft^3•F) and L = 0.133 m (5.25 in.) [divided into four layers, each ℓ = 0.033 m (1.3125 in.)]. Results for this case are shown in figure 2 for T at x = 0, L/4, L/2, 3L/4 and L. Figure 3 shows the heat flux curve for x = L/2. The curves are sinusoidal in less than 3 hours as the exponential term in equation 5b becomes negligible. Enough terms are used in the infinite series to get a constant value for the series despite further increases in m. This solution can be used to examine some of the features of PROPOR.

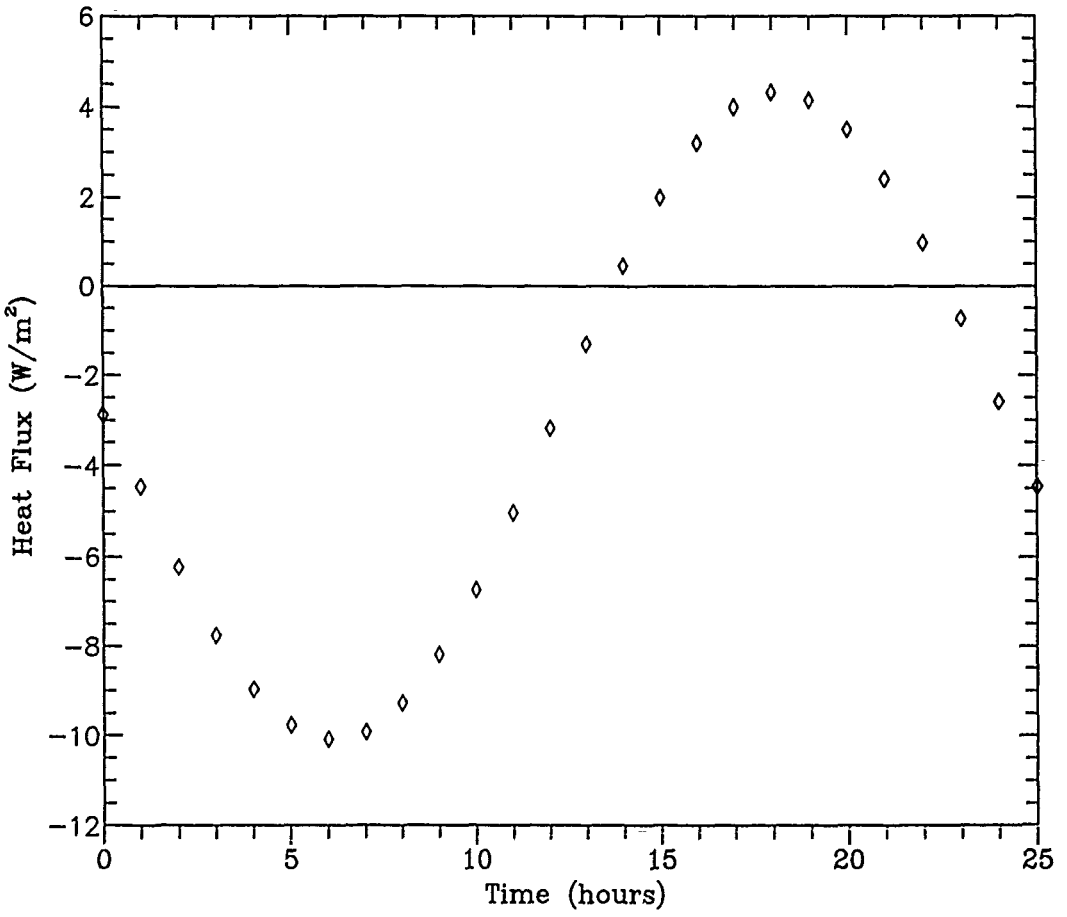

Figure 3. Test case for PROPOR. Calculated heat flux at mid-plane for H = 1.

Sensitivity Coefficients

In estimating the thermal properties k and ρc from measurements of T and q, the "sensitivity coefficients" defined by the following notation are useful indications of the success of PROPOR (Beck and Arnold, 1977):

$$S_{T,k} = \frac{\partial T}{\partial k} \qquad S_{q,k} = \frac{\partial q}{\partial k} \qquad S_{T,\rho c} = \frac{\partial T}{\partial \rho c} \qquad S_{q,\rho c} = \frac{\partial q}{\partial \rho c}$$

Good experiments for estimating parameters have k and ρc sensitivity coefficients that are large and uncorrelated, *i.e.*, have quite different shapes. When PROPOR is applied to data from a field test, it generates a data file with sensitivity coefficients tabulated at each internal location and time. One must review these numbers or create plots of them to examine the behavior of the sensitivity coefficients. Since this problem has an analytic solution, it is much easier to study the sensitivity coefficients.

In order to display simple expressions, and thus gain insight, the location x = L/2 is selected for $H \geq 1$ and $Fo \geq 0.5$. The exponential term in N(m,t) of equation 5a is neglected. The magnitude of $Hm^2\pi^2\cos(\omega t)$ is generally large compared to $\sin(\omega t)$ in equation 5b except at times when $\cos(\omega t)$ goes through zero. The magnitude of $H^2m^4\pi^4$ is much larger than 1 in equation 5c. Moreover, the value of the infinite series in equation 4 is then dominated by the first non-zero term. Temperature and heat flux at the mid-plane for any time can then be written as

$$T(L/2, t) = T_0 - \Delta T_{ss}\cdot\frac{1}{2} + \Delta T_L\left[\frac{1}{2}\sin(\omega t) - \frac{2}{H\pi^3}\cos(\omega t)\right] \qquad (7a)$$

$$q(L/2, t) = \frac{k\Delta T_{ss}}{L} - \frac{k\Delta T_L}{L}\left[\sin(\omega t) - \frac{1}{2H\pi^2}\cos(\omega t)\right] \qquad (7b)$$

Using equations 7a and 7b, the sensitivity coefficients have the form

$$kS_{T,k} = -\rho cS_{T,\rho c} = \frac{2\Delta T_L}{H\pi^3}\cos(\omega t) \qquad (8a)$$

$$kS_{q,k} = \frac{k}{L}\left[\Delta T_{ss} - \Delta T_L \sin.(\omega t)\right] \qquad (8b)$$

$$\rho cS_{q,\rho c} = \frac{k\Delta T_L}{L}\frac{1}{2H\pi^2}\cos(\omega t) \qquad (8c)$$

Notice that $kS_{T,k}$ and $\rho cS_{T,\rho}$ both have units of temperature and can be compared directly with one another and also with the temperature. The relationship between $kS_{T,k}$ and $\rho cS_{T,\rho c}$ given by equation 8a is a special case for this temperature distribution. It indicates that the effect on T of increasing k is equivalent to that of decreasing ρc. This is a very strong correlation between these sensitivities. As a consequence, without heat flux measurements in experiments with sinusoidal outside temperature variations like equation 3a, it would not be possible to estimate both k and ρc with high accuracy.

Equations 8b and 8c show that changes in k and ρc have effects on the calculated heat flux q different from their effects on T. The sensitivity of q to k, given by equation 8b, has a nonzero average value (if $\Delta T_{ss} \neq 0$). Its amplitude is much larger than that of the sensitivity of q to ρc, from equation 8c for H ≥ 1. These differences in the sensitivities of q are important because they permit the simultaneous determination of accurate values for k and ρc from experiments providing T and q data.

Test Case for ρc = 26.8 kJ/m^3·K (0.4 BTU/ft^3·F)

Accurate values for sensitivities are obtained by differentiating equations 4 and 6. The resulting sensitivity of temperature to thermal conductivity, $kS_{T,k}$, is plotted in figure 4. Its sensitivity to the product of density x specific heat is the same except for the sign. The most remarkable aspect is that the values of these coefficients are so small, only ranging from -1.7° to +1.7°C (-3° to +3°F) while the boundary temperature at x = L varies from 7° to 63°C (45° to 145°F). Hence, only if measurement errors are somewhat less than ±1.7°C (±3°F) will the measurements of temperature contain significant information

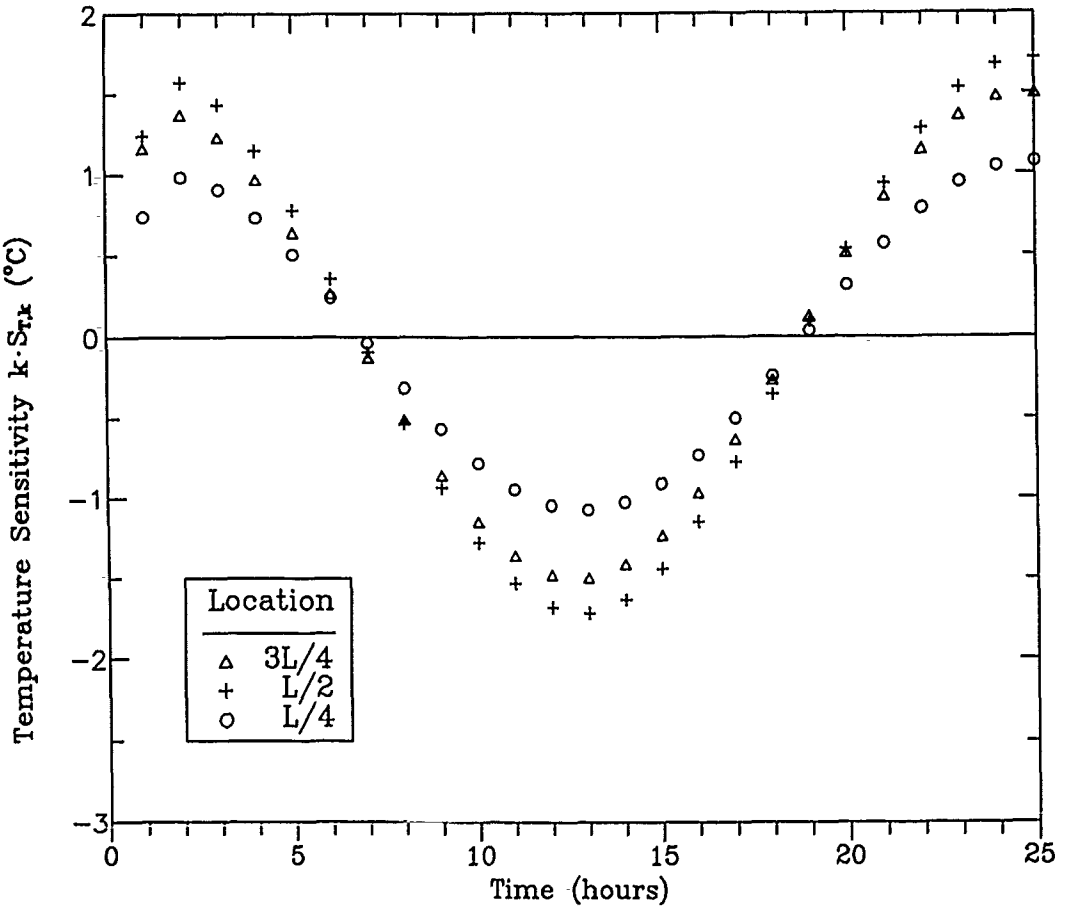

Figure 4. Test case for PROPOR. Temperature sensitivities at internal locations for H = 1.

regarding k or ρc.

The sensitivity coefficients for heat flux are shown in figure 5. Sensitivities to k and ρc are quite different. The values for $kS_{q,k}$ in figure 5 are essentially equal to the heat fluxes themselves in figure 3. This means that accurate estimates for thermal conductivity can be obtained from heat flux data. The sensitivity $\rho cS_{q,\rho c}$ is very small, usually between ±0.95 W/m² (±0.3 BTU/h·ft²). Such small ρc sensitivities mean that ρc cannot be estimated from heat fluxes as accurately as k in this test case.

Test Case for ρc = 268 kJ/m³·K (4.0 BTU/ft³·F)

Consider a case where the ρc value is ten times larger than above, *i.e.*, ρc = 268 kJ/m³·K (4 BTU/ft³·F). This makes the dimensionless thermal diffusivity H from equation 5d equal to 0.1. The resulting sensitivities of temperature to thermal conductivity and the product of density x specific heat are shown in figure 6. Note that they are much larger in magnitude than in figure 4. Thus, the temperatures have the potential to provide much more information than in the previous case. Locations L/2 and L/4 are farther from the heated surface at L than

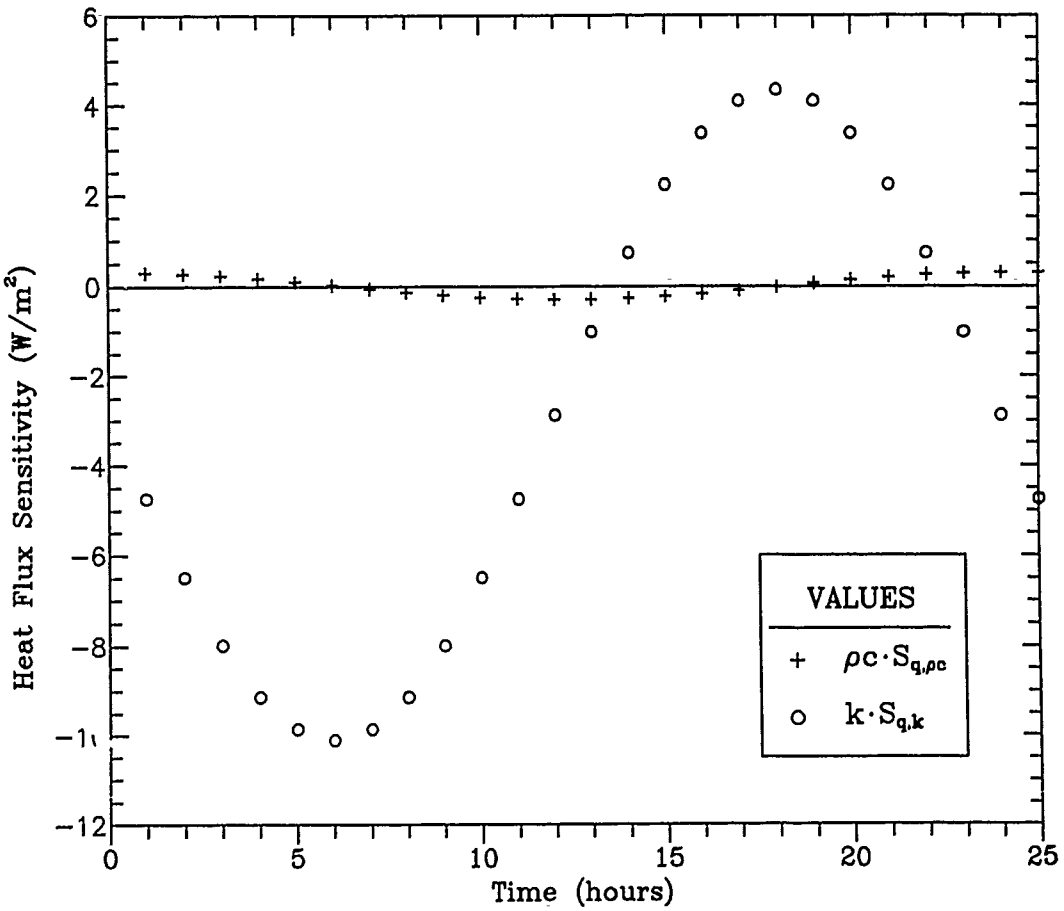

Figure 5. Test case for PROPOR. Heat flux sensitivities at mid-plane for H = 1.

location 3L/4. The sensitivities at L/2 and L/4 lag much more noticeably behind ones at 3L/4 than they did in figure 4. However, all temperature coefficients shown in figure 6 are of the same magnitude.

Since the k and ρc sensitivities of T are proportional, q measurements are required to estimate both k and ρc simultaneously. The q sensitivities are depicted in figure 7 for this case. As expected from equation 8b, the sensitivity of q to k is not appreciably changed with the decrease in H from 1 to 0.1. On the other hand, the sensitivity to ρc is increased in magnitude by a factor of 10, as can be seen by comparing figures 5 and 7 and also from equation 8c. Even though the heat flux sensitivities in figure 7 are of equal magnitude, they are out of phase with each other and, therefore, not correlated.

The conclusion is that an experiment with H = 0.1 should provide better estimates of k and ρc than an H = 1.0 experiment, provided that heat fluxes are measured with the same accuracy in both experiments. An H = 0.1 experiment can be obtained with the same materials as in an H = 1.0 experiment by increasing the frequency by a factor of 10 (in a climate simulation facility) or by increasing the thickness of the specimens by a factor of 3.2. Also, materials with higher products of density x specific heat will allow more accurate values to be obtained

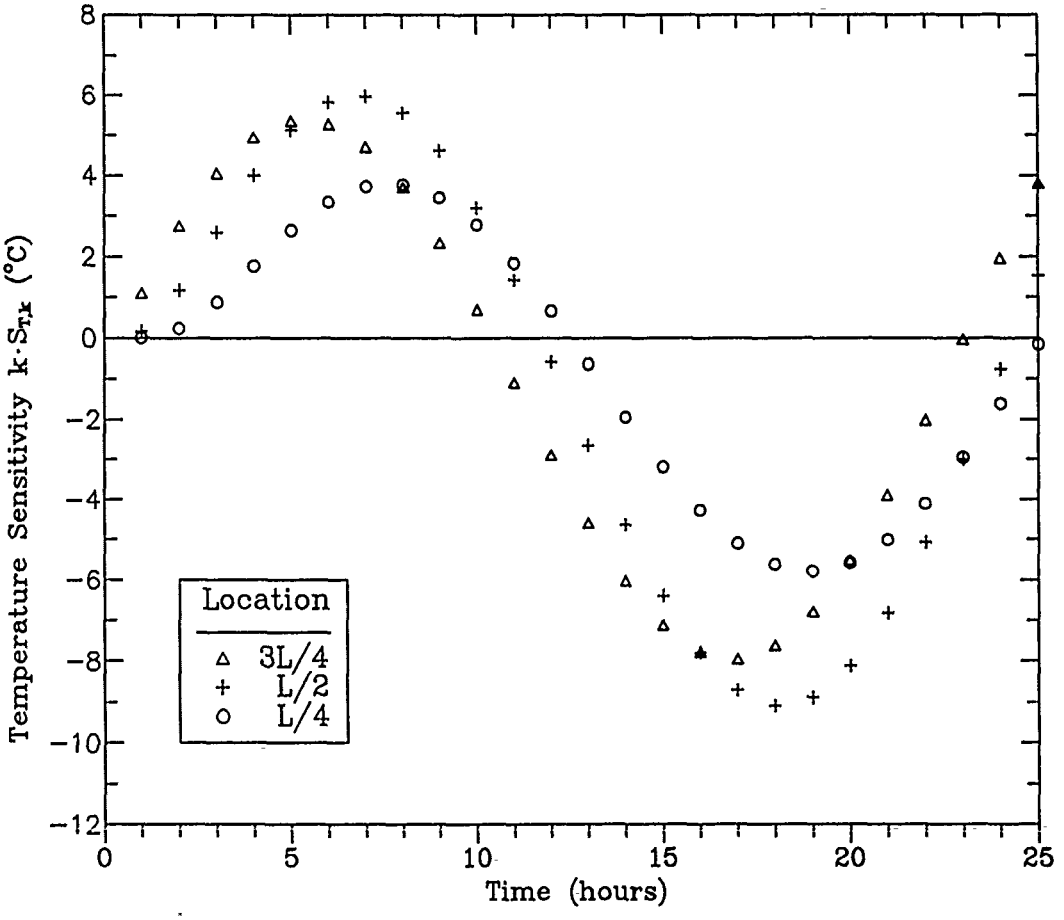

Figure 6. Test case for PROPOR. Temperature sensitivities at internal locations for H = 0.1.

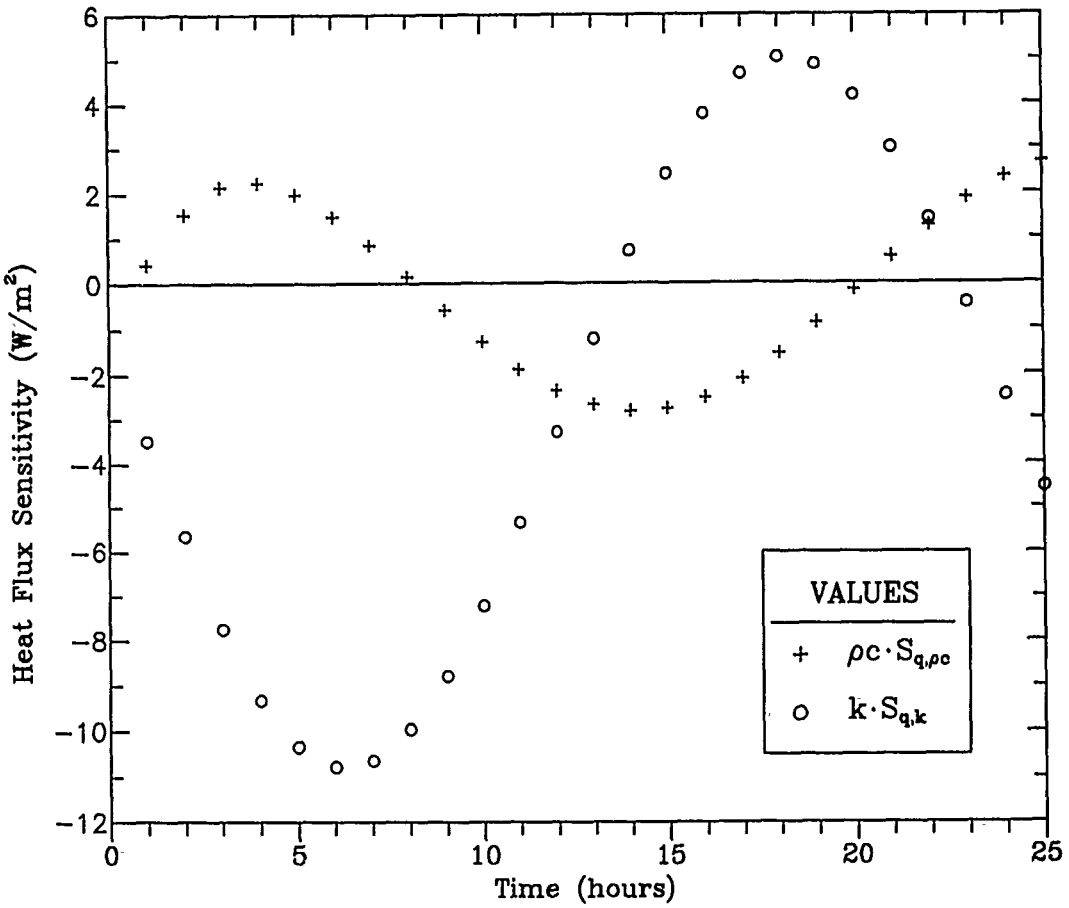

Figure 7. Test case for PROPOR. Heat flux sensitivities at mid-plane for H = 0.1.

simultaneously for k and ρc. On the other hand, if only k is desired, the case of $H \geq 1$ is an excellent design because the value of ρc does not greatly affect the estimates for k.

ESTIMATION OF THERMAL PROPERTIES

To obtain the temperature and heat flow inputs for PROPOR, equations 4 to 6 are solved to yield four different sets of calculations. In the first one, the k-value is 0.035 W/m•K (0.02 BTU/h•ft•F) and ρc is 26.8 kJ/m³•K (0.4 BTU/ft³•F). PROPOR simulations predict the best constant values of k and ρc. The results are shown in Table 1. Next, k is kept the same and ρc is changed to 268 kJ/m³•K (4.0 BTU/ft³•F). The corresponding PROPOR results are in Table 2. In the third set, k and ρc are again 0.035 W/m•K and 26.8 kJ/m³•K, respectively, but now PROPOR is asked to predict the best linear function of temperature for k with ρc still constant. Finally, in the fourth set, PROPOR predicts the best linear functions for both k and ρc. The results for these latter cases are in Table 3. Each table lists the values of input parameters ICAL (which is the number of calculational time steps for each of the measured time steps), $L/\Delta x$ (which is the number of finite

difference elements of length Δx in each layer of insulation of thickness $\mathbb{L}$) and the ratio of weights σ_q^{-2} and σ_{Tj}^{-2} (see equation 2). The estimates of thermal properties with confidence intervals are shown along with the overall root mean square value (RMS) of the difference between measured and calculated temperatures at the internal nodes.

In Table 1, the first 10 cases are for a simulated experiment duration of 48 hours. In each case, the ratio of weights is fixed at 2. The input parameters varied were ICAL and $\mathbb{L}/\Delta x$. In general, the predicted k-values vary from 0.03461 to 0.03472 W/m•K (0.02000 to 0.02006 BTU/h•ft•F), which is a maximum error of 0.3%. The 95% confidence intervals, which vary from ±0.00005 to ±0.00031, are not strongly related to ICAL or to $\mathbb{L}/\Delta x$. The confidence intervals for k for cases 1 to 10 contain the true value (0.0346) in eight of the ten cases. The overall RMS value is less than 0.06 compared, *e.g.*, to boundary temperatures from 7.2° to 62.8°C.

The percent error in the ρc values is as large as 1.25%, which is larger than any for k. The inspection of the sensitivity coefficients above suggested this outcome. Notice also that the confidence intervals for ρc are much larger than for k. Each of these confidence intervals for ρc contains the true value (26.8). In general for 95% confidence, 19 out of 20 estimated regions should contain the true value. Here, for k and ρc, 18 out of 20 are achieved.

Cases 11 and 12 reveal the effects of using fewer data, by using data to 24 hours, instead of to 48. The actual estimates are about the same as in cases 1 through 10 but the confidence intervals for ρc almost double. The last two cases of Table 1 show the effect of changing the weights. Case 13 uses a ratio of weights equal to 200,

Table 1. Use of PROPOR for test case with H = 1.0 and constant k = 0.0346 W/m•K and constant ρc = 26.8 kJ/m^3•K. PROPOR estimates constant parameters.

Case	ICAL	$\mathbb{L}/\Delta x$	$\sigma_q^{-2}/\sigma_T^{-2}$	k ± u_k	ρc ± $u_{\rho c}$	RMS
1	1	4	2	0.03461±.00029	26.51±0.45	0.043
2	1	8	2	0.03461±.00007	26.49±0.34	0.047
3	2	4	2	0.03470±.00031	26.79±0.63	0.051
4	2	8	2	0.03472±.00022	26.77±0.55	0.049
5	2	16	2	0.03472±.00028	26.76±0.56	0.048
6	3	40	2	0.03472±.00017	26.80±0.63	0.051
7	4	8	2	0.03470±.00009	26.79±0.70	0.053
8	4	16	2	0.03470±.00007	26.79±0.68	0.052
9	4	32	2	0.03470±.00005	26.79±0.67	0.052
10	8	32	2	0.03470±.00010	26.81±0.76	0.054
11 (24h)	4	16	2	0.03470±.00007	26.83±1.17	0.052
12 (24h)	8	16	2	0.03470±.00012	26.85±1.35	0.055
13	4	16	200	0.03470±.00010	26.84±0.67	0.052
14	4	16	Variable *	0.03470±.00007	26.93±0.64	0.043

* PROPOR adjusts weighting factors after each iteration for as many times as specified by input parameter IWEIGH. If IWEIGH = 0, factors remain fixed at input values. Here, IWEIGH > number of iterations needed for convergence. The final ratios varied from 260 to 1000.

yet the estimates change little. Case 14 reveals the same insensitivity of k and ρc estimates when PROPOR changes the weights after each iteration. Its weights of 316, 91, 81 for T and 81200 for q do not significantly affect the estimates either even though the ratios vary from 260 to 1000.

Table 2, for ρc increased to 268 kJ/m^3•K (4.0 BTU/ft^3•F) so that H = 0.1 by equation 5d, shows the same general behavior as Table 1. The main difference is that the relative sizes of the confidence intervals for ρc are now reduced. In cases 15 and 16 their size is about ±2, which is 0.75% of ρc. In contrast, for case 8, the relative error given by the confidence interval is about 2.5%. Cases 17 and 18 again show that truncating the data to use only 24 hours decreases confidence in the estimates (increases the confidence intervals), mostly for ρc.

Table 3 shows results for estimating k_1 at 18.3°C (65°F), k_2 at 51.7°C (125°F) and constant ρc (cases 19 to 22) and for both properties estimated at 18.3°C and 51.7°C (cases 23 to 26). Observe that PROPOR estimates no significant difference between k_1 and k_2 or $(\rho c)_1$ and $(\rho c)_2$, if applicable. In all cases the "correct" constant values of k

Table 2. Use of PROPOR for test case with H = 0.1 and constant k = 0.0346 W/m•K and constant ρc = 268 kJ/m^3•K. PROPOR estimates constant parameters.

Case	ICAL	$\mathbb{L}/\Delta x$	$\sigma_q^{-2}/\sigma_T^{-2}$	$k \pm u_k$	$\rho c \pm u_{\rho c}$	RMS
15	4	16	2	0.03475±.00019	267.54±1.81	0.051
16	4	16	200	0.03477±.00016	268.88±1.95	0.056
17 (24h)	4	16	2	0.03475±.00024	267.41±2.82	0.051
18 (24h)	4	16	200	0.03475±.00021	268.82±3.15	0.056

Table 3. Use of PROPOR for test case with H = 1.0 and constant k = 0.0346 W/m•K and constant ρc = 26.8 kJ/m^3•K. PROPOR estimates variable parameters.

Case	ICAL	$\mathbb{L}/\Delta x$	$\sigma_q^{-2}/\sigma_T^{-2}$	$k_1, k_2 \pm u_k$	$\rho c_{(1,2)} \pm u_{\rho c}$	RMS
19	2	16	200	0.03461±.00036 0.03479±.00064	26.79±0.62	0.044
20	2	24	200	0.03461±.00036 0.03479±.00066	26.77±0.61	0.044
21	4	16	200	0.03460±.00036 0.03479±.00036	26.82±0.62	0.046
22	4	24	200	0.03460±.00035 0.03479±.00036	26.80±0.61	0.046
23	2	16	200	0.03461±.00038 0.03479±.00066	26.79±1.10 26.90±2.09	0.044
24	2	24	200	0.03461±.00038 0.03479±.00066	26.71±1.11 26.85±2.09	0.044
25	4	16	200	0.03461±.00038 0.03479±.00066	26.72±1.10 26.90±2.09	0.044
26	4	24	200	0.03460±.00036 0.03479±.00036	26.66±0.95 27.04±1.53	0.046

and ρc are within the confidence intervals for the parameters. In general, as more properties are estimated, the estimates become less accurate. Since the estimates of ρc are found with confidence regions approaching 8% in cases 23 to 26, it would not be wise to estimate ρc as a function of temperature in an analogous actual experiment. In an actual experiment, measurement errors would be present and would cause much larger uncertainty in the estimates. This would be reflected by even larger increases in the size of the confidence intervals than cases 23 to 26 show compared to cases 19 to 22.

APPLICATION TO TESTS IN THE LSCS

Analysis of Data Files for Expanded Polystyrene under Summer Conditions

Data for expanded polystyrene (EPS) insulation designated as SUMEPS and CSUMEPS came from two simulations of typical east Tennessee summer conditions in the ORNL Roof Research Center's Large Scale Climate Simulator. The set SUMEPS came from simulation with normal 24-hour days. The set CSUMEPS came from a time-compressed simulation, with 6-hour "days." Figures 8 and 9 show the temperature and heat flux

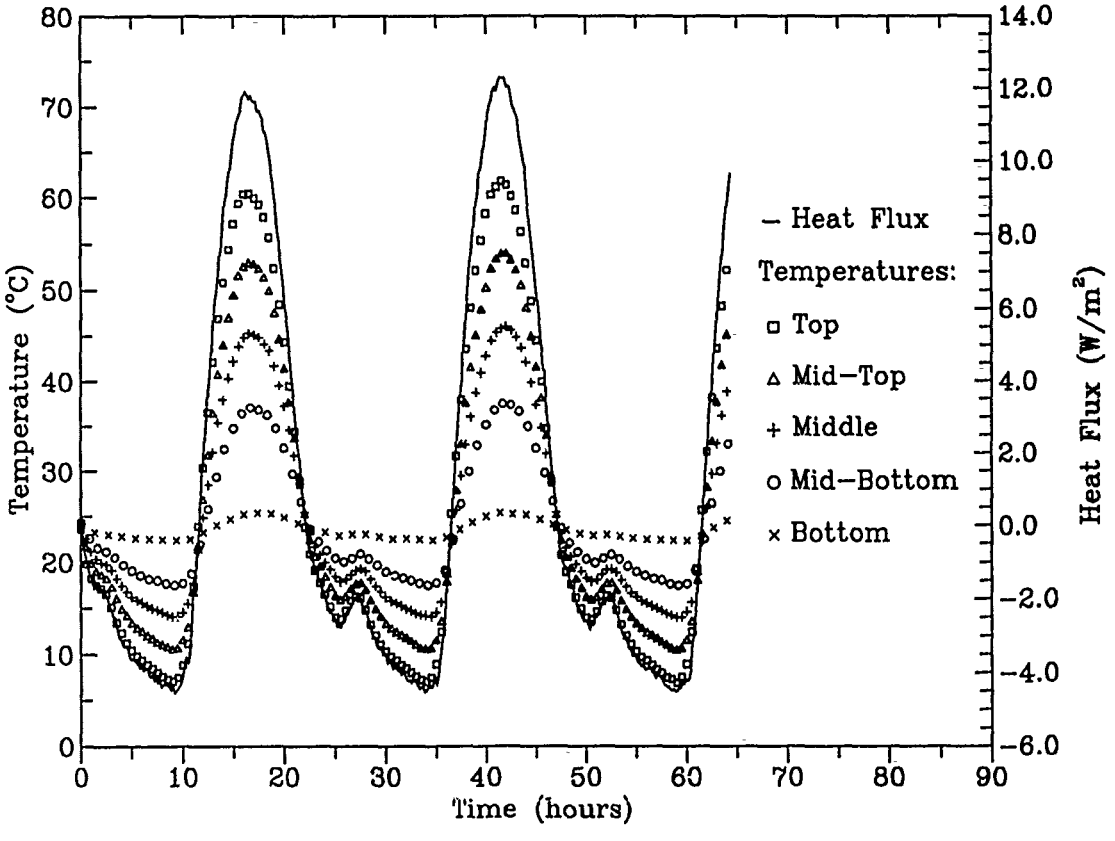

Figure 8. Heat flux and temperature profiles for test of expanded polystyrene with normal summer days yielding SUMEPS for PROPOR.

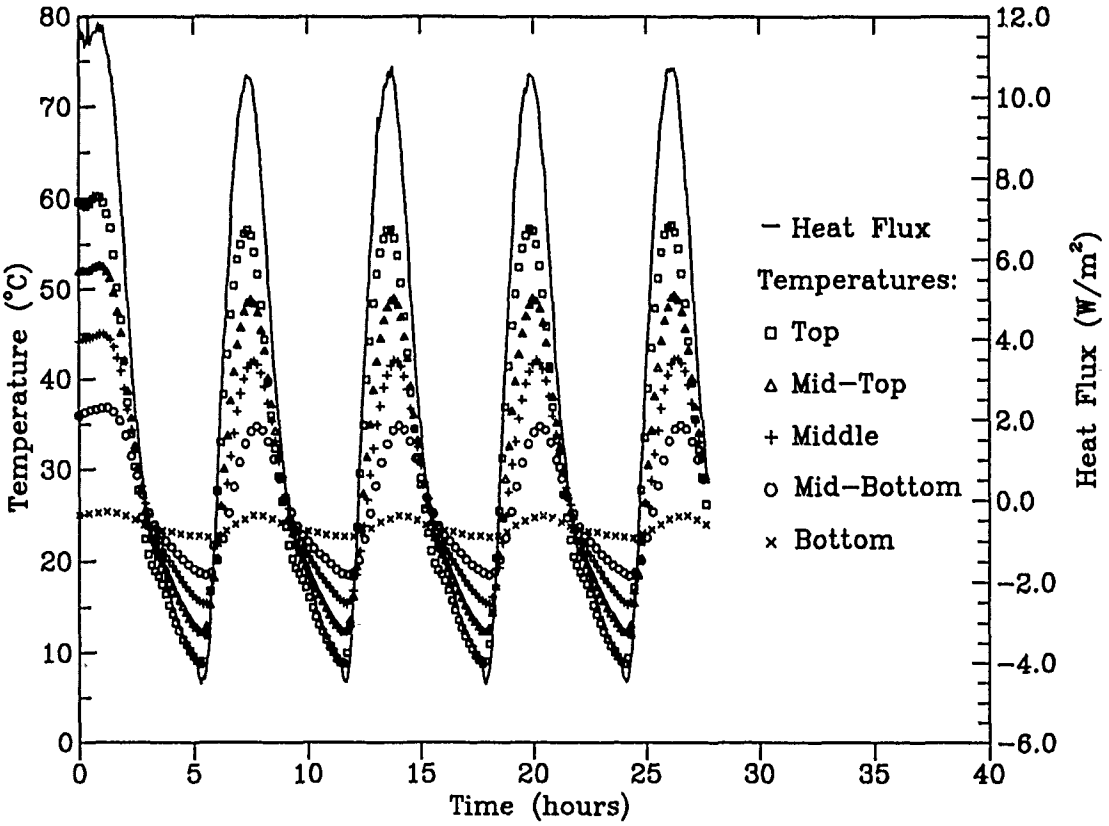

Figure 9. Heat flux and temperature profiles from test of expanded polystyrene with compressed summer days yielding CSUMEPS for PROPOR.

data that resulted. The profiles have the shape expected from data collected with the center's Roof Thermal Research Apparatus (RTRA), which is exposed to real outdoor conditions. However, the small irregularities caused by subtle changes in outdoor conditions are not present. For example, there are no effects of wind gusts or momentary cloudiness on the upper boundary temperature.

The test panel from which these data came had four EPS insulation layers, with thicknesses of 0.025 m (1 in.), 0.025 m (1 in.), 0.025 m (1 in.) and 0.038 m (1.5 in.), respectively. The configuration is like that shown in figure 1. There were five thermocouples, one at each surface exterior to this layered sandwich (labeled top and bottom in figures 8 and 9) and one at each interface (labeled mid-top, middle and mid-bottom). A heat flux transducer was located at the mid-plane.

The average heat flux for the variation shown in Fig. 8 is 0.902 W/m^2 (0.286 $BTU/h \cdot ft^2$). The average temperature at the top of the EPS is 25.7°C (78.3°F). The average temperature at the bottom is 23.4°C (74.2°F). Thus, the average temperature difference is 2.3°C (4.1°F). The R-value for 0.114 m (4.5 in.) of EPS calculated from the average temperature difference divided by the average heat flux is 2.55 $K \cdot m^2/W$ (14.3 $F^\circ \cdot h \cdot ft^2/BTU$), 19% lower than the accepted value of this thickness of EPS at the average temperature of 24.4°C (76°F). The data in

figure 9 show an average heat flux of 2.476 W/m^2 (0.785 BTU/h•ft^2) and an average temperature difference of 7.3°C (13.1°F). This yields R_{SI} = 2.9 (R_{USCS} = 16.6) for 0.114 m (4.5 in.) of EPS, 5% lower than the accepted value at the average temperature of 27.2°C (81°F). These discrepancies illustrate the difficulty of estimating R-values accurately from time-varying data that average to small values.

The tests used the same test panel, with all the thermocouples and the heat flux transducer in the same locations. But, the measurement time steps and total durations of the tests were different. For SUMEPS, the time steps were $^1/_8$ hour and the total time period was about 64 hours, resulting in a total of 387 measurement time steps. For CSUMEPS, the time steps were $^1/_{20}$ hour and the total time period was about 28 hours, resulting in a total of 555 measurement time steps. Every two to six points of those measured are plotted in figures 8 and 9 to keep the graphs readable. Program PROPOR was used with five finite difference elements in each of the four layers. The number of calculated time steps per measured time step was four.

Temperature-Independent Thermal Property Analysis for k and ρc

A series of computer runs was made with PROPOR for exactly equal time steps (0.166665 h for SUMEPS and 0.050000 h for CSUMEPS). The first set of runs estimates constant k and ρc values for various inputs. The cases run are shown in Table 4, along with the resulting estimates, their confidence intervals and the overall RMS values for the runs. The RMS values are slightly larger than in the ideal case (see Tables 1 to 3), but no larger than the experimental uncertainty in, *e.g.*, the measured temperatures. The most striking aspect of the results is that the k value is the same to four significant figures [0.03650 W/m•K (0.02109 BTU/h•ft•F)] for the four cases. Cases EPS1 and EPS2 use the SUMEPS simulation with normal 24-hour days. Case CEPS1 uses the compressed data.

Cases EPS1, CEPS1 and their combination CEPS1+EPS1 have 160 as the ratio of weights of the heat fluxes to the temperatures. Case EPS2 has

Table 4. Use of PROPOR for EPS data to estimate constant parameters k (W/m•K) and ρc (kJ/m^3•K).

Case	Time	$\sigma_q^{-2}/\sigma_T^{-2}$	k ± u_k	ρc ± $u_{\rho c}$	RMS
EPS1	0-64	160	0.03650±.00104	28.20±6.08	6.08
EPS2	0-64	Variable*	0.03650±.00256	28.65±7.06	7.05
CEPS1	0-28	160	0.03650±.00125	28.59±2.23	2.23
CEPS1 +EPS1	0-28 +0-64	160	0.03650±.00090	28.58±2.02	2.01

*PROPOR adjusts weighting factors after each iteration for as many times as specified by input parameter IWEIGH. If IWEIGH = 0, factors remain fixed at input values. Here, IWEIGH > number of iterations needed for convergence. The final ratios varied from 5 to 13.

weights recalculated by PROPOR for all iterations, resulting at the final iteration in a weight of about 91 for the heat flux and weights of about 9, 7 and 17 for the three interior temperatures. Only the ratio of these values, which varies from 5 to 17, is important. Notice that the results are insensitive to the ratio of the weights because the k values are unaffected and ρc values differ by less than 2% from values for EPS1.

Even though the estimated k values are all the same in Table 4, the confidence intervals are not. For the non-combined runs, the confidence intervals are amazingly small with the smallest and, thus, the best being for case EPS1. For it, the confidence interval is less than ±3%, which is very good. The confidence interval for the internally calculated weights should be even smaller, but this is not true. The reason is that the weights have been calculated simply on the basis of the RMS values of each temperature or heat flux history. When there are several temperature histories in the sum of squares function (three in this example) but only one heat flux history, the correlation between the temperature histories is not considered. This assigns more weight than is justified to the temperature histories than the heat flux history. The result is a poorer confidence interval for case EPS2 than EPS1.

The estimated ρc values, unlike the k values, are not exactly the same. They vary from 28.20 kJ/m^3•K (0.4205 BTU/ft^3•F) to 28.64 kJ/m^3•K (0.4271 BTU/ft^3•F), a variation of only -1.0% to +0.6% from the average. The confidence intervals are consistent in that there is a common region shared by all of them. The compressed data case, CEPS1, has the smallest confidence interval, which is expected because this case has the greatest rate of variation with time, resulting in larger sensitivity of the data to ρc.

The combined case CEPS1+EPS1 in Table 4 analyzes the data for the compressed days first and then introduces them into the data for the normal days. It uses the regularizing term in equation 2. As expected, the thermal conductivity value does not change and the confidence interval decreases slightly. The ρc value is between the other values, but is much closer to the value from CEPS1. This is expected since the ρc confidence interval for the compressed data is smaller than for the normal data. Also, the run with combined data has a slightly smaller confidence interval for ρc than case CEPS1, its main constituent. This is so because case EPS1 adds more data described by the same ρc to the data of case CEPS1 alone.

Residual Analysis

PROPOR has additional features that are useful for data analysis. One of them is an ability to review residuals, *i.e.*, the difference between measured and calculated values at each time step. It is known from statistical treatises that there are two extreme patterns for residuals: a completely random distribution which suggests that the model assumptions cannot be improved; and, an orderly array which suggests that the model is incorrect. Given the latter, one can examine the physics of the model and improve it until the distribution of residuals becomes random.

In the analysis of the SUMEPS and CSUMEPS data, both k and ρc were assumed to be independent of temperature. One expects some variation of k for expanded polystyrene over the temperature regime of the experiment. Examination of the residuals from the PROPOR calculations can help resolve this matter.

In case EPS1 in Table 4, PROPOR compared measured and calculated temperatures at all three interfaces between EPS insulation boards, *i.e.*, the mid-top, middle and mid-bottom planes. Thus, residuals are available for three thermocouple sites. Residuals for the mid-plane interface are plotted in figure 10 against time. The data for the other sites behave similarly. Note the pattern that persists, nearly cyclical peaking of the residuals at 24-hour intervals. This suggests a correlation with temperature.

To test this insight, figure 11 is a plot of the same residuals as a function of the measured temperature at the mid-plane. The orderly dependence of the residuals on temperature is more obvious than in figure 10. The greatest deviation from a zero average of the residuals is for the higher temperatures, which suggests that the model is not

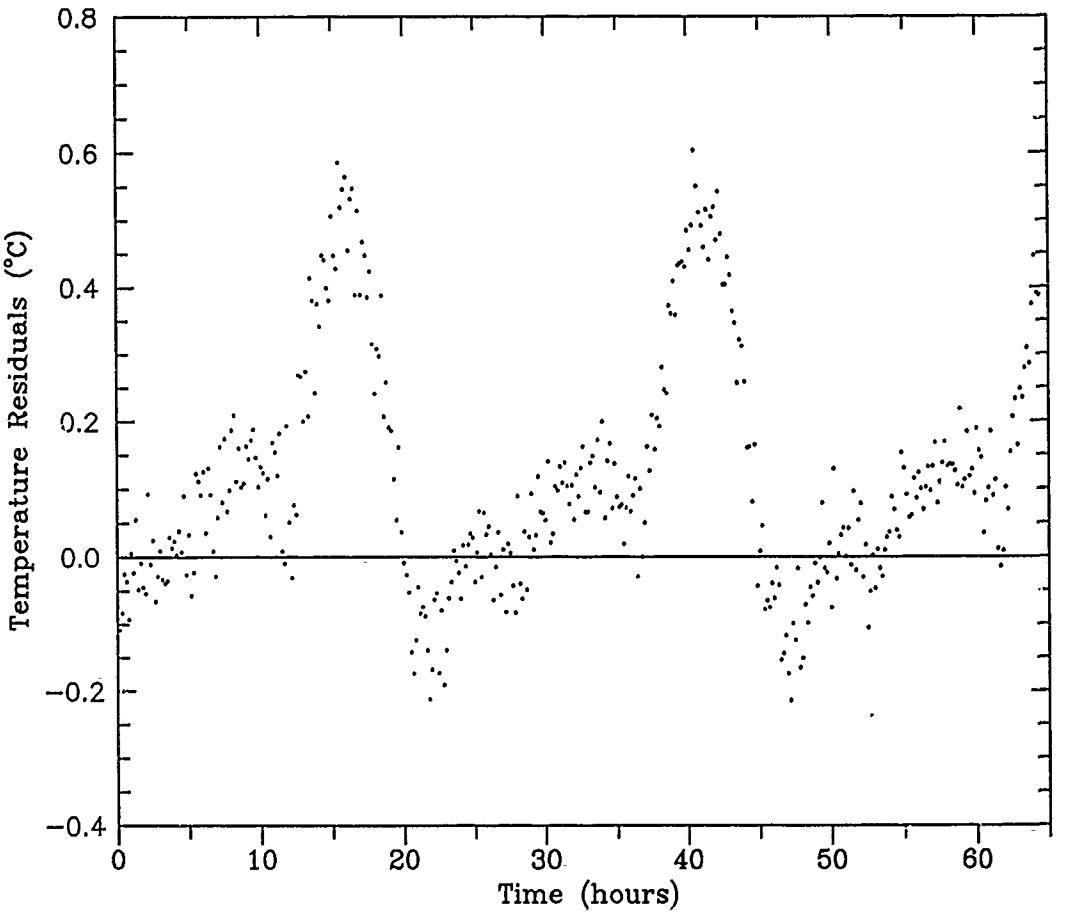

Figure 10. PROPOR analysis of SUMEPS to estimate constant properties. Temperature residuals at mid-plane for each measurement time.

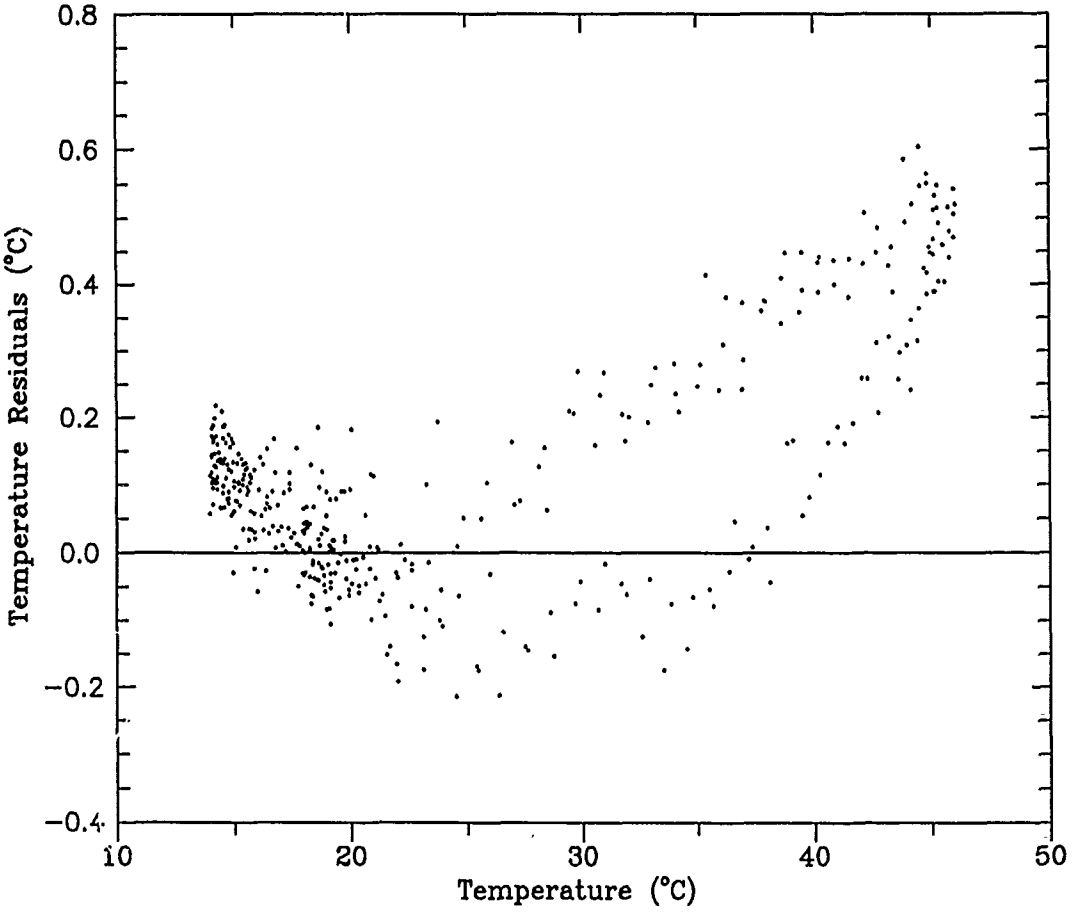

Figure 11. PROPOR analysis of SUMEPS to estimate constant properties. Temperature residuals at mid-plane as a function of the measured temperature.

capturing all the pertinent characteristics. One of the effects that has not been considered is the temperature dependence of the thermal conductivity. There is a possibility of estimating the temperature dependence of k because the estimated constant values varied so little and the confidence intervals were small.

As noted in the discussion of the k and ρc values in Table 4, the values of ρc are quite varied and their confidence intervals are large compared to k. Because the temperatures are sinusoidal, their sensitivities to k and ρc are correlated. Thus, heat flux data must be used to estimate ρc. The heat flux residuals are shown in figure 12 and again show periodic behavior. The residuals vary from -0.6 to 0.6 W/m^2 (-0.2 to 0.2 $BTU/ft^2 \cdot h$). These values can be compared with heat flux values from -4.7 to 12.3 W/m^2 (-1.5 to 3.9 $BTU/ft^2 \cdot h$). The high frequency fluctuations in figure 12 are about ±0.08 W/m^2 (±0.025 $BTU/ft^2 \cdot h$). Improvements in the model cannot reduce the heat flux residuals below this value because these fluctuations are random. Estimating slight temperature dependence of ρc in the data would be difficult.

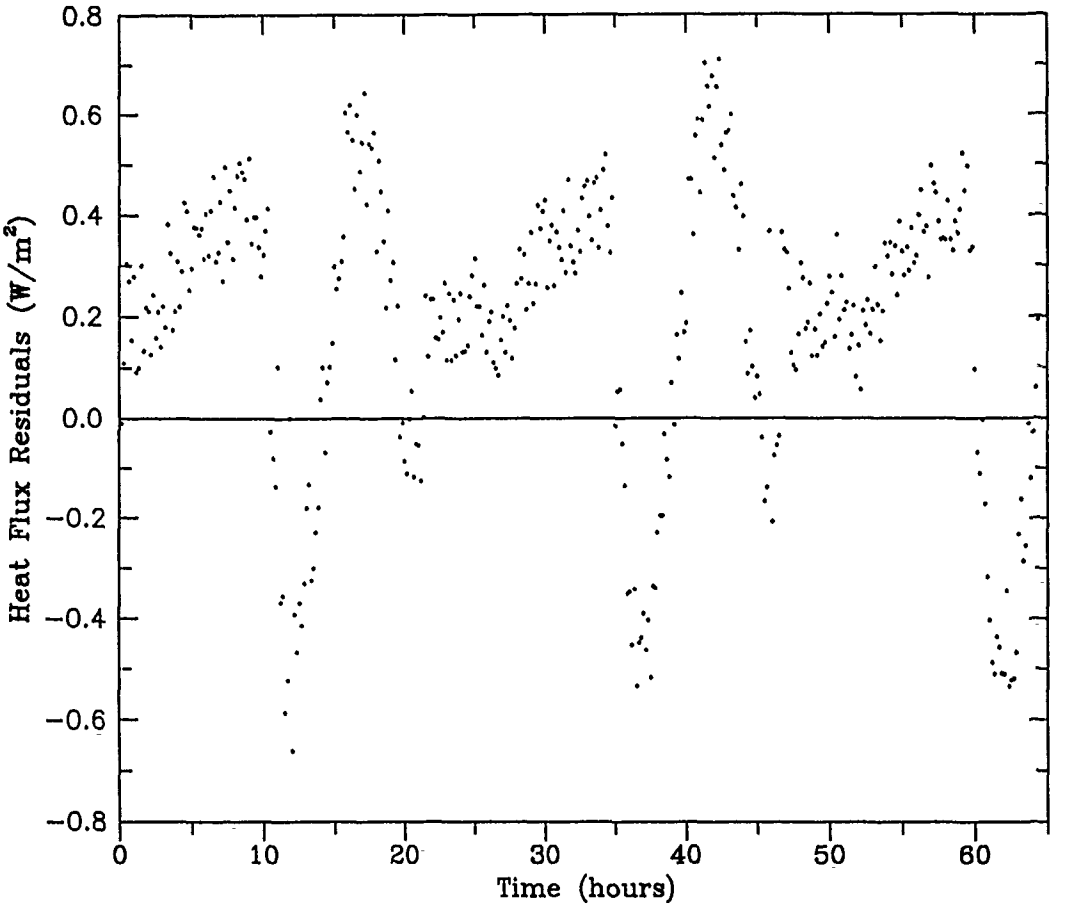

Figure 12. PROPOR analysis of SUMEPS to estimate constant properties. Heat flux residuals at mid-plane for each measurement time.

Figures 13, 14 and 15 are for CSUMEPS data, case CEPS1 in Table 4. Figure 13 shows the k estimates as they evolve during the run, called the sequential values. Figure 14 shows the sequential values of ρc. Both curves drift downward with time. It is just coincidental that the k values happened to be exactly the same in the three cases of Table 4. For example, if a few measurements less had been selected in case CEPS1, the final estimate of k would be slightly lower. The 95% confidence intervals are shown by the horizontal lines in figures 13 and 14. The confidence interval for ρc is much smaller than for the cases analyzing SUMEPS data.

Figure 15 shows the same trends in the residuals for compressed days as did figure 11 for normal days, both from the thermocouple at the mid-plane. There is again a slight positive bias and, more importantly, evidence of temperature dependence of the residuals at the higher temperatures. Because of this evidence in the data for both the compressed and normal days, temperature dependence on k is now examined.

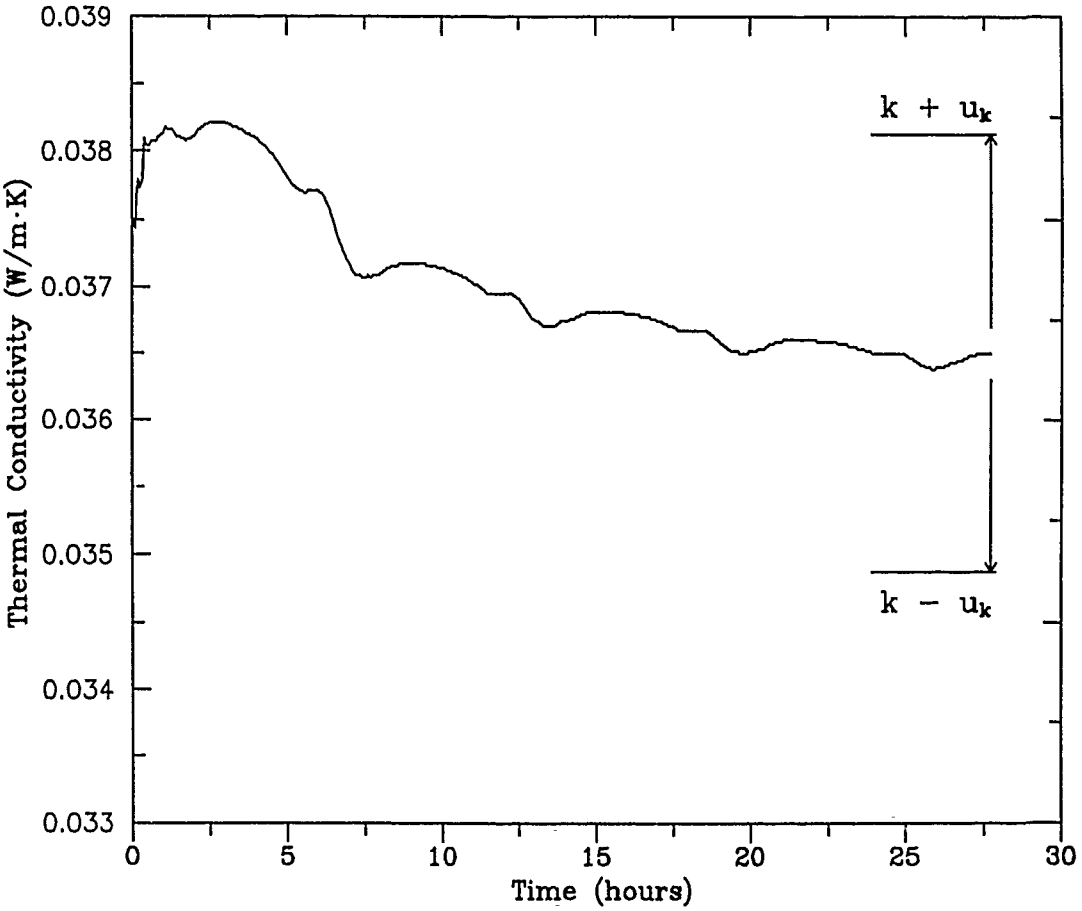

Figure 13. PROPOR analysis of CSUMEPS to estimate constant properties. Sequential values of thermal conductivity with confidence interval of final estimate.

Estimation of the Temperature Dependence of Thermal Conductivity

Table 5 displays results from PROPOR for estimating k_1 at 15.6°C (60°F) and k_2 at 48.9°C (120°F). EPS3 is for the data from normal 24-hour days and CEPS2 is for the compressed days. The sequential values for k_1 and k_2 are shown in figure 16 for EPS3. The two values of k are remarkably steady with time and the confidence intervals, shown by the horizontal lines, are quite small. The ρc values as a function of time are shown in figure 17 for the same case. Surprisingly, the ρc confidence intervals are smaller than in the corresponding analyses for constant k given in Table 4. Case CEPS2 behaves similarly.

The most interesting aspect, however, is shown in figure 18. The temperature residuals of the mid-plane thermocouple no longer show the clear dependence upon temperature noted previously in figures 11 and 15. In figure 18, the residuals are nearly zero on the average. Not shown are residuals for the other internal thermocouples. Residuals at

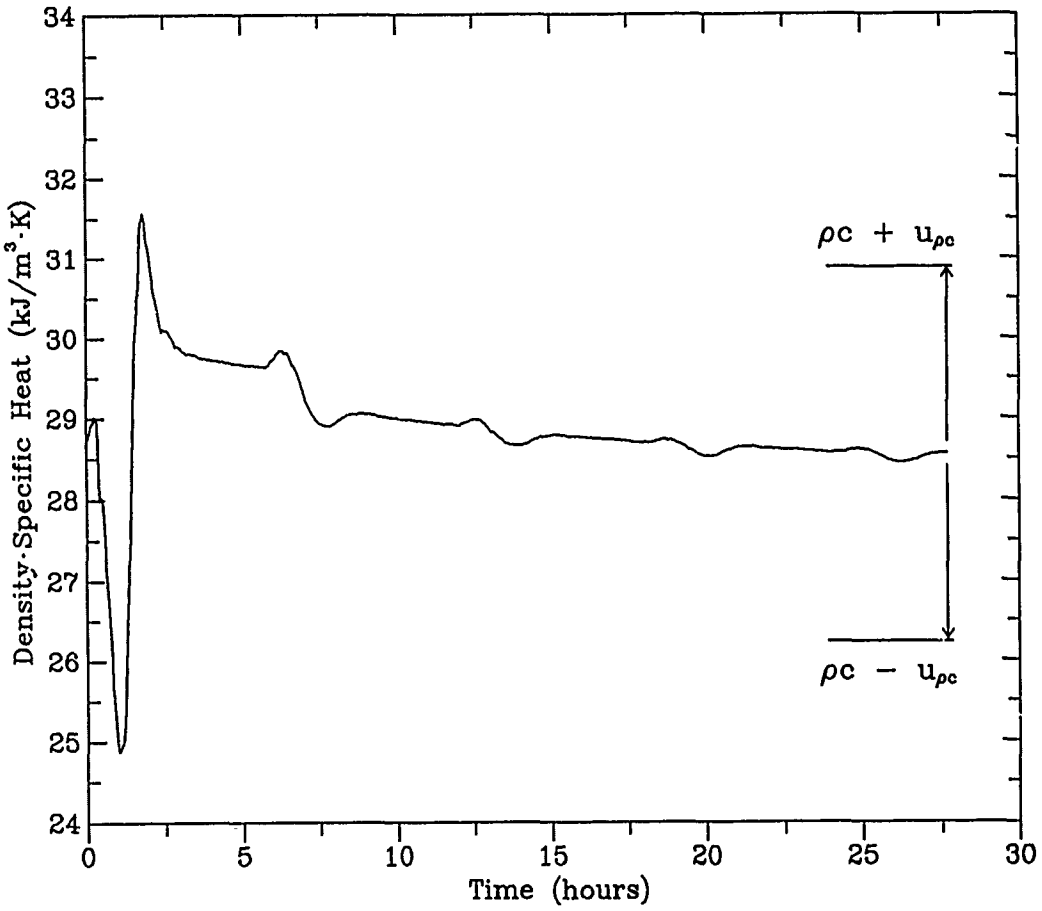

Figure 14. PROPOR analysis of CSUMEPS to estimate constant properties. Sequential values of density x specific heat with confidence interval of final estimate.

the mid-top location behave like the ones shown, except for a small positive bias. Residuals at the mid-bottom location, which sees the smallest temperature variation of the three interior sites, do retain temperature dependence. On the whole, however, the temperature dependence has been greatly reduced, indicating that the assumption of linear dependence of k on T is good. This conclusion is strengthened by the small confidence intervals shown in figure 16 and Table 5.

Table 5. Use of PROPOR for EPS data to estimate temperature-dependent parameter k (W/m•K) and constant parameter ρc (kJ/m³•K).

Case	$\sigma_q^{-2}/\sigma_T^{-2}$	$k_1 \pm u_k$	$k_2 \pm u_k$	$\rho c \pm u_{\rho c}$	RMS
EPS3	160	0.03444±.00076	0.03861±.00045	28.09±1.41	0.157
CEPS2	160	0.03435±.00154	0.03775±.00071	28.32±1.15	0.219
CEPS2 +EPS3	160	0.03861±.00093	0.03783±.00052	28.09±0.98	0.136

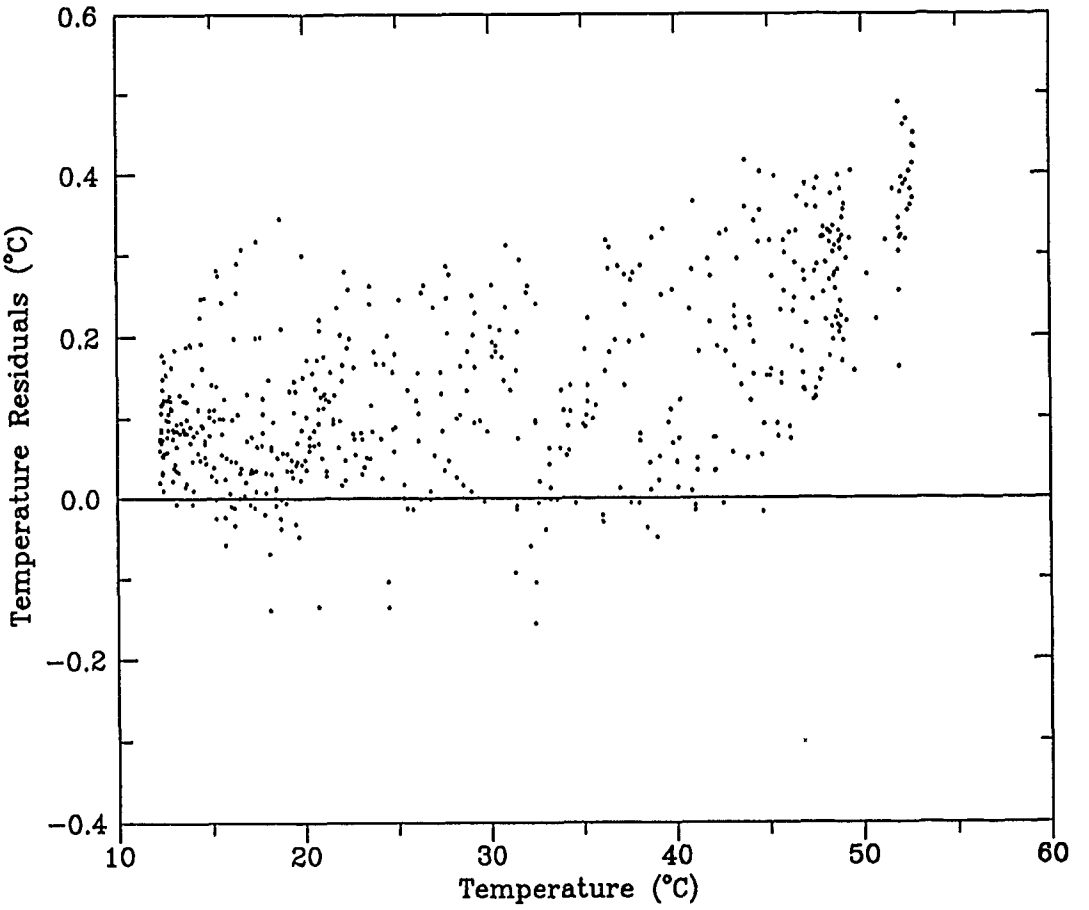

Figure 15. PROPOR analysis of CSUMEPS to estimate constant properties. Temperature residuals at mid-plane as a function of the measured temperature.

Comparison of Results to Previous Data for EPS

It is remarkable that PROPOR estimates for k and ρc of EPS from the data for the normal and compressed days are so close to each other. It indicates that the heat conduction model gives an excellent description of the physics of the situation and that the data obtained from the Large Scale Climate Simulator are very accurate.

Figure 19 depicts the thermal conductivity estimates in Tables 4 and 5, including the confidence intervals as lines above and below the data to which they belong. The important feature of figure 19 is it shows how consistent the estimates are. There is a great deal of overlap in the confidence intervals. If the average k_1 and k_2 values are used, the recommended values are 0.0341 W/m•K (0.0197 BTU/h•ft•F) at 15.6°C (60°F) and 0.0382 W/m•K (0.0221 BTU/h•F) at 48.9°C (120°F), with confidence of ±0.007 W/m•K (±0.004 BTU/h•F) in each.

Additional data shown on figure 19 were obtained from earlier steady-state tests of the same panel in the LSCS at various mean

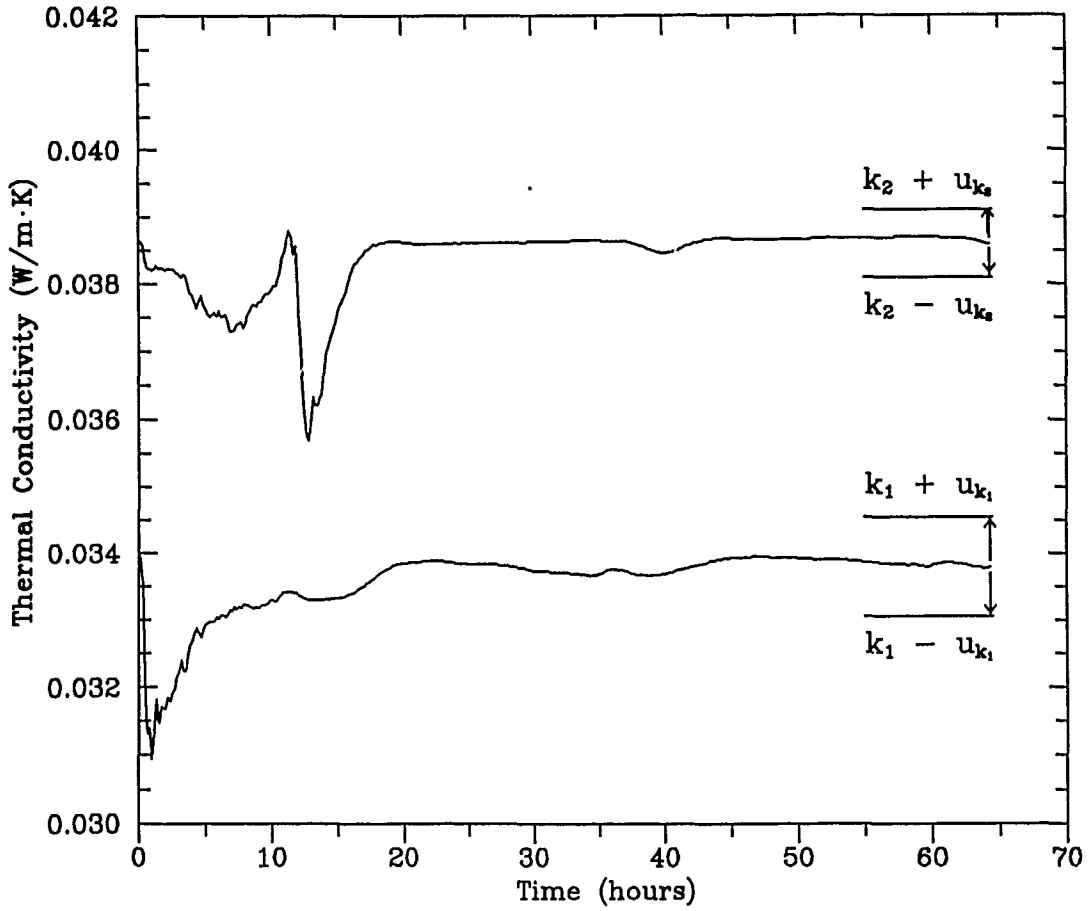

Figure 16. PROPOR analysis of SUMEPS to estimate variable thermal conductivity. Sequential values of thermal conductivities with confidence intervals of final estimates.

temperatures between -11.1° and 59.4°C (12° and 139°F). Each data point required several hours to reach a steady heat flux at the middle of the insulation for the desired temperature levels above and below the panel. Then, at least four and up to as many as 10 hours of operation were needed to collect each point. Only steady-state data which fall in the range from 10° to 55°C (50° to 131°F) are shown in figure 19, but the best fit straight line includes all the steady-state data. The k-value shown by the star at 23.9°C (75°F) is the value recommended for EPS in the NRCA Roofing Materials Guide (NRCA, 1988).

Considering the confidence intervals of the PROPOR estimates and scatter of the steady-state data, agreement among k-values measured in the LSCS is excellent. Slightly different compositions of the EPS used in it and in the NRCA test could account for the slightly higher NRCA value. The ρc value can be compared with that from an earlier use of PROPOR (Courville and Beck, 1988), which gave 33.5 to 38.2 kJ/m^3•K (0.50 to 0.57 BTU/ft^3•F), with an average of 36.9 kJ/m^3•K (0.55 BTU/ft^3•F). The present average value of 28.2 ± 1.0 kJ/m^3•K (0.420 ± 0.015 BTU/ft^3•F) is much closer to the accepted value for the EPS used in the experiments: 29.6 kJ/m^3•K (0.441 BTU/ft^3•F).

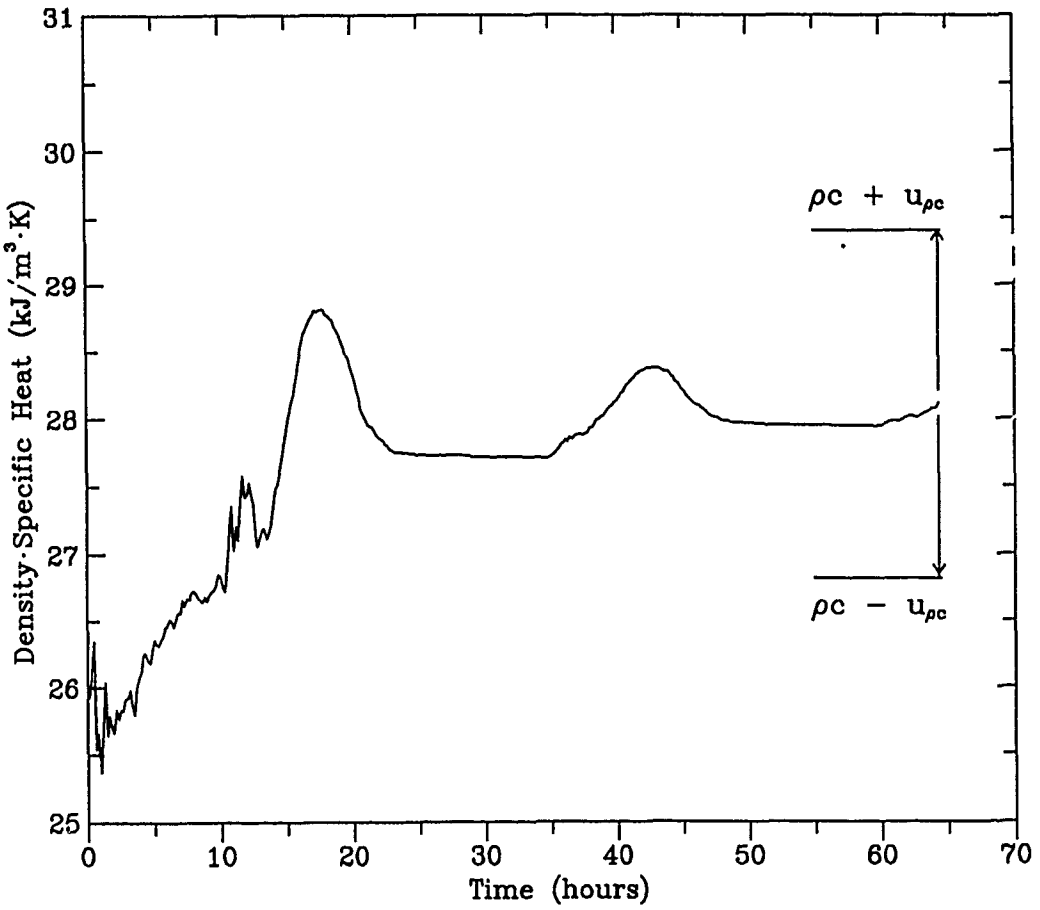

Figure 17. PROPOR analysis of SUMEPS to estimate the temperature dependence of thermal conductivity. Sequential values of the product of density x specific heat with confidence interval of final estimate.

This application of PROPOR shows that the data obtained as SUMEPS and CSUMEPS from a relatively short experiment are excellent for estimating the thermal properties of EPS at mean temperatures from 15.6° to 48.9°C (60° to 120°F). PROPOR is capable of providing accurate estimates for thermal conductivity as a function of temperature despite the fact that the average heat fluxes and average temperature differences are small for these two sets of data. The product of density x specific heat is more accurately estimated than previously, mainly because the data obtained for compressed days are more sensitive to it.

SUMMARY AND CONCLUSIONS

The program PROPOR has been applied to a problem with sinusoidally varying temperatures across a simple region with constant thermal

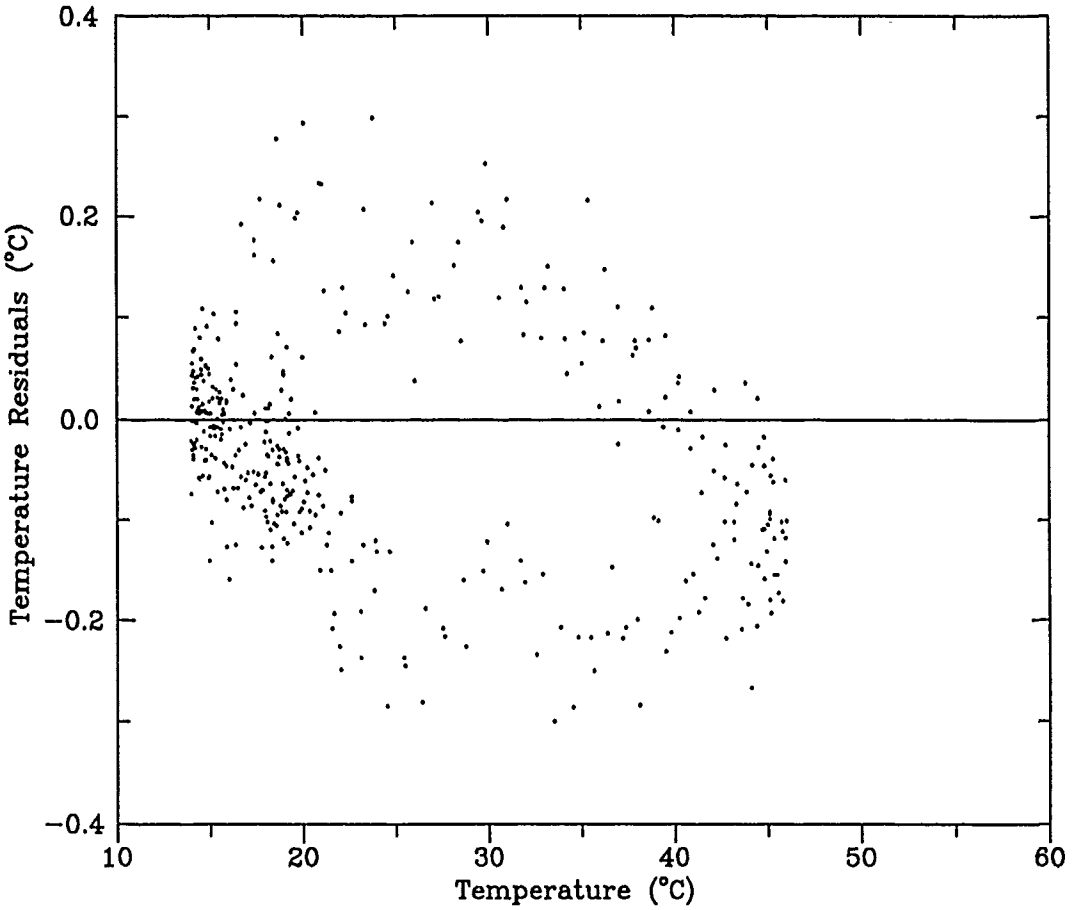

Figure 18. PROPOR analysis of SUMEPS to estimate the temperature dependence of thermal conductivity. Temperature residuals at mid-plane as a function of the measured temperature.

properties. An exact analytic solution can be generated to describe the temperatures and heat fluxes as a function of time and location. PROPOR reproduces the values of the constant thermal conductivity and the product of density x specific heat which are used to produce its input temperatures and heat fluxes. Moreover, PROPOR does not estimate nonexistent temperature dependence in these properties. The confidence in the estimates is consistent with sensitivity coefficients, values of which can be calculated from the analytic expressions for temperature and heat flux.

PROPOR has also been applied to data from a test of a fully instrumented roof system with EPS insulation in the Large Scale Climate Simulator. Temperature variation at the boundaries was typical of indoor and diurnally varying outdoor temperatures in east Tennessee on a clear summer day. The simulation was done on a non-compressed and a compressed time scale. Confidence in estimates of thermal conductivity for the EPS is better than it is for the product of density x specific heat, especially for the data on the non-compressed time scale. However, the compressed data allowed more confidence in the product of

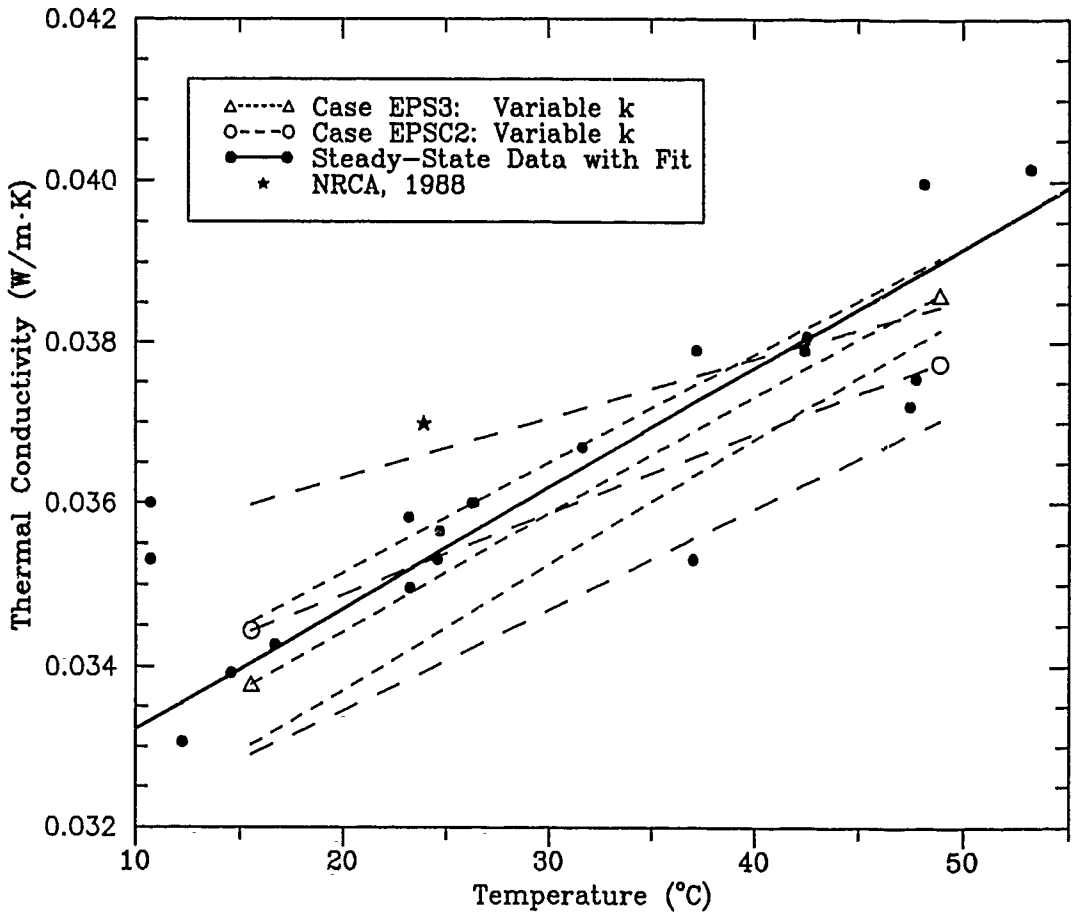

Figure 19. Summary of results from steady-state and dynamic data to estimate thermal conductivity of expanded polystyrene insulation.

density x specific heat than the non-compressed data. Both phenomena are expected from the insight to sensitivities gained from the exact solution for sinusoidal temperature variation. In addition, residual analysis showed that the thermal conductivity had temperature dependence. PROPOR was able to estimate a linear function of temperature for thermal conductivity from the dynamic data of these relatively short tests. The k-values agreed with those for the same EPS obtained from earlier, steady-state tests that took much longer to conduct because of the need to attain and verify steady-state conditions at each set of temperatures above and below the test section.

The results in this paper validate the reliability, flexibility and versatility of PROPOR for application to data from real roof systems. The sensitivity coefficients, residual analysis and confidence intervals generated during its operation show how well PROPOR estimates the values of thermal properties which describe the test materials. Very importantly, PROPOR explicitly gives the temperature range over which the estimates are valid and shows the temperature dependence of them if requested to do so. It does not matter to PROPOR

if the average heat flux and temperature difference during the test are small, or even zero.

ACKNOWLEDGMENTS

Research sponsored by the Office of Buildings and Community Systems, Building Systems Division, U.S. Department of Energy, under Contract DE-AC05-840R21400 with Martin Marietta Energy Systems, Inc. Also acknowledged is the partial support of T.W. Petrie while on sabbatical leave at the U.S. DOE Roof Research Center at the Oak Ridge National Laboratory, under Contract 19X-SE-265V with Martin Marietta Energy Systems, Inc.

REFERENCES

Beck, J.V. and Arnold, K.J. *Parameter Estimates in Engineering and Science*. John Wiley and Sons, New York, 1977.

Carslaw, H.S. and Jaeger, J.C. *Conduction of Heat in Solids, Second Edition*. Oxford University Press, London, 1959.

Courville, G.E. and Beck, J.V., Measurement of Field Thermal Performance Parameters of Building Envelope Components, *ASHRAE Transactions*, v. 94, Part 2 (1988).

Courville, G.E. and Beck, J.V., Techniques for in-Situ Determination of Thermal Resistance of Lightweight Board Insulations, *J. of Heat Transfer*, v. 111, p. 274-280 (1989).

Courville, G.E. and Childs, P.W., Measurement of Thermal Drift in Foam Insulation, ORNL/TM-11290, Oak Ridge National Laboratory, 1989.

Flanders, S.N., Time Constraints on Measuring Building R-Values, CRREL Report 80-15, U.S.A. Cold Regions Research and Engineering Laboratory, Hanover, New Hampshire, June 1980.

National Roofing Contractors Association, NRCA Roofing Materials Guide, v. 13 (Rosemont, Illinois, August 1988).

James V. Beck

Q: Can you use this method (PROPOR), for example in wet soil, when k, ρ and C_p all vary with moisture content in the same way, that is, when I expect that they are all correlated?—Ashley F. Emery.

A: The method can be used to estimate these parameters, as a function of moisture content, provided that there are adequate data and models for the phenomena. Determination of which parameters can be estimated is found by seeing if the sensitivity coefficients are large and uncorrelated. One can always try the program even though it does not explicitly treat the moisture movement.

Some suggestions for determining if the program is satisfactory are the following: a) The purposes of the study should be examined. Are the properties of intrinsic interest or is it necessary to predict temperatures only in very similar cases? b) The required accuracy should be determined. It may not be necessary to model the moisture movement to get the needed accuracy. c) The residuals for several similar and dissimilar cases should be examined to determine if there are systematic deviations rather than random ones. If the residuals are random, and on the order of the measurement errors, then the model is adequate. If not, then improvements in the model would help and the systematic deviations in the residuals contain information that can be used to improve the model.

Q: Can the PROPOR computer program be used to estimate transport parameters for moisture transfer problems?—Douglas M. Burch.

A: PROPOR presently solves only the transient heat conduction equation for thermal properties that vary with temperature. If there are negligible temperature gradients and significant moisture gradients which are described by the diffusion equation, then the moisture parameters can be measured using PROPOR, if analogous measurements are made. The diffusion coefficient could also be estimated by knowing the total weight, as a function of time.

If there are significant temperature and moisture gradients, then a model allowing for simultaneous heat and mass transfer is needed. The same principles in PROPOR could be used to estimate the parameters in such cases, provided that appropriate measurements were made, such as, temperatures, moisture content, and heat fluxes. The principles include minimization of a sum of squares function with respect to those parameters, and the use of the sensitivity coefficients to investigate what parameters can be estimated.

Q: What are the data requirements for PROPOR, for example, is temperature measurement at each change of material required?—Stephen N. Flanders.

A: The key is in examining the sensitivity coefficients. The sensitivity coefficients should be large and uncorrelated. After saying that, some general guidelines can be given. a) There must be "excess information" given. That is, the boundary value problem must have the minimum number of boundary, interface and initial conditions given or measured. b) There also must be additional measurements to determine the thermal properties. For example, to determine the thermal conductivity and volumetric specific heat of a single material with known boundary temperature histories, it is necessary also to measure the heat flux history either at some boundary or inside the body. Interior temperature measurements would help also.

Now, consider a plate composed of two layers, each with unknown thermal properties. It is theoretically possible to estimate the properties of both materials, using temperature histories and heat flux histories in one material only, in addition to known boundary conditions. However, the experiment would yield better values with temperature measurements in both materials. Confidence intervals become larger, increasing uncertainty, as the number of parameters is increased for a particular data set. See Beck and Arnold, 1977, Chap. 8, for further discussion related to use of the sensitivity coefficients and on the subject of optimal experiments.

PREDICTION OF ERRORS FOR IN-SITU MEASUREMENT OF THERMAL RESISTANCE

S.N. Flanders — U.S. Army Cold Regions Research and Engineering Laboratory, Hanover, New Hampshire USA

R.T. Mack — Dow Chemical, Freeport, Texas USA

ABSTRACT

A sufficient measurement time is key to the accurate determination of thermal resistance from in-situ heat flux and temperature data. Given some assumed thermal properties of the construction to be measured, this paper presents a means for predicting an error that might result from anticipated temperature conditions or for estimating the error that may be attributable to a temperature history. The error-prediction procedure is useful for deciding in advance whether to make in-situ thermal resistance measurements, during expected temperature conditions, of buildings and of structures that contain hot or cold media. This procedure estimates errors in the calculation of thermal resistance only, that result from obtaining non-steady-state temperature and heat flow data over a finite period of time. Random errors due to instrumentation techniques should be analyzed separately, using propagation of errors or other methods. Errors that result from changes in the apparent thermal conductivity of the constituent materials of the element studied are also beyond the scope of this paper. Such changes may be due to variation in internal temperatures, moisture migration or air movement.

INTRODUCTION

This paper is about predicting the accuracy of calculating thermal resistance of constructions used for buildings or industrial processes from in-situ measurements of heat flux that would result from expected changes in temperature. The paper also addresses the accuracy of calculation of thermal resistance based on a finite history of heat flux and temperature data. The most convenient way to study these is with a mathematical model of the thermal responses of different constructions to varying temperatures. The work reported here employs

such a mathematical model in a computer program that allows one to investigate a variety of different materials in layers of the user's choice, subject to user-defined temperature boundary conditions. The model provides the heat fluxes that would result from measurement and allows one to see how long would be necessary for a calculation of thermal resistance to achieve a desired accuracy.

Calculation of thermal resistance from in-situ temperature and heat flux data is useful for knowing the performance of a wide range of engineered items that require insulation, including clothing, buildings, and cryogenic or high-temperature containers for industrial and aerospace applications. This paper discusses how to predict the errors that result from the calculation of thermal resistance in buildings and industrial processes from periodically changing temperature and heat flux data over a limited time period. Reference [1] provided the basis for predicting the error in the thermal resistance calculated from in-situ data over a finite measurement time, when compared with the value for thermal resistance that would be determined by a steady-state laboratory test.

Typically, heat flux data are obtained with heat flux transducers (HFTs) and with temperature sensors (thermocouples, thermistors, etc.). The temperature sensors are placed on either side of a cross-sectional segment of interest to register a difference in temperature across that segment (ΔT) and the HFTs are placed on a surface of the same segment that is accessible, representative, and with as few uncontrollable thermal influences as possible.

In-situ measurement has several possible sources of error, including sensor calibration and sensor placement [2]. Calculating thermal resistance and other thermal parameters from in-situ data introduces further problems that arise from how well the location of temperature and heat flux sensors, on or within the construction, characterize the delays inherent in heat transfer [3-5]. Data about heat flux and temperature collected at several points within the thickness of the construction offer a more rapid determination of thermal resistance than do data obtained only at the surfaces of the construction. However, this report limits the discussion to data obtained on the surfaces of the construction.

This paper reviews the structure of a menu-driven computer program and then illustrates its use with several examples of components that would be used in 1) building construction and 2) industrial processes. The examples of building components illustrate the effects of mass and insulation at a low ΔT across the construction. In such cases the HFTs are typically on an indoor surface where a controlled, stable temperature exists. The examples of industrial process components illustrate the effect of a high ΔT with heat flow going in one direction for cryogenic cases and in the other direction for high temperature cases. In these examples, the HFTs are on the weather side where the magnitude of temperature change is great and the period of variation is long.

BACKGROUND

Overview of ASTM HFT standards

This paper assumes that heat flux transducers (HFTs) are used to obtain in-situ heat flux data. The issues discussed here may also apply to other methods for measuring heat flux. Several ASTM Standards offer a good overview of the issues of calibrating thin HFTs, instrumenting buildings with HFTs, and calculating thermal resistance from the resulting in-situ data. The standards and references contained within them address the following topics:

1. ASTM C 1130 discusses calibration of HFTs to obtain a factor that converts the electrical output of the HFT to a heat flux value. This conversion factor depends on the conductivities of the particular materials that surround the HFT when it is installed in situ.
2. ASTM C 1041 deals with the use of HFTs in industrial applications. It includes a test for essentially steady-state conditions, which, when satisfied, permit the calculation of the thermal conductivity of the insulation that was instrumented.
3. ASTM C 1046 describes how to apply HFTs and temperature sensors on buildings so that they will provide readings that are representative of the construction on which they are placed. The idea is to ensure that heat transfer across the surface of each sensor is similar to heat transfer across the surrounding surface.
4. The goal of ASTM C 1155 is to permit calculations of thermal resistance from in-situ data. It further constrains the placement of HFTs and temperature sensors so that they fall within chosen regions that are apparently thermally consistent throughout, as seen by thermography. The defined region must have no significant heat flow that bypasses the instrumentation in a manner uncharacteristic of where the instrumentation was placed. For example, one should characterize and instrument a stud as a region separate from an insulated stud bay. A borderline case would be an insulated stud bay that contained a convection cell. Multiple HFTs might adequately characterize the total heat loss through that region.

Time effects on thermal resistance calculations

In the absence of thermal storage effects, the calculation of thermal resistance or conductance is, in principle, a constant ratio between difference in temperature across a construction (ΔT) and heat flux (q). Ideally, determining this quality requires unvarying temperatures, assuring a sufficiently steady heat flux after a time. When ΔT and, as a result, q change periodically, the long-term trend for the ratio between the averages of these transient values tends toward the laboratory steady-state value for thermal resistance ($\Delta T/q$) or conductance ($q/\Delta T$). This relationship is made complicated under actual conditions by changing thermal conductivity of the constituent materials as a function of temperature and by the possible presence of convection or other nonconductive heat transfer effects.

Even when instrumentation accuracy and appropriate placement of sensors are achieved, varying temperature conditions usually make accurate calculation of thermal resistance or conductance difficult. Temperature variations over time produce a response in heat flux that

is a delayed history of previous temperature variations. Mass and thermal resistance make the delay more pronounced. Calculational techniques are available that are designed to overcome these problems [6,7], but these techniques have different strengths and failings, depending on the data that are fed into them.

For anyone who tries to determine thermal resistance from values of ΔT and heat flux, measured in situ, the problem is something like this. At first, when one instruments a component with temperature sensors on both sides and an HFT on one side, the data that one starts to see are the current temperatures, but the heat flux values represent temperature histories from before the time the equipment was turned on. When the measurement is completed, one observes heat fluxes from temperature variations that occurred during the measurement period, but the temperature variations last observed will be affecting future, unobserved heat flux. Therefore, information is missing about the temperature history that caused the heat flow observed at the beginning of the measurement and about heat flow that resulted after the measurement was over from observed temperature histories. The missing information introduces inaccuracy into a calculation of thermal resistance, e.g., the ratio, (average ΔT)/(average q), obtained under varying conditions only approximates the ratio, $\Delta T/q$, obtained under steady-state conditions. As a result, it becomes necessary to measure for a long enough period that the uncertainties of the startup and finishing phases of measurement are small compared to the total accumulation of data.

With some reasonable knowledge of the thermal properties of the construction to be measured and of the temperature variations to be encountered, one may anticipate how long such a measurement may require. This paper presents a thermal model environment that simulates the heat flow resulting from defined driving temperatures. The model permits using different means of calculating thermal resistance to determine how much time would be required to achieve an acceptably accurate calculation.

Previous thermal modeling of transient temperatures and heat flow

Modera et al. [1] offer a model for investigating the time effects of varying temperature in making thermal resistance calculations. They offer an exact calculation of heat flow that results from temperature variations through a defined sequence of materials. This technique can also be found in Buffington [8] and in Reddy and Krishnamoorthy [9]. A sketch of thermal properties is possible by calculating the effective thermal diffusivity of the constituent layers of the construction, a technique presented by Schimmel et al. [10]. The present study expands on the work of Modera et al. to allow a convenient way to examine multiple frequencies, drawn from actual data, if desired.

Infrared mapping of thermal resistance

A promising future means for in-situ measurement of thermal resistance incorporates the use of thermography with HFTs to characterize larger areas than with the HFTs alone. Flanders and Marshall [11,12] advocated interpolating the values between extreme

values that were characterized with HFTs. Mack [13] is developing a technique based on just one HFT location. The use of infrared thermography for calculation of heat flux is based on developments by Anderson [14] and McIntosh [15]. However, thermographic characterization of thermal resistance requires appropriate use of corroborating data from HFTs and temperature sensors, and requires that the imagery be obtained at an appropriate time during the temperature cycling of the surface that is being measured.

CALCULATION OF THERMAL RESISTANCE FROM SIMULATED IN-SITU DATA

The program that models the thermal behavior of construction components and simulates the calculation of thermal resistance, using the results of temperature and heat flux measurements, requires the following steps:

1. Create a menu of materials and their thermal properties. The menu constitutes the choice of materials for defining the construction.
2. Define the order of layers of materials from (1) and the thicknesses of those layers, starting from the side that has the HFTs placed on it.
3. Define a set of periodic temperatures on the near and far sides of the construction.
4. Calculate admittances for the construction based on the 12 largest periods defined in (3).
5. Calculate a time series of temperatures and heat fluxes on the near and far surfaces of the component.
6. Calculate the thermal resistance in the same manner that would be done if the data were obtained from in-situ measurements, determine whether the calculation is stabilizing on a single value, and compare whether the calculated value is within a defined accuracy.

Materials Menu

The materials are available from a file that contains entries based in SI units or from one based in customary English units. The entries are for a material name, density, thermal conductivity, and specific heat, as demonstrated in Table 1. A simple editor menu permits viewing, adding and deleting complete line entries.

Layer definition

The order and thicknesses of constituent materials are essential parts of calculating the behavior of the component. If one defines a "near" and a "far" side of the component, such that the HFT is assumed to be on the near side, then the order of the component materials would start at the far side. Typically the near side on a building would be indoors, where the temperature is usually controlled and direct solar radiation is avoidable. In industrial processes the near side would be on the outside of the container, since placing the HFT in a cryogenic or high-temperature environment would not be practical.

To illustrate the use of the model, six types of components are illustrated in this paper, three each from building construction and from industrial processes. These are illustrated in Tables 2 and 3.

Table 1. Sample materials properties available to the model [16].

Description	Density (kg/m^3)	Conductivity (W/m·°C)	Specific Heat (kJ/kg·°C)
Brick - common	1920	0.720	0.800
Gypsum wallboard	800	0.1605	1.220
Glass fiber insulation	100	0.036	0.960
Extruded polystyrene insulation	42	0.029	1.220
Polyisocyanurate insulation	32	0.020	0.920
Cellulose insulation	42	0.042	1.380
Stainless steel	8025	1.356	0.502
Monel	8826	2.136	0.0532
Inconel	8498	1.255	0.456
Cellular glass insulation	136	0.050	0.754
Fireclay brick - 260 °C	2002	1.040	0.959
Fireclay brick - 427 °C	2002	1.070	0.959

Table 2. Examples of modeled building components. Thermal resistance in SI units (RSI) of $m^2 \cdot K/W$.

Description	Thickness (cm)
Low-Mass, Insulated (RSI = 2.67)	
1. Gypsum wallboard	1.91
2. Glass fiber insulation	8.89
3. Gypsum wallboard	1.27
Low-Mass, Uninsulated (RSI = 0.12)	
1. Gypsum wallboard	1.91
Medium-Mass, Insulated (RSI = 2.69)	
1. Brick - common	10.16
2. Glass fiber insulation	8.89
3. Gypsum wallboard	1.27
Medium-Mass, Uninsulated (RSI = 0.22)	
1. Brick - common	10.16
2. Gypsum wallboard	1.27
High-Mass, Uninsulated (RSI = 1.39)	
1. Brick - common	100.00

Table 3. Examples of modeled industrial components. Thermal resistance in SI units (RSI) of $m^2 \cdot K/W$.

Description	Thickness (cm)
Cryogenic Storage (RSI = 7.63)	
1. Inconel	1.27
2. Polyisocyanurate	15.24
Uninsulated Furnace (RSI = 0.290)	
1. Fireclay brick - 427 °C	30.5
2. Stainless steel	0.63
Insulated Furnace (RSI = 3.34)	
1. Fireclay brick - 427 °C	30.5
2. Stainless steel	0.63
3. Cellular glass insulation	15.2

Define periodic temperature changes

Up to 12 frequencies may be defined for temperature changes. The user actually specifies amplitude of temperature swing (in °F or °C) and period of swing (in minutes). These may be split between the near and far sides of the component at the discretion of the user.

Frequencies are sorted with the longest period (inverse of frequency) first, to determine the most dominant 12 frequencies to use. The other associated factors of amplitude and the nearside-farside flag are sorted at the same time. Ramp-like behavior is handled by using long-period sine waves.

The user must choose a calculation period that is compatible with the temperature frequencies. In the examples in this paper the calculation period was 20 min. Therefore it was possible to see effects that occurred at 30-min intervals that would have been hidden by a 30-min calculation period. In the examples that were tested on the simulation program, temperature values were chosen as shown in Table 4.

Table 4. Temperature variations used in examples.

	Near Side			Far Side		
Component	Temperature (°C)	± Variation (°C)	period (h)	Temperature (°C)	± Variation (°C)	period (h)
Building - simple case	20	0	0	0	20	24
Building - multiple frequencies	20	2	0.5	0	5	156
					20	24
					5	3.75
					4	0.38
					3	0.22
Furnace	20	11	24	427	3	0.15
Cryogenic	20	22	24	-200	3	0.15

Calculation of admittances

Admittances must be calculated (see App. A) for each of the 12 or fewer frequencies chosen. The admittances are derived from a matrix that relates temperature and heat flux on the near and far sides of the component.

Calculation of temperatures and heat fluxes

The specification of baseline nearside and farside temperatures, together with up to 12 frequencies and magnitudes of variation distributed between the two sides allow for the calculation of a temperature time series. This periodic time series and the admittances determined for each frequency allow for calculation of heat flow (q) at the near surface (with the HFT), according to the following formula, which is derived in Appendix A:

$$q = \bar{q} + \sum_{i=1}^{12} q_{near}(\omega_i) \qquad (1)$$

where:

i = subscript for frequency.

$$\bar{q} = (\bar{T}_{near} - \bar{T}_{far}) \cdot U \qquad (1a)$$

= The average heat flux through the near side.

$$q_{near} = (Y_{near} \cdot T_{near}) - (Y_{across} \cdot T_{far}) \qquad (1b)$$

= The instantaneous heat flux through the near side.

where:

U = overall conductance of layers 1 to N.

$\bar{T}$ = the baseline temperature about which sinusoidal variation takes place.

$\bar{q}$ = the baseline q.

Y = admittance for a given frequency (ω_i).

Near and far are subscripts referring to the surfaces of the construction when referring to temperature (T), heat flux (q), or admittance (Y).

Across is a subscript referring to the admittance across the construction.

Calculation of thermal resistance and convergence

The time series of calculated near and far side temperatures and of near side heat fluxes are taken to be the measured output of temperature sensors and an HFT. The estimate of thermal resistance is then calculated on a continuing basis, according to the formula:

$$R_e(t) = \sum_{t=0}^{t'} [T_{near}(t) - T_{far}(t)] \Big/ \sum_{t=0}^{t'} q_{far}(t) \qquad (2)$$

where resistance (R) and temperature (T) are defined at specific times (t) at the surfaces denoted by the subscripts, near and far. The subscript e indicates that R is a working estimate.

As an indicator of whether the calculation of thermal resistance, R_e, is converging on a stable value, the following calculation of a convergence parameter, CONV, is made:

$$CONV(t,interval) = [\ R_e(t) - R_e(t - interval)\ ] / R_e(t) \qquad (3)$$

where the interval is chosen by dividing the longest harmonic period by four. The complete time series for the temperatures, heat flux, estimate of thermal resistance and convergence indicator (CONV(t,interval)) are placed in a file for examination. In this way a comparison may be made between when CONV(t,interval) indicates that the stability of the solution remains within chosen bounds (e.g. $|CONV(t,interval)| \leq 0.1$) and when the estimate of thermal resistance remains within defined error bounds about the true thermal resistance, defined by:

$$ERR(t) = [R_{ref} - R_e(t)] / R_{ref} \qquad (4)$$

where R_{ref} is the steady-state thermal resistance that would be obtained in a thermal test apparatus at steady-state surface temperatures that are the mean temperatures observed on the inside and outside surfaces in the field.

EXAMPLES THAT USE THE SIMULATION

The simulation program was tested using examples that are 1) typical of building components with the HFT on a temperature-controlled indoor surface and significant variation in temperature occuring outdoors and 2) typical of industrial processes with the HFT mounted on the outside of the vessel that was assumed to have either a cryogenic or high-temperature fluid within. The error due to calculation, ERR(t), is the primary object of interest. A look at CONV(t,1/4ω) and CONV(t,6h) gives us insights into their value for estimating ERR(t) while monitoring the data as they are recorded, since we cannot know ERR(t) in the field. Table 4 contains the specific temperature assumptions. Appendix B contains a sample session, using the program.

Building component examples

There is a large set of causes for such factors as thermal resistance, thermal mass, average ΔT, periodic variation of surface temperatures and their effects on ERR(t). Modera et al. [1] have explored a set involving ΔTs and periodic variation in amplitudes that are about half those illustrated in this paper. One's expectations about measurement time needed to achieve a desired accuracy can be very different, based on seeing the different sets of assumptions presented in this paper. The outdoor temperature extremes (Table 4) are greater here than in Modera et al., but are plausible values for a south-facing wall in winter or for a roof. There are many more

possible assumptions not explored in either paper, hence the need to put the software described here in the hands of the would-be investigator of thermal resistance or conductance.

The building examples illustrate the effects of frequency of ΔT, phase of ΔT as the measurement commenced, thermal mass, and superimposition of frequencies. The following examples shared the temperature conditions described in Table 4. The five cases of low-mass walls, both insulated and uninsulated, of medium-mass brick walls, both insulated and uninsulated, and of an uninsulated high-mass wall are also described in the materials specifications of Table 2.

Calculated thermal resistance

Figure 1 shows the relationship between ΔT and calculated thermal resistance. The ΔT represents the multiple frequencies case in Table 4 and the construction is the lightweight insulated wall. Notice that, although thermal resistance appears to stabilize, 10% error bars drawn around the true value, R_{ref}, show that the estimate of thermal resistance, R_e, exceeds the 10% error value well into the second week of measurement. This demonstrates the need to track the progress of R_e long after it has appeared to stabilize. Another important consideration is that the oscillations of R_e don't have R_{ref} as their mean. Therefore, visual monitoring of R_e may also result in a bias.

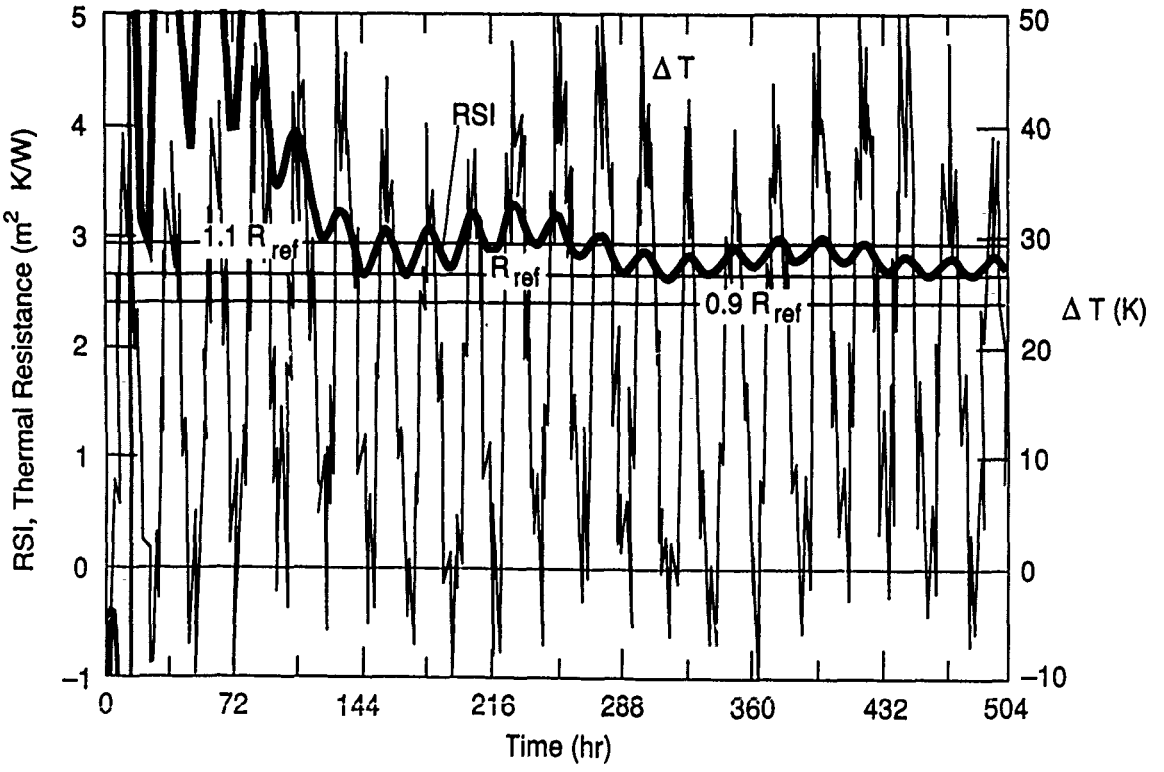

Figure 1. ΔT and R_e for the lightweight, insulated wall example and the multiple-temperature frequency case (Table 4).

Low-frequency variation of ΔT

Figure 2 suggests that long-period components of the change in ΔT are significant contributors to this long time required for calculating R-value within the error range chosen. ERR(t) is shown in relation to CONV(t,1/4ω) and CONV(t,6h). CONV(t,6h) is clearly an inadequate indication of the stability of R_e, whereas CONV(t,1/4ω) works much better to represent ERR(t), the actual deviation of R_e from the true thermal resistance.

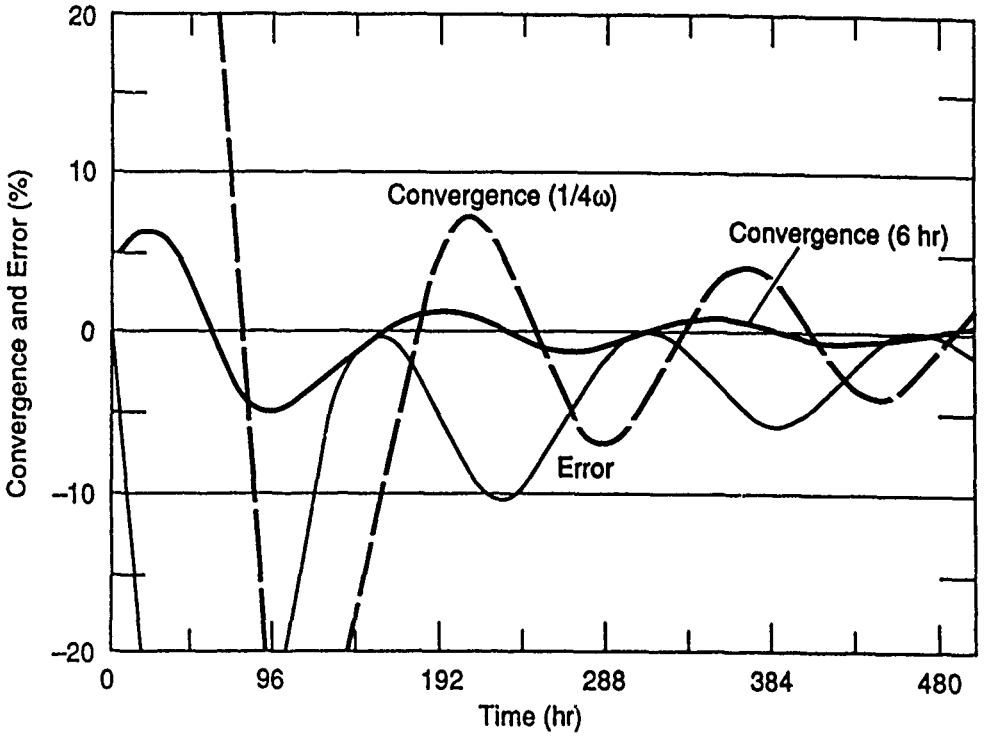

Figure 2. ERR (t), CONV(t,1/4ω), and CONV(t,6h) for the low-mass, insulated wall example and a ΔT that varies ± 5 K over a period of a week from a mean ΔT of 20 K.

Effect of frequency

Figure 3 demonstrates how much more rapidly ERR(t) comes to within 10% bounds for a four-hour period of ΔT with a an average value of 20K and a swing of 20K about the mean value than for a 24-hour period with the same mean and amplitude values. Also, it can be seen that CONV(t,1/4ω) slightly underpredicts the magnitude of ERR(t).

Effect of phase angle

Figure 4 demonstrates that even with purely cyclical changes in ΔT, it matters when during the cycle the measurement begins. The graph uses the simple ΔT case, but changes the phase by starting the measurement 0, 6, 8, 12, and 18 hours into the 24-hour cycle. Starting the calculation at a phase of other than 0 hours offers significant penalties in having the error quickly confine itself within a desired bounds.

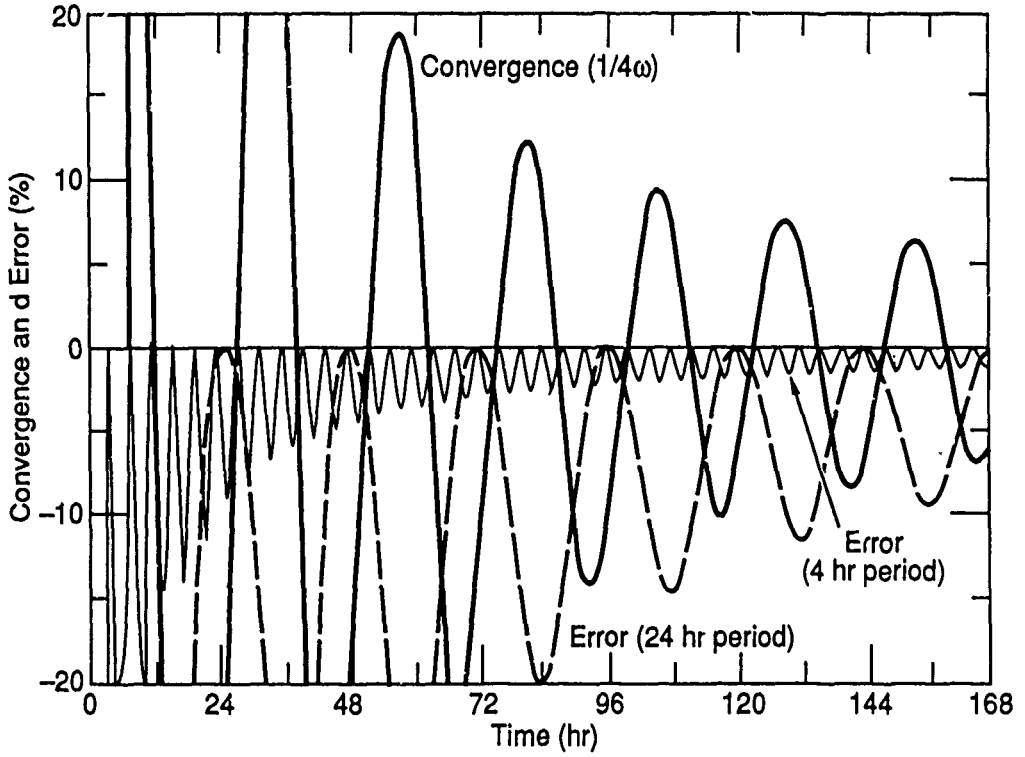

Figure 3. ERR(t) for simple variation of ΔT cases where the periods is 4 h or 24 h. CONV(t,6h) is shown for the 24-hour case.

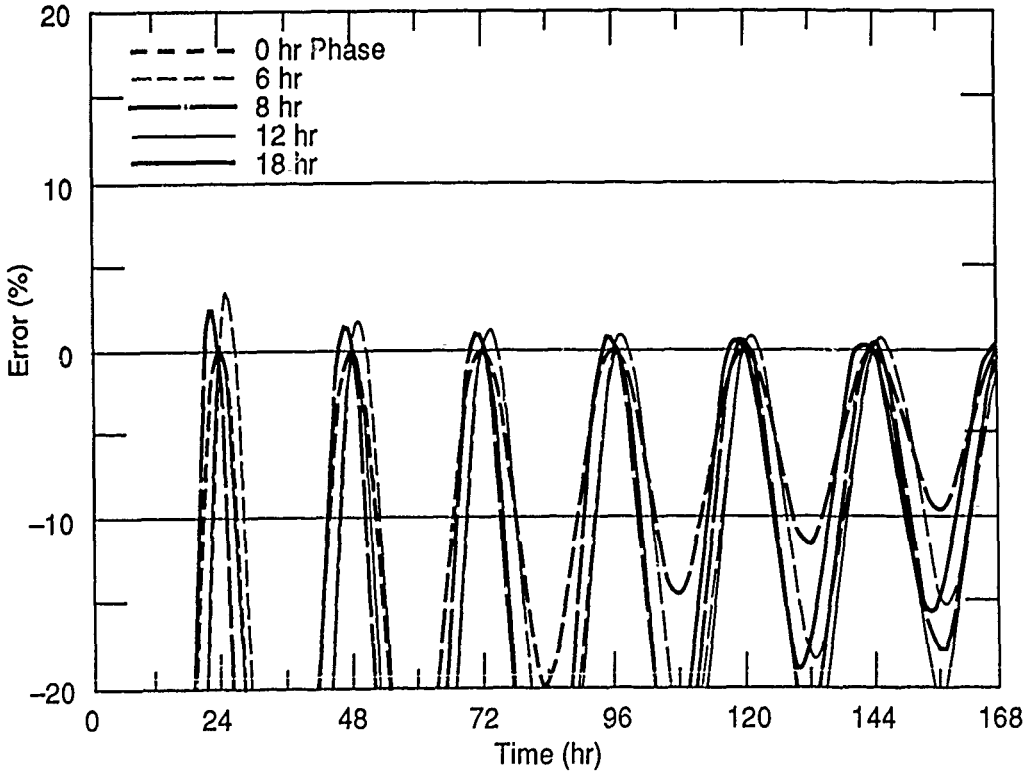

Figure 4. ERR(t) for a 24-hour period with the measurement commencing 0, 6, 8, 12, and 12 hours after the beginning of the ΔT cycle for the simple variation case (Table 4).

Effect of phase angle

Figure 4 demonstrates that even with purely cyclical changes in ΔT, it matters when during the cycle the measurement begins. The graph uses the simple ΔT case, but changes the phase by starting the measurement 0, 6, 8, 12, and 18 hours into the 24-hour cycle. Starting the calculation at a phase of other than 0 hours offers significant penalties in having the error quickly confine itself within a desired bounds.

Effect on different constructions

Figure 5 illustrates the effect of the multiple-frequencies case of temperature variation on four constructions, 1. low mass, insulated, 2. medium-mass, insulated, 3. medium-mass, uninsulated, and 4. high-mass, insulated. The uninsulated constructions, both of medium and high mass, approach any given criterion for accuracy more quickly than the insulated cases. The two insulated cases, one with a brick veneer, the other with a gypsum external layer perform virtually identically. The insulation is the dominant factor and the thermal capacitance of the exterior layers is surprisingly similar in both examples.

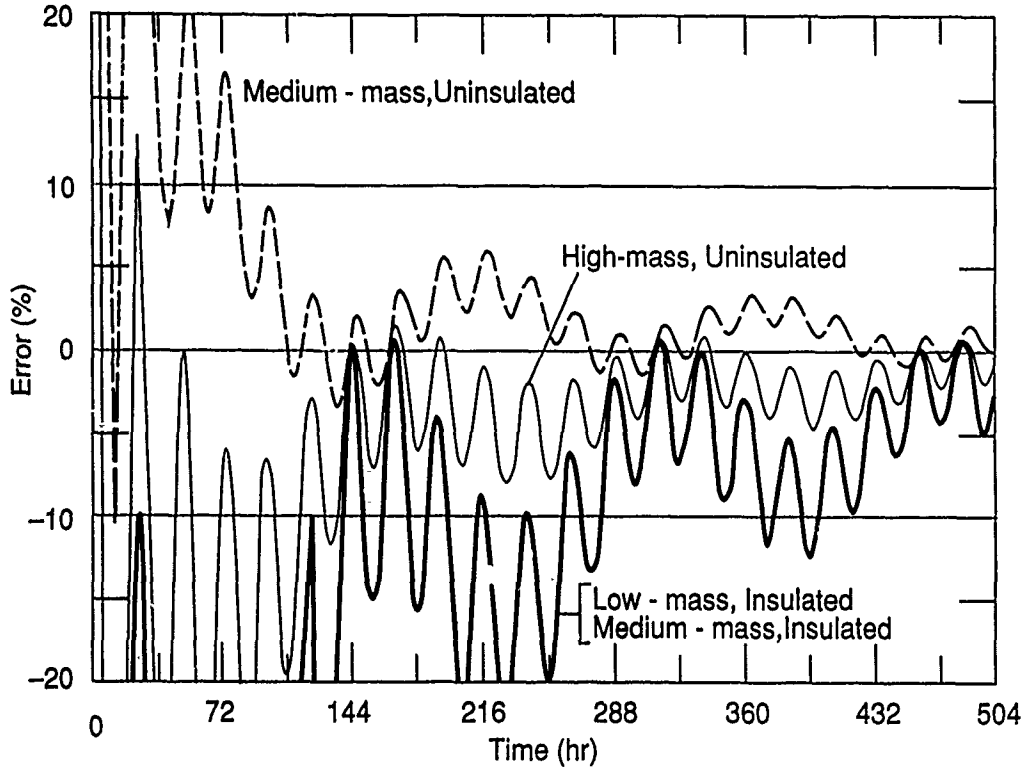

Figure 5. ERR (t) for the multifrequency case (Table 4) for four constructions: 1) low-mass,insulated, 2) medium-mass, insulated, 3) medium-mass, uninsulated, and 4) high-mass, uninsulated.

Equation 2 cannot compute thermal resistance, except within bounds of the precision chosen by the user. Table 5 demonstrates for the three building examples how long it was necessary to measure for 1) the calculated thermal resistance, R_e, to remain within 10% of the true value and 2) the convergence parameter, CONV(t,1/4ω), to remain within ± 0.10. The Discussion makes three points about estimating ERR(t) with R_e(t) and CONV(t,1/4ω).

Table 5. Time (hours) until R_e from Eq. 2 remains within 10% of R_{ref} and CONV(t,1/4ω) from Eq. 3 remains within ± 0.1 for the simple case of a 24-hour cycle in outdoor temperature.

Description	Remain:>0.9 R	<1.1 R	Conv =	-0.1	+0.1
Medium mass, insulated	15.7	>167		117	105
Medium mass, Uninsulated	39.7	0		35	45
Light mass, Insulated	0	134.3		95	83.3

These results show that, because of the happenstance of calculation cycles, the convergence parameter is not guaranteed to bracket the calculation of thermal resistance with the desired precision. Therefore, it is wiser to choose a more conservative acceptable value for CONV(t,1/4ω) than the desired precision.

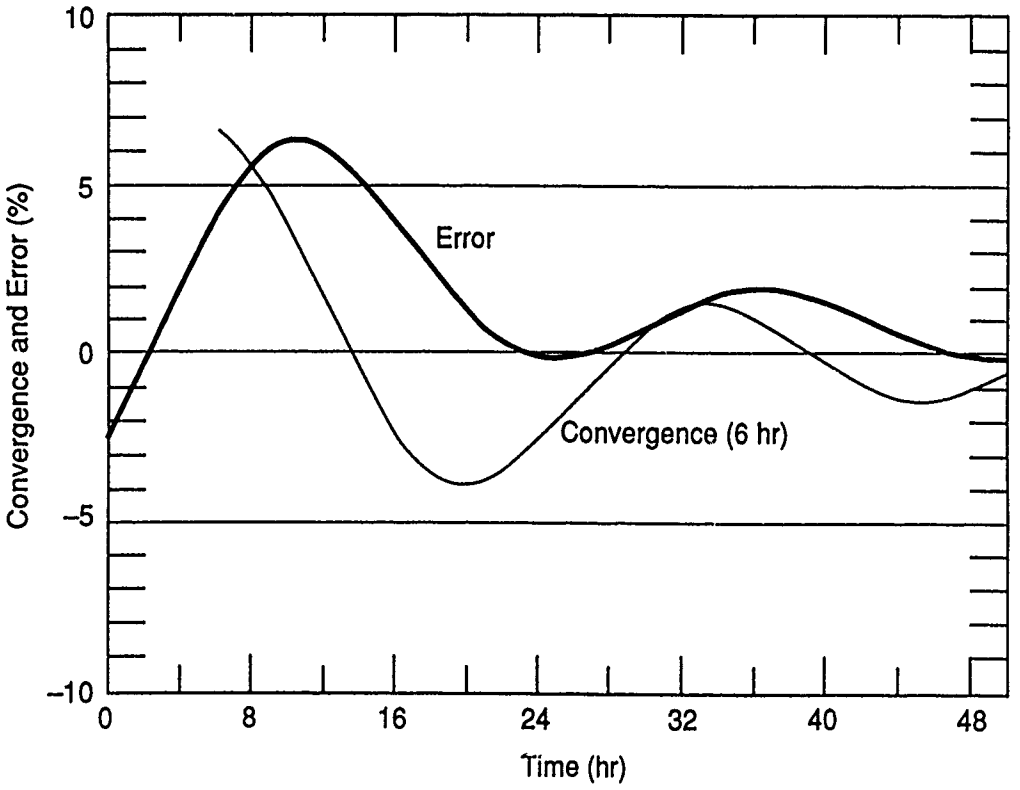

Figure 6. ERR(t) and CONV(t,6h) for the insulated furnace case (Tables 3 and 4).

Industrial component examples

The large ΔT makes in-situ determination of thermal resistance much more reliable for industrial components than for building components. Figure 6 illustrates that, for the insulated furnace in the example (Tables 3 and 4), R_e can be considered to be within 10% error soon after the measurement commences and within 2% bounds within the first 24 hours.

Cryogenic storage typically incorporates a much higher thermal resistance than high-temperature applications. Figure 7 illustrates that this causes a requirement for a longer measurement period - the ERR(t) takes at least 39 hours before it remains within 10% of R_{ref} and 109 hours before it remains within 5% in the simple 24-hour period example shown.

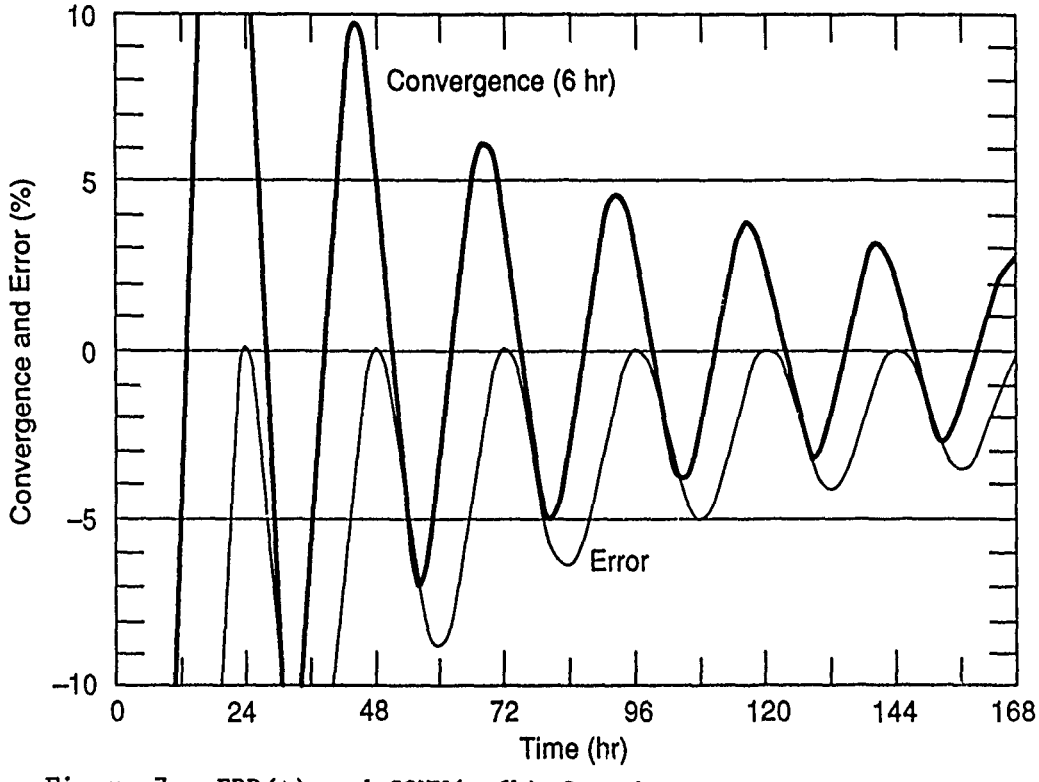

Figure 7. ERR(t) and CONV(t,6h) for the cryogenic storage case (Tables 3 and 4).

Table 6 demonstrates for the industrial components how long it was necessary to measure for 1) the calculated thermal resistance to remain within 5% of the true value and 2) the convergence parameter to remain within ± 0.05. The Discussion makes three points about estimating ERR(t) with $R_e(t)$ and CONV(t,1/4ω).

Table 6. Time (hours) until R_e from Eq. 2 to remains within 5% of R_{ref} and CONV(t,1/4ω) from Eq. 3 remains within ± 0.05 for the examples in this paper.

Description	Remain: >0.95 R	<1.05 R	Conv = -0.05	+0.05
Cryogenic storage	109.0	0.0	82.7	70.3
Furnace, uninsulated	0.0	0.0	0.0	0.0
Furnace, insulated	0.0	15.7	21.0	9.0

DISCUSSION

The examples of fractional error in averaged U-value illustrated in Modera, et al. [1] are based on an average ΔT that varies by 5.6 K on the outside surface and 1.1 K on the inside surface. These temperature variations are benign compared to those assumed in Table 4, although their ΔT of 11.1 K is less favorable to speedy diminution of ERR(t). Both sets of assumptions are plausible for different climates, but those in Table 4 require much longer measurement periods to achieve a calculational error that is below a criterion level, for example 10%. This underscores the importance of anticipating temperature variations when planning the duration of such tests, by using a model like that reported in this paper.

ASTM C 1155 requires that the convergence test be applied using an interval of 6 hours for buildings that are exposed to a diurnal temperature cycle. It recommends that other intervals between 2 and 12 be tried to determine which is the worst-case test for convergence. It then requires the user to determine the time elapsed before equation 2 reached an absolute value of 0.1 or less. The user must continue calculating R_e and CONV(t,1/4ω) for three more intervals of 6 hours (or the worst-case example) to assure that |CONV(t,1/4ω)| remains below 0.1. This criterion still offers only mild assurance that CONV(t,1/4ω) is an indication of ERR(t). A major flaw is that the range of intervals for CONV(t,1/4ω) should be extended up to at least 7 days.

With in-situ measurements it is seldom possible to know ERR(t). In the absence of a plotter to follow recommendation (1), choosing multiple test intervals or doing a running Fourier transform to determine the longest significant frequency present may help avoid this pitfall. Tables 5 and 6 suggest that extending the measurement by half again the time elapsed before CONV(t,1/4ω) last came within the desired error bounds would provide a good estimate of ERR(t).

The simulation runs in this paper suggest the following approaches to estimate the progress of ERR(t) during an in-situ measurement:

1. Looking at a plot of R_e vs time is the single most effective means to determine whether enough data have been obtained. Even this approach has its drawbacks, because one can fail to appreciate that an apparent stabilization of R_e is temporary because of low frequency temperature inputs (see Fig. 2) and because of bias of the envelope of R_e.
2. The convergence parameter, CONV(t,1/4ω), can be a good indicator of precision of the calculation <u>if</u>: 1) the period for the test, 1/4ω, is about 1/4 the longest period observed in the change of ΔT, and 2) the measurement continues 0.5

times longer than would be indicated when CONV(t,1/4ω) does not meet the accuracy criterion for ERR(t). Otherwise, this approach can be an optomistic indicator.

3. R_e will oscillate in an envelope. The flatter side of this envelope may trend tangentially toward R_{ref} faster than R_e itself. This may be a fruitful indicator that is more effective than the current use of CONV(t,interval) in ASTM C 1155.

CONCLUSIONS

The simulation program presented in this paper permits an investigator to determine in advance how much time may be required to obtain sufficient data for a calculation of in-situ R-values, given reasonable assumptions about probable ambient temperature changes and about thermal properties of components that may be encountered. It would also represent an appropriate environment to test various calculational techniques for detemining thermal resistance, although only one (eq. 2) was tried here.

Yet to be implemented is the use of actual data or allowing a non-periodic component, like a ramp. In these cases a Fourier transform [10] will be used to characterize such data sets in terms of frequencies and amplitudes. For now, ramp-like behavior is handled by using long-period sine waves. This still does not account for changes in the apparent thermal conductivity of the elements being measured. Therefore, the greater the amplitude and the longer the period of the temperature input, the less well will the model simulate its effects.

ASTM C 1155 should be revised to incorporate better means for assuring that ERR(t) is within the desired bounds before ΔT and q measurements stop. The three points outlined in the Discussion are probably useful tools to incorporate: 1) using real-time plots of R_e, 2) continuing the measurement half again as long as CONV(t,1/4ω) took to remain within the criterion for ERR(t), and 3) using the shape of the envelope of R_e to find R_{ref}.

The tendency of the envelope of R_e to approach the R_{ref} on its flatter side, according to these calculations, should be examined for actual, noisier data. An intermediate step would be to generate data about known values of ΔT and q with varying periodic amplitudes and randomization, and use it in this simulation program. While the bias can be made small, as ASTM C 1155 is currently written, it may be possible to make the calculation more efficient in converging on the correct value.

In industrial thermal resistance measurements using HFTs, it has often been the assumption that a measurement lasting a few minutes would suffice. The above results indicate that it would be wise to model the range of temperature conditions that may be encountered, in order to have a realistic expectation of how long the measurement period should be to bring ERR(t) within desired bounds. Even with such a model to forecast the measurement time, monitoring of R_e, CONV(t,1/4ω), and the envelope of R_e are still appropriate for industrial measurements.

ACKNOWLEDGEMENTS

The authors wish to thank Mark Modera of Lawrence Berkeley Laboratory and George Courville of Oak Ridge National Laboratory for their ideas that helped shape this paper.

REFERENCES CITED

1. Modera, M.P., Sherman, M.H., and Sonderegger, R.C., Determining the U-Value of a Wall from Field Measurements and of Heat Flux and Surface Temperatures. Building Applications of Heat Flux Transducers, ASTM STP 885, E. Bales, M. Bomberg, and G.E. Courville, Eds., American Society for Testing and Materials, Philadelphia, 1985, pp. 203-219.
2. ASTM C 1046, Standard practice for in-situ measurement of heat flux and temperature on building envelope components. . American Society for Testing and Materials, Philadelphia.
3. Flanders, S. Confidence in Heat Flux Transducer Measurements of Buildings. ASHRAE Transactions, Vol. 91, Part 1, 1985. Pp. 515-531.
4. Flanders, S. Measured and Expected R-Values of 19 Buildings. ASHRAE Transactions, Vol. 91, Part 2, 1985, American Society of Heating, Refrigerating and Air-Conditioning Engineers, Atlanta.
5. Brown, W.C., Schuyler, G.D., In-Situ Measurements of Frame Wall Thermal Resistance. ASHRAE Transactions 1982, Vol. 88, Part 1, American Society of Heating, Refrigerating and Air-Conditioning Engineers, Atlanta.
6. Courville, G.E. and J.V. Beck. Measurement of field thermal performance parameters of building envelope components. ASHRAE Transactions, Vol. 94, Part 2, Pp. 1595-1612, 1988, American Society of Heating, Refrigerating and Air-Conditioning Engineers, Atlanta.
7. Beck, J.V., Comparison of averaging and least squares techniques for calculating U for periodic surface temperatures. Memo to G. Courville, dated 23 January, 1989, Michigan State University, East Lansing.
8. Buffington, D.E., Heat gain by conduction through Exterior Walls and Roofs - Transmission Matrix Method. ASHRAE Transactions, Vol. 81, Part 2, American Society of Heating, Refrigerating and Air-Conditioning Engineers, Atlanta, 1975, pp. 89-100.
9. Reddy, M.S. and S. Krishnamoorthy, Heat Flux and Surface Temperature Variations in an Unconditioned Room of Brick Masonry Construction in a Composite Climate. Energy and Buildings, Vol. 13, 1989, pp. 159-174.
10. Schimmel, W.P., J.V. Beck, and A.B. Donaldson, Effective Thermal Diffusivity for a Multimaterial Composite Laminate. Journal of Heat Transfer, Vol. 99, No. 3, August 1977, American Society of Mechanical Enginneers, Pp. 466-470.

11. Flanders, S.N. and S.J. Marshall, Measuring building R-values for large areas. Proceedings of the Society of Photo-Optical Instrumentation Engineers, Volume 254, "Thermal Infrared Sensing Applied to energy conservation in building envelopes (Thermosense III)", Bellingham, Washington, 1981, pp. 137-138.
12. Flanders, S.N. and S.J. Marshall, Interpolating R-values from thermograms. Proceedings of the Society of Photo-Optical Instrumentation Engineers, Volume 313, "Thermal Infrared Sensing Applied to energy conservation in building envelopes (Thermosense IV)", Bellingham, Washington, 1982, pp. 157-164.
13. Mack, R.T., Energy loss profiles: Foundation for future profit in imager sales and service. 1985 IRIE V Proceedings, AGEMA Infrared Systems, Secaucus, New Jersey, 1986, pp. 1-6.
14. Anderson, L.J., Energy conservation with thermography. IRIE Proceedings, AGA Corporation, Pine Brook, New Jersey, 1977, pp. 61-62.
15. McIntosh, G.B., Recent advances in the quantification of industrial heat loss using thermography. Proceedings of the Society of Photo-Optical Instrumentation Engineers, Volume 313, "Thermal Infrared Sensing Applied to energy conservation in building envelopes (Thermosense IV)", Bellingham, Washington, 1982, pp. 213-218.
16. ASHRAE, ASHRAE Handbook, 1985 Fundamentals (SI Edition). American Society of Heating, Refrigerating and Air-Conditioning Engineers, Atlanta, Georgia, 1985.
17. Stearns, Samuel D., Signal Processing Algorithms. Prentice-Hall, Englewood Cliffs, New Jersey, 1988

APPENDIX A. DERIVATIONS

The relationship between nearside and farside temperatures (T) and heat fluxes (q) across each homogeneous layer may be characterized as follows, starting with the far layer with index n = 1, to the near layer with index n = N:

$$\begin{vmatrix} T_n \\ q_n \end{vmatrix} = \begin{vmatrix} A_n & B_n \\ C_n & D_n \end{vmatrix} \begin{vmatrix} T_{n+1} \\ q_{n+1} \end{vmatrix}$$

where for a given frequency ω:

$A = \cosh(Fx + iFx)$
$B = \sinh(Fx + iFx)/(kFx + ikFx)$
$C = (kFx + ikFx)\sinh(Fx + iFx)$
$D = A$

and

$F = (\omega/2\alpha)^{0.5}$
α = thermal diffusivity of the layer, n
x = thickness of the layer, n
k = thermal conductivity of the layer, n
i = the complex operator.

Then a transfer matrix may be calculated layer by layer as follows:

$$\begin{vmatrix} A & B \\ C & D \end{vmatrix} = \begin{vmatrix} A_1 & B_1 \\ C_1 & D_1 \end{vmatrix} \cdots \begin{vmatrix} A_n & B_n \\ C_n & B_n \end{vmatrix} \cdots \begin{vmatrix} A_N & B_N \\ C_N & B_N \end{vmatrix} .$$

This defines the relationship between nearside and farside temperatures and heat fluxes as follows:

$$\begin{vmatrix} T_{near} \\ q_{near} \end{vmatrix} = \begin{vmatrix} A & B \\ C & D \end{vmatrix} \begin{vmatrix} T_{far} \\ q_{far} \end{vmatrix} .$$

This, in turn may be solved for the admittances <u>for each frequency</u>, as follows:

$$q_{near} = (Y_{near}\ T_{near}) - (Y_{across}\ T_{far})$$

$$q_{far} = (Y_{across}\ T_{near}) - (Y_{far}\ T_{far})$$

where

$Y_{near} = D/B$

$Y_{across} = 1/B$

$Y_{far} = A/B$.

The heat fluxes may then be summed for each frequency and added to the average heat flux that results from the expression:

$$q = \bar{q} + \sum_{i=1}^{12} q_{near}(\omega_i)$$

where

$$\bar{q} = (\bar{T}_{near} - \bar{T}_{far})\ U$$

and

U = overall conductance of layers 1 to N

$\bar{T}$ = the baseline temperature about which sinusoidal variation takes place.

APPENDIX B. SAMPLE SESSION

RERR(t) [Return]

```
 Default RERR(t) Program Specifications Menu
 1. Edit Materials Selection
 2. Select Layers
 3. Edit Temperature Specifications
 4. Calculate Admittances for the Layers
 5. Calculate Temperatures and Heat Fluxes
 6. Calculate R-Values and Error
 7. QUIT Program
 Your COMMAND, a number from 1 to 7:

1 [Return]


        Current MATERIALS Specifications
        No. MATERIAL                 Density    Conductivity  Spec.Ht.
   1 BRICK - Common                  1920.0000       .7200       .8000
   2 GYPSUM Wallboard                 800.0000       .1605      1.0900
   3 GLASS FIBER                      100.0000       .0360       .9600
   4 Extruded POLYSTYRENE              42.0000       .0290      1.2200
   5 POLYISOCYANURATE                  32.0000       .0200       .9200
   6 CELLULOSE                         42.0000       .0420      1.3800
   7 Stainless Steel                 8025.0000      1.3560       .5020
   8 Monel                           8826.0000      2.1360       .0532
   9 Inconel                         8498.0000      1.2550       .4560
  10 Cellular glass insulation        136.0000       .0500       .7540
  11 Fireclay brick - 500F           2002.0000      1.0400       .9590
  12 Fireclay brick - 800F           2002.0000      1.0700       .9590
  13 Mild Steel - 100 C              7833.0000     52.0000       .4650
  14 Mild Steel - 4^0 C              7833.0000     42.0000       .4650


 Edit MATERIALS Specifications
 1. Change Units from                                              SI
 2. Add NEW Items
 3. Delete an Existing Item
 4. FILE Changes, then Leave Edit Mode
 5. Leave Edit Mode with NO CHANGES.
 Your COMMAND, a number from 1 to 4:

5 [Return]

 Default RERR(t) Program Specifications Menu
 1. Edit Materials Selection
 2. Select Layers
 3. Edit Temperature Specifications
 4. Calculate Admittances for the Layers
 5. Calculate Temperatures and Heat Fluxes
 6. Calculate R-Values and Error
 7. QUIT Program
 Your COMMAND, a number from 1 to 7:

2 [Return]
```

```
 Input Layers File Name, Default=LAYFIL.DAT

BRICK.DAT [Return]


        Current LAYERS Configuration
        No. Name                          Thickness
   1 BRICK - Common                        0.2000
   2 GLASS FIBER                           0.0889
   3 GYPSUM Wallboard                      0.0127


 Edit LAYER SPECIFICATIONS
 1. Insert NEW Items
 2. Delete an Existing Item
 3. FILE Changes and Leave Edit Mode
 4. Leave Edit Mode with NO CHANGES
 Your COMMAND, a number from 1 to 4:

4 [Return]


 Default RERR(t) Program Specifications Menu
 1. Edit Materials Selection
 2. Select Layers
 3. Edit Temperature Specifications
 4. Calculate Admittances for the Layers
 5. Calculate Temperatures and Heat Fluxes
 6. Calculate R-Values and Error
 7. QUIT Program
 Your COMMAND, a number from 1 to 7:

3 [Return]

 Input Definitions File Name, Default=TEMPDEF.FIL

TEMPDEF.FIL [Return]

DEFAULT FILE NAME IS:
TEMPDEF.FIL
 Default TEMPERATURE SPECIFICATIONS Menu
    Current IP or SI Temperature Units:                C
 1. Time Interval (s):                                 20.0000
 2. Baseline Nearside, Farside Temperatures (F or C):  20.0000
.0000
 3. Rate of linear Temperature Change (F/s or C/s):      .0000
 4. Dsplay Amplitudes, Periods, & Phases, Near-/Farside
 5. Change Amplitude, Period, & Phases: Near-/Farside
 6. File new assumptions.
 7. QUIT Menu
 Your COMMAND, a number from 1 to 7:

7 [Return]
```

```
 Default RERR(t) Program Specifications Menu
 1. Edit Materials Selection
 2. Select Layers
 3. Edit Temperature Specifications
 4. Calculate Admittances for the Layers
 5. Calculate Temperatures and Heat Fluxes
 6. Calculate R-Values and Error
 7. QUIT Program
 Your COMMAND, a number from 1 to 7:

4 [Return]

  The first four numbers are A, B
  The second two numbers are YIN, YOUT
     0.9993    0.0501
     2.8259    0.0704
     -.0056    0.1823
     0.9953    0.4651
No.                YIN                 YOUT                  YACR
 1    0.3538    0.0032    0.3538    0.0002    0.3538    -.0002
 2    0.3561    0.1557    0.3538    0.0089    0.3536    -.0088
Press RETURN

[Return]
 Default RERR(t) Program Specifications Menu
 1. Edit Materials Selection
 2. Select Layers
 3. Edit Temperature Specifications
 4. Calculate Admittances for the Layers
 5. Calculate Temperatures and Heat Fluxes
 6. Calculate R-Values and Error
 7. QUIT Program
 Your COMMAND, a number from 1 to 7:

5 [Return]


                                (Computing Temperatures - Please
Wait)
                                  (Computing Heat Flows - Please
Wait)
Total Conductance is:               0.353813
Total R-Value is:                   2.826350
Press RETURN

[Return]


         The following is the synthesized heat flow history
          Time   Temp Near Temp Far      Q Near   Q Far
        0.0000   20.0000    0.0000     7.3901    6.9937
        0.3333   18.2679    1.7433     3.4705    3.5452
        0.6667   21.7320    3.4732     5.1626    5.2799
        1.0000   20.0000    5.1768     2.2132    1.8192
```

```
1.3333   18.2679    6.8409   -1.6274   -1.5488
1.6667   21.7320    8.4530    0.1826    0.3053
2.0000   20.0000   10.0007   -2.6111   -2.9982
2.3333   18.2680   11.4723   -6.2592   -6.1724
2.6667   21.7320   12.8566   -4.2215   -4.0892
3.0000   20.0000   14.1430   -6.7540   -7.1302
3.3333   18.2679   15.3218  -10.1094  -10.0103
3.6667   21.7320   16.3839   -7.7496   -7.6040
4.0000   20.0000   17.3213   -9.9330  -10.2951
4.3333   18.2679   18.1269  -12.9153  -12.8012
4.6667   21.7321   18.7945  -10.1610   -9.9996
5.0000   20.0000   19.3191  -11.9316  -12.2771
5.3333   18.2679   19.6965  -14.4858  -14.3546
5.6667   21.7320   19.9241  -11.2915  -11.1126
6.0000   20.0000   20.0000  -12.6135  -12.9412
6.3333   18.2679   19.9237  -14.7139  -14.5648
6.6667   21.7320   19.6957  -11.0641  -10.8672
Continue writing data to screen  OK? ('Y' or 'N'):
```

N [Return]

```
 Default RERR(t) Program Specifications Menu
 1. Edit Materials Selection
 2. Select Layers
 3. Edit Temperature Specifications
 4. Calculate Admittances for the Layers
 5. Calculate Temperatures and Heat Fluxes
 6. Calculate R-Values and Error
 7. QUIT Program
 Your COMMAND, a number from 1 to 7:
```

6 [Return]

```
 The following is the calculated R-VALUE progress.
 Time      Temp Near Temp Far  R Near    R Far
0.0000   20.0000    0.0000    2.7063    2.8597
0.3333   18.2679    1.7433    3.3630    3.4657
0.6667   21.7320    3.4732    3.4190    3.4632
1.0000   20.0000    5.1768    3.8169    3.9464
1.3333   18.2679    6.8409    4.8789    5.0365
1.6667   21.7320    8.4530    5.6167    5.7527
2.0000   20.0000   10.0007    7.3560    7.7867
2.3333   18.2680   11.4723   14.0264   15.3805
2.6667   21.7320   12.8566   32.4299   38.2757
3.0000   20.0000   14.1430  -41.2025  -31.4956
3.3333   18.2679   15.3218   -9.7836   -9.1952
3.6667   21.7320   16.3839   -6.4139   -6.2071
4.0000   20.0000   17.3213   -4.4353   -4.2882
4.3333   18.2679   18.1269   -3.1296   -3.0634
4.6667   21.7321   18.7945   -2.5943   -2.5572
5.0000   20.0000   19.3191   -2.1346   -2.0986
5.3333   18.2679   19.6965   -1.7319   -1.7107
```

```
      5.6667   21.7320   19.9241   -1.5382   -1.5246
      6.0000   20.0000   20.0000   -1.3521   -1.3374
      6.3333   18.2679   19.9237   -1.1710   -1.1612
      6.6667   21.7320   19.6957   -1.0870   -1.0803
      Continue writing data to screen  OK? ('Y' or 'N'):
File Name:  RIN.FIL
New values will overwrite old. OK? ('Y' or 'N'):


N [Return]


No writing to file took place.


File Name:  ROUT.FIL
New values will overwrite old. OK? ('Y' or 'N'):

N [Return]

No writing to file took place.

       The following is the CONVERGENCE PARAMETER progress
       Time     Temp Near Temp Far R Near Convergence
      0.0000   20.0000    0.0000    2.7063    0.0000
      0.3333   18.2679    1.7433    3.3630    0.0000
      0.6667   21.7320    3.4732    3.4190    0.0000
      1.0000   20.0000    5.1768    3.8169    0.0000
      1.3333   18.2679    6.8409    4.8789    0.0000
      1.6667   21.7320    8.4530    5.6167    0.0000
      2.0000   20.0000   10.0007    7.3560    0.0000
      2.3333   18.2680   11.4723   14.0264    0.0000
      2.6667   21.7320   12.8566   32.4299    0.0000
      3.0000   20.0000   14.1430  -41.2025    0.0000
      3.3333   18.2679   15.3218   -9.7836    0.0000
      3.6667   21.7320   16.3839   -6.4139    0.0000
      4.0000   20.0000   17.3213   -4.4353    0.0000
      4.3333   18.2679   18.1269   -3.1296    0.0000
      4.6667   21.7321   18.7945   -2.5943    0.0000
      5.0000   20.0000   19.3191   -2.1346    0.0000
      5.3333   18.2679   19.6965   -1.7319    0.0000
      5.6667   21.7320   19.9241   -1.5382    0.0000
      6.0000   20.0000   20.0000   -1.3521    3.0015
      6.3333   18.2679   19.9237   -1.1710    3.8720
      6.6667   21.7320   19.6957   -1.0870    4.1454
      Continue writing data to screen  OK? ('Y' or 'N'):
Convergence File Name, Default=CONV.FIL
File Name:  CONV.FIL
New values will overwrite old. OK? ('Y' or 'N'):

N [Return]

No writing to file took place.
```

```
Default RERR(t) Program Specifications Menu
1. Edit Materials Selection
2. Select Layers
3. Edit Temperature Specifications
4. Calculate Admittances for the Layers
5. Calculate Temperatures and Heat Fluxes
6. Calculate R-Values and Error
7. QUIT Program
Your COMMAND, a number from 1 to 7:

7 [Return]
```

Stephen N. Flanders

Q: Is there an interest in looking at the average value of the heat fluxes on both sides of the wall to obtain more rapid convergence?—Pierre Thery.

A: In principle, monitoring heat flux on both sides of the wall would be beneficial both to obtain a more rapid convergence and to help verify the absence of lateral heat flow. In practice, placing HFTs on the outside surface of buildings presents shielding problems when direct solar radiation is present. It may be difficult to mask the HFT so that it absorbs solar radiation at the same rate as the surrounding construction.

Q: On which side should one position the heat flux transducer on a multi-layer structure to obtain more rapid convergence, if one side is massive and the other side insulated?—Pierre Thery.

A: An envelope segment with significant mass on one side and insulation on the other will respond to the same WT history differently, depending on which way around it faces. However, the cumulative effect which contributes to the R-value calculation will converge about equally quickly, no matter which side of the structure is facing out.

Q: One-shot data collection can still lead to errors if you do not characterize the R-value in a relationship that is a function of insulation mean temperature. For instance, extrapolation to 75°F may not be accurate, using a linear extrapolation from R-value measurements taken at very cold temperatures. This is particularly true with some of the foam insulations, which have blowing agents that condense at some point in the application.—Jeffrey Christian, Martin-Marietta Corporation, Oak Ridge National Laboratory.

A: Jeffrey Christian's observations are correct. One can often develop an appreciation of how much variation in thermal resistance might have occurred during the measurement period with a back of the envelope calculation of the maximum, minimum and average temperatures that were likely to have occurred in the insulation. References that detail the effects of temperature on thermal resistance of the insulation in the construction can bracket the possible error. Situations where convection loops reverse or phase changes take place warrant special caution.

INNOVATIVE APPLICATIONS AND TECHNIQUES

THERMISTOR-BASED SYSTEM FOR THERMAL CONDUCTIVITY MEASUREMENT

R.T. Atkins
E.A. Wright

U.S. Army Cold Regions Research and Engineering Laboratory
Hanover, New Hampshire USA

ABSTRACT

This report describes a patented method for using commercially available thermistors to make in-situ thermal conductivity measurements with commonly available electronic equipment such as digital voltmeters. The emphasis is on the use of a single thermistor to measure the thermal conductivity of soils. Calibration techniques are explained and examples provided. Limits on this technique are discussed, including measurement range, material grain size, the amount of material needed for a valid measurement, and temperature stability. Specific examples of the use of this technique are provided for thermal conductivity measurements of soils, building materials, and the sludges in a sewage treatment plant. Data analysis is provided, including a statistical approach to finding the thermal conductivity in large volumes of material.

INTRODUCTION

The original intent of the work described in this report was to develop a method for measuring point thermal conductivities that uses inexpensive sensors readily available from commercial sources, requires no specialized instruments, gives reasonably accurate measurements of thermal conductivities, can be checked using readily available "standard materials," and is field operable. The only specific restrictions on the use of this method for thermal conductivity measurements are that 1) there must be sufficient material to ensure that measurements are taken in a large volume compared to the volume of the thermistor, 2) the material must have a reasonably uniform temperature distribution and be relatively stable in temperature during the measurement interval (about 10 minutes), and 3) the grain size of the material must be small enough to ensure that intimate thermal contact is maintained over the entire surface of the thermistor.

A number of other studies (e.g., Hayes and Valvano 1985, Dougherty 1987a,b and Nieto de Castro 1988) have developed techniques that use thermistors for determination of thermal conductivity. All these methods require the use of specialized equipment specifically dedicated to the measurement of thermal conductivity. However, the methodology described in this report differs from all others in that it uses only readily available, inexpensive equipment and that a time measurement is not necessary for calculation of the thermal conductivity values.

Examples of materials for which this thermal conductivity measurement technique is appropriate are fine-grained soils, building materials such as polystyrene, gel-like materials such as silicone grease, and fiberglass insulations. This measurement technique was awarded a U.S. Patent (Patent 4,522,512) on 11 June 1985; however, there are no restrictions on its use. Throughout this report thermal conductivity measurements are reported in calories per square centimeter per centimeter per second per degree Celsius (cal/cm-s, or cal/cm-s-°C). To convert these values to BTU per square foot per inch per hour per degree Fahrenheit (BTU/ft^2-in.-hr-°F) divide by 3.44×10^{-4}.

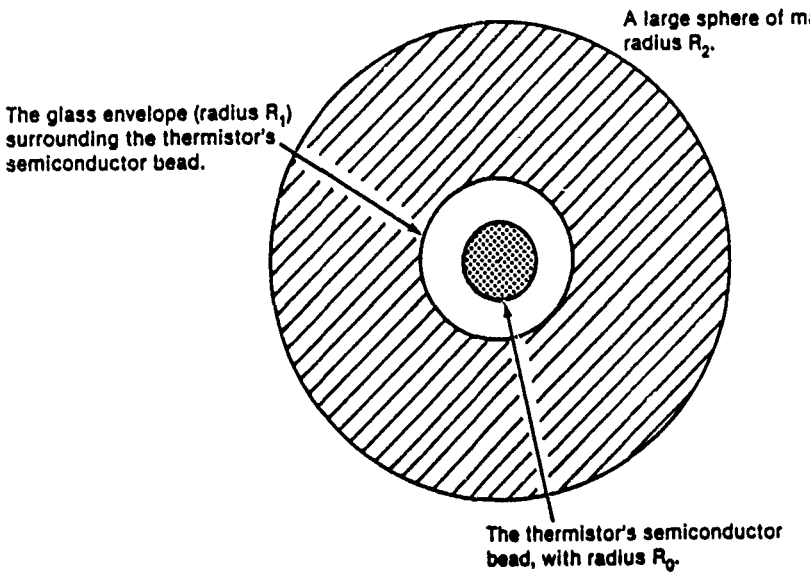

Figure 1. Typical glass bead thermistor configuration.

THEORY

Assume that a thermistor is a perfect sphere embedded in a material such as is shown in Figure 1. When the thermistor's semiconductor bead is heated slightly (electrically) the steady-state heat flow equation (e.g., Kreith 1961) into the glass envelope is

$$Q = K_t \sqrt{A_0 A_1}\, \frac{T_0 - T_1}{R_1 - R_0} \tag{1}$$

where Q = thermal energy being generated in the semiconductor bead
K_t = thermal conductivity of the glass envelope of the thermistor
A_0 = surface area of the semiconductor sphere
A_1 = surface area of the glass sphere
T_1 = surface temperature of the glass sphere
T_0 = surface temperature of the semiconductor bead
R_0 = radius of the semiconductor bead (sphere)
R_1 = radius of the glass bead (sphere).

Since the surface area of a sphere is $4\pi R^2$, eq 1 can be written as

$$Q = K_t\, 4\pi (T_0 - T_1)\, \frac{R_1 R_0}{R_1 - R_0}. \tag{2}$$

If the sphere of test material is assumed to completely surround the glass sphere of the thermistor, then at steady state the thermal energy flowing into the glass bead can be assumed to flow on into the material, so that

$$Q = K_m\, 4\pi (T_1 - T_2)\, \frac{R_2 R_1}{R_2 - R_1} \tag{3}$$

where K_m = thermal conductivity of the material
T_2 = temperature of the surface of the sphere of material
R_2 = radius of the sphere of material.

Solving eq 3 for the thermal conductivity of the material, K_m

$$K_m = \frac{Q}{4\pi(T_1-T_2)}\left(\frac{1}{R_1}-\frac{1}{R_2}\right).$$

If the volume of material is so large that the radius R_2 can be assumed to be infinite with respect to R_0 and R_1

$$K_m = \frac{Q}{4\pi R_1(T_1-T_2)}. \tag{4}$$

This equation can be used to find the thermal conductivity of the material provided a means can be found to find a value for T_1 (the surface temperature of the glass envelope). This means is provided by eq 2, which, when solved for T_1, gives

$$T_1 = T_0 - \frac{Q(R_1 - R_0)}{K_t\, 4\pi\, R_0\, R_1}.$$

When the thermistor is heated, the value of Q can be found by

$$Q = 0.2389\, I^2\, R_{hot}$$

where I = current in the thermistor
R_{hot} = resistance of the thermistor when it is heated
Q = heat flow in calories per second.

In theory, then, a thermistor can be used to measure the thermal conductivity of a bulk material by using the following three equations:

$$Q = 0.2389\, I^2\, R_{hot}$$

$$T_1 = T_0 - \frac{Q(R_1 - R_0)}{K_t\, 4\pi\, R_0\, R_1}.$$

$$K_m = \frac{Q}{4\pi R_1(T_1-T_2)}.$$

For any given thermistor the values of R_0, R_1 and K_t will all be constants. Therefore, the second equation can be written as

$$T_1 = T_0 - AQ$$

where

$$A = \frac{R_1 - R_0}{K_t\, 4\pi\, R_0\, R_1}.$$

This equation can then be substituted in the third equation so that

$$K_m = \frac{BQ}{T_0 - AQ - T_2}$$

where

$$B = \frac{1}{4\pi R_1}$$

or

$$K_m[(T_0-T_2)-AQ] = BQ. \tag{5}$$

This equation can be used to calibrate a thermistor that can then be used to measure the thermal conductivity of a material. All that is needed is to solve for A and B by using two materials whose thermal conductivities are known and measuring the Q, T_0 and T_2 associated with those materials.

T_2 is the "unheated" temperature of the material and is found by measuring the temperature of the material before heating the thermistor, using standard thermistor- temperature measurement techniques. T_0 is found by measuring the heater current to the thermistor and the voltage across it. This is simplified to just a voltage measurement if a known constant current is used to heat the thermistor. Since both the current and the voltage of the heated thermistor are known, its resistance is known (by Ohm's law) and, therefore, the temperature T_0 of the semiconductor bead. Q is the heater current times the voltage across the thermistor times 0.2389:

$$Q = 0.2389\, I \cdot V$$

or by Ohm's law,

$$Q = 0.2389\, I^2R.$$

The complete technique for using a thermistor to measure bulk thermal conductivity is therefore as follows.

Calibration

1. Measure Q, T_0 and T_2 for the thermistor in each of two materials whose thermal conductivity is known.
2. Use these values to solve for A and B in the equation

$$K_m\,[(T_0-T_2)-AQ] = BQ \tag{6}$$

using standard two equation-two unknowns techniques.

Measurement

1. With A and B known, place the thermistor in an unknown material and measure Q, T_0 and T_2.
2. Calculate the thermal conductivity using

$$K_m = \frac{BQ}{(T_0-T_2) - AQ}. \tag{7}$$

All measurements must be taken during a thermally steady-state condition. This condition is determined by monitoring the voltage across the thermistor. When the voltage is steady, the thermal conditions are in steady state.

This technique measures thermal conductivity at a single point. To obtain an average value for the thermal conductivity of a nonhomogeneous material, statistically valid sampling techniques must be used.

MEASUREMENT PROCEDURES

The thermistors used in the measurements described in this report were Fenwal GB32P101-T. Earlier tests used similar glass bead thermistors manufactured by Victory Engineering Corporation. Any glass bead thermistor is suitable, including double bead thermistors that match a known curve. When selecting a thermistor, some care must be taken to ensure the glass diameter is large compared to the grain size of the material being tested (i.e., that there is good thermal coupling between the thermistor and the material). To make it easier to insert the

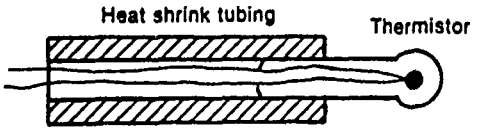

Figure 2. Thermal conductivity probe.

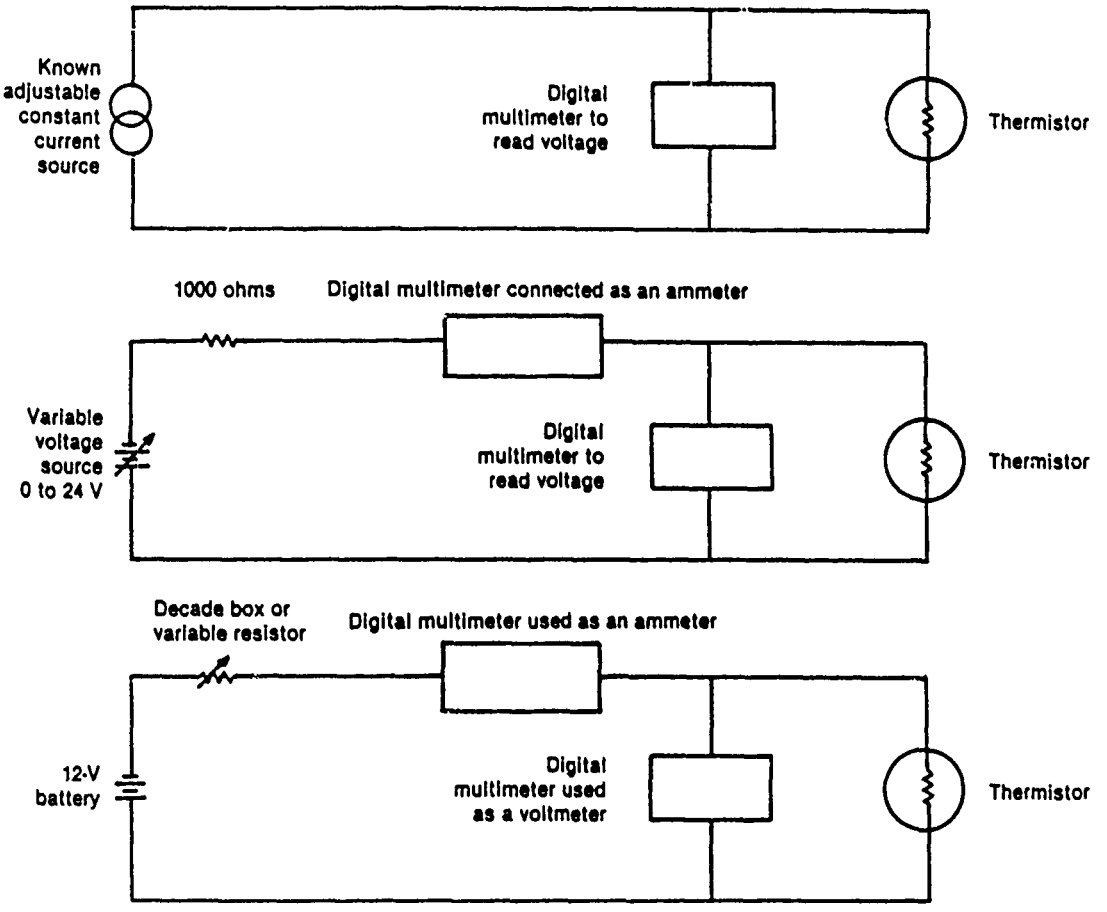

Figure 3. Three possible circuit configurations.

thermistor into a test material, a piece of dual-wall heat-shrink tubing can be shrunk onto the thermistor's glass bead extension to form a convenient probe (Fig. 2).

A number of different circuit configurations are possible (Fig. 3). No matter which circuit is used, they all do the same thing; namely, they provide a small current to read the lower ("cold") temperature and then a larger current to heat the thermistor, while at the same time reading the higher ("hot") temperature. Typical lower temperature currents are 30 to 70 μA, and typical higher temperature currents are 2 to 5 mA.

For the lower temperature reading it is necessary to know the current in the thermistor and the voltage across the thermistor so that the thermistor resistance can be determined. The lower temperature is then found using standard thermistor- temperature measuring techniques (discussed briefly in the following section).

At the higher temperature, the energy being applied is calculated, as well as the temperature itself. Since the current in the thermistor and the voltage across it are known, $Q = 0.2389\ I \cdot V$ is the energy flow in calories per second.

Typical measurement

The step-by-step procedure for a typical measurement is as follows:

1. Insert the thermistor in the test material and connect the electrical circuit.
2. Apply a small, lower-temperature current, for instance, 40 μA.
3. Observe the voltage across the thermistor; when it becomes steady (a change of only 1 or 2 mV/min), record the voltage and the current. These two values are then used to calculate the thermistor's resistance and, hence, the lower temperature.
4. Apply a heater current, for example, 3 mA. Note the time when this current is applied.

5. Observe the voltage across the thermistor; when it becomes steady, record the current and voltage. Typically, at room temperature, it takes from 5 to 10 minutes for the temperature to stabilize. The time interval over which the heater current was applied should also be recorded.

6. Calculate the higher temperature and the thermal energy Q being dissipated in the sample.

7. Reapply the lower-temperature current and wait the same time interval over which the heater current was applied.* Record the current and voltage and calculate the lower temperature again.

8. Average the two lower temperatures.

9. Calculate the thermal conductivity of the test material using:

$$K_m = \frac{BQ}{(T_{hot} - T_{cold}) - AQ}.$$

The calibration process is exactly the same as above except that K_m is known for the two calibration materials and the values of A and B are calculated using the two equations-two unknowns method. Typical calibration materials are as follows:

Water:

$$K_m = 1.43 \times 10^{-3} \text{ cal/cm-s-°C}$$

Silicone oil:

$$K_m = 0.30 \times 10^{-3} \text{ cal/cm-s-°C.}$$

Example: Test material: dry silt

As an example, we will consider the thermal conductivity of a sample of dry Fairbanks silt (from Fairbanks, Alaska), which produces the following three readings:

Time	Current (μA)	Volts
0845	30	0.06982
0850	3000	5.254
0855	30	0.06966

First lower temperature:

$$R = \frac{0.06982}{30 \times 10^{-6}} = 2327.3 \text{ ohms}$$

First lower temperature = 21.19°C. (This was obtained from the resistance- temperature data supplied by the thermistor manufacturer. See also the following section.)

Higher temperature:

$$R = \frac{5.254}{3 \times 10^{-3}} = 1751.3 \text{ ohms}$$

Higher temperature = 28.51 °C.

Second lower temperature:

$$R = \frac{0.06966}{3 \times 10^{-3}} = 2322.0 \text{ ohms}$$

*The assumption here is that the sample is changing temperature slowly and that the "hot" reading should be taken equidistant in time between the two "cold" readings to account for this temperature change.

Second lower temperature = 21.25°C.

Average lower temperature:

$$\frac{21.19 + 21.25}{2} = 21.22\,°C$$

$$Q = 0.2389 \times 3\times10^{-3} \times 5.254 = 3.7655 \text{ mcal/s.}$$

From eq 7 with $A = 792.3573$; $B = 0.36003$:

$$K_m = \frac{0.36003 \times 3.7655 \times 10^{-3}}{(28.52 - 21.22) - 792.3573 \times 3.7655 \times 10^{-3}} = 0.315 \times 10^{-3} \text{ cal/cm-s-°C}$$

or

$$K_m = \frac{0.315 \times 10^{-3}}{3.44 \times 10^{-4}} = 0.916 \text{ BTU/ft}^2\text{/in./hr/°F.}$$

If this had been a calibration process, the procedure would have been exactly the same except the value of K_m would have been known (for instance, using distilled water). By using two "standard" materials whose K_m values are known, the values for A and B for a particular thermistor could then be calculated.

Thermistor thermometry

There are several methods of converting a thermistor's resistance to temperature. The method used for this report was to purchase thermistors calibrated at three temperature points: –38°, 0.01° and +40°C. These three known points were then used to generate resistance-temperature tables in 0.1°C increments from –40°C to +40°C using the Steinhart equation:

$$\frac{1}{T_{abs}} = C_1 + C_2 \ln R + C_3 (\ln R)^3$$

where T_{abs} is the absolute temperature in kelvins, R is the resistance (in ohms) of the thermistor, and C_1, C_2 and C_3 are constants that may be determined by using the three calibration points supplied with each thermistor. For the resistance temperature tables, the absolute temperature is usually converted to °C by subtracting 273.15.

Once the values for C_1, C_2 and C_3 have been found, it is often convenient to program a small hand-held calculator to solve the Steinhart equation so that resistance values can be converted to temperature without bothering to look them up in a table.

Typical results

To demonstrate the use of this technique, two measurement programs were conducted, one on Fairbanks silt and one on typical building insulation. Typical data for these two initial test programs are shown below. A third set of data taken on wastewater sludges is also included.

Table 1. Calibration data for one of the three thermistors.

Standard	Q ($\times10^{-3}$)	T(*hot*) (°C)	T(*cold*) (°C)
water	4.2880	26.82	22.30
water	4.2952	26.78	22.25
silicone oil	3.6967	30.72	23.08
silicone oil	3.6931	30.75	23.12

For water:
$K_m = 1.43\times10^{-3}$ cal/cm-s-°C at 23°C.
For silicone:
$K_m = 0.3\times10^{-3}$ cal/cm-s-°C at 23°C.

Fairbanks silt

The calibrations for the tests on Fairbanks silt are illustrated in Table 1. All tests were run with a cold-temperature current of 30 μA and a hot-temperature current of 3 mA. The calibration constants for the thermistor were obtained by calculating an A and B for each possible combination of raw calibration data and then averaging these values:

A	B
785.2716	0.38443
785.4557	0.38417
785.9818	0.38422
786.1658	0.38395

$\bar{A} = 785.7187 \quad \bar{B} = 0.38419$

$$K_m = \frac{0.38419}{[T(\text{hot}) - T(\text{cold})] - 785.7187\ Q}.$$

Test data

Measurements were taken at three soil moisture contents: 3%, 17% and 26%. Four measurements were taken for each soil moisture content. The results are illustrated in Table 2. Each data set was examined statistically to ensure that every specific measurement should be included in the results as a valid number. The technique used was the "outlier detection" method described by Abernathy and Thompson (1973).

These results (Fig. 4) are in agreement with those of other researchers who have measured the thermal conductivity of Fairbanks silts at various soil moisture contents (Farouki 1981).

Table 2. Results of the tests on Fairbanks silt.

$Q \times 10^{-3}$	T(hot)	T(cold)	$K_m \times 10^{-3}$
3% moisture content			
3.7598	30.28	22.87	0.325
3.7734	30.18	22.95	0.340
3.7670	30.23	23.09	0.346
3.7670	30.23	23.15	0.351
		Average	0.340
		Standard deviation	0.011
17% moisture content			
4.3862	26.23	21.63	1.448
3.3812	26.27	21.65	1.430
4.3697	26.33	21.73	1.431
4.3661	26.36	21.73	1.404
		Average	1.428
		Standard deviation	0.018
27% moisture content			
4.4184	26.05	21.70	1.929
4.4012	26.15	21.86	2.037
4.3991	26.16	21.86	2.002
4.3798	26.27	21.98	1.964
		Average	1.428
		Standard deviation	0.047

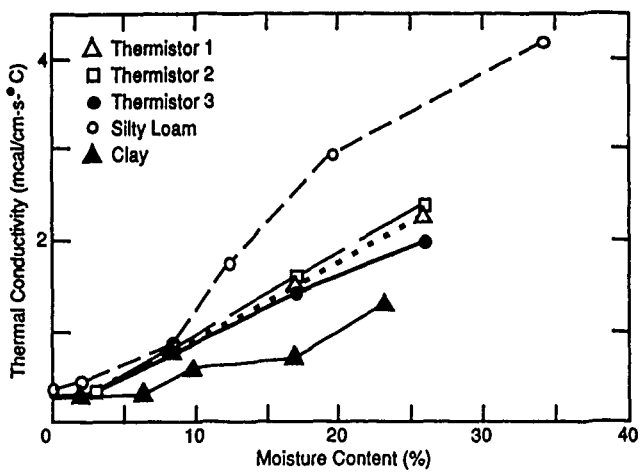

Figure 4. Thermal conductivity tests, Fairbanks silt (data for silty loam and clay are from Farouki 1981).

Insulation material

These tests were conducted by the Mechanical Engineering Department of the University of Alaska, not by the authors, so only the results are reported, as received (Table 3). These tests measured the thermal conductivity at $^1/_4$-in. intervals through the 2-in. test batts of insulation, and these values were averaged for a total figure for the batt. At the same time a total value for the batt was obtained using the guarded hot box technique. As can be seen, the hot box reading and the average value using this thermistor method agree quite closely. The reason the thermistor readings increase as they proceed through the sample is that moisture was purposely introduced on one side of the sample for several hours prior to these measurements in order to determine l) how much moisture was absorbed by the insulation batt, 2) to what depth the moisture had penetrated, and 3) how much the thermal insulation of the batt had deteriorated as a result of the moisture absorption. For sample 4-4 the original hot box measurement of 0.591 was considered suspect by the technician who was running the tests. Therefore, a second hot box measurement was made, resulting in the

Table 3. Results of the tests on 2-in. blue foam insulation.

Depth (in.)	K_m *(BTU-in./hr-ft²-°F)*		
Sample 4-3			
1/4	0.317		$K_{\text{hot box}} = 0.622$
1/2	0.320		
3/4	0.551	$K_{\text{avg}} = 0.610$	
1	0.746	$s = 0.221$	Water by volume = 20.9%
1 1/4	0.730		Water by weight = 752%
1 1/2	0.885	wt= 298.93 g	
1 3/4	0.709		
Sample 4-4			
1/4	0.329		
1/2	0.841		
3/4	0.660	$K_{\text{avg}} = 0.537$	$K_{\text{hot box}} = 0.591$
1	0.860	$s = 0.255$	$K_{\text{hot box}} = 0.541$
1 1/4	0.516		
1 1/2	0.277		Water by volume= 16.7%
1 3/4	0.276		Water by weight = 621%

0.541 BTU in./hr-ft^2-°F measurement. (It is interesting to note that the technician decided that the thermistor measurements were more likely to be correct than the initial hot box measurement.)

Wastewater sludges

A third use of this thermal conductivity measurement technique is reported by Vesilind and Martel (1989) in their study of the thermal conductivity of sludges. For this particular application, the requirement was to determine the thermal conductivities of the liquids and slurries that are present in wastewater. These thermal conductivities were later used in predictive studies of freeze–thaw cycles of open lagoons in wastewater treatment plants. The results of these studies were reported for six different sludges (Fig. 5–10). As

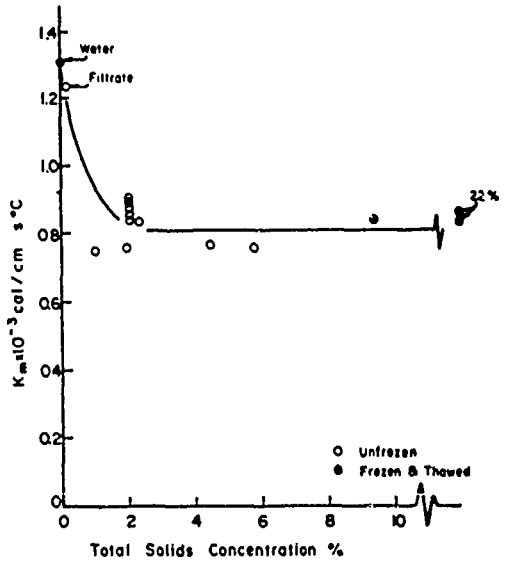

Figure 5. Thermal conductivity of Lebanon, N.H., water treatment sludge (from Vesilind and Martel 1989).

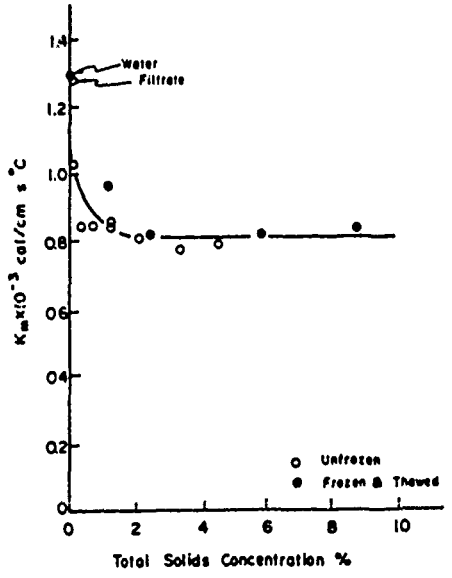

Figure 6. Thermal conductivity of West Lebanon, N.H., return activated sludge (from Vesilind and Martel 1989).

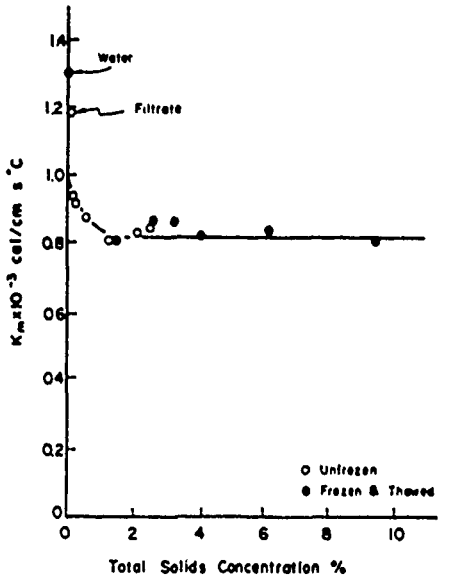

Figure 7. Thermal conductivity of Woodstock, Vt., return activated sludge (from Vesilind and Martel 1989).

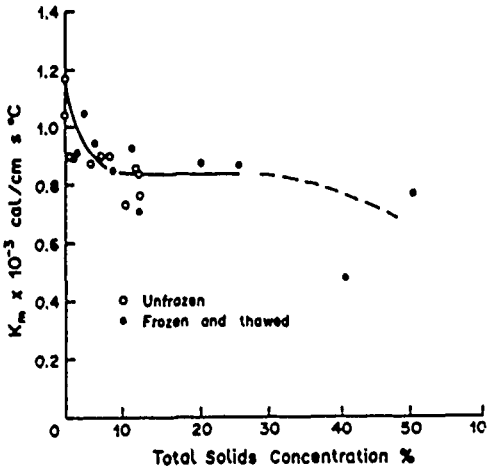

Figure 8. Thermal conductivity of Hanover, N.H., digested primary sludge (from Vesilind and Martel 1989).

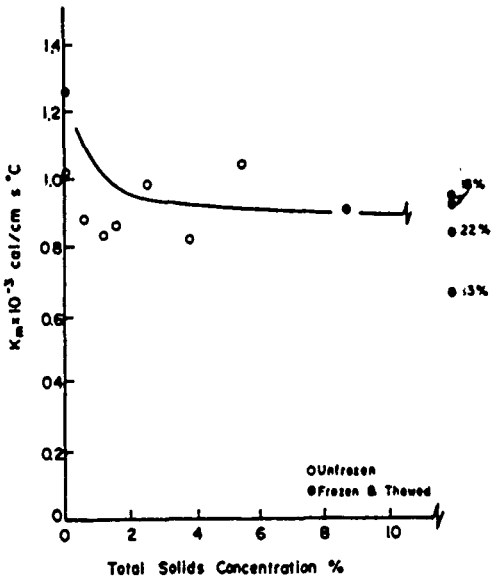

Figure 9. Thermal conductivity of Watervliet Arsenal (Watervliet, N.Y.) chrome sludge (from Vesilind and Martel 1989).

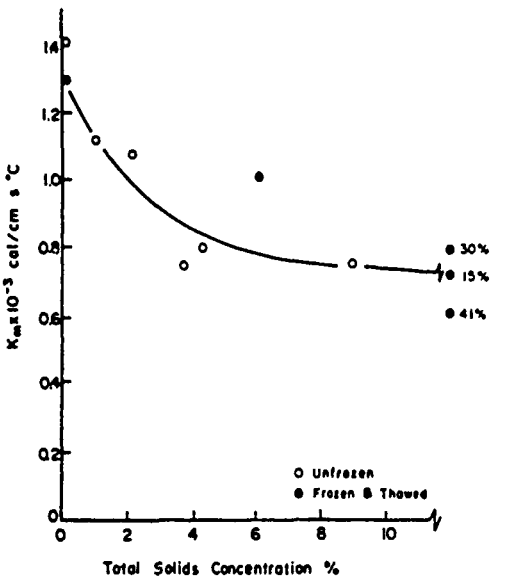

Figure 10. Thermal conductivity of Watervliet Arsenal oily sludge (from Vesilind and Martel 1989).

can be seen, a value of 0.8 mcal/cm-s-°C was found to be a good representative thermal conductivity for the sludges once the total solids concentration exceeded approximately 2%. In addition, the authors reported that this measurement technique produced repeatable data that were in general agreement with those of other researchers.

DISCUSSION OF RESULTS

The results reported here demonstrate the use of a technique that meets the requirements as stated in the

Introduction. Two initial measurement programs were reported, one where relatively high thermal conductivities were measured (soil) and one where low conductivities were measured (insulation). A later series of tests involving wastewater sludges is also reported. In each case the results were compared to typical values obtained by other researchers using different measurement techniques. The results are in general agreement in all cases; however, the emphasis here is to describe the measurement technique. The accuracy comparisons do not have a great deal of meaning serving only to show that the sampling techniques used produced data in general agreement with other measurement techniques. This point measurement technique does have some unique characteristics for certain applications, such as profiling insulations that have absorbed moisture, or monitoring building insulations to detect moisture penetration.

The calibration materials used for all the measurements in this report were distilled water and silicone oil. The thermal conductivity for water at 25°C was obtained from a physics handbook. The silicone oil's conductivity was obtained from the manufacturer's specification sheets. The manufacturer warns that the data given are average values. However, a review of thermal conductivity tables shows that nearly all machine oils have a thermal conductivity of approximately 0.3×10^{-3} cal/cm-s-°C.

The use of water and silicone oil as calibrating standards will certainly have some small error due to convective cooling of the thermistor. This error is discussed in some detail in the thermal conductivity literature. Generally, the errors are dismissed as "acceptable" (less than 10% error) if the temperature difference between the sensor and the test material is small, (i.e., 10°C or less). On the other hand, a temperature of 5°C or more is necessary to make an accurate measurement. To stay within these temperature boundaries, it is necessary to choose the heater current with a little discretion. In general, low-conductivity materials will require only 2 or 3 mA while high conductivity materials will need 4 or 5 mA to achieve an acceptable temperature difference.

This measurement technique will ultimately result in the destruction of the thermistors since they are not designed to be heating devices. However, if care is taken to never exceed 40°C when heating the thermistor, a minimum of 40 tests can be expected. With a sample size of five thermistors available, the average tests per thermistor were 70, and two were used for over 100 tests before failing. A good rule- of-thumb test to see if a thermistor is still giving correct temperatures is to place the thermistor in a constant-temperature environment (such as an ice bath) and take a forward and reversed reading. If the difference between the forward and reverse reading is more than 4 or 5 ohms, the thermistor is likely unstable and should be discarded.

CONCLUSIONS AND RECOMMENDATIONS

This method can be used to determine thermal conductivities that are reasonably close to, or below, the values for the calibration standards. However, for bulk materials it is imperative that statistically valid sampling techniques be used.

The test results in this report do not guarantee accurate measurements much above the thermal conductivity of water (1.43×10^{-3} cal/s-cm-°C). Although no tests were conducted, there is a high probability that the useful measurement range could be extended to higher conductivity materials by using higher-conductivity standards. Heat conductive compounds could probably be used as higher conductivity standards, although there might be some problems in accurately determining their thermal conductivity.

Obviously this technique will no longer be applicable once the thermal conductivity of the material starts to exceed the thermal conductivity of the glass on the thermistor (since the glass then becomes the material that is limiting heat flow).

LITERATURE CITED

Abernathy, R.B. and J.W. Thompson (1973) Uncertainty in gas turbine measurements. Air Force Handbook AEDC-TR-73-5, Engine Test Facility, Arnold Engineering Development Center, Air Force Systems Command.

Dougherty, B.P. (1987a) An automated probe for thermal conductivity measurements. Master's Thesis, Department of Mechanical Engineering, Virginia Polytechnic Institute and State University (unpublished).
Dougherty, B.P. (1987b) Thermophysical property measurement in building insulation materials using a spherically-shaped, self-heated probe. *Thermal Conductivity*, **20**: 47–59.
Farouki, O.T. (1981) Thermal properties of soils. USA Cold Regions Research and Engineering Laboratory, CRREL Monograph 81-1.
Nieto de Castro, C.A., B. Taxis, H.M. Roder and W.A. Wakeham (1988) Thermal diffusivity measurement by the transient hot-wire technique: A reappraisal. *International Journal of Thermophysics*, **9**(3): 293–316.
Kreith, F. (1961) *Principles of Heat Transfer*. Scranton: International Textbook Company.
Vesilind, P.A. and C.J. Martel (1989) Thermal conductivity of sludges. *Water Resources*, **23**(2): 241–245.

Ronald Atkins

Q: Does the thermistor you describe have a limited measurement life?—Jeffrey Christian.

A: Yes, this measurement technique has a limited life for any given thermistor, since the heating process uses a current much higher than is necessary for a single temperature measurement. The recommended heating of the thermistor by the manufacturer is in the microvolt range and heating the thermistor with a few millivolts will ultimately polarize the thermistor so that it will not read the same when current is reversed in it. For the thermistors that I have tested, 75 to 85 measurements are the average number of measurements; the highest was 125 and the lowest was in the 50s.

Q: What is the cause of the short life of the sensor?—Jeffrey Christian.

A: The shortened life is caused by the polarization of the thermistor by putting too large a current through it.

Q: Can one do anything to extend the life of the sensor?—Jeffrey Christian.

A: To extend the life as much as possible: 1) Reverse the current for every other measurement. 2) Keep the heater current as low as possible while still maintaining a ΔT of at least 8°C. Ten degrees Celsius or more gives better accuracy.

Q: When the thermistor probe is used in wet thermal insulation, what is the temperature rise of the probe with respect to the far-field temperature?—Douglas M. Burch.

A: The temperature rise is the same with respect to the far field as it is for a dry insulation, at least within the limits of error for this particular measurement technique. That is: to the extent that the *cold* temperature measurement is representative of the far-field temperature regardless of whether the insulation is wet or dry, the ΔT will be a good measurement for determination of the thermal conductivity of the insulation.

Q: Wouldn't a temperature rise in wet insulation cause significant moisture transfer and latent heat transport?—Douglas M. Burch.

A: There will be some effect from moisture transfer; however, it will be a function of the porosity of the material. Calculations, not measurements, that were made for pure water—a worse case condition—indicated that because of the small ΔT, the error due to flow phenomena in general will be small.

Q: You mentioned that you used thermistors to measure the thermal conductivity of fibrous insulations. What is the lowest density that you believe could be measured with reasonable accuracy?—Anne Silberstein.

A: I tried this measurement technique on standard fiberglass insulations that are used in typical house construction and it worked well, giving excellent representative values of what the

manufacturer claimed. I believe that lower density materials could be successfully measured, but I have not actually done it.

Q: Did you notice any variability in the measurements, depending on the location of the transducer?—Anne Silberstein.

A: The tests that I ran were on 4-in.- (100-mm-) thick fiberglass batts, with the thermistor in the middle. The variability of several readings was about 10% of the average value of all the readings. Although I didn't place the thermistor near the edge and take readings, I would assume that the 10% variability would hold as long as I was more than 2 in. from any surface.

Q: Is there any influence from heat transport from thermistor to the surroundings by conduction of the connecting wires? Is there any influence from heat produced in the connecting wires?—Rik van der Graaf.

A: Thermistor manufacturers go to great lengths to ensure that heat conduction along the wires to the thermistor lead is kept very small. Therefore, heat conduction along the wires leading to the thermistor is undetectably small.

Q: Is there any influence from heat produced in the connecting wires?—Rik van der Graaf.

A: The resistance of the lead wires is so small and the currents in the wires so small that heat generation is not a problem. For example, the loop resistance for 100 ft (30 m) of no. 18 hookup wire is only 1.5 ohms. Therefore, the power lost in this entire 100-ft length is:

Measuring (50 μA): Power = $I^2R = (50 \times 10^{-6})^2(1.5) = 3.75 \times 10^{-9}$ W

Heating (5 mA): Power = $I^2R = (5 \times 10^{-3})^2(1.5) = 37.5 \times 10^{-6}$ W

Q: Have you encountered any problems with acquiring thermistor data directly with an analog to digital (A/D) converter through a multiplexer? We at ORNL have had trouble with our high-output thermopile type heat flux transducer signal being biased by a mercury-wetted type multiplexer to A/D system.—Thomas Petrie, Martin-Marietta Corporation, Oak Ridge National Laboratories.

A: 1. Yes, we have encountered such problems. We thought it was caused by either one or a combination of the following:

a. The time constant caused by long cables and large thermistors caused errors, since the circuit hadn't stabilized before the multiplexer had switched, read, and moved to the next channel.

b. Too low an input impedance for high resistance thermistors.

c. Leakage in thermistor cables.

d. Insufficient isolation between multiplexer channels (for high resistance thermistors).

e. Autoranging readout systems are too slow for scan speeds selected for the multiplexer.

2. For our data loggers (Campbell CR-10's), we found that they read correctly on any monitoring of an individual channel, but read with errors up to 4°C when scanning. We also found that any channel reads correctly, if a single thermistor (not one in a whole cable of thermistors) is connected to it.

3. The Campbell thermistor readout circuit is rather unique and may be contributing to the problem.

AN IN-SITU METHOD FOR THERMAL CONDUCTIVITY AND DIFFUSIVITY MEASUREMENTS

P. Morabito

Hydraulic and Structural Research Center
Italian National Electricity Board
Milan, Italy

ABSTRACT

The analysis of the thermal effects arising in civil structures requires an accurate knowledge of the thermal properties of structural and porous materials such as concrete, rock and soil in their actual service conditions.

To this aim an in-situ measurement method has been developed. It allows the conductivity and thermal diffusivity to be determined simultaneously. The method, called the two linear and parallel probe method (TLPP), is based on the linear-heat-source theory and consists of inserting two probes in parallel holes drilled in the material to be tested. One probe is used as a heating source, the other one, used as a temperature sensor, detects the rate of the temperature rise of the material at a given distance from the heating probe.

The measurements are performed by a portable and automatic data acquisition system.

Among the different applications an example of monitoring of the conductivity and thermal diffusivity of an Italian concrete dam is presented.

INTRODUCTION

The knowledge of the thermal properties of structural and heterogeneous materials such as concrete, rock and soil plays a leading role in many engineering applications where the effects of the heat propagation must be taken into account.

Besides the usual problems concerning the thermal insulation, particular importance must be given to the effects of the thermal stresses arising in massive structures under service conditions.

Dams, cooling towers, chimneys, etc., in normal working environmental conditions are subjected to variations of the temperature of several tens of degrees Celsius. Such variations produce cyclic

stresses that can cause the propagation of microcracks in the structures.

Current numerical calculation methods can give an accurate evaluation of the space-time distribution of the temperature inside and outside the structure and then of the corresponding thermal stresses, provided the conductivity and thermal diffusivity of the materials are accurately known.

The materials for civil engineering are damp and porous so that their thermal properties, besides depending on the composition, are affected by the temperature and moisture content. For a material under service, they depend on environmental factors which, in turn, vary during the year.

Since core boring of samples for laboratory tests alters their actual thermo-hygrometric conditions, direct in-situ measurements are to be preferred to the laboratory tests.

The Hydraulic and Structural Research Center (CRIS) of the Italian National Electricity Board (ENEL) has developed, in cooperation with CISE (Centro Informazioni Studi ed Esperienze), an in-situ method to determine the conductivity and thermal diffusivity of concrete, rock and soil. It is based on the non-steady-state theory of the linear heat source and consists of detecting the temperature rise produced in the material from a heating probe without pulling out samples, thus leaving untouched the tested structures, except for drilling two holes for the probes' introduction.

THE TRANSIENT THERMAL PROBE METHOD

One of the most used methods for in-situ measurements is the transient thermal probe method. This method allows one to measure only the thermal conductivity and is based on the theory developed by Carslaw and Jaeger [1], which refers to an infinite linear heat source of infinitely small diameter, with no thermal inertia, buried in an infinite homogeneous medium. Briefly, it states that the temperature rise T at a radial distance r from the heat source is given by

$$T(r,t) = -\frac{q}{4\pi\lambda} E_i\left(-\frac{r^2}{4Dt}\right) \qquad (1)$$

where E_i is an exponential integral, q (W/cm) is the power input for unit length of the heat source, λ (W/cm/°C) and D (cm^2/sec) are the thermal conductivity and thermal diffusivity respectively, and t (sec) the time computed from the start of heating (t>0).

By expanding the exponential integral in a power series, it is possible to show that, for small r and long time t, equation 1 becomes

$$T(t) = \frac{q}{4\pi\lambda}\left(\ln t + \ln\frac{4D}{r^2} - C\right) \qquad (2)$$

where C is the Euler's constant.

Equation 2 shows that the temperature rise against the natural logarithm of the time is a straight line whose slope is proportional to

the thermal resistivity of the material to be tested.

The experimental linear heat source is realized by a suitable thermal probe, having a high ratio length/diameter to satisfy as completely as possible the assumptions of the theory, and equipped with a heating element and a temperature sensor.

The probe is housed in a hole drilled in the structure or in the soil to be investigated. The air gap between probe and material is usually filled with grease or similar fluids in order to have a good thermal contact between the probe and material to be tested.

Figure 1 shows a typical graph of the temperature rise of the probe against the natural logarithm of time, in comparison with the ideal infinite linear heat source response.

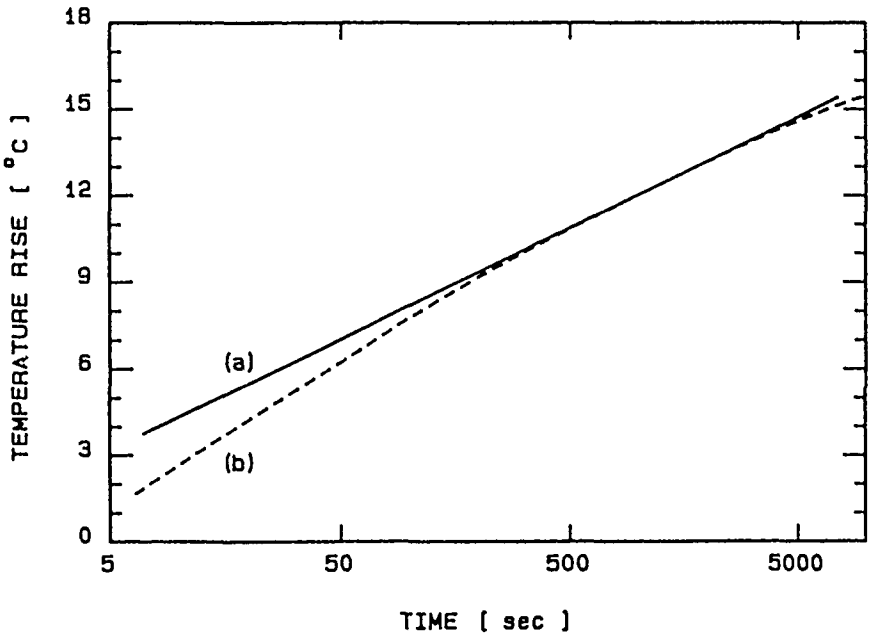

Figure 1. Comparison between the ideal linear heat source (a) and the experimental thermal probe response (b).

At short and long times of heating, the behavior of the thermal probe is slightly different from the ideal response. This results from some probe factors such as finite length, finite diameter and the contact resistance at the probe/material interface. An analysis of their effects has been reported by other authors [2], [3].

From a practical point of view, the result is that it is very difficult to single out on the experimental data the right interval of time over which equation 2 must be applied, although, with an appropriate selection of the time interval, the method gives sufficiently repetitive results.

The method proposed in this paper is the so-called two linear and parallel probe (TLPP) method. Based upon the same theory, this method allows the conductivity and thermal diffusivity to be measured simultaneously through a different test configuration.

THE TWO LINEAR AND PARALLEL PROBE MEASUREMENT METHOD

By differentiating equation 1 against time we obtain:

$$\frac{dT}{dt}(r,t) = \frac{q}{4\,\pi\,\lambda\,t}\exp\left(-\frac{r^2}{4\,D\,t}\right) \qquad (3)$$

Equation 3 is plotted in Figure 2 for different values of r.

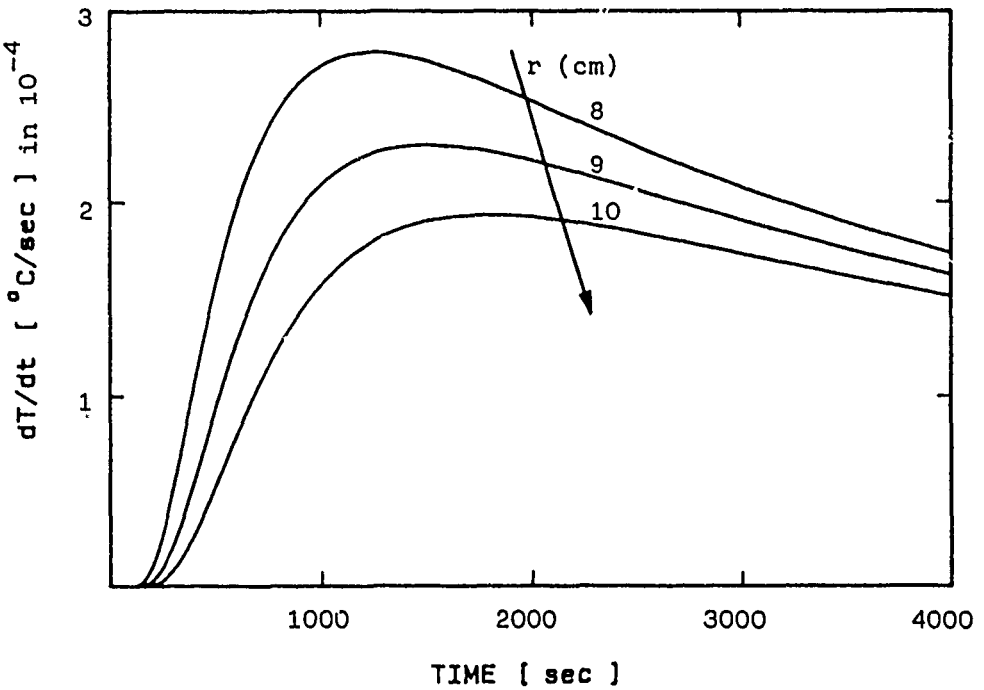

Figure 2. Plot of equation 3 for λ = 3.6 (W/m/°C), D = 50 (cm^2/h), q = 0.34 (W/cm).

Differentiating again against time and equalizing to zero it follows that:

$$\frac{r^2}{4\,D\,t} = 1 \qquad (4)$$

which gives the time t_x when equation 3 reaches the maximum value $(dT/dt)_x$:

$$t_x = \frac{r^2}{4\,D} \qquad (5)$$

Substituting $t=t_x$ in equation 3, the maximum value $(dT/dt)_x$ is given from:

$$\left(\frac{dT}{dt}\right)_x = \frac{q}{4\,\pi\,\lambda\,t_x}\exp(-1) \qquad (6)$$

Equations 5 and 6 lead to the following expressions:

$$D = \frac{r^2}{4\ t_x} \tag{7}$$

$$\lambda = \frac{q}{4\ \pi\ \exp(1)\ \left(\frac{dT}{dt}\right)_x\ t_x} \tag{8}$$

which allow the thermal diffusivity and conductivity to be determined from the experimental detection of the maximum value of equation 3 and of the corresponding time.

The experimental plot of equation 3 is obtained using a second probe, as temperature sensor, inserted in the material to be tested at a distance r of 6-8 cm from the heating probe and parallel to it. Detecting the temperature rise of this probe at a fixed rate, the first member of equation 3 is obtained by applying the finite differences method.

The effects of the finite dimensions of the heating probe are such that they can be simulated by a thermal capacity in series with a thermal resistance, which takes into account the thermal resistance of the heating probe and the thermal resistance at the probe/material interface. The result is that the thermal wave supplied from the heating wire inside the probe spreads into the material to be tested with a time delay t_o from the start of heating.

Consequently for a right evaluation of t_x, and then of the thermal conductivity and diffusivity, the experimental data of equation 3 must be reduced for t_o in a such way that the experimental points fit well into equation 3.

The time delay t_o must be evaluated during each test because it is dependent on the thermal probe/material interface, which is strongly affected by the random distribution of the thermal contact areas between probe and material. The evaluation of t_o is performed using the following procedure suggested by Mason and Kurtz [4].

If we consider the temperature rise of the heating probe, which is described from the equation 2, the assumption r=0 being true, and introduce the thermal delay t_o in this equation, we obtain:

$$T(t) = \frac{q}{4\ \pi\ \lambda}\left[\ln\frac{4\ D\ (t-t_o)}{r^2} - C\right] \tag{9}$$

Differentiating against the time and inverting,

$$\frac{dt}{dT} = \frac{4\ \pi\ \lambda}{q}\ (t-t_o) \tag{10}$$

Equation 10, plotted against the time, is a straight line whose intersection with the time axis allows the thermal delay t_o to be estimated. An experimental graph of equation 10 is given in Figure 3.

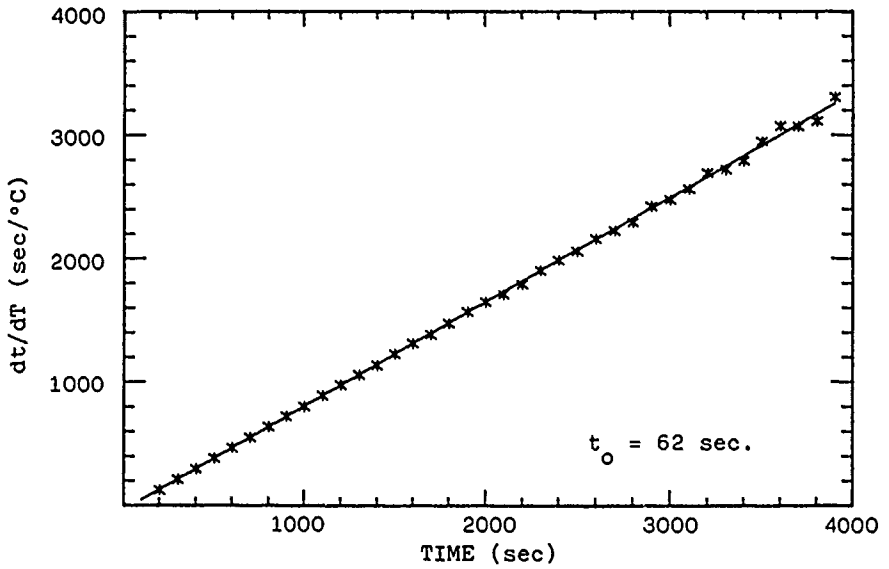

Figure 3. An experimental plot of equation 10.

THE THERMAL PROBES

The thermal probes we have adopted (Fig. 4) have the following main features:

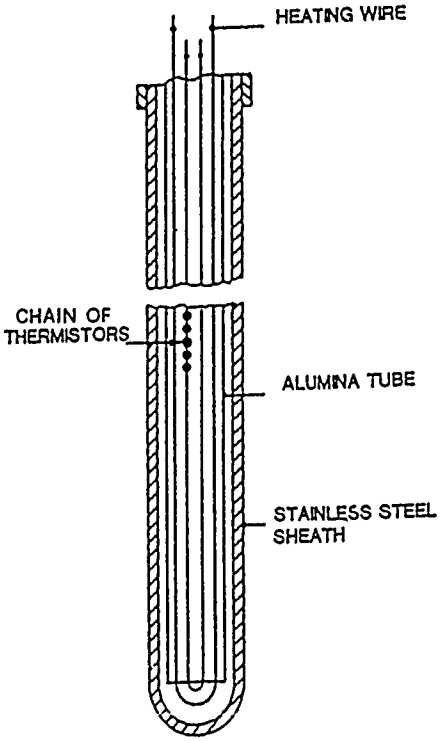

Figure 4. Details of the heating probe.

- An outer stainless steel sheath with a diameter of 15 mm and a length of 900 mm for the heating probe and a diameter of 8 mm and length of 600 mm for the second probe.

- A four-holed Al_2O_3 tube, as an electric insulator, where the heating wire and the temperature sensor are housed.
- A heating component made of a resistance wire.
- A temperature sensor, made of a chain of five thermistors connected in series and set in the center of the probe.

After the probe has been assembled, the temperature sensors are calibrated in a thermostatic bath with temperature stability and uniformity of about $\pm$ 0.005°C.

Thermistors were chosen as temperature sensors because their sensitivity is higher than that of other sensors.

The configuration of the TLPP test is shown in Figure 5.

A typical test result is presented in figure 6.

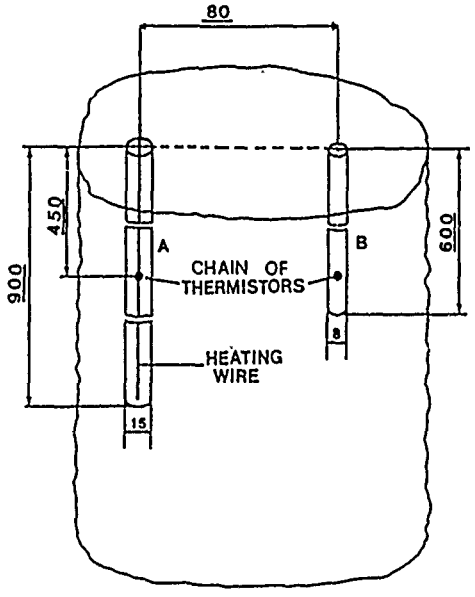

Figure 5. Configuration of the TLPP test (all the dimensions in mm).

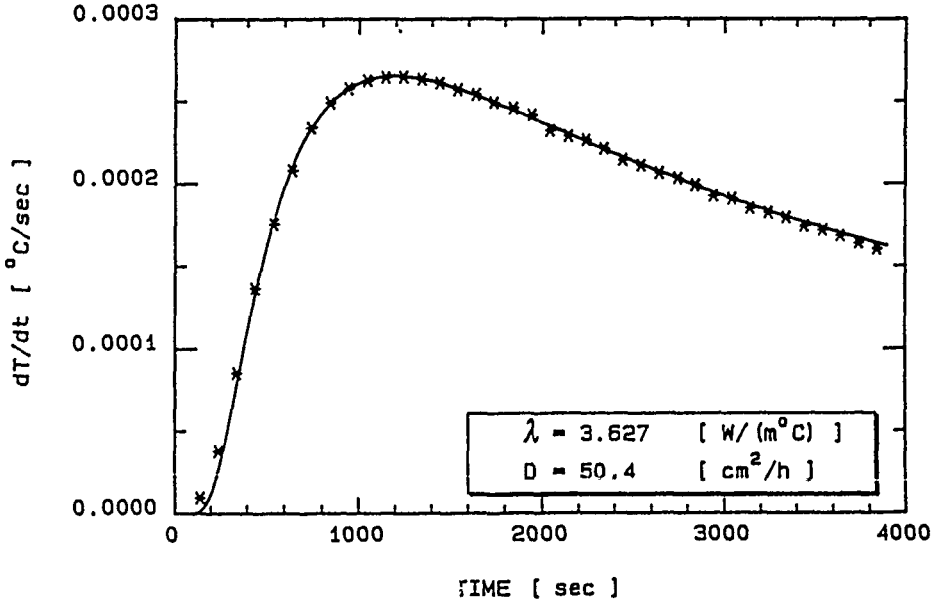

Figure 6. Example of an in-situ test result performed with a heating power q = 0.34 (W/cm).

TEST PROCEDURE AND DATA ACQUISITION SYSTEM

The typical sequence of an in-situ TLPP test for thermal conductivity and diffusivity measurements is the following:

1st stage: placement of the probes and conditioning.
2nd stage: detection of the thermal drift.
3rd stage: supply of the heating probe.
4th stage: data reduction.

1st stage

The two probes are smeared with grease and then placed into the two parallel holes drilled in the structure to be tested. As probes and materials are initially at different temperatures, it is necessary to wait 15-20 minutes to be sure that the probes and materials are in thermal equilibrium.

2nd stage

Usually, the material is under thermal drift due, for example, to the daily temperature variations. This thermal drift can introduce a large error in the measurement results so it must be taken into account. To do this, temperature readings are performed for 4000 sec at a rate of 100 sec. The data are then fitted with a quadratic function by the method of least squares which gives the relative coefficients.

3rd stage

The heating probe is supplied by a step function at constant power q, whose value ranges from 0.017 to 0.39 W/cm. The actual value is assigned in order to satisfy the opposite requirements of introducing

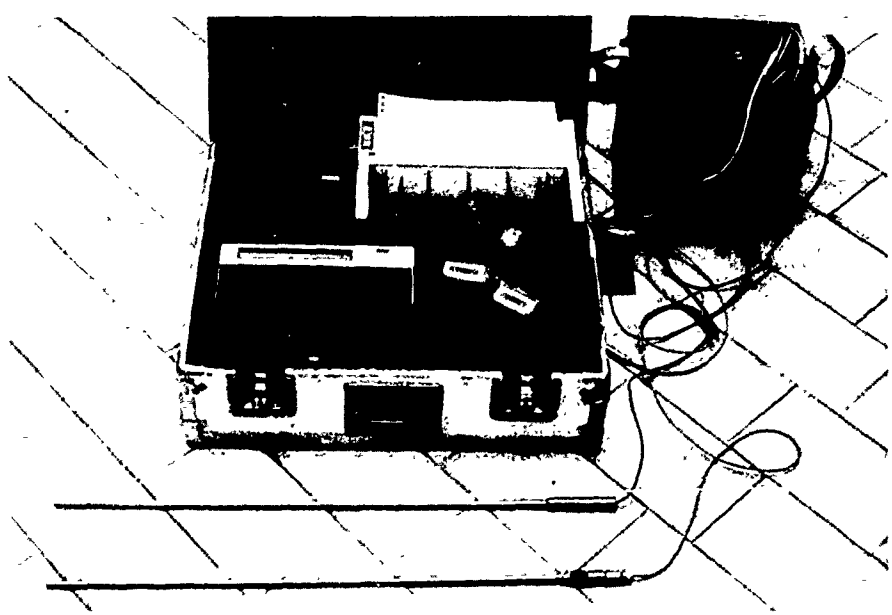

Figure 7. The portable and automatic data acquisition system.

low thermal gradients into the material to reduce the deleterious effects of the moisture migration and having sufficient temperature rises in the material, of the order of one degree Celsius 8 cm from the heating probe. This stage runs for 4000 sec during which the temperature increases of both probes are detected at a rate of 100 sec.

4th stage

The temperature readings performed during the heating stage are corrected according to the thermal drift coefficients previously determined.

Then the calculation of the time delay t_o is performed. The experimental data of the probe B (see Fig. 5) are reduced for t_o and a best fit on them with equation 3 allows t_x and $(dT/dt)_x$ to be determined. The thermal conductivity and diffusivity coefficients are then calculated from the equations 7 and 8.

The last step is performed in the laboratory with a personal computer; the other steps are carried out in situ with a portable and automatic data acquisition system (Fig. 7). It is made up from battery-operated components including a digital multimeter, a scanner and a cassette recorder; their functions are controlled by a programmable calculator with an internal digital clock.

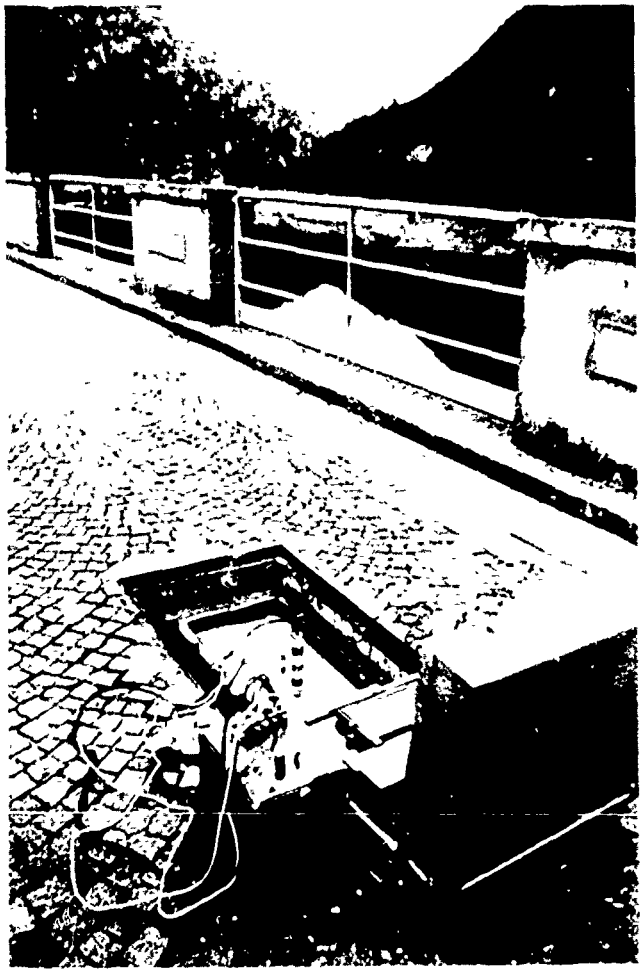

Figure 8. Application of the TLPP method on an Italian concrete dam.

APPLICATIONS

The reliability of the method has been verified through laboratory tests on a concrete sample, 100 cm in diameter and 140 cm in height, kept at constant temperature and moisture content. The measurements of thermal conductivity and diffusivity have shown good repeatibility (within 3%) and compare quite well with those obtained on the same concrete sample by other laboratory test methods.

To ascertain the possibility of monitoring a large structure from the viewpoint of the thermal phenomena and their effects, monthly measurements on an Italian concrete dam (Ponte Cola Dam) have been carried out (Fig.8). The results obtained during the years 1984-1989 are shown in Figure 9.

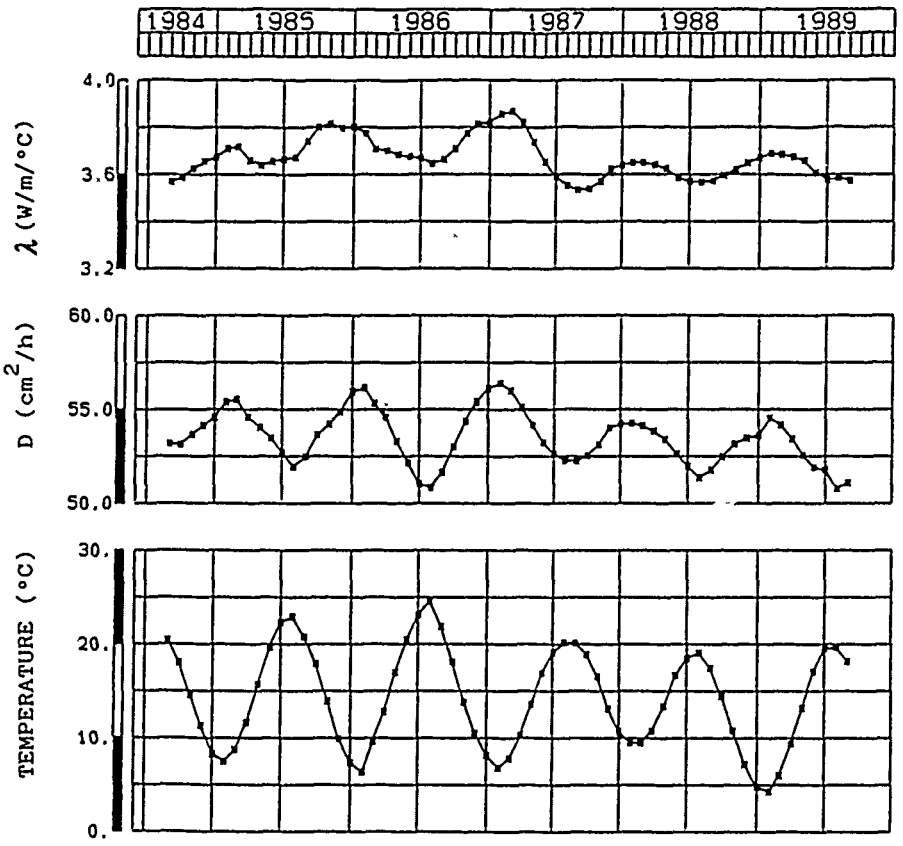

Figure 9. Thermal conductivity λ and thermal diffusivity D monitoring at the Ponte Cola Dam over the years 1984-1989.

The Ponte Cola data clearly show the seasonal variations of the thermal conductivity and diffusivity of the structure and that such variations are in phase opposition with the temperature. These results are in fair agreement with some experimental correlations obtained in the laboratory [5] to study the influence of the temperature on the thermal properties of concrete (Fig.10); the laboratory tests were carried out with a laboratory version of the TLPP method.

The in-situ apparatus has also been employed in different Italian sites to evaluate the capability of the soil to drain the heat produced by electrical cables or the effects of the seasonal temperature variations at the boundary of buried hot water pipes. For example,

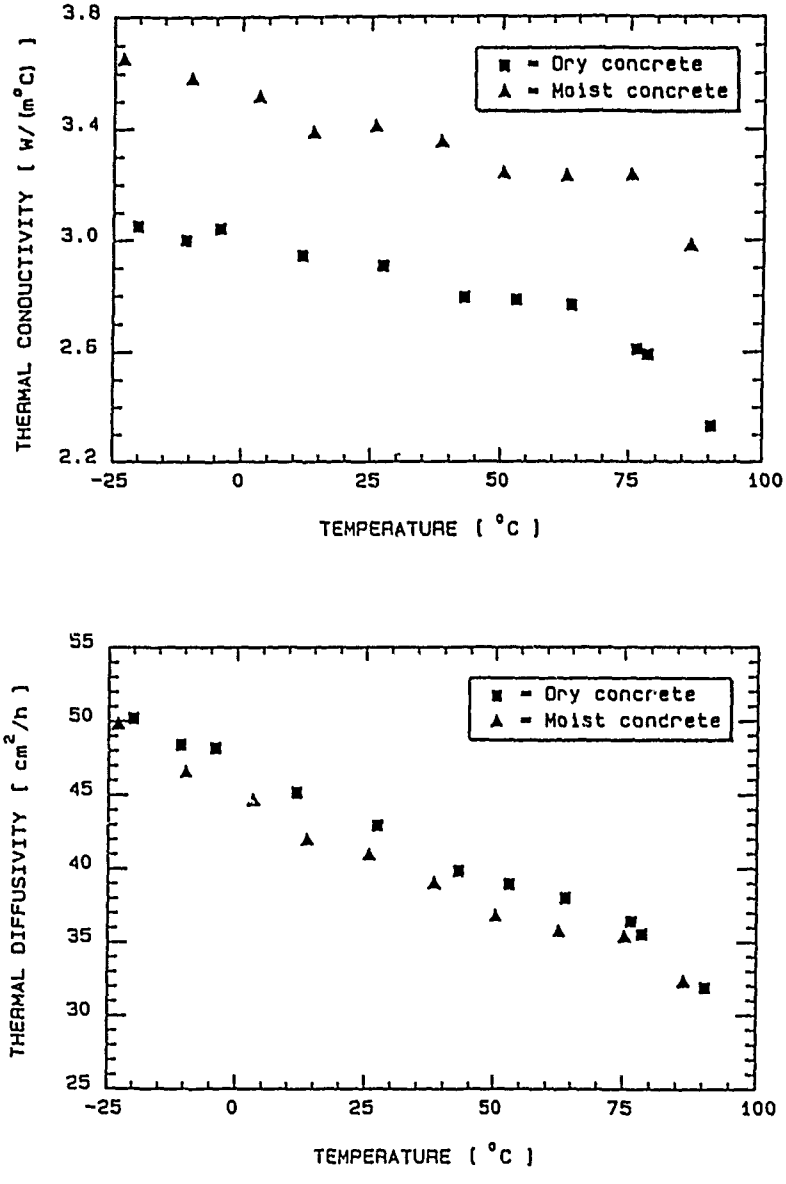

Figure 10. Thermal conductivity and diffusivity against the temperature of concrete

measurements performed in a clay soil have given a thermal conductivity of 1.7 W/m/°C and a thermal diffusivity of 24 cm^2/h. In such situations the use of the TLPP method for in-situ tests is particularly suitable, being quite impossible to reproduce in laboratory soil samples with the same unit weight and moisture content as in the real conditions.

CONCLUSIONS

An in-situ method for measuring thermal conductivity and diffusivity in structural materials for civil engineering has been described. The method is particularly suitable in all those events where the thermal properties of the material are strongly affected by the environmental

conditions or when it is impossible to retrieve undisturbed samples for laboratory tests. Such situations are very frequent.

Measurements performed on an Italian concrete dam have shown that the TLPP method allows monitoring of the thermal conductivity and diffusivity of the structure and their seasonal variations.

The good reliability of the test method is also due to the high quality of the probes; their main features are high resolution in the temperature measurements, ease of connection to the data acquisition system and suitability for carrying out tests on different materials.

ACKNOWLEDGMENTS

The author wishes to thank the technicians of CISE and ENEL-CRIS for their valued cooperation and assistance.

REFERENCES

1. Carslaw H. S., Jaeger J. C. Conduction of heat in solids. Oxford University Press, 1959.
2. Singh G., Ergatoudis J., Siah B. S. A laboratory method of measuring in-situ density distribution in dry sand. Geotech. Testing J., vol.2, n.3,1979.
3. Goodrich L. E. Field measurements of soil thermal conductivity. Can. Geotech. J., vol.23, 1986.
4. Mason V. V., Kurtz M. Rapid measurement of the thermal resistivity of soil. Trans. of the Am. Inst. of Electr. Eng., vol. 71, 1952.
5. Morabito, P. Measurements of the thermal properties of different concretes. High Temperatures. High Pressures, vol.21, n.1, 1989.

Paolo Morabito

Q: Have you done experimentation with various diameters of your apparatus? In Carslaw and Yaeger, they assume an infinitely small diameter and an infinite length. Does the diameter of the heat source probe you used seem too large?—Unsigned.

A: We have not done tests with probes of various diameters, since they are expensive to make. However, more so than the diameter of the heating probe, we have to take into account its length/diamcter ratio, which for our probe is 60. The effects of the length/diameter ratio have been studied by performing tests with different distances between the heating probe and the receiving one. Of course, the greater this distance, the greater bias of the actual conditions from the ideal. Preliminary results have shown that there are no significant variations cn the thermal conductivity and diffusivity measurements as long as the distance between the two probes does not exceed 10 cm.

CALIBRATION TRANSFER STANDARDS FOR FENESTRATION SYSTEMS

W.P. Goss	University of Massachusetts Amherst, Massachusetts USA
H.A. Elmahdy	National Research Council of Canada
R.P. Bowen	Ottawa, Ontario, Canada

ABSTRACT

Calibration transfer standards are large heat flux transducers primarily used in the calibration of the surface conductances of fenestration systems (e.g., windows, doors and glazed curtain walls) that are to have their overall thermal transmittance and conductance determined in an ASTM C236 (1990) Guarded Hot Box, an ASTM C976 (1990) Calibrated Hot Box, or a similar hot box arrangement. A secondary use is for verifying the conductance of the surround panel in which the fenestration system is mounted. A calibration transfer standard consists of a homogeneous, thermally well characterized core calibration material sandwiched in between two sheets of glass. The core calibration material is made from an insulation board that has a known thermal conductivity measured by an ASTM C177 (1990) Guarded Hot Plate or an ASTM C518 (1990) Heat Flow Meter. A number of area weighted temperature sensors, which are soldered to a thin copper shim material, are adhered to the inner surfaces of the glass sheets before the glass sheets are assembled with the core material in a sandwich configuration. This allows the heat flux through the calibration transfer standard to be determined from measurement of the temperature difference across the core material. The paper describes the design and fabrication of calibration transfer standards and their use in laboratory measurements of the thermal transmittance and conductance of fenestration systems. Also included is a discussion of their potential use for in-situ thermal transmittance measurements of installed fenestration systems.

INTRODUCTION

There has been significant interest in the past several years in the United States and Canada in developing a consensus test method for measuring the thermal transmittance of fenestration systems (windows and doors). This interest has been amplified by the possibility of having required energy performance rating labels on windows produced in Canada and the United States. One of the parameters that would be a significant portion of a window energy performance rating label would be the thermal transmittance or U-value. A joint task group from ASTM Committee C16 (Thermal Insulation) and Committee E6 (Performance of Building Constructions) has been developing two companion documents (ASTM CXX3 1990, ASTM EXYZ 1990; both documents are in their 10th drafts and are currently being balloted at the committee level) that specify how to use either a guarded hot box (ASTM C236 1990), or a calibrated hot box (ASTM C976 1990) to

determine a standard U-value for fenestration systems. Since it is desirable to have as accurate a U-value as economically and technically possible, an important part of the new test method (ASTM CXX3 1990) is the large heat flux transducer used for calibration purposes. Such large heat flux transducers are called calibration transfer standards (hereafter denoted as CTS). The reason for this terminology is that these large heat flux transducers are used to simulate a simple fenestration system (a sealed window glazing unit) mounted in a homogeneous surround panel that is supposed to simulate a well insulated building wall or roof. The large heat flux transducers are primarily used as independent calibration standards to estimate as accurately as possible the surface heat transfer coefficients of more complex fenestration systems, such as a window incorporating several sealed glazing units in an operable sash/frame configuration. The assumed similarity of surface heat transfer performance from the simple geometry of a large heat flux transducer to the more complex geometry of a real fenestration system mounted in the same surround panel is an assumption that can be verified only by very costly and complex convective heat transfer calculations. The use of the large heat flux transducers as calibration standards to transfer the surface heat transfer performance of simple to complex fenestration systems mounted a simulated building opening is quite different from the typical use of estimating the heat flux at surfaces. To emphasize this difference in use, these specially designed large heat flux transducers are called calibration transfer standards (CTS). This paper describes the design and fabrication of a prototype CTS and discusses how it may be used for calibration purposes.

BACKGROUND

The concept of using some type of device for calibration purposes in the determination of the window U-value is not unique. The American Architectural Manufacturers Association (AAMA, formerly the American Aluminum Manufacturers Association) developed in the 1970s an industry voluntary test method (AAMA 1503.1 1980) to determine fenestration U-values. It is specified in this test method that a "...standard calibration panel of known conductance..." has to be used to calibrate the fenestration test facility's cold and warm side surface heat transfer coefficients. The calibration panel consists of two 3.18-mm (1/8-in.) glass sheets mounted in a wood frame so that they are separated by a 50.8-mm (2.0-in.) airspace. The assumed constant thermal conductance of the calibration panel is calculated by using simple correlations for the airspace thermal conductance and as such are not traceable by any measurement technique to a known accurate conductance value as a function of the calibration panel temperatures. However, the AAMA test method (AAMA 1503.1 1980, and AAMA 1503.1 1988) does recognize the need to have a calibration procedure when making fenestration system U-value measurements.

Large heat flux transducers have been used in the MoWITT test facility (Klems and Selkowitz 1981) in determining the heat flux through the walls of this mobile window thermal test facility. The description of these heat flux transducers is presented in Klems and DiBartolomeo (1982) and Klems (1983). These large (up to 1.2-m by 0.6-m or 2-ft by 4-ft) heat flux transducers are aluminum faced with either a fiberglass-filled phenolic honeycomb or rigid fiberglass board core. The temperature difference measurements are made using specially designed resistive temperature sensors and the entire heat flux transducer was calibrated in a guarded hot plate and a large calibrated hot plate.

In Norway, there is mention made of a glass-faced, expanded polystyrene core heat flux sensor used for calibration purposes in the Norwegian Standard NBI-138 (1982, see also McCabe and Goss 1986 for a translation of NBI-138) for determining the thermal resistance and surface temperature of sealed glazing units. However, it seems that this heat flux sensor is not currently in use by the Norwegian Building Research Institute.

More recently, Bowen and Solvason (1987) presented a description of a Canadian CTS used in calibrating the fenestration hot box at the National Research Council of Canada's Institute for Research and Construction. More details about the Canadian CTS are given in the following sections of this paper.

DESIGN AND FABRICATION

The calibration transfer standard (CTS) described in this section was designed at the Building Performance Section, Institute for Research in Construction, National Research Council of Canada (NRCC). Figure 1 shows a schematic of a CTS for use in the determination of a fenestration system's surface heat transfer coefficients.

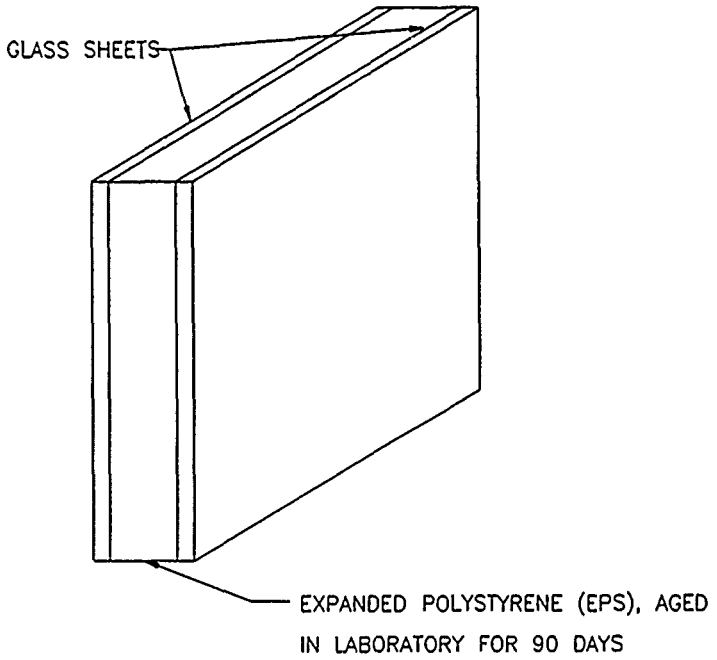

FIGURE 1. CALIBRATION TRANSFER STANDARD SCHEMATIC.

The CTS consists of a core insulation board of known thermal conductivity sandwiched between two edge-ground glass sheets. A suitable facing material is 3- or 6-mm (0.12- or 0.24-in.) float glass. A recommended CTS core material is expanded polystyrene (sometimes called beadboard) having a density of approximately 20 kg/m^3 (1.25 lbm/ft^3) which has been aged (conditioned) unfaced in thelaboratory where the hot box is located for a minimum of 90 days. This allows the thermal conductivity of the expanded polystyrene (EPS) to reach a steady state value. It is required, prior to assembly of the CTS, that the thermal conductivity of the material used for the core of the calibration transfer standard be measured in a guarded hot plate (ASTM C177 1990) or a heat flow meter (ASTM C518 1990) at a minimum of three temperature settings. Typically, these temperature settings represent extreme winter, moderate winter and summer temperature conditions.

For the prototype CTS, the EPS material used had a measured thermal resistance (the thermal conductivity can be obtained by dividing the thickness [0.013 m] of the EPS material by the thermal resistance) as given by Equation (1):

$$R_{si} = 0.4146 - 0.0014 * T_{mean} \qquad (1)$$

where: R_{si} = thermal resistance ($m^2 \cdot {}^\circ C)/W$
T_{mean} = mean temperature ($^\circ C$)

$$R\ (ft^2 \cdot hr \cdot {}^\circ F)/Btu = 5.6745 * R_{si}$$

Figure 2 shows the prototype CTS that was fabricated jointly by National Research Council of Canada (NRCC) and University of Massachusetts personnel at the NRCC. The prototype CTS consisted of a 13-mm (0.51-in.) EPS core sandwiched between two sheets of 3-mm (0.12-in.) nominal thickness float glass sheets.

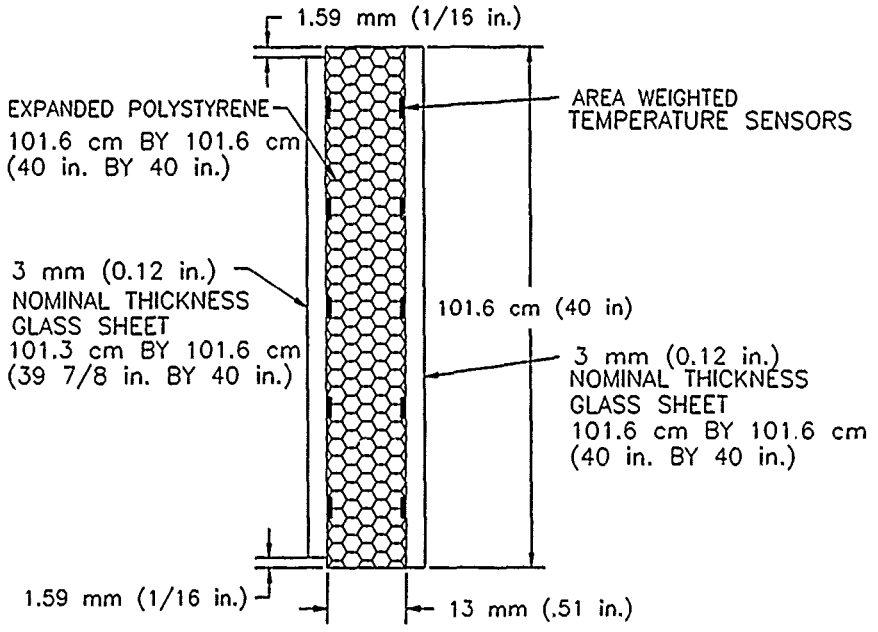

FIGURE 2. PROTOTYPE CALIBRATION TRANSFER STANDARD

The actual thickness was measured to be 2.94 mm. The overall dimensions of the CTS normal to the direction of heat flow were 101.6 cm by 101.6 cm (40 in. by 40 in.). These dimensions were used to simulate a standard sealed double-glazed unit with two single strength glass panes separated by a 1/2-in. airspace. As illustrated in Figure 2, one of the glass sheets has an extra 1.59 mm (1/16 in.) taken off the top and bottom to allow for the thermocouple wire leads from the area-weighted temperature sensors to exit the CTS without being wedged between the CTS and the surround panel it is mounted in.

Figure 3 shows the area-weighted temperature sensor locations on the prototype CTS. Each sensor represents the temperature in a rectangular area x by y (where x = 20.32 cm (8 in.) and y = 25.4 cm (10 in.)).

Similar area weighting of approximately 1 sensor per 500 cm^2 (80 $in.^2$) should be used for other size CTSs. Figure 4 shows the design of the temperature sensors for the prototype CTS. Each sensor consisted of a 30-gage, special limit, type T (copper-constantan) bare thermocouple element, which was twisted and soldered to a thin 3-mil (0.003-in.) copper shim that was cut to a rectangular size of 1.91 by 3.81 cm (0.75 by 1.5 in.).

The general fabrication procedure of the CTS from components designed as illustrated in Figures 1 through 4 proceeds as follows. The expanded polystyrene (EPS) board is accurately surface ground, using a milling machine, to have as flat a surface as feasible. The size of the EPS boards used to make up the CTS core will be dependent upon the size of the milling machine used. For the prototype CTS shown in Figures 2 and 3, four boards 60.96 by 60.96 cm (24 by 24 in. - the maximum size the milling machine could handle) were cut to size to make up the total CTS dimensions of 101.6 by 101.6 cm (40 by 40 in.).

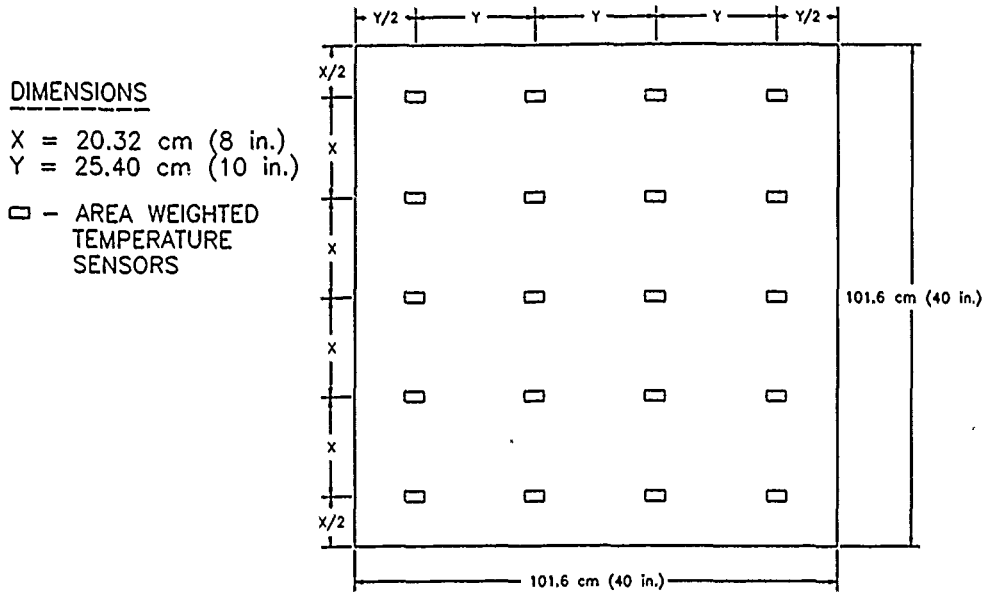

FIGURE 3. TEMPERATURE SENSOR LOCATION ON PROTOTYPE CALIBRATION TRANSFER STANDARD.

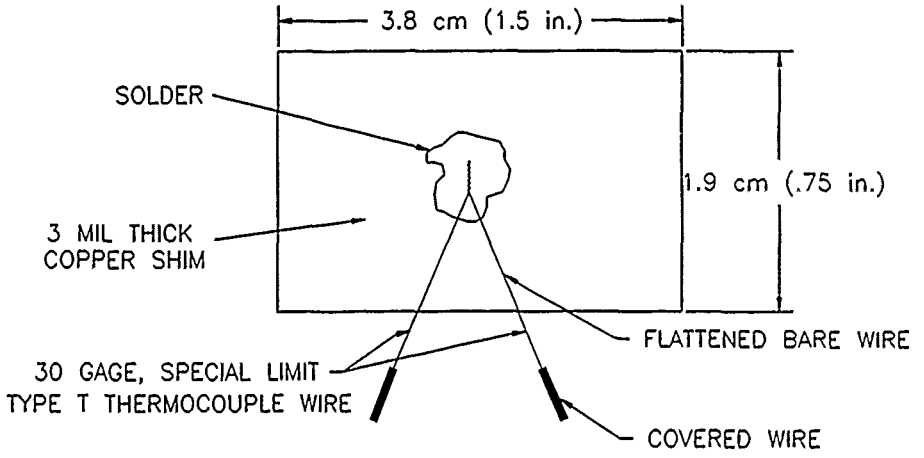

FIGURE 4. PROTOTYPE CALIBRATION TRANSFER STANDARD TEMPERATURE SENSORS.

After aging (laboratory conditioning), the thermal conductivity of the EPS boards is measured in a guarded hot plate (ASTM C177 1990) or a heat flow meter (ASTM C518 1990) at a minimum of three temperatures covering the range from extreme winter [cold side: -32°C (-25°F); warm side: 24 C (75 F)] through moderate winter [cold side: -15 C (5 F); warm side: 24 C (75 F)] to summer [cold side: 24 C (75 F); warm side: 52 C (125 F)] temperature conditions. All of the temperatures given above can vary 5 C (9 F) as per ASTM C1058 (1990).

The glass sheets are cut to size from 3 or 6 mm (0.12 or 0.24 in.) float glass and are edge ground. One of the glass sheets has 1.59 mm (1/16 in.) taken off the top and bottom as illustrated in Figure 2. To fabricate the temperature sensors, the small diameter thermocouple wires should be stripped back approximately 1.9 cm (0.75 in.) and then twisted into a bare thermocouple element (see ASTM STP 470A 1974, Figure 17), which is then hammered as flat as possible. The resulting twisted thermocouple junction should be carefully inspected to ensure that the wire leads are not cracked or broken in the flattening process. The flattened twisted thermocouple junction is then soldered to a thin (approximately 3-mil) copper shim material approximately 1.91 cm (0.75 in.) by 3.81 cm (1.5 in.) in size, as shown in Figure 4. As indicated in Figure 4, the bare or stripped portion of the wire leads that have been hammered flat should extend past the copper shim material so that only the thicker covered portion of the wire will be imbedded in the core insulation material. This makes the very thin and nearly flat sensor less apt to introduce undesirable effects in the heat transfer from the core insulation material to the glass faces. To assemble the CTS, the area-weighted temperature sensor locations are marked on the inside of the glass sheets. Next, the reverse smooth (or non-thermocouple) side of a temperature sensor shim material is adhered with a latex bond contact cement to the glass sheet inner surfaces at each of the specified temperature sensor locations. The thermocouple wire leads are then split back to either the top or bottom edges of the glass sheets and temporarily folded over the edges and taped to the glass sheet outer faces. An equal number of wire leads should be exiting the top and bottom edges, and crossing of the wires should be avoided. The EPS boards are then butted together and carefully adhered to the glass sheet inner surfaces with a polystyrene compatible contact cement (a latex bond contact cement is also recommended here). Finally, after allowing 24 hours for the cement to dry, the thermocouple lead wires are untaped and labeled.

CALIBRATION PROCEDURE

Since the thermal resistance of the core material is known, the rate of heat transfer through the calibration transfer standard (CTS) can be determined from a measurement of the temperature difference across the core material as shown in Equation (2):

$$Q = A^{*}\check{S}T/R \qquad (2)$$

where: Q = heat transfer rate
A = CTS surface area
ŠT = measured temperature difference across the EPS core material
R = thermal resistance of EPS core material

There are a number of different methods for measuring the temperature difference across the EPS core material. One method is to wire the thermocouples on either side of the EPS core as a thermopile system to obtain an average temperature difference. Another method is to measure each temperature separately and to the calculate an average temperature difference. The latter method will also show the temperature distributions on each side of the CTS. The method selected will depend upon the accuracy of the data acquisition system used and the amount of information desired.

The calibration procedure for determining the CTS inside and outside surface heat transfer coefficients is specified in ASTM CXX3 (1990) and the details will not be repeated here. Essentially, the CTS is installed in the surround panel in place of the fenestration system as shown in Figure 5 for a parallel outside air flow and in Figure 6 for a perpendicular outside air flow.

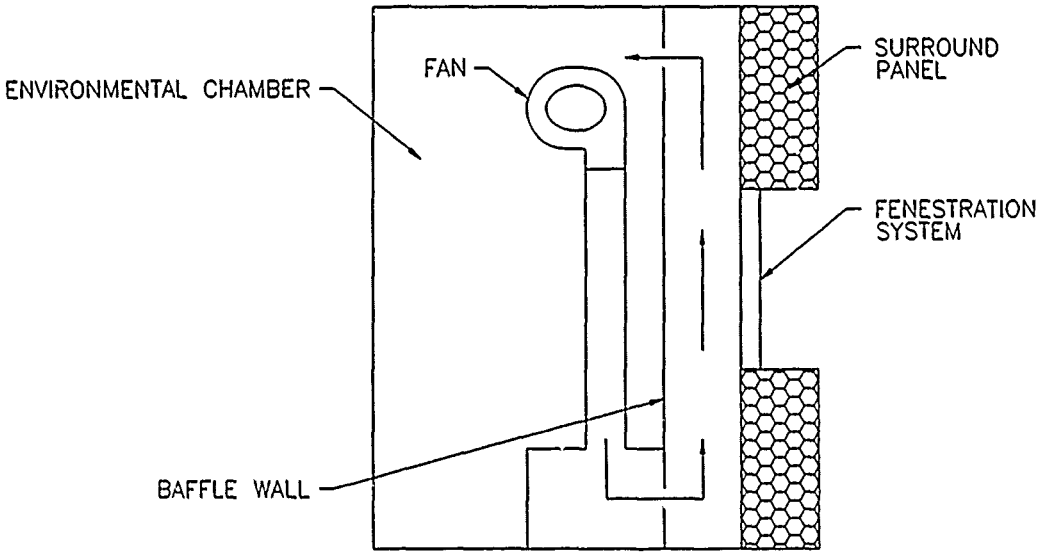

FIGURE 5. HOT BOX ENVIRONMENTAL CHAMBER, PARALLEL FLOW

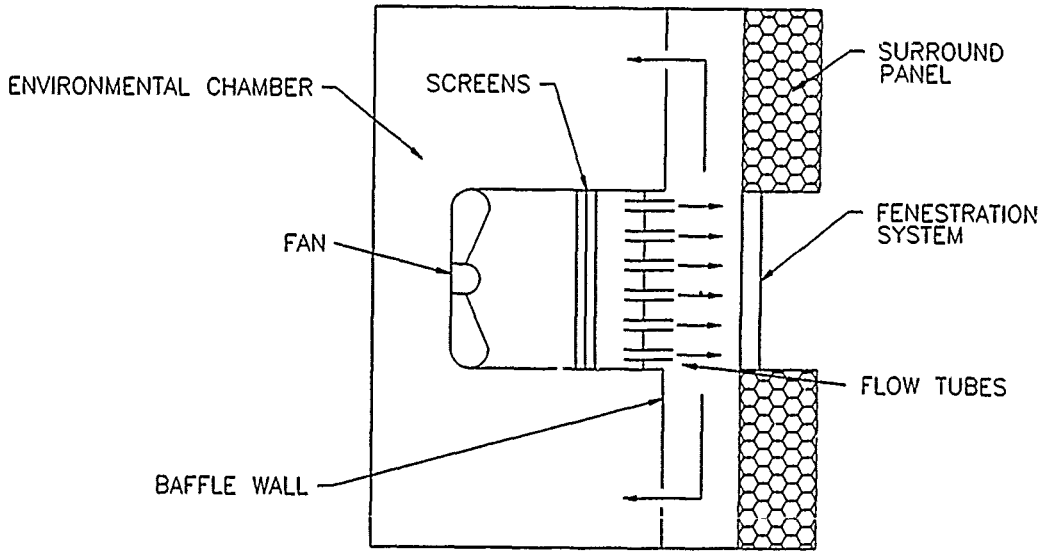

FIGURE 6. HOT BOX ENVIRONMENTAL CHAMBER, PERPENDICULAR FLOW.

When free (or natural) convection heat transfer conditions are simulated on both sides of the surround panel, calibration of the surround panel thermal resistance (or thermal conductance) at different surround panel surface temperatures and CTS positions in the surround panel is possible. This provides information on the surround panel's thermal resistance (or thermal conductance) as a function of the surround panel area weighted average temperature difference, mean temperature, and CTS position. Once the surround panel's thermal resistance is well characterized, the CTS surface heat transfer coefficients can be determined by utilization of the air temperature, and air speed and direction measurements specified in ASTM CXX3 (1990).

While all of the prior discussion has been directed towards laboratory measurements under controlled conditions, the same CTS design, fabrication and calibration procedures could be utilized to facilitate in-situ fenestration U-value measurements in actual buildings once a consensus portable hot box test method is developed.

CONCLUSIONS

The prospect of window thermal performance labeling in Canada and the United States in the near future has put added emphasis on the development of a consensus fenestration system U-value test method such as ASTM CXX3 (1990). Since it is desirable to have as accurate a U-value measurement as possible, an accurate calibration procedure for this test method is necessary. This need has led to the development of a large heat flux transducer called a calibration transfer standard (CTS), which can be utilized in current guarded and calibrated hot boxes and in future portable in-situ hot boxes for measuring fenestration system U-values.

REFERENCES

AAMA 1503.1 (1980) Voluntary test method for thermal transmittance of windows, doors and glazed wall sections. American Aluminum Manufacturers Association, Des Plaines, Illinois.

AAMA 1503.1 (1988) Voluntary test method for thermal transmittance and condensation resistance of windows, doors and glazed wall sections. American Architectural Manufacturers Association, Des Plaines, Illinois.

ASTM C177 (1990) Standard test method for steady-state heat flux measurements and thermal transmission properties by means of the guarded hot plate. 1990 Annual Book of ASTM Standards, Vol. 4.07, American Society for Testing and Materials.

ASTM C236 (1990) Standard test method for steady-state thermal performance of building assemblies by means of a guarded hot box. 1990 Annual Book of ASTM Standards, Vol. 4.07, American Society for Testing and Materials.

ASTM C518 (1990) Standard test method for steady-state thermal heat flux measurements and transmission properties by means of the heat flow meter. 1990 Annual Book of ASTM Standards, Vol. 4.07, American Society for Testing and Materials.

ASTM C976 (1990) Standard test method for thermal performance of building assemblies by means of a calibrated hot box. 1990 Annual Book of ASTM Standards, Vol. 4.07, American Society for Testing and Materials.

ASTM CXX3 (1990) Standard test method for measuring the steady state thermal transmittance of fenestration systems using hot box methods (Draft 10). American Society for Testing and Materials Committee C16.30.

ASTM EXYZ (1990) Standard practice for determining the steady-state thermal transmittance of fenestration systems (Draft 11). American Society for Testing and Materials Committee E06.51.

ASTM C1058 (1990) Standard practice for selecting temperatures for reporting and evaluating thermal properties of thermal insulation. 1990 Annual Book of ASTM Standards, Vol. 4.07, American Society for Testing and Materials.

ASTM STP 470B (1974) Manual on the use of thermocouples in temperature measurement. American Society for Testing and Materials.

Bowen, R.P., and K.R. Solvason (1987) A calorimeter for determining heat transmission characteristics of windows. In Thermal Insulation: Materials and Systems, American Society for Testing and Materials, ASTM STP 922, pp. 567-581.

Klems, J.H., and S.E. Selkowitz (1981) The mobile window thermal test facility (MoWITT). Proceedings of the ASHRAE/DOE-ORNL Conference on the Thermal Performance of the Exterior Envelopes of Buildings, ASHRAE, pp. 930-941.

Klems, J.H., and D. DiBartolomeo (1982) Large-area, high-sensitivity heat-flow sensor. American Institute of Physics, Review of Scientific Instruments, V. 53, N. 10, Feb. pp. 1609-1612.

Klems, J.H. (1983) Use of large-area heat flow sensors to measure building heat flows. Proceedings of the ASHRAE/DOE Conference on the Thermal Performance of Buildings II, ASHRAE, pp. 734.

McCabe, M.E. and W.P. Goss (1986) Interim procedure to measure the thermal performance of window systems. NBSIR 87-3569, National Bureau of Standards.

NBI-138 (1982) Sealed glazing units: Thermal insulation and surface temperature. Norwegian Standard.

William P. Goss

Q: When window systems are mounted in real wall construction, there is often a significant thermal bridge and flanking loss associated with the frame-wall interface. In the proposed test method, this framing loss is considerably smaller when a window test article is installed in an idealized polystyrene wall. Please comment—Unsigned.

A: Due to the wide variety of residential, commercial and industrial building wall constructions and the further variability of the methods used to construct the rough opening in walls to install window systems, it is not feasible to select a typical wall/rough opening configuration for use in performing laboratory window U-value tests. The selection of a homogeneous, high insulation surround panel was guided by the desire to limit the magnitude of the flanking heat transfer so that the heat transfer through the window system can be more accurately determined. It also allows window systems to be compared on an equal basis.

Q: Will air leakage be on the window label?—Jeffrey Christian.

A: It is anticipated that along with the window U-value and solar heat gain factor, air leakage will be one of the parameters reported on future fenestration system energy labels.

Q: Will thermal tests be made on the same device as air leakage tests?—Jeffrey Christian.

A: While a test facility could be constructed to perform both thermal and air leakage tests, most windows are tested for air leakage in a test facility designed to perform the ASTM E 283 window air leakage test method.

Q: You only calibrate *k* of the expanded polystyrene between glass. Have you attempted to calibrate the full assembly?—Jeffrey Christian.

A: There are very few ASTM C 177 guarded hot boxes or ASTM C 518 Heat Flow Meter Apparatuses that are large enough to measure the thermal conductivity of the fully assembled calibration transfer standards. Also, the relatively high and well-known thermal conductivity of glass allows the glass surface temperatures to be determined quite accurately.

Q: What is the specific density of expanded polystyrene?—Jeffrey Christian.

A: The recommended expanded polystyrene density is 20 kg/m^3 (1.25 lbf/ft^3).

☆U.S. GOVERNMENT PRINTING OFFICE:1991-500-063/22070